GEOLOGICAL AND GEOPHYSICAL INVESTIGATION OF THE SOUTHEASTERN KAROO BASIN, SOUTH AFRICA

BAIYEGUNHI, CHRISTOPHER

A dissertation submitted in fulfilment of the requirements for the degree of

MASTER OF SCIENCE

In the

Department of Geology

Faculty of Science and Agriculture

University of Fort Hare, South Africa

Supervisor: Prof O Gwavava

May, 2015

GENERAL DECLARATION BY THE CANDIDATE

I, Christopher Baiyegunhi, declare that this research study was carried out under the supervision of Prof O Gwavava. The research reported in this dissertation, except where otherwise indicated, contain the original research results and has not been previously accepted or concurrently submitted to any other university for any degree award or examination purposes. Also, where other written sources have been quoted, their words have been re-written and the general information attributed to them appropriately referenced.

Christopher Baiyegunhi

DECLARATION ON PLAGARISM BY THE CANDIDATE

I, Christopher Baiyegunhi with student number 201201530, declare that I am fully aware of the University of Fort Hare's policy on plagiarism and I have taken every precaution to comply with the regulations.

Christopher Baiyegunhi

ABSTRACT

Geological and geophysical methods were used to investigate the southeastern Karoo Basin of South Africa in an area extending from longitudes 24 ^{o} E to 29° E and latitudes 32° S to 35° S. This was undertaken in order to reveal geologic structures, isochore thicknesses of the geologic sequence and their variations across the study area, proffer the possible provenance of the sediments and assess the potential of oil and gas accumulation. The methodology used includes field investigation, rock sampling, preparation of thin sections, petrographic studies, X-ray diffraction analysis, density measurements, porosity calculations, extraction of elevation data from Google Earth, 2½ D gravity profile modelling, generating of isochore (true vertical) thicknesses and depositional surfaces maps from the models, PetroMod 1D modelling and qualitative interpretation of magnetic, gravity and radiometric maps.

Petrographic study was carried out on twenty six thin sections of rocks from the eleven geologic formations that cover the study area. Petrographic studies on the diamictite of the Dwyka Group shows abundance of monocrystalline quartz, granite and quartzite components in the breccias which possibly indicate the existence of granitic and metamorphic rocks in the source areas. The sandstones of the Ecca and Beaufort Groups are immature, greywacke and the heavy mineral assemblages signify that the minerals are of granitic, volcanic and metamorphic origin.

The magnetic maps show two main magnetic anomalies, a major one trending in a northeast to southwest direction which is part of the Beattie magnetic anomaly and another that is a "bean-shaped" anomaly. The radially averaged power spectrum shows two depths to magnetic sources. The first depth is about 0.6 km which is the average depth to the top of the shallow sources, while the average depth to the top of the deep sources is about 15 km. The shallow sources are connected to magnetic minerals within the Beaufort Group while deep magnetic sources were inferred to be in the basement.

The gamma ray spectrometric map shows areas with relatively high gamma radiation count. The high radiation count is possibly due to the uranium and thorium in the detrital materials, as well as the enrichment of radioelements in the feldspars (k-feldspar), calcite, quartz, zircon and clay minerals in the fluvial channel sandstones of the Beaufort Group.

iii

A total of two hundred and fifty-eight (258) rock samples were collected in the field and densities (dry, wet and grain densities) and porosities were determined in the laboratory. The Karoo Supergroup density values range from 2.526 – 2.828 g/cm^3. The average porosities range from 0. 49 – 3.31 %. The dry densities and porosities of all the formations are inversely correlated with correlation coefficient values (R) that range from 0.9491 - 0.9982. The density of the dolerite intrusions (mostly sill) ranges from 2.700 – 2.837 g/cm^3 whilst the porosity range from 0.1118 – 0.3868 %.

The Bouguer anomaly map shows an increase in gravity values from -140.7 mGal in inland to about 60.1 mGal in coastal areas. This dominant gravity variation is inferred to be due to a deeper basement and/or Moho that get shallower from inland towards the coast. The Moho is at about 45 km depth inland and shallows to about 42 km at the coast.

The 2½ D gravity modelling was done for fourteen (14) profiles with each profile having three (3) models corresponding to minimum, average and maximum densities to obtain the thicknesses of the geologic sequence. The current isochore thicknesses extracted from the gravity models show that the Beaufort Group is the thickest of all the groups that make up the Karoo Supergroup with maximum vertical thickness of up to 6342 ± 295 m, followed by the Ecca and Dwyka Groups with maximum vertical thicknesses of about 3207 ± 263 m and 727 ± 25 m, respectively. The maximum elevation for the Dwyka, Ecca and Beaufort sediments are about 500 m, 400 m and 285 m, respectively, whilst the maximum depth below sea level are around 8500 m, 7000 m and 5500 m, respectively.

The PetroMod1D model result yield average vitrinite reflectance and temperature values of about 6 % and 500 ℃ respectively for the lower Ecca Group which belong to the dry gas window based on classification by several authors. Thus the rocks of the lower Ecca Group are thermally matured for hydrocarbon (shale gas) generation that can merit gas exploration in the Karoo Basin.

Keywords: Gravity, modelling, Karoo Basin, provenance, density, porosity, thickness, elevation, depth and sea level.

DEDICATIONS

This research work is dedicated to God Almighty (giver of life and wisdom) and in blessed memory of my wonderful parents, Late (Mr) and Late (Mrs) D.F. Baiyegunhi.

ACKNOWLEDGEMENTS

TABLE OF CONTENTS

x

LIST OF FIGURES

LIST OF TABLES

CHAPTER ONE

GENERAL BACKGROUND

1.1 Introduction

The Karoo Basin is an extensive, dry, relatively flat area at high altitude that covers most of the internal part of South Africa and is bordered in the southern part by several Proterozoic basement rocks whilst the northern part is held by the firm Archean Kaapvaal Craton (Catuneanu *et al*., 1998). Johnson (1991) envisaged that the Karoo Basin is a retro-arc foreland basin that was formed in Late Carboniferous-Middle Jurassic at the anterior of the Cape Fold Belt due to the Late Palaeozoic to Early Mesozoic subduction event of the palaeo-Pacific plate beneath the Gondwana plate and covers approximately 700,000 km^2 (Johnson, 1991).

Cole (1992) stated that the Karoo Basin experienced episodic tectonic uplift and lithospheric sagging at about 292 Ma. This was followed with the southern overridden of the ancient-Pacific plate (Cole, 1992). Turner (1999) alludes that the numerous intrusions of dolerite sills and dykes (about 180 Ma) in the basin instigate the complex network structures of fractures and results in the formation of several shallow and deep underground permeable layers that produce water around the basin. The dolerite intrusions possibly control the morphology, recharge, drainage patterns and discharge rate at the surface through springs (Turner, 1999; Johnson *et al*., 1997).

De Wit and Ransome (1992) and Catuneanu (2004) envisaged that the Karoo basin is one of the Gondwana foreland basins (plus the Parana, Beacon, and Bowen basins) that developed in response to a convergent-margin setting along the southern margin of Gondwana during the Late Paleozoic. Tankard *et al*. (2009) alludes that each basin episode consists of a three-stage evolution comprising of crustal uplift, fault controlled, and large extents or periods of regional subsidence with subordinate faulting or erosional truncation. The large-scale episodes of subsidence were probably the result of lithospheric deflection due to subduction-driven mantle flow (Tankard *et al*., 2009).

The Karoo Supergroup in the study area comprises of the Dwyka Group, the Ecca Group and the Beaufort Group. The Lower Ecca Group comprises the Prince Albert Formation (cherty shale beds), the Whitehill Formation (black, carbonaceous shale with pelagic organisms) and the Collingham Formation (fine-grained turbidites and intercalated ashes). The Upper Ecca Group includes the Ripon Formation, Fort Brown Formation and the Waterford Formation. The Beaufort Group comprises of the Adelaide and Tarkastad Subgroups. The Adelaide Subgroup comprises of the Koonap, Middleton and Balfour Formations whilst the Tarkastad Subgroup is made up of the Katberg and Burgersdorp Formations.

Due to differences in facies, provenance, direction of transport, age of units and stacking patterns, Catuneanu *et al*. (1998) divided the Karoo Basin into three lithostratigraphic provinces which include the western province (west of 24° meridian), southeastern province (east of 24° meridian) and northern province (north of latitude 30°). Much geological work has been carried out on the northern and the western provinces compared to the eastern province of the Karoo Basin because of the presence of coal and other economic minerals such as uranium and molybdenum.

Aeromagnetic data in the southern Karoo Basin shows a clear set of magnetic anomalies such as the Beattie magnetic anomaly (BMA) and the Southern Cape Conductivity Belt (SCCB). These anomalies run east to west and are confined to the basement that underlies the Karoo Basin. Weckmann *et al*. (2007a and 2007b) envisaged that the Beattie magnetic anomaly (BMA) is the largest, with magnitude which ranges from 200 - 500 nT making the BMA one of the largest magnetic anomalies in the world (Lindeque *et al*., 2007; 2011). Pitts *et al*. (1992) proposed that the anomaly may be due a body that stretches from 7 - 30 km below the surface and they concluded that serpentinised oceanic crust could be the source of the anomaly. However, recent magnetotelluric surveys show no sign or proof for such a body (Branch *et al.,* 2007; Weckmann *et al*., 2007a and 2007b).

In South Africa, unconventional shale gas was identified in the Whitehill and Collingham Formations of the Ecca Group in the 1960s, but exploration stopped in the late 1970s due to poor technical know-how (Cole, 1992; Branch *et al*., 2007). Recently, shale gas has become important in the last few years and the main exploration target is focused onshore (Karoo Basin) due to the recent global success in technological advancements in recovering petroleum from low permeability reservoirs (i.e., shale), belief that natural gas is an

economically feasible fossil fuel for generating electricity and high productivity of gas turbines with lower carbon emission. Thus reducing pollution and increasing the decarbonisation of the world economy (De Wit and Horsfield, 2006).

The report presented by the Energy Information Administration (2013) indicates that South Africa generates most of its energy from coal (67 %), oil (19 %), solid biomass and waste (10 %). A small quantity of energy derived from natural gas (2 %), nuclear (2 %) and hydroelectricity (< 1 %). South Africa is the leading emitter of greenhouse gases in Africa and the 12th leading emitter in the world because of its high dependence on hydrocarbons, especially coal (which are high in carbon emission) for energy generation which is regulated by the National Energy Regulator of South Africa (NERSA).

Recent analysis by Decker and Marot (2012) and Advanced Resources International (2013) suggests that the Southern Karoo has potential reserves that range from 32 - 485 trillion cubic feet of technically recoverable shale gas resources. The main concern on shale gas exploration and exploitation is the water usage and environmental impact of hydraulic fracturing. However, it is possible to frack shale gas with only liquefied propane gas that greatly reduces environmental degradation (Bajus, 2014).

The development of a simple tectonic model will help in understanding and interpretation of the possible source of the Beattie magnetic anomaly, establishing relationships between geologic structures (e.g. dolerite sills and dykes) at depth and the possible environmental impacts of fracking the Karoo for possible shale gas which will serve as an alternative source of energy generation in order to meet the increasing demand for power generation and reduce the dependence on coal which is the major source of environmental pollution. If the relationships are established and related to fracking the Karoo for shale gas, if feasible, will lead to the development of a new natural gas plant that would assist in meeting the increasing demand for energy by providing the country with a reliable fuel alternative to coal for generating electricity for houses and businesses.

1.2 Problem statement

This research study aims at addressing the following issues:

- More geophysical studies still need to be carried out in the southeastern part of the Karoo Basin in order to reveal the basin dynamics and depositional systems. However, several researchers like Weckmann *et al*. (2007a; 2007b), Lindeque *et al*. (2007; 2011) Tankard *et al*. (2009; 2012) have investigated the area.

- Up to now, no relationship between geological structures (interconnectivity of dolerite intrusions) at depth has been established. Therefore the environmental impact of fracking the Karoo for shale gas could not be assessed despite the fact that dolerite dykes are groundwater localizers in the Karoo, which is the major source of water to the country at large (Chevallier *et al*., 2001; Van Zijl, 2006; Kakaba, 2010).

- Variation in thicknesses within the geological sequence (group) in the southeastern Karoo Basin has not been established. The Southern Oil Exploration Corporation (SOEKOR) deep borehole in the coastal area near East London gives the thickness of the groups, but this thickness varies across the study area as a result of deformation. Thus, there is need to derive sediment thicknesses and how it varies across the study area, as well as ascertains if the thickness of the sediments across the study area will support accumulation of hydrocarbons in areas that host source rock potential for hydrocarbon generation with the presence of other factors that favours hydrocarbon accumulation.

- To date, the precise source for the Beattie magnetic anomaly (BMA) that is linked to the continuous shallow and regional band of high magnetic susceptibility is still debatable.

1.3 Objectives of the research

The main objective of this research study is to investigate the southeastern Karoo Basin in the Eastern Cape Province of South Africa, with the use of existing geophysical data and field inspections in order to have an overview into the basin dynamics and depositional systems involved. The aims of this research study include:

- To use existing aeromagnetic data to generate geophysical maps in order to reveal sub-surface geologic structures of interest such as dolerite intrusions in the study area and conduct radially averaged spectrum analyses to determine depths.

- To elucidate the structure of the southeastern Karoo Basin by building a simple model using forward modelling of gravity data along a number of profiles traversing the study area.

- To develop an isochore thickness map (an isochore thickness map shows/connects lines of equal thickness in a layer where the thicknesses are measured vertically) from the gravity models that will show variation in sediment thicknesses for the geological groups that make up the Karoo Supergroup.

- To investigate the sedimentary structures, study rock thin-sections and complement the observations with XRD analyses in order to determine the mineralogical composition and possibly indicate the sediment source area.

- To use geological and geophysical results to generate the petroleum models and check whether the rocks of the lower Ecca Group possess potential to generate hydrocarbons that can enhance exploration of gas (i.e., shale gas) in the Karoo Basin.

1.4 Delineation and limitations

This research work covers the southeastern part of the Karoo Basin, South Africa. The gridded radiometric and magnetic data supplied by the Council for Geoscience, South Africa could only be used for qualitative interpretation. In 1982, magnetic and radiometric surveys were flown over the Eastern Cape Province, South Africa by Fugro Airborne Surveys. The gamma ray survey was flown in blocks along a north-south direction at 80 m above the

ground level with 200 m line spacing and data (total count) were collected over a sample interval of 1 s. The fixed-wing aircraft traverses about 55 m along the line during the sample interval. The magnetic data had a 1975 IGRF removed and the different datasets merged. This produced magnetic values that were negative and a constant of 3960 nT was added to give positive values.

The limitation of this work includes;

- This research study uses geological and geophysical results to generate the petroleum models and check whether the rocks of the lower Ecca Group possess potential to generate hydrocarbons.

- The geophysical work is limited to profile modelling using only the gridded gravity data rather than the station data. The magnetic dataset was used for depth determination using radially averaged power spectrum.

- The research study considers field investigation (sedimentary structures), thin sections and x-ray diffraction analysis (the grain size, shape, and heavy minerals) for possible source area of the sediments. The petrographic work does not consider graphical plot (quartz or microcrystalline quartz - feldspar- lithic fragments), modal and geochemical analysis for sediment provenance.

1.5 Location of the study area

The study area lies between longitudes 24 ^{o} and 29 ^{o} E and between latitudes 32 ^{o} and 35 ^{o} S in the Eastern Cape Province of South Africa (Figure 1.1). The area covers the northwest of Graaff-Reinet, extends to the northeast of Butterworth and continues to the west of Humansdorp (see Figure 1.2). The area is linked by two major regional routes (R63 and R75) and one national route (N2). The N2 between Humansdorp and Port Elizabeth connect to Butterworth and R63 connects the N2 between East London and Butterworth to Graaff-Reinet via Pearston which is hilly to mountainous. The R75 from Graaff-Reinet connects the N2 between Humansdorp and Port Elizabeth via Uitenhage (Figure 1.2).
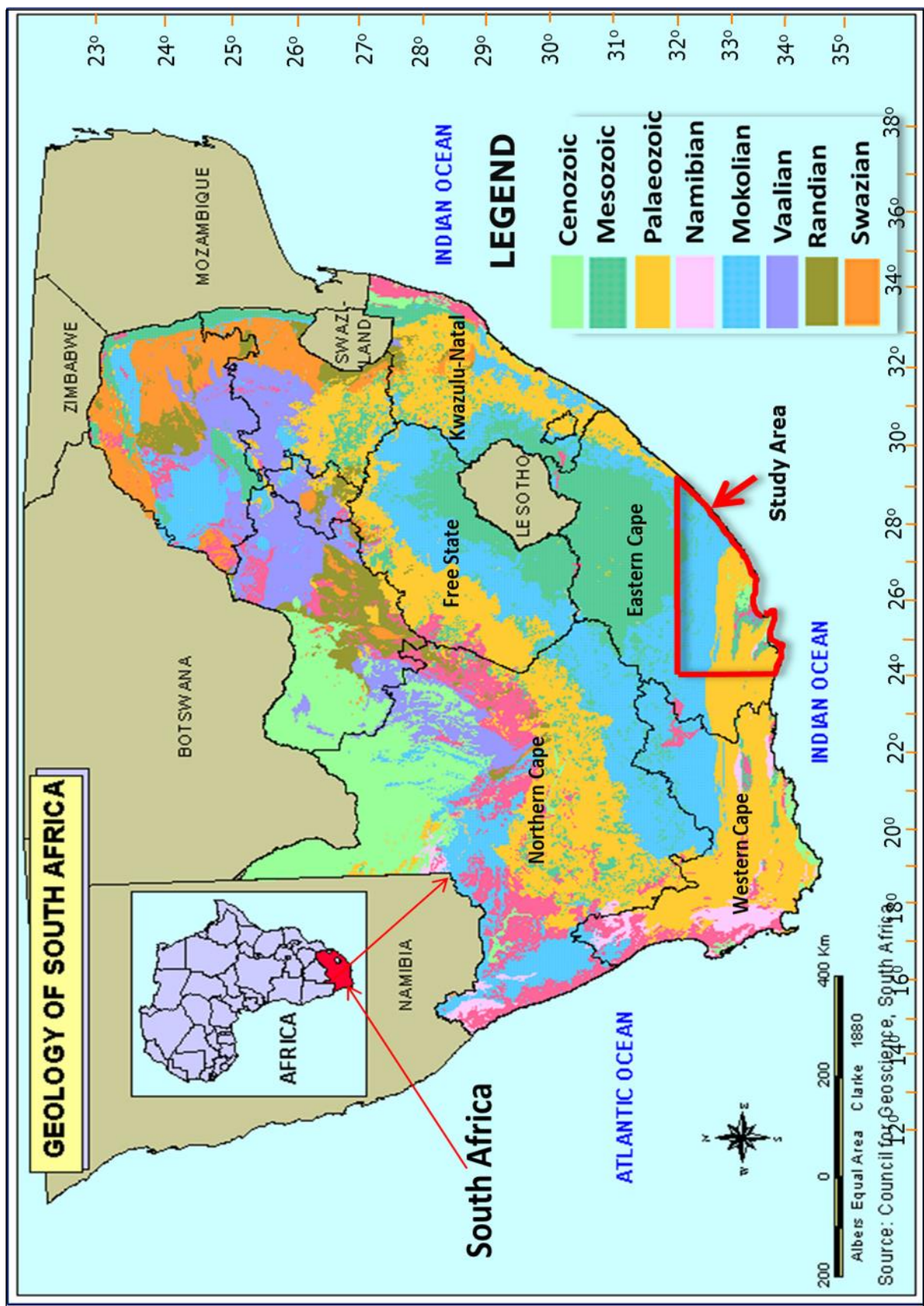
Figure 1.1 Geological map showing location of the study area (Modified after Council for Geoscience, 1995).
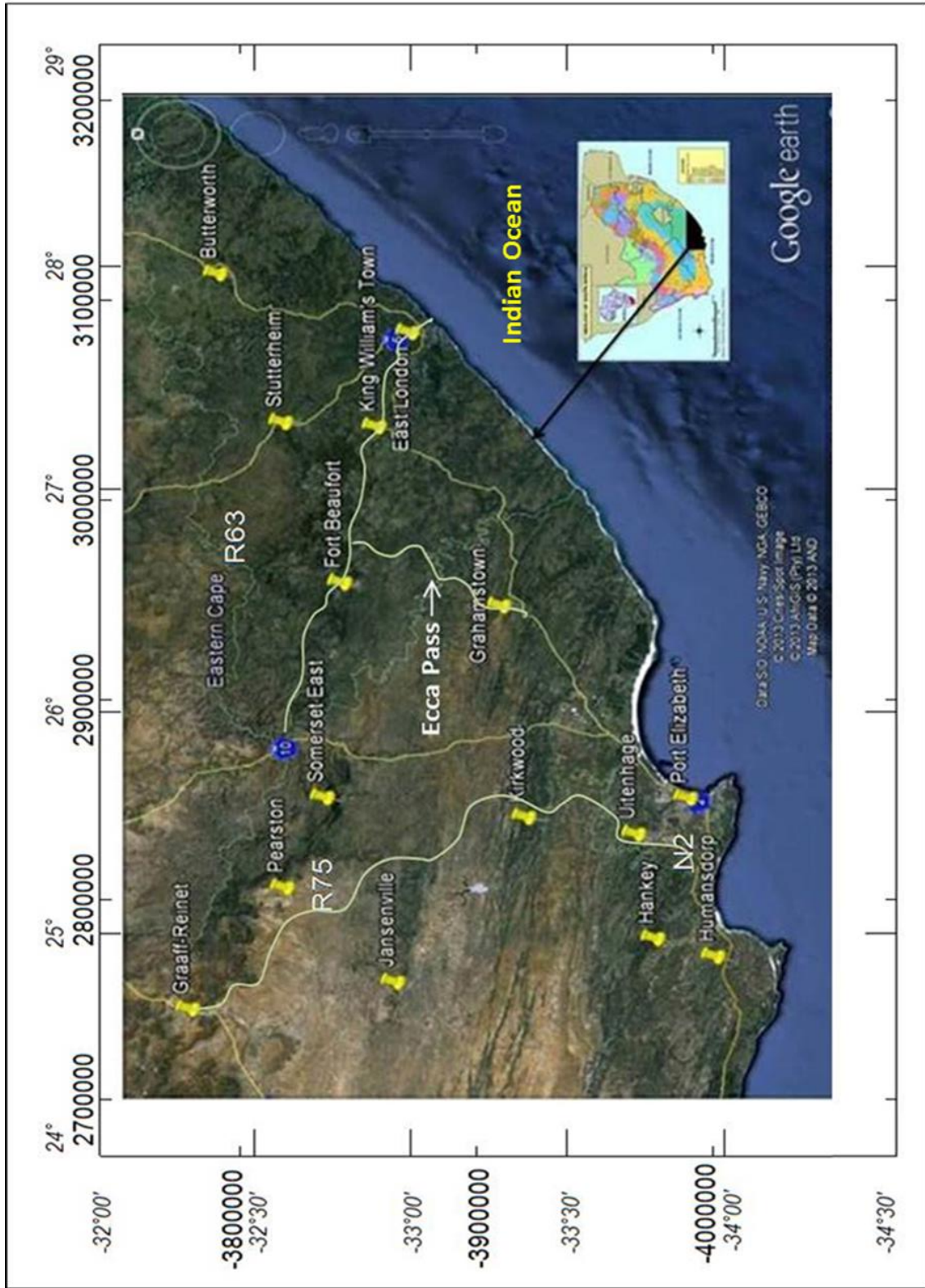
Figure 1.2 Google Earth view of the study area (Google Earth, 2013).

GEOLOGICAL SETTING

2.1 Geological background

The main Karoo Basin in South Africa is a unique type of basin of all the Karoo basins in southern Africa (see Figure 2.1) because it contains the most complete, thickest and large sequence of the Late Carboniferous - Early Jurassic age basins of palaeo-southwestern Gondwana that serves as a datum for classifying Karoo basins in central and southern Africa. According to Catuneanu *et al.* (1998), the Karoo Supergroup is believed to have developed from the Gondwana Supercontinent. Evidence in support of this has been noted from the similarities in strata of the Carboniferous to Jurassic period in all the continents and islands of the Southern Hemisphere (Johnson *et al*., 2006).

Figure 2.1 The Karoo basins in Southern Africa (Modified from Segwabe, 2008).

9

According to Geel *et al*. (2013), the Karoo Basin of South Africa covers up to 300, 000 km^2 and represents about 100 Ma of sedimentation spanning from 280 Ma to 180 Ma, and has its rocks covering almost half of the area of South Africa (Johnson *et al*., 2006). Geel *et al*. (2013) also envisaged that the deposition of Karoo sedimentary rocks occurred during the Late Carboniferous across the Gondwana, and span until the breakup of the Gondwana supercontinent during the Middle Jurassic (about 183 Ma). This resulted in the building of the wide fold thrust belt that is known today as the Cape Fold Belt. Smith *et al*. (1993) stated that orogenic loading and unloading in the Cape Fold Belt controls deposition of the different formations in the basin and indicates that the environment changes gradually from glacial to deep marine, deltaic, fluvial and finally to aeolian.

Catuneanu *et al*. (1998) stated that the Cape Supergroup was deposited prior to, and in early stages of folding whilst the Karoo Supergroup is inferred to represent syn-tectonic sedimentation in a foreland basin. The Cape Fold Belt was deformed in a Carboniferous - Permian compressional event (De Wit and Ransome, 1992) generally known as the Cape orogeny. The compressive foreland system that existed north of the Cape Fold Belt developed in response to the Late Palaeozoic - Early Mesozoic subduction of the Palaeo- Pacific plate beneath the Gondwana plate (Catuneanu *et al*., 1998). Hancox (1998) and Catuneanu *et al*. (1998) envisaged that the flexural tectonism of the foreland system was drawn to a close during the first order unloading event which persisted from the Late Triassic until the Middle Jurassic. Visser (1993) alludes that the northward subduction of the Panthalassan plate beneath Gondwana result in the formation of a magmatic arc situated between the Karoo basin and the southern margin of Gondwana.

Smith (1990) in Catuneanu *et al*. (1998) alludes that the maximum preserved thickness of the mega-sequence which is adjacent to the Cape Fold Belt is greater than 6 km in thickness. Sedimentation in the Karoo Basin continued across Gondwana until the rifting of the supercontinent in the Middle Jurassic, thus resulting in the difference of the Karoo-age successions (Catuneanu *et al*., 2005). The Karoo Basin was formed as a result of block subsidence along major marginal faults and the sedimentary fill of the Karoo Basin were accumulated under the influence of tectonism and climate (Catuneanu *et al*., 2005).

Tankard *et al.* (2009) stated that the Cape and Karoo basins represent two large-scale episodes on intermittent subsidence and sedimentation within the interior of Gondwana.

According to Cloetingh *et al*. (1992), the Early Ordovician to Early Carboniferous Cape basin (160 Ma) is suggested to have formed as a result of extensional processes in an episutural setting. After a 30 Ma hiatus, the Late Carboniferous to Jurassic Karoo basin (125 Ma) developed as a tabular cratonic cover. Geel *et al*. (2013) allude that the Karoo basin has been interpreted as a foreland trough that was formed due to the shallow-angle subduction of the paleo-Pacific plate beneath Gondwana supercontinent. Tankard *et al*. (2012) stated that the Cape Fold Belt is a strike slip belt and referred to the adjacent Karoo Basin as a flexural foreland basin based on the basement architecture, timing of the Cape orogeny, and stratigraphic relationships which indicate a flexural foreland basin.

De Wit and Ransome (1992) and several researchers like Veevers *et al*. (1994), Visser (1995) and Catuneanu *et al*. (1998) envisaged that the Karoo Basin is a retro-arc foreland basin. However, Tankard *et al*. (2009) give an alternative interpretation for the tectonosedimentary evolution of the Karoo Basin by dividing it into a pre-foreland phase and a foreland phase. According to Tankard *et al*. (2009), the pre-foreland Karoo Basin that comprises of the Dwyka, Ecca and lower Beaufort Groups, developed within the continental interior of Gondwana due to vertical movement of rigid or firm blocks and intervening crustal faults. The foreland Karoo Basin (comprising of the upper Beaufort Group) developed as a response to the uplift of the Cape Fold Belt during the Early Triassic. Lindeque *et al*. (2011) and Pangaro and Ramos (2012) suggested that the Cape Fold Belt could be a (Jura-type) fold belt that developed as a result of arc-continent collision with subduction to the south.

The Karoo Basin is well-known globally due to its large quantity of fossil tetrapods and this led to the generation of enormous amounts of scientific information. The large quantity of tetrapod fossils from the rocks has enhanced stratigraphic correlation (Catuneanu *et al*., 2005). Much geological investigation in the southern Karoo Basin, South Africa, has been carried by researchers like Geel *et al*. (2013), Tankard *et al*. (2012), Tinker *et al*. (2007), Catuneanu *et al*. (2005), Stavrakis (1980), Tordiffe (1978), Kingsley (1977), and Johnson (1976). Geel *et al.* (2013) studied shale gas characteristics of Permian black shales in South Africa, Tankard *et al*. (2012) worked on the geodynamic interpretation of the Cape and Karoo basins, South Africa, Tinker *et al*. (2007) investigated the Mesozoic uplift of southern Africa using fission track thermochronology and offshore sediment volumes to test the balance between onshore denudation and offshore accumulation since Gondwana break-up. Catuneanu *et al*. (2005) examined the Karoo basins of south-central Africa; Stavrakis (1980)

worked on the Katberg Formation. The hydrogeochemistry of the Karoo Sequence in the Fish River Basin was studied by Tordiffe (1978), while Kingsley (1977) investigated the depositional sequence in the Cape and Karoo Supergroup.

2.2 Tectonic setting of the Karoo Basin

The Karoo Supergroup is believed to have originated from the Gondwana Supercontinent (Catuneanu *et al.,* 1998). The several lithospheric plates that separated to form the current Southern Hemisphere continents and India (see Figure 2.2) was once together as the Gondwana supercontinent. The southern African remnant of these continents contains the Karoo basins that include the main Karoo Basin and Great Kalahari Basin (Kalahari Karoo, Aranos, and Mid-Zambezi Basins), as well as other smaller basins in South Africa, Namibia, Zimbabwe and Mozambique (Figure 2.1). According to Smith (1995), the Karoo Supergroup is a 12 km thick sequence of sedimentary rocks that was deposited in a large intracratonic retroarc foreland basin in southwestern Gondwana. The strata record 100 million years of almost continuous sediment accumulation from the Permo-Carboniferous (300 Ma) through the Early Jurassic (about 190 Ma) under different climatic regimes and within several tectonically controlled sub-basins (Catuneanu *et al.,* 1998; 2005).

Catuneanu *et al*. (2005) stated that the Karoo Supergroup has evolved from two distinct tectonic regimes sourced from the southern and the northern margin of Gondwana. The southern tectonic regimes are believed to be related to processes of subduction and orogenesis along the Panthalassan (paleo-Pacific) margin of Gondwana, this resulted in the formation of a retroarc foreland system known as the "main Karoo Basin" in association with the primary subsidence mechanism represented by flexural and dynamic loading. The northern event was associated with extensional stresses that propagated southwards into the supercontinent from the divergent Tethyan margin of Gondwana. Superimposed on the tectonic control on basin development, climate fluctuations also left a mark on the stratigraphic record, which shows evidence of a general shift from cold and semi-arid conditions during the Late Carboniferous - Earliest Permian interval, to warmer and eventually hot climates with fluctuating precipitation during the rest of the Karoo time (Keyser, 1996 in Catuneanu *et al*., 2005).

Figure 2.2 Palaeogeography reconstruction of the Karoo basin and Gondwanaland during the Late Paleozoic showing accretionary foreland basins (Turner, 1999).

According to Catuneanu *et al.* (2005) in Alao and Mikes (2011), the Karoo Basin in South Africa was deposited behind a magmatic arc and formed at the anterior of the Cape Fold Belt. Visser (1995) stated that the Permian Karoo tectonic framework in most of southern Africa was characterized by a transition from the back-arc basin to a foreland basin setting. The loading and unloading event (thrusting and extension) in the Cape Fold Belt occurred due to the "Late Palaeozoic - Early Mesozoic subduction episode of the paleo - Pacific plate beneath the Gondwana plate" thus resulting in crustal thickening and shortening (Catuneanu *et al.*, 2005; Johnson *et al.*, 2006; Flint *et al.*, 2011; Figure 2.3). According to Flint *et al.* (2011), the detailed record for southern Africa, is still less complete when compared to South America and Antarctica, as a result of the major Mesozoic regional strike-slip and extensional tectonics that removed most of the late Palaeozoic record to the south of the present day South Africa.
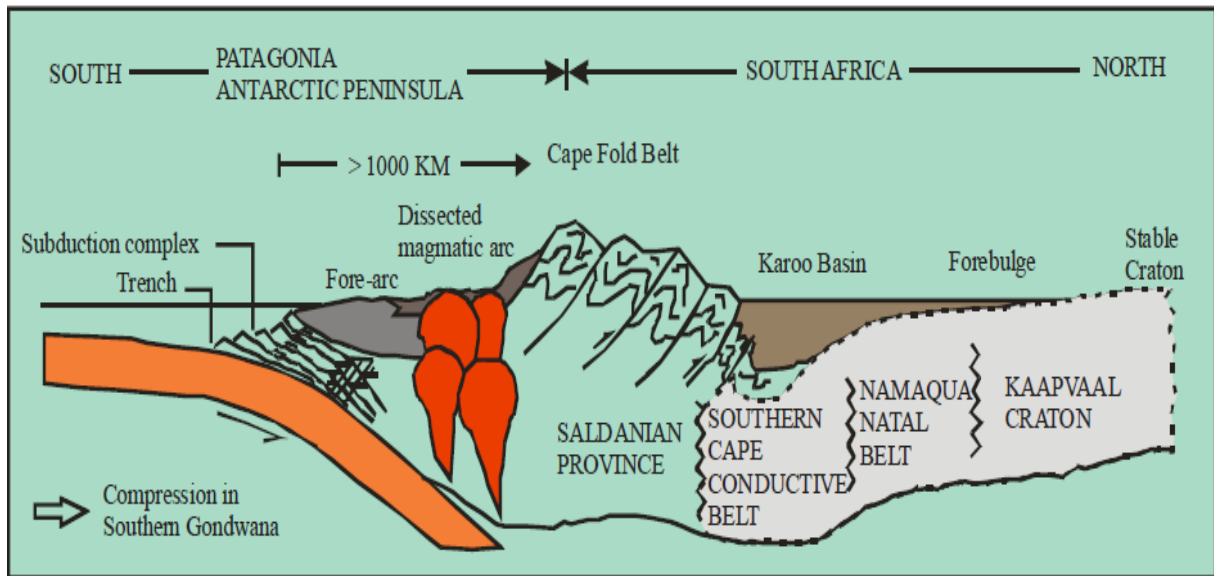
Figure 2.3 The generalized foreland basin model of the Karoo basin during the Triassic period, showing the location of the foredeep and forebulge parts of the basin in relation to the Cape Fold Belt, and the inferred position of the arc and subduction zone (Turner, 1999).

Visser (1997) and Tankard *et al*. (2009) explained that, from the Early Ordovician to Early Jurassic, two sedimentary mega-successions (Cape and Karoo basins) separated by a major unconformity were deposited in two laterally offset major sedimentary basins in southern Africa. The Cape Supergroup (Cape basin) spans from the Early Ordovician to Early Carboniferous (Veevers *et al*., 1994), and consists of up to 8 km of shallow marine, deltaic and fluvial deposits that thicken southwards into an east-west trending depo-axis (Rust, 1973; Turner, 1999). According to Tankard *et al*. (1982), these sediments were believed to have been derived from a cratonic source to the north. The overlying Karoo Supergroup (Karoo Basin) that spans from the Late Carboniferous to Early Jurassic period and consists of about 12 km of deep marine to fluvial deposits. Visser and Praekelt (1996) stated that the Karoo-Falklands basin, the Sierra Australise Colorado basins (Argentina), as well as the Central Antarctic Mountains basin were developed as extensional back-arc basins, in relation to the oblique subduction of the paleo-Pacific plate beneath the western Gondwana. Several major strike-slip systems begin to develop, with the Southern Trans-African Shear system, within the Damara mobile belt. According to Stollhofen *et al*. (2000), all the Karoo basins in southern Africa can be attributed to the extensional intracratonic rifts, in relation to the N-S trending basement shear zones.

14

Catuneanu and Elango (2001) stated that the episodes of thrusting (loading) and extension/erosion (unloading) in the Cape Fold Belt closely controlled deposition of sediment in the Karoo Basin. Catuneanu (2004) alludes that these episodes of thrusting and extension/erosion in the Cape Fold Belt resulted in the different depocentre within the Karoo Basin. The loading was more pronounced or evident during Late Carboniferous - Middle Triassic time. This resulted in the accumulation of thick "foredeep sequences that are rich in forebulge correlatives" whilst extension/erosion was dominant during Late Triassic-Middle Jurassic time leading to more sediment deposition in the "distal region of the foreland system and coeval bypass and modification of the older foredeep sequences" (Catuneanu *et al*., 1998). The main Karoo Basin becomes thinner from the south to the north as shown in Figure 2.4. This idea is also supported by Catuneanu *et al*. (2005) who described the Molteno Formation as northerly thinning (Figure 2.4).
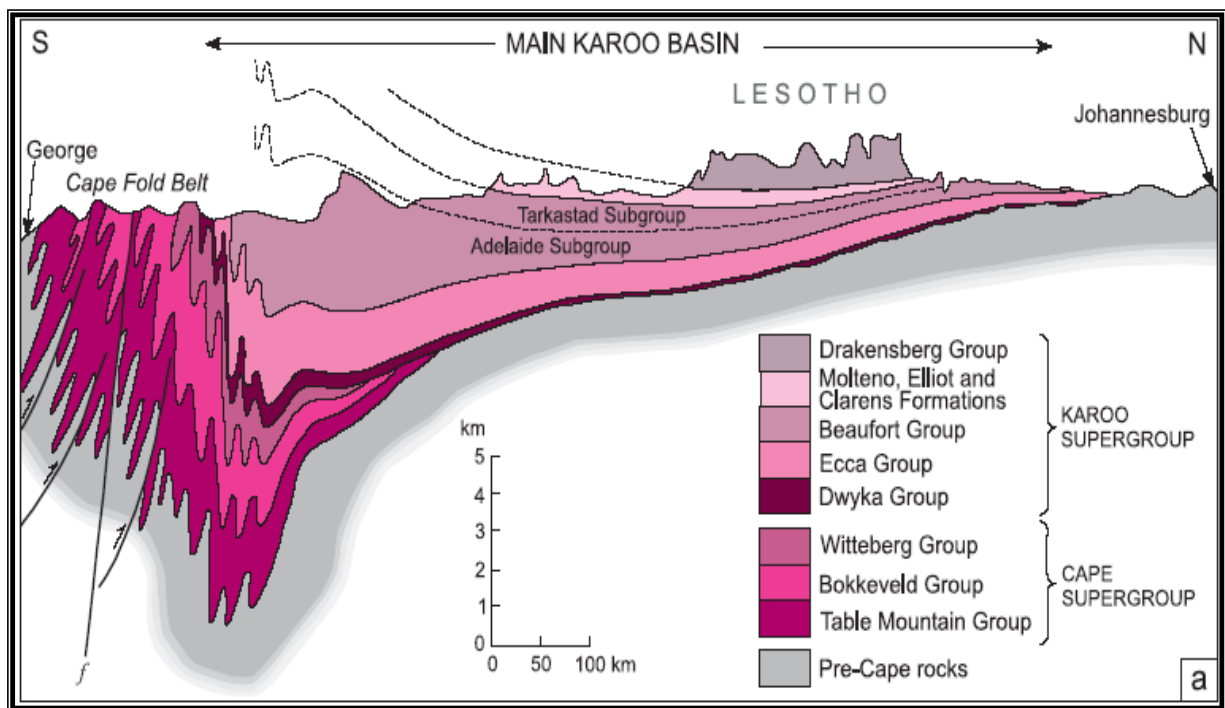
Figure 2.4 Section view of Karoo Supergroup, showing the thinning effect and also the tectonic settings (Johnson *et al*., 1997).

Catuneanu and Elango (2001) envisaged that the main Karoo Basin can be categorised as a retro-arc foreland basin (De Wit and Ransome, 1992; Johnson et al., 2006). De Wit *et al.* (1988) in Smith (1995) stated that the interior position of the basin was possibly controlled by

15

the re-activation of the Late Proterozoic Cape Conductive Belt in which the sediments of the Cape Supergroup had previously accumulated. The importance of the tectonic control on Karoo Basin development and sedimentation was first proposed by Rust (1975) and subsequently modified by several authors (e.g. Tankard *et al*., 1982; Smith *et al*., 1993; Veevers *et al*., 1994; Johnson *et al*., 1996). However, Visser (1987) and Catuneanu *et al*. (1998; 2002, and 2005) suggested the evolution of the retro-arc foreland Karoo Basin in relation to fold-thrust belt inboard of magmatic arc. Williamson (1996) and King (2005) associated it with the Cape fold belt subduction.

Ingersoll and Busby (1995) define a retro-arc foreland basin as a "foreland basin on the continental flanks of continental-margin arc-trench systems developed by collision, compression and subduction". This definition of a retro-arc foreland basin matches the general interpretation of the Karoo Basin. Smith (1990) envisaged that the continual re-initiation of the Late Proterozoic Southern Cape Conductive Belt (SCCB) possibly results in the present internal location of the southern Karoo Basin. Lindeque *et al*. (2007) documented that the foreland system of the Karoo Basin has been subdivided into foredeep and forebulge flexural provinces by a hinge-line (Johnson *et al*., 1997). Catuneanu *et al*. (2002) stated that the result of the mapping of this hinge-line in the Cape Fold Belt for successive time-slices shows that the hinge-line has slightly changed along a dip due to the restructuring of sediments through erosion during the Late Carboniferous - Middle Triassic time within the Cape Fold Belt (Catuneanu *et al*., 1998). The foreland system migrates during crustal extension/erosion of the depocentre towards the extreme end of the system creating contrasting stratigraphy between the nearby and faraway regions within the Karoo basin (Cole, 1992; Catuneanu *et. al*., 1998; Lindeque *et al*., 2007).

A regional aeromagnetic survey in the southern Karoo Basin shows a clear set of magnetic anomalies (Beattie magnetic anomaly and Southern Cape Conductivity Belt) that runs east to west and confined to the basement that underlies the Karoo Basin (Weckmann *et al*., 2007a and 2007b; Figure 2.5). The largest known magnetic anomaly in the southern Karoo Basin is the Beattie magnetic anomaly (Lindeque *et al*., 2007). Weckmann *et al*. (2007a) envisaged that the magnitude of the Beattie magnetic anomaly (BMA) ranges from 200 - 500 nT, thus making the BMA one of the world's largest magnetic anomalies. The Beattie magnetic anomaly (BMA) was observed in the southern part of the basin and runs east to west for approximately 1000 km across South Africa.
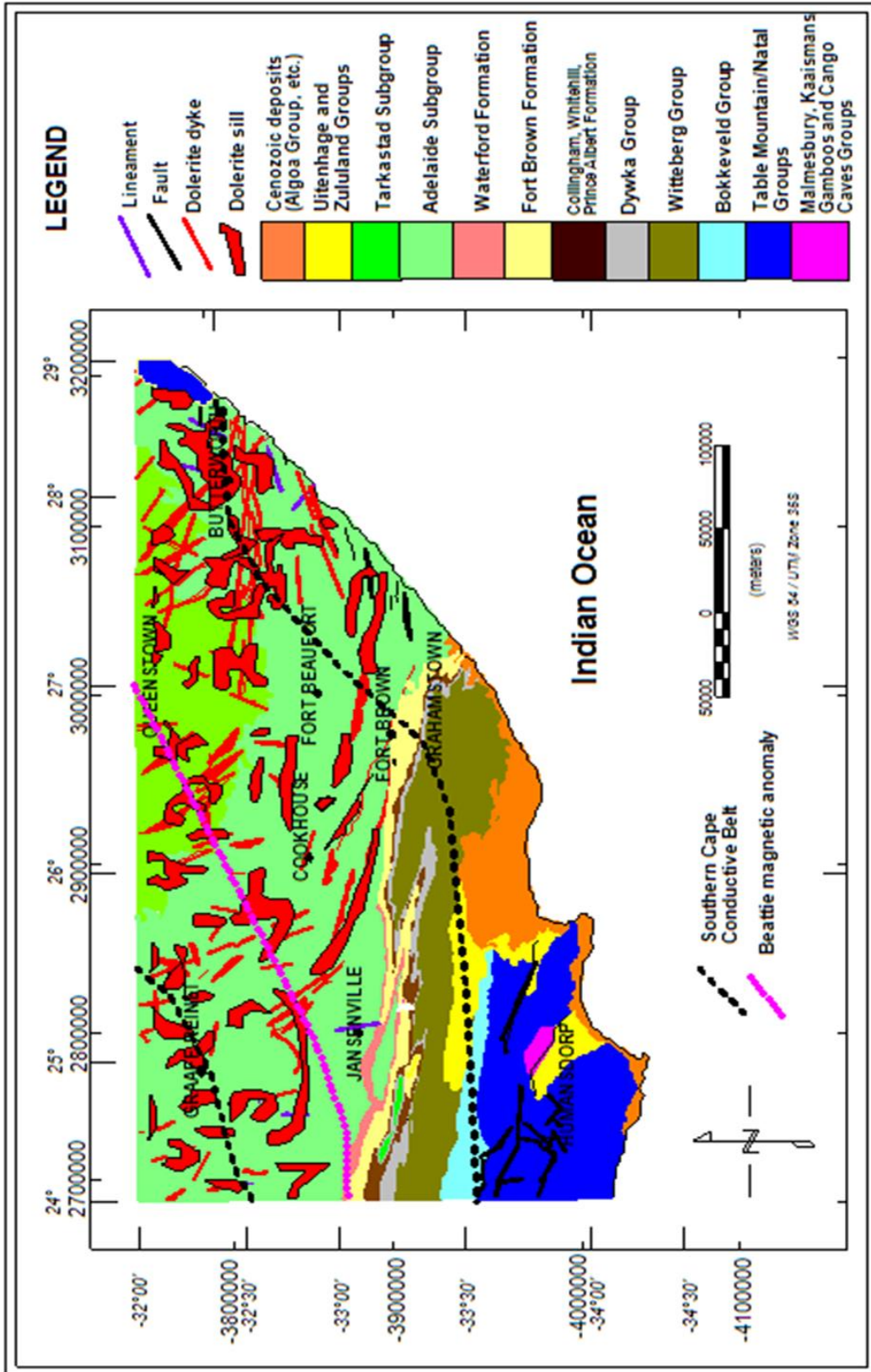
Figure 2.5 Geological map of the study area. The map also shows dolerite intrusions (sills and dykes), faults, part of the Beattie magnetic anomaly and the Southern Cape Conductive Belt (After Council for Geoscience, 1995).

The crustal source of the BMA was proved with the use of Curie isotherms by De Beer and Gough (1980). Pitts *et al.* (1992) proposed that the BMA may be due to a magnetic body that extends from 7 - 30 km underneath the surface, they resolved that serpentinised oceanic crust could be the source of the anomaly (BMA). But, a recent magnetotelluric survey shows no indication or sign for such a body (Weckmann *et al.*, 2007a). The BMA was first detected by Beattie (1909) and several reasons have been proposed for the anomaly (Stephanie *et al.*, 2013). Due to insufficient geophysical information, the source of the BMA still remains unknown to date (De Wit and Horsfield, 2006).

Harvey *et al.* (2001) suggested that the upper and lower boundaries of the magnetic anomaly are due to two crustal discontinuities in the region that were identified at depths of $7 - 11$ km and from 17 - 19 km. A zone of electrical conductivity was observed in the region known as the Southern Cape Conductive Belt (SCCB) which was first identified by Gough *et al.* (1973) and later compared with the Beattie magnetic anomaly (Lindeque *et al.*, 2007). They suggested that the BMA and SCCB have a common source and that the conductive material which trends east-west beneath the southern Karoo Basin and Cape Fold Belt lies in the crust. Both anomalies were seen to be parallel to the tectonic edge or margin of the Namaqua-Natal Mobile Belt (NNMB) and the Cape Fold Belt (CFB) which infers that the tectonic structures resulted from the continual addition or deposition of sediments over time (Harvey *et al.*, 2001; Lindeque *et al.*, 2007).

According to Gough *et al.* (1973), the BMA spatially coincides with a $100 - 200$ km wide electrically conductive zone known as the Southern Cape Conductivity Belt (Lindeque *et al.*, 2007). Stephanie *et al.* (2013) also emphasized on the importance of understanding the source of the BMA in order to ascertain or create a precise potential model of the Karoo Basin and to know the evolutionary history of the Karoo Basin. The model (see Figure 2.6a) shows a high conductivity anomaly at a depth of 7 - 15 km beneath the BMA and a "shallow, sub-horizontal conductive band that is regionally continuous in the Karoo sedimentary basin" and was linked to the pyritic carbonaceous marker horizon with thickness of 50 - 70 m in the Whitehill Formation (Thomas *et al.*, 2007; Lindeque *et al.*, 2007; 2011; Tankard *et al.*, 2012).
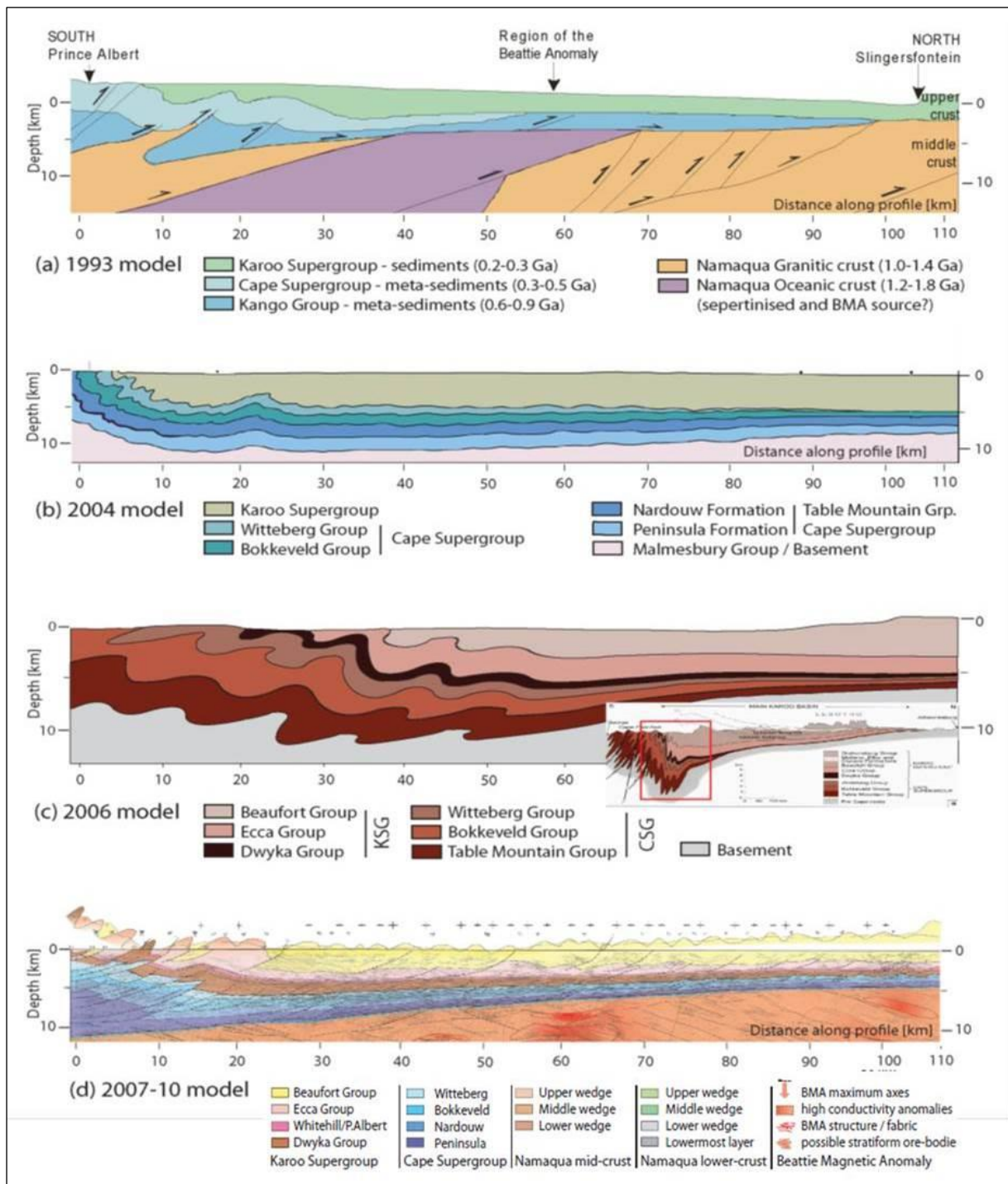
Figure 2.6 Comparing models of the Cape and Karoo Basins in the upper crust (< 15 km). (a) Hälbich *et al*. (1993) model: Ophiolite wedge/serpentinised palaeoceanic crust as the possible source of BMA. (b) Chevallier *et al*. (2004) model: Karoo Supergroup undifferentiated. (c) Johnson, *et al*. (2006) model: Close-up from the regional model. (d) 2007- 2010 model: these models show intense folding, deepening and thickening of the Karoo Supergroup before the Cape Fold Belt which was interpreted as a fore-deep basin (Taken directly from Lindeque *et al*., 2011).

Lindeque *et al*. (2007) stated that a seismic survey across the western part of the BMA shows an anomaly source depth of 10 - 15 km within the mid-crust which was earlier assumed to be due to the partially serpentinized oceanic lithosphere probably connected to a suture zone (De Beer and Meyer, 1983; Hälbich *et al.,* 1983; Hälbich, 1993). However, Lindeque *et al*. (2011) as well as Stephanie *et al*. (2013) suggested that the BMA is part of the tectono-metamorphic Namaqua-Natal Mobile Belt (NNMB) and associated shear zones.

Weckmann *et al*. (2007a and 2007b) explained that the base of the high conductivity anomaly fits perfectly on top of the unconformity between the Karoo and the underlying basement. The inversion result indicates that the conductive anomaly that is lesser than the peak of the BMA cannot be used to explain the SCCB and the narrow region of high electrical conductivity could be due to a mineralized shear zone that cuts through the magnetic source (Weckmann *et al*., 2007a; 2007b).

The tectonic model shown in Figure 2.6d signifies deformation along low angle listric fault that was observed in the local décollement surfaces of the Whitehill and Prince Albert Formation of the Ecca Group, absence of a remarkable fore-deep basin in the southern Karoo and shortening at the Cape Fold Belt tectonic-front with the aid of numerous low-angle listric thrusts and folds that were detached from the Namaqua-Natal Metamorphic Belt basement and the Karoo Supergroup (Lindeque *et al*., 2011).

2.3 Stratigraphy of the Karoo Basin

The Karoo Basin fill that is seen along the Eastern Cape Province of South Africa started with the deposition of the glacial sediments of the Dwyka Group with a thickness of approximately 600 m - 700 m (Johnson *et al*., 2006). This formation is overlain by the postglacial Ecca Group (Prince Albert, Whitehill, Collingham, Ripon, Fort Brown and the Waterford Formations), followed by the Beaufort Group (Koonap, Middleton, Balfour, Katberg and Burgersdorp Formations) and Stormberg Group (Molteno, Elliot and Clarens Formations). The whole sequence of deposition is covered by the basalt and pyroclastic deposits of the Drakensberg Group (see Table 2.1).

Table 2.1 Lithostratigraphy of the Karoo Supergroup in the Eastern Cape Province compiled by the Council for Geoscience (Johnson *et al*., 2006).

SUPERGROUP	GROUP	SUBGROUP	FORMATION	MEMBER	LITHOLOGY	MAXIMUM THICKNESS (M)
KAROO			Drakensberg		Basalt Pyroclastic Deposits	1400
			Clarens		Sandstone	300
			Elliot		Red Mudstone Sandstone	500
			Molteno		Coarse Sandstone Grey & Khaki Shale Coal Measures	450
	BEAUFORT	TARKASTAD	Burgersdorp		Red Mudstone Light Grey Sandstone Grey Shale	1000
			Katberg		Light Grey Sandstone Red Mudstone Grey Shale	900
		ADELAIDE	Balfour	Palingkloof	Red Mudstone Light Grey Sandstone Grey Shale	50
				Elandsberg	Sandstone Siltsone	700
				Barberskrans	Light Grey Sandstone Khaki Shale	100
				Daggaboersnek	Grey Shale Sandstone Siltsone	1200
				Oudeberg	Light Grey Sandstone Khaki Shale	100
			Middleton		Grey & Black Shale Light Grey Sandstone Red Mudstone	1500
			Koonap		Grey Sandstone Shale	1300
	ECCA		Waterford (Not present in Ecca Pass)		Sandstone Shale	800
			Fort Brown		Shale Sandstone	1500
			Ripon		Sandstone Shale	1000
			Collingham		Grey Shale Yellow Claystone	30
			Whitehill		Black Shale Chert	70
			Prince Albert		Khaki Shale	120
			Dwyka		Diamictite, Tillite, Shale	750

The stratigraphy of the Karoo Supergroup indicates distinct changes between the southern and northern parts of the basin. These changes across the flexural hinge line of the basin reveal conflicting tectonic pasts (Catuneanu *et al.*, 1998). Johnson (1991) stated that the filling of the Karoo Basin started with the carbonaceous glaciogenic Dwyka Group. The Dwyka Group consists of glacial diamictites and shales. These glacigenic sediments were deposited from Late Carboniferous - Early Permian and attained a thickness greater than 750 m (Johnson, 1991; Cole, 1992).

Catuneanu and Elango (2001) stated that the deeper marine glacial facies of the Dwyka Group including those of the early Ecca Group accumulated during the under-filled phase of the foreland basin. In the south, as Catuneanu *et al.* (1998) explained, the Dwyka succession has a uniform character with lateral continuity of layers, suggesting deposition from floating ice within a large marine basin was a dominant process. Bamford (2004) also agrees with this idea by explaining that the tillites are uniform and laterally extensive, having formed in a glacial marine environment with deposition from both grounded and floating ice, with the latter being dominant.

Visser (1997) recognised up to nine fining upward cycles, and each cycle exhibits a change from terrestrial or subaqueous moraines to glacio-lacustrine shales (from the base to the top). The ice-flow direction signifies origin from the north (Cargonian Highlands), east (Eastern Highlands now in East Antarctica), and southwest (Southern Highlands now in West Antarctica) (Visser, 1997). Cole (1992) also stated that the ice flow markers indicate provenances to the north, east and south with Precambrian rocks dominating the northern and eastern sources whilst the southern source is believed to have been a magmatic arc associated with subduction of the Palaeo-Pacific plate margin beneath the Gondwana plate. The foreland loads that are associated with the subduction instigated the deposition of the Dwyka Group diamictites (Johnson, 1991; Catuneanu and Elango, 2001).

According to Katemaunzanga and Gunter (2009), the Karoo Basin followed the distinctive evolution trend of foreland basins, with the overlying Stormberg and Beaufort Groups representing the 'mollase' fluvial type sediments while the underlying Ecca Group represents the 'flysch' component, although a 'local décollement' is seen on the field and on seismic image between the upper boundary of the Whitehill Formation and the base of the overlying Collingham Formation (Johnson, 1991).

The fluvio-lacustrine Beaufort Group is categorized into two subgroups, namely the lower Adelaide Subgroup and the upper Tarkastad Subgroup. The Adelaide Subgroup comprises the Koonap, Middleton and Balfour Formations respectively, while the Tarkastad Subgroup is made up of the Katberg and Burgersdorp Formations. The upper part of the Karoo Supergroup is made up of three formations which includes, the Late Triassic coarse-grained sandstone-dominated Molteno Formation, the Late Triassic-Early Jurassic red mudstones and sandstone-dominated Elliot Formation, and Early Jurassic aeolienates-dominated Clarens Formation. The whole sequence is capped by the pyroclastic basaltic deposits of the Drakensberg Group (Veevers *et al*., 1994; Catuneanu *et al*., 1998).

2.3.1 Dwyka Group

The geology of the Dwyka Group has been summarised and documented by several authors (e.g. Johnson 1991; Visser, 1992a; 1992b; 1997; Johnson *et al.,* 2006). Johnson (1991) stated that the Late Carboniferous - Early Permian Dwyka Group rests on the glaciated Precambrian bedrock surfaces along the northern basin margin, although it unconformably overlies the Cape Supergroup in the south whilst it conformably overlies the Natal Group and Msikaba Formation in the east. According to Catuneanu and Elango (2001), the initiation of the Dwyka sedimentation is estimated at about 300 Ma, following the 30 Ma stratigraphic breaks after the end of Visean when sedimentation in the Cape basin was terminated.

Visser (1986) recognised up to seven lithofacies in the Dwyka Group and the lithofacies are believed to have been deposited in a marine basin. The facies include; massive diamictites, stratified diamictites, massive carbonate-rich diamictites, conglomerate facies, sandstone facies, mudrock with drop-stone facies and finally the mudrock facies. The Dwyka facies grade upward into finer-grained clastic rocks indicating that the deposition of sediments in the glacial environment is from both grounded and floating ice (Catuneanu *et al*., 1998). However, there is no clear contrast between the Dwyka successions in the south (proximal) and the north (distal) (Catuneanu *et al*., 1998).

According to Visser (1991), the stratified diamictites facies consist of argillaceous diamictite containing sub-round to rounded extra-basinal clasts as much as 3 m across. The stratification contains faint bedding planes within the diamictite as well as thin interbedded mudrock beds and laminae. Johnson *et al*. (2006) allude that these stratified diamictites have been formed

by sediment gravity flows, although intermittent reworking of subglacial diamictons and rain-out of glacial debris also occurred during deposition.

Wickens (1994) reported that the withdrawal of ice in the Early Permian was complemented by the deposition of the marine Ecca Group which started with the Prince Albert Formation. The Prince Albert Formation is overlain by the black carbonaceous shale of the Whitehill Formation. Johnson *et al*. (2006) suggested that the deposition of the homogeneous black muds of the Whitehill Formation under reduced (anoxic) settings indicates a tectonic quietness and the inactivity of the Cape Fold Belt.

The mudrock with drop-stone facies consists primarily of rhythmite, and angular to round detrital stones varying from small to large (maximum ± 1 m across) are commonly found deforming the rhythmite (Visser, 1991). The facies represent deposits in a distal iceberg zone. The mudrock with stone facies is different from the ordinary mudrock facies in the sense that the mudrock facies do not have any kind of detrital stone, but just consist of greenish grey mudstone with black pyrite shale (Visser, 1991) and they are product of suspension settling of mud as well as fall-out of silt from sediment–laden underflows.

Von Brunn (1994) in Deynoux (1994) allude that the massive sandstone diamictite facies consist of either very fine to medium grained, massive to ripple-laminated sandstones or medium to coarse grained, trough cross bedded, immature sandstones. The ripple laminated sandstones are interpreted as turbidite deposits, whereas in the case of trough cross bedded sandstones, tractional fall-out from subaqueous outwash streams was envisaged. Visser (1991) described the massive carbonate-rich diamictites facies as the clast poor diamictites, containing thin carbonate beds (up to 5 cm), with stringers and concretions forming the thick facies units. These facies are formed from the rain-out of debris, with the carbonate probably originating by crystallization from interstitial water.

The conglomerate facies ranges from single layered boulder beds to poorly sorted pebble and granule conglomerate, with boulder beds interpreted as lodgement deposits, whereas the poorly sorted conglomerates are a product of water reworking of diamictons by high density sediment gravity flow (Johnson *et al*., 2006). Generally, the formation ranges in thickness from 600 m - 750 m and rests disconformably on the Witteberg Group (SACS, 1980; Johnson, 1991). Some researchers suggested a marine depositional environment for part of the glacial deposits (Cole, 1992; Johnson *et al.,* 1996; Catuneanu *et al*., 1998; Rubidge *et al*.,

2000). There is no unequivocal evidence for the marine setting, but there is a possibility that the majority of the Dwyka sequence was deposited in a terrestrial setting (Du Toit, 1926 in Rubidge *et al.*, 2000).

2.3.2 Ecca Group

The Ecca Group is a rock sequence that accumulated between the Late Carboniferous Dwyka Group and the Late Permian-Middle Triassic Beaufort Group, occupying most of the Permian time of the Karoo Supergroup (Catuneanu *et al.*, 2005). The term Ecca is suggested by Rubidge (1858) in Catuneanu *et al.* (2005) for argillaceous sedimentary strata exposed in the Ecca Pass, near Grahamstown in the Eastern Cape Province, South Africa. Thus, the use of the term Ecca outside the main Karoo Basin is sometimes questionable as the rock types could be totally different. The group comprises of shale, mudstones, siltstones, sandstones, minor conglomerate and coal. It consists of six formations, namely, the Prince Albert Formation, Whitehill Formation, Collingham Formation, Ripon Formation, Fort Brown Formation and the Waterford Formation. Cadle *et al.* (1993) stated that deep and shallow water environments with a cool climate predominated during the Ecca times, with coal forming in alluvial fan, fan delta and fluvial systems of the formation.

According to Catuneanu *et al.* (1998), the marine clays and mudstones of the Prince Albert Formation were deposited on the diamictites of the Dwyka Formation in the southeastern part of the Karoo Basin. This was followed by the carbonaceous shale of the Whitehill Formation. Subsequently, the Collingham Formation that is made up of persistent grey shales alternating with yellow-claystones, as well as the sandstones and shales of the Ripon, Fort Brown and Waterford Formations were deposited on the submarine fans, shelf and deltas (Johnson, 1976). Visser and Loock (1978) allude that the Dwyka and Ecca Groups were deposited during the seaway transgression into the interior part of the southern Karoo Basin. Nevertheless, at the end of Ecca time, complete regression in the Ecca Group occurred from the limits of the preserved basin (Catuneanu *et al.*, 1998).

During the Dwyka-lower time, the bathymetric condition of this inner seaway changed from deep marine to shallow marine during the upper Ecca time (Smith *et al.*, 1993; Catuneanu *et al.*, 1998). Johnson (1976) stated that the change from glacial (Dwyka) to post-glacial (lower

Ecca) sedimentary environments occurred first in the southwestern part before the northern and eastern parts of the Karoo Basin. Smith *et al*. (1993) envisaged that the organic-rich Whitehill Formation of the Lower Ecca is the only synchronous basin-wide sedimentary unit in the Karoo Sequence (Alao and Mikes, 2011).

The Whitehill Formation is overlain by the siliciclastic turbidites and intercalated tuffs of the Collingham Formation (Wickens, 1994). The quick lithological change from black carbonaceous shales of the Whitehill Formation to siliciclastic turbidite deposits that are associated with abundant tuff beds of the Collingham Formation suggests a change in the tectonic environment (Johnson *et al*., 2006). The distal turbidites and volcanic ash layers of the Collingham Formation is the only layer of the Ecca Group that can be directly linked to the southern volcanism with evidence of active volcanic ash. There is likelihood that the tuffs beds in the Collingham Formation are products of the Permian silicic-andesitic and plutonic rocks volcanoes (Veevers *et al*., 1994; Wickens, 1994).

Williamson (1996) divided the Ecca Group into the lower, middle and upper parts. The lower part of the Ecca Group with maximum thickness of approximately 107 m consists of a succession of fine-grained arenaceous to silty beds that are typically dark-coloured (Johnson *et al*., 2006). The middle part of the Ecca Group with maximum thickness of approximately 165 m is characterized by the development of yellow and white, medium to coarse-grained feldspathic sandstones (Johnson *et al*., 2006). The sandstone bands become thinner upward and eventually disappear completely, leaving an entirely argillaceous and carbonaceous succession which is known as the upper part of the Ecca Group with maximum thickness of approximately 138 m (Van Straten, 1959; Johnson *et al*., 2006).

Smith (1982) envisaged that the base of the Ecca Group is defined at the top of the glaciogenic succession of the Dwyka Group with varied sequences predominantly of carbonaceous mudstones, siltstones, sandstones and coals (Johnson *et al*., 1996). Viljoen (1994) stated that the presence of ash beds in the Collingham Formation indicates volcanism in the area. The relatively cool and humid climatic conditions in the north, favours the thick accumulations of peat on the fluvial and delta plains that matured into coal beds (Cadle *et al*., 1993). Katemaunzanga and Gunter (2009) also reported that the Ripon and Fort Brown Formations represent a turbidite fan complex with the direction of movement from the southeast in a deep to medium aqueous. According to Segwabe (2008), the Ecca Group rests

directly on the pre-Karoo surface in some places, indicating a significant post-Dwyka Group topography and localized pre-Ecca erosion, such as non-deposition or erosion of the Dwyka Group (Smith, 1984; Williamson, 1996). The non-carbonaceous that is usually silty and calcareous mudstones with small amounts of fine- to coarse-grained sandstones and siltstones marks the start of the upper part of the Ecca Group (Williamson, 1996; Johnson *et al*., 1996).

2.3.3 Beaufort Group

The lower Adelaide Subgroup and the upper Tarkastad Subgroup made up the Beaufort Group that overlain the Ecca Group. The Late Permian Adelaide Subgroup comprises the Koonap, Middleton and Balfour Formations in the southeastern part of the basin while the Abrahamskraal and Teekloof Formations in the western part are approximately equivalents of the Koonap and Middleton Formations, and a single Normandien Formation in the northern part (Johnson *et al.,* 1996; Catuneanu *et al*., 1998). Johnson *et al.* (1996) documented that in the western part of the basin, the lower Abrahamskraal Formation attain a maximum thickness of about 2,500 m while the upper Teekloof Formation attain a thickness of approximately 1,400 m with its upper contact being eroded. Cole and Smith (2008) used the presence of chert beds with more abundant sandstone and a paucity of reddish-maroon mudrock to distinguish between the Abrahamskraal and Teekloof Formations.

According to Johnson *et al.* (1996), the Adelaide Subgroup reaches a maximum thickness of about 5, 000 m in the southeastern part and consists of a succession of bluish-grey, reddish-maroon and greenish-grey mudstones and subordinate fine-to medium-grained, tabular and lenticular sandstone, although the thickness decreases to 800 m in the centre of the main Karoo Basin. Subsequently, the thickness gradually decreases to around 100 m - 200 m in the far north of the main Karoo Basin. The Koonap, Middleton and Balfour Formations attain a maximum thickness of approximately 1,300 m, 1,600 m and 2,000 m, respectively.

Johnson *et al.* (1996) envisage that the Early Triassic Tarkastad Subgroup is rich in both sandstone and red mudstone than the Adelaide Subgroup. The Tarkastad Subgroup reaches a maximum thickness of approximately 2, 000 m in the south and decreases to around 150 m or less in the far north (Johnson *et al.,* 1996). The Tarkastad Subgroup comprises of a lower Katberg Formation (sandstone-rich) and an upper Burgersdorp Formation (mudstone-rich) in

the south. The light brownish grey or greenish grey sandstones in the Katberg Formation are fine to medium grained, with scattered pebbles that are up to 15 cm in diameter that are usually present in coastal outcrops (Johnson *et al.,* 1996). The sedimentary structures that are mostly seen on the sandstones of the Katberg Formation are horizontal lamination with parting lineation and cross-bedding (both trough and planar) (Johnson *et al*., 2006). The fine grained sandstones of the Burgersdorp Formation are light brownish grey or greenish grey in colour and show a distinct horizontal lamination, cross-bedding and ripple lamination (Johnson *et al*., 2006). Paleocurrent studies of the Beaufort Group indicate a centripetal drainage pattern of fluvial systems into the basin (Veevers *et al*., 1994; Cole and Wipplinger, 2001).

2.3.4 Stormberg Group

The Stormberg Group comprises of the fluvial and aeolian-lacustrine successions of the Molteno, Elliot and Clarens Formations (Johnson *et al.,* 1996). According to Cole (1992) in Catuneanu *et al*. (1998), the sandstone-rich Molteno Formation was deposited by low-meandering braided rivers, whereas the Elliot Formation was deposited by high- meandering (sinuosity) rivers. The Late Triassic-Early Jurassic age Stormberg Group in the southwestern region was deposited as a result of the final deformational phase in the Cape Fold Belt and subsidence of the Southwestern Karoo Basin due to the compressive nature of tectonic regime of the Karoo Basin region was still active during the Late Triassic-Early Jurassic time (Hälbich *et al*., 1983). According to Turner (1975), in the southern outcrop area, the Late Triassic Molteno Formation attains a maximum thickness of about 600 m and can be subdivided into five members, although the thickness is less than 10 m in the far north of its outcrop area. The Molteno Formation is made up of medium- to coarse-grained sandstones that alternate with grey mudstones (Johnson *et al.,* 1996).

Johnson *et al.* (1996) envisaged that the Molteno Formation consists of two main coarsening-upward sequences in the southern region of the basin, the Bamboesberg Member and Indwe Sandstone Members made up the basal sequence whilst the upper sequence is made up of the Transitional Member. The formation is dominated by horizontal tabular sheets of cross stratified medium- to coarse grained sandstone which were deposited by braided streams (Catuneanu *et al*., 1998). Johnson (1991) elucidated that the relatively quartz-rich nature of

the Molteno Formation sandstones coupled with the absence of clasts other than quartzite, presently shows that the rocks of the Cape Supergroup that were uplifted in the Cape Fold Belt had replaced the magmatic arc as the main provenance for the Karoo Basin. Turner (1980) emphasized that the northward-tapering wedges in the Molteno Formation are due to fault-controlled uplift of granitic provenance along the southeastern basin margin. The Late Triassic Elliot Formation is a typical "red bed" fluvial deposit and consists of alternating sequence of mudstone and subordinate fine to medium-grained sandstone, with sandstones dominating in the east and south, and mudstones in the northwest (Johnson *et al*., 1996; Catuneanu *et al*., 1998). The formation attains a maximum thickness of approximately 500 m in the south. The climate was hotter and drier than in any of the preceding ages (Visser and Botha, 1980; Johnson *et al*., 1996).

Madi and Zhao (2010) explained that the transported sediments from the source areas were eroded and lowered in these areas while filling the Stormberg basin at the same time although it became shallower with time. Katemaunzanga and Gunter (2009) reported that the red floodplain mudstones with subordinate channel and crevasse splay deposits dominate the Elliot Formation which were interpreted as mixed loads that dominate the meandering system in an increasing arid setting (Bordy *et al*., 2005; Visser and Botha, 1980; Catuneanu *et al*., 1998 and 2002). According to Eriksson (1984), the meandering streams deposited the sediments under highly oxidizing conditions with reduced energies. The uppermost part of the Elliot Formation contains evidence of aeolian conditions (Johnson *et al*., 2006). The final stage of the Karoo sedimentation is represented by the Late Triassic - Early Jurassic Clarens Formation that attains a thickness of 100 m in the north and about 300 m in the south of its outcrop area. The Clarens Formation consists of fine-grained sandstones, sandy siltstones and (Johnson *et al*., 2006; Catuneanu *et al*., 1998).

The Clarens Formation contains a central zone that indicates a true desert condition which is dominated by an aeolian dune environment and the westerly wind transported the sand (Johnson *et al*., 1996). Smith (1990) also documented that towards the final stage of deposition of the Clarens Formation, the climate became fairly moderate and wet desert processes of stream and sheet flood became more dominant (Catuneanu *et al*., 1998). The Clarens Formation is overlain by the basaltic lavas of the Drakensberg that forms the top of the Karoo sequence, and is believed to have terminated sedimentation within the basin in the Middle Jurassic (Johnson *et al*., 1996, 2006; Cole and Smith, 2008).

2.3.5 Drakensberg Group

Johnson *et al*. (2006) documented that prior to the Middle Jurassic period, the environmental conditions in the Karoo Basin changed rapidly, coupled with the large movement of the Earth's mantle, the crust experienced a large-scale lifting, and eruption of massive volumes of basaltic lava that constitute the Drakensberg Group. The outpourings of the basaltic lava spread across much of Gondwana about 180 million years ago indicating the start of Gondwana breakup. The magma (molten rock) made its way to the surface along a complex system of fractures. Crystallisation of the magma within these fractures resulted in the dolerite sills and dykes (about 180 Ma). The presence of numerous sills in the main Karoo Basin fed the erupted lava and these sills were linked to the breakup of Gondwana (Johnson *et al*., 1996). The Drakensberg lava that form the upper parts of the Drakensberg Mountain is made up of a thick succession of basalts that caps the Karoo sedimentary succession and covers some part of Lesotho, northern part of the Eastern Cape and range along the western Kwazulu-Natal border. This succession of lava attained a thickness of approximately 1,370 m which is preserved in Lesotho (Smith *et al*., 1993; Johnson *et al*., 1996).

2.4 The Karoo Dolerite Suite

Chevallier and Woodford (1999) allude that the Karoo dolerite, which comprises of several petrological facies (ranging from a leucogabbro to a dolerite-pegmatite), consists of interconnected networks of dykes and sills and it is very difficult to single out any particular intrusive or tectonic event due to the fact that, an individual sill can be fed by many dykes of different orientations or a dyke can act as a feeder to two different sills or more. Chevallier and Woodford (1999) and Svensen *et al*. (2007) concluded that during the intrusive phases, the molten magma concurrently filled in the numerous fractures, and that the dolerite intrusive network probably behaved as a shallow stockwork-like reservoir or storage system where molten magma of different viscosities intruded the fractures. It appears that there is a lithological control on the emplacement of dykes within the Western Karoo Basin, as the bulk of the dykes are strata bound and concentrated in the Upper Ecca and Beaufort Group (Woodford and Chevallier, 2002).

According to Hunter and Reid (1987) in Duncan *et al*. (1997), the Carboniferous-Permian Karoo sediments were intruded by the Jurassic Karoo volcanics (183 Ma) during a period of

prolonged magmatic activity that covers almost the whole of the southern African subcontinent during one of the phases in the break-up of the Gondwana. This resulted in one of the four major preserved continental flood basalts in the world (White, 1997). Chevallier *et al.* (2001) stated that the igneous products of the Main Karoo Basin show a larger extent of dolerite dykes and sills when compared to the extrusive (Lesotho basalt). The geographical distribution of the Karoo dolerite sills and ring-complexes are the same as the dolerite dykes and they are the most common type of intrusion (sills) in the Karoo basin (Chevallier *et al.*, 2001; Figure 2.7).
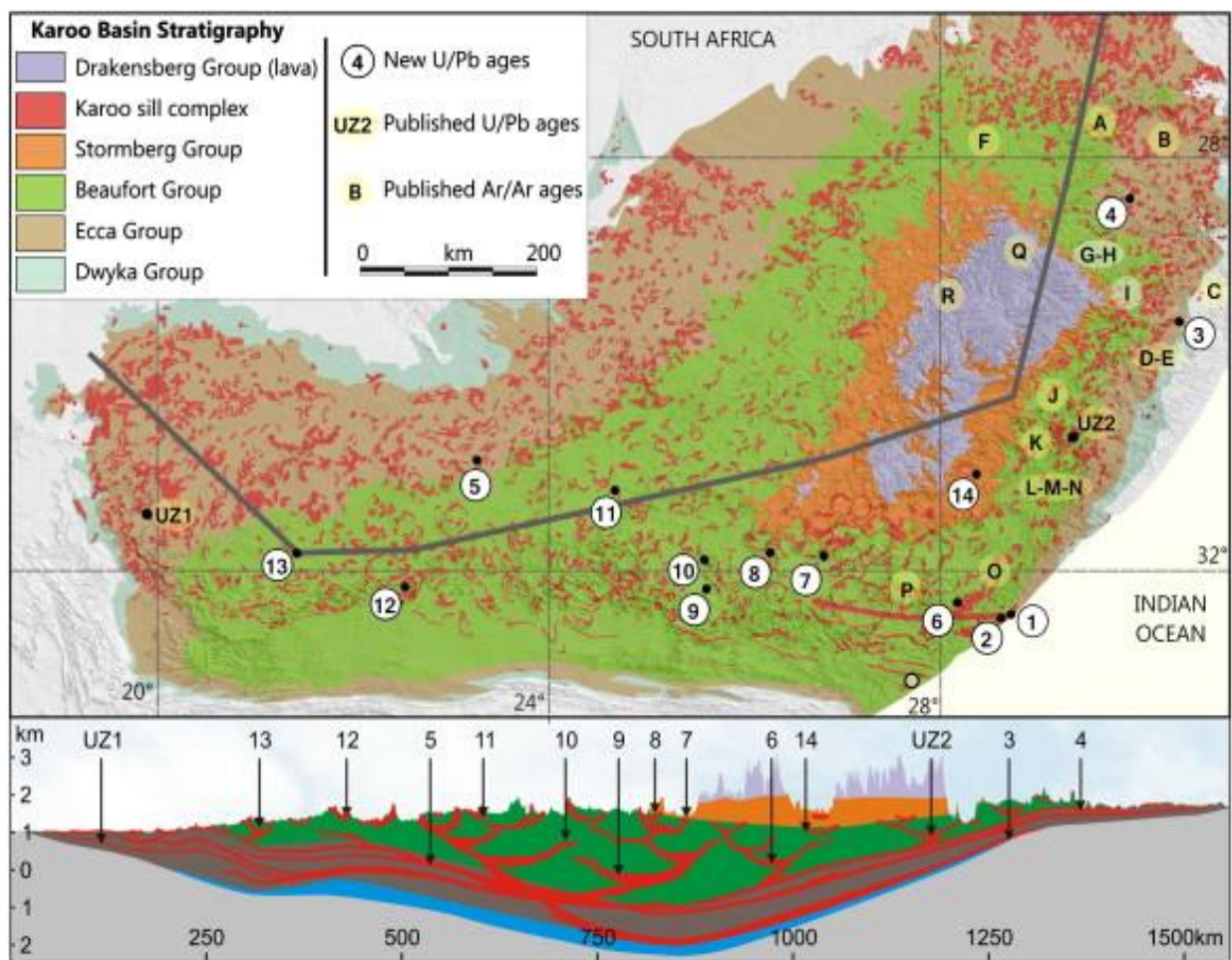
Figure 2.7 The geographical distribution/widespread of the dolerite intrusions throughout the Karoo Basin of South Africa (http://karoospace.co.za/dolerite-karoos-fracking-game-changer).

31

Svensen *et al*. (2007) stated that the dolerite sills occur throughout the Karoo Basin, the thickest sills is about 200 m thick, and it represents mainly the extensive (greater than 200 km) sheets emplaced in the carbonaceous shale of the Permian Ecca Group. In the Beaufort Group, the sills form nested saucer-shaped intrusions with thickness of about 100 m. The sills are less common in the uppermost part of the Karoo basin (Stormberg Group) when compared to the dykes that form about 120 -180 km long lineaments (e.g. the 100 - 200 m wide Gap dykes) (Johnson *et al*., 1996; Catuneanu *et al*., 2005; Svensen *et al*., 2007).

Svensen *et al*. (2007) suggested that, the absence of sills in the Drakensberg Group lavas indicates that the sills were emplaced prior to the main phase of flood volcanism or that sills emplacement within the lava was prevented. Galerne *et al*. (2011) envisaged that the Karoo sills are mostly tholeiitic basalts to basaltic andesite, however, some present-day sills evolved locally. One of the most noticeable features of the present Karoo landscape is the numerous dolerite sills and ring-complexes. These structures usually show a sub-circular saucer-like shape, the rims of which are mostly seen as topographic highs and form ring-like outcrops (Svensen *et al*., 2007; Figure 2.9). According to Chevallier *et al*. (2001), three major structural domains that are indicated by dyke distribution have been identified in the Main Karoo Basin (Figure 2.8). These domains are:

- The Western Karoo Domain: It extends from Calvinia to Middelburg and is characterised by two distinctive structural features; east west trending zone of long and thick dykes associated with right lateral shear deformation and north northwest dykes.
- The Eastern Karoo Domain: It extends from Middelburg to East London and comprises two major dyke swarms, namely; a major curvi-linear swarm of extensive and thick dykes diverging from a point offshore of East London and minor north northeast trending dykes.
- The Transkei-Lesotho-Northern Karoo Domain: It consists of two swarms; northwest trending dykes in the Transkei Region, curving to east-west in the Free State and northeast trending dykes mainly occurring within and alongside the Lesotho basalt.

The geographical distribution of these structures (sills) are more than the dykes, thus they are the major tectonic style that possibly controls the geomorphology and drainage system of the Main Karoo Basin (Chevallier *et al*., 2001; Woodford and Chevallier, 2002).
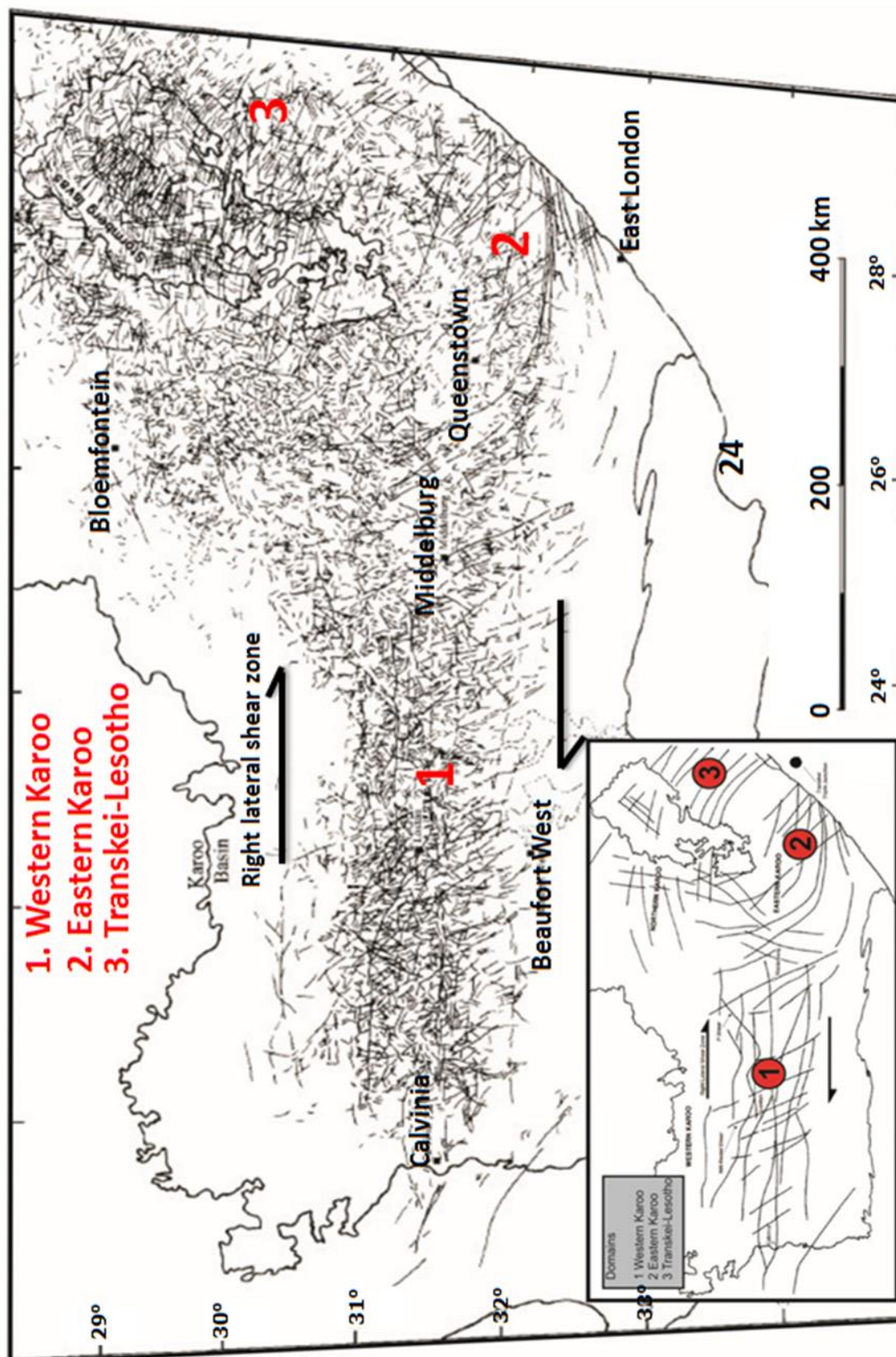
Figure 2.8 Dolerite dykes of the Main Karoo Basin. Insert is a simplified structural map showing the three structural domains (After Woodford and Chevallier, 2002).

The relationship between the dykes and sill or ring complexes is very complex. The dykes are characteristically encountered in massive arenaceous rocks, while the sills are more common in laminated argillaceous rocks of the Karoo Supergroup (Lurie, 1981). Du Toit (1920) referred to the dolerite injections as ubiquitous, but explained that the intrusion of dolerite is usually along a preferential horizon, such as the contacts between the Dwyka-Ecca Group, the Prince Albert-Whitehill Formation, Upper Ecca-Lower Beaufort Group as well as other lithological boundaries within the Beaufort Group. This was investigated and later confirmed by the deep oil-exploration drilling in the Karoo Basin (Winter and Venter, 1970). Dolerite sill and ring complexes are prominent features of the Karoo landscape. These structures are easily identified on satellite images (Figure 2.9).
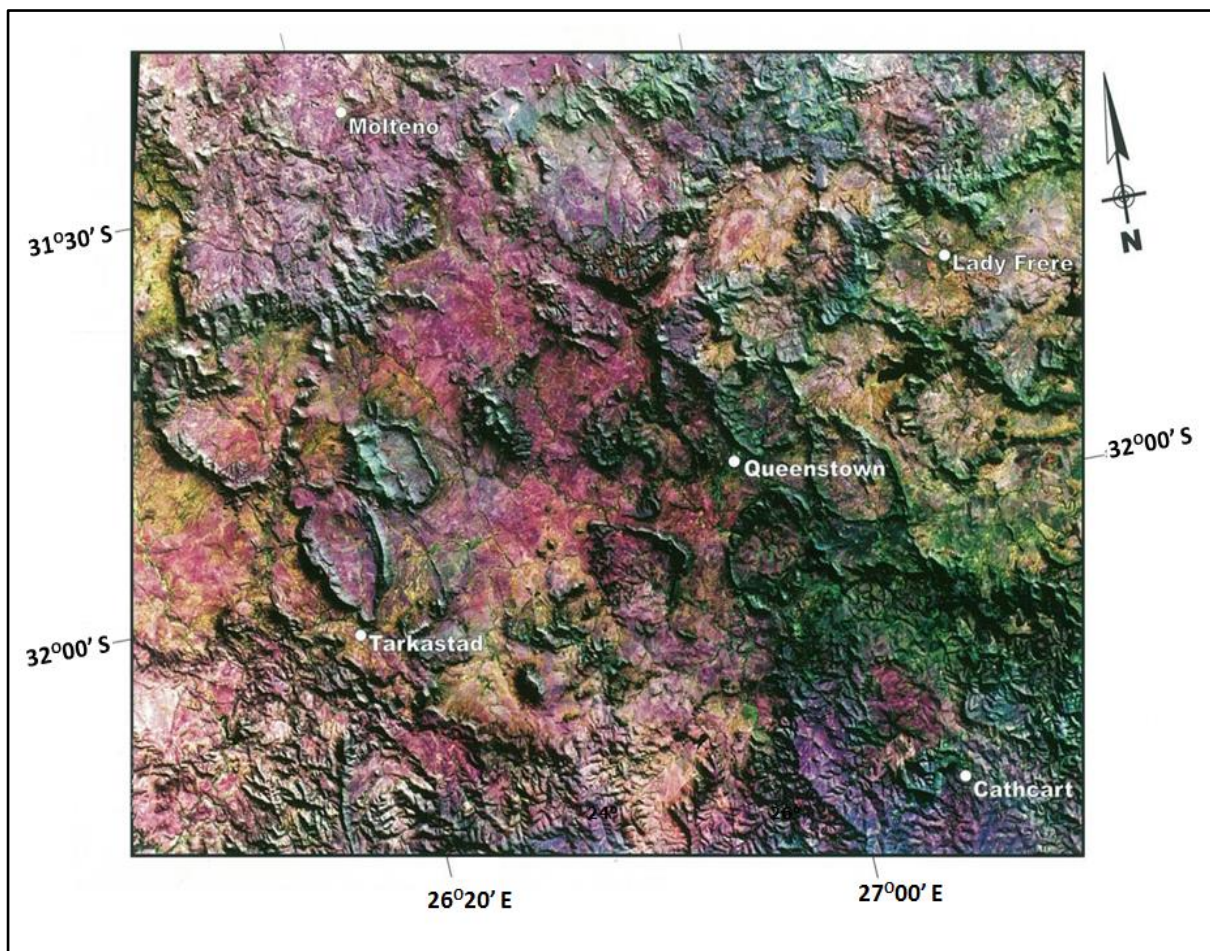
Figure 2.9 Satellite image (Landsat-5 TM Band 745) of dolerite ring structures in the Queenstown area (Smart, 1998).

34

Woodford and Chevallier (2002) developed two models for the emplacement of Karoo dolerite sills, the models depict that the rim of the ring-structure is the most tectonised unit within the sill/ring complex (Figure 2.10). The two models could vary considerably, especially concerning the development of fracturing below the ring and above the centre of the inner sill. Chevallier and Woodford (1999) envisaged that the comparative morpho-tectonic analysis of the three sill-ring systems of the western Karoo (Williston, Fraserburg and Victoria West complexes) suggests that their shape is saucer-like with an internal sill at the base, an external sill on the rim, as well as an arcuate inclined sheet/ring on the periphery.

Chevallier and Woodford (1999) proposed that the dolerite dykes feed into the inclined sheets, then propagate into an external sill and finally into an internal sill (see Figure 2.10). Chevallier *et al*. (2001) stated that the preferential erosion of the trapped sediments within the structure, usually accentuate the rims of the ring topographically. Thus, resulting in the overall appearance of a ring-like structure that was first described around Queenstown by Du Toit (1920).The Karoo dolerites have been mapped and studied by several researchers (e.g. Du Toit, 1920; Reid and Rex, 1994; Duncan, *et al*., 1997; Chevallier and Woodford, 1999; Svensen *et al*., 2006; Galerne *et al*., 2008; Svensen *et al*., 2012). Du Toit (1920) investigated the behaviour of some of the inclined sheets and sills in the Eastern Cape, Reid and Rex (1994) mapped the dolerite dykes of the western coast of South Africa. Duncan *et al*. (1997) studied the timing and duration of the Karoo igneous event, southern Gondwana. Chevallier and Woodford (1999) studied the morpho-tectonics and mechanism of emplacement of the dolerite rings and sills of the Western Karoo, South Africa. Svensen *et al*. (2006) examined the structure and evolution of hydrothermal vent complexes in the Karoo Basin. Galerne *et al*. (2008) investigated the emplacement mechanisms of sill complexes while Svensen *et al*. (2012) studied the rapid emplacement in the Karoo Large Igneous Province (KLIP).
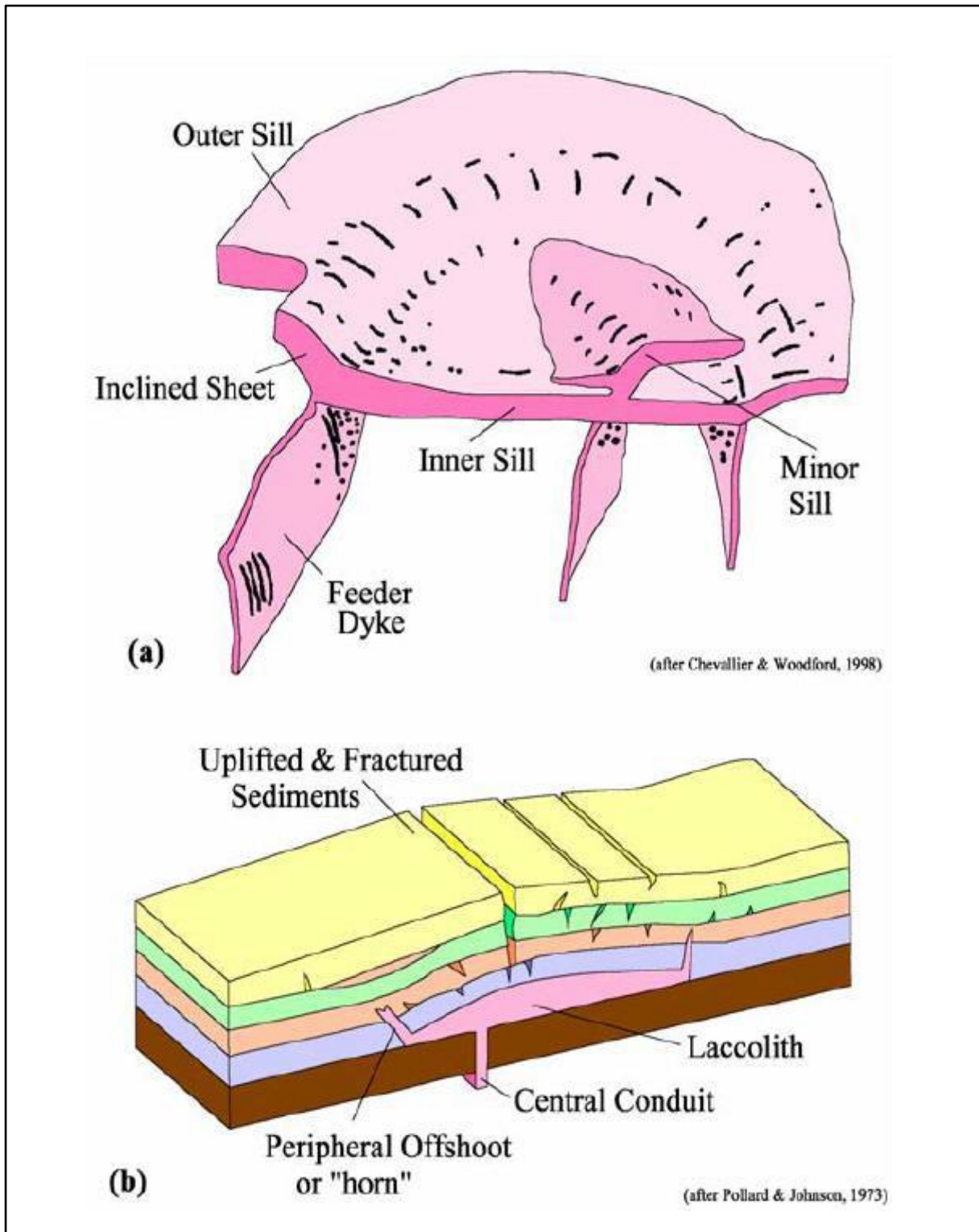
Figure 2.10 Dolerite sill/ring emplacement models; (a) Ring dyke model; (b) Laccolith model (Woodford and Chevallier, 2002).

2.5 Depositional history

Smith *et al*. (1993) and Johnson *et al*. (1996) documented summaries of the depositional processes and environmental condition of the Karoo Supergroup. However, the type of palaeoenvironments that prevailed during the deposition of the main Karoo Basin can be implied from the lithostratigraphic shown in Table 2.1.

Johnson *et al*. (1996) argues that the deposition of the main Karoo Basin started with the deposition of different glacigene rock types (Dwyka Formation) signifying ground debris that was deposited by the withdrawing glaciers and residue from the floating ice sheets. The withdrawal of ice in the Early Permian was followed by the deposition of the marine Ecca Group which started with the post glacial Prince Albert Formation, Whitehill, Collingham, Ripon, Fort Brown and Waterford Formations respectively (Johnson *et al*., 1996).

Catuneanu *et al*. (1998) emphasized that the Beaufort Group and part of the Stormberg Group (Molteno and Elliot Formations) consist mainly of fining upward fluvial sediments that are believed to have been deposited by relatively high- meandering types of river, with wide floodplain muds prevailing over lenticular channel sands, although, the high percentage of sandstones in the Katberg and Molteno Formations indicate that the sediments might have been deposited by braided low-meandering rivers.

Johnson *et al*. (1996) envisaged that the Clarens Formation was deposited when arid and aeolian conditions were dominant. This was suggested due to the presence of massive, loess-type deposits and cross- bedded dunes in the formation. Capping the sedimentary sequence are the basalts and pyroclastic deposits of the Drakensberg Formation, which also contain the products of an intrusive phase.

2.6 Conclusions

The lithostratigraphy of the Karoo Supergroup in South Africa indicates gradual change in environmental condition from glacial to continental slope - deltaic, then fluvial and finally aeolian (Johnson *et al*., 2006). The underlying processes and order of geologic events are revealed in each formation, the order started with diamictites and other glacigene rock types, followed by the shale, sandstones and mudstones of the Ecca and Beaufort Groups respectively (Johnson *et al*., 2006). Sedimentation in the Karoo Basin is closely controlled by the orogenic cycles of loading and unloading in the Cape Fold Belt (Johnson *et al*., 2006).

A regional aeromagnetic survey in the southern Karoo Basin shows a clear set of magnetic anomalies that trends east-west and confined to the basement that underlies the Karoo Basin. Gough *et al*. (1973) explained that this set of magnetic anomalies (BMA and SCCB) that were observed parallel to the supposed tectonic edge/margin of the Namaqua-Natal Mobile Belt (NNMB) and the Cape Fold Belt (CFB) have a common source. The conductive material that trends east-west underneath the southern Karoo Basin and Cape Fold Belt lies in the crust. Karoo Basin's rocks potentially host majority of South Africa's onshore fossil fuel reserve. Petroleum exploration in the Karoo is presently focused on the shale gas, coal-bed methane gas and biogenic gas of the Ecca Group and if viable, it will be the main alternate source of energy in South Africa.

CHAPTER THREE

METHODOLOGIES

3.1 Introduction

To achieve the aims and objectives of this project, several operations were carried out systematically which include: desktop study, literature review, field work, laboratory analysis, modelling and interpretation of the different datasets. The aeromagnetic, gravity and radiometric data were acquired from Fugro Airborne Surveys (geophysical survey specialist that offers ground geophysical surveys, geophysical data processing, interpretation and consulting services) and Council for Geoscience respectively. The geophysical data were presented in the form of maps, profiles and models.

3.2 Desktop study

The desktop study was carried out before and after the fieldwork. This involves different activities such as analyses of satellite images, aerial photographs and geophysical maps. Online articles, Geosoft modelling manuals and past research work on the study area and other related areas were consulted in order to have an overview of the geology of the area, lithostratigraphic sequence, geologic structures and the economic potential of the area.

3.3 Field work

Field excursions were conducted within the study area for field investigation and sampling. Strike and dip of outcrops, photographs, elevation and coordinates were recorded. In 1982, aeromagnetic and radiometric surveys were flown along parallel lines with spacing of 200 m by Fugro Airborne Surveys over the Eastern Cape Province of South Africa at a constant height of 60 m above the ground surface. The resolution of the aeromagnetic data is 0.01 nT. Gravity data from the Council for Geoscience is along accessible roads at 20 km station spacing. The acquired dataset were supplied as ers and grd files covering the southeastern part of the Karoo Basin (longitude 24° - 29° E and latitude 32° - 35° S). The original space domain grids were further processed, enhanced and presented in the form of geophysical

maps and profiles. Forward and inverse gravity modelling was carried out using GM-SYS in Geosoft Oasis Montaj software.

Locations within the Eastern Cape Province, where the Dwyka, Ecca and Beaufort Groups outcrop were visited for field investigation and sampling. Most of the outcrops visited are road cut exposures. A total of two hundred and fifty-eight (258) samples were collected on road cut exposures from the eleven (11) geologic formations that cover the study area for density measurements and laboratory analysis. The coordinates and elevations of sampling locations were recorded by a GPS receiver (Garmin eTrex-10). The samples were prepared for microscopic observations, X-ray diffraction analyses and density measurements.

3.3.1 Research instruments

The instruments used for this research study includes;

- Adam electronic weighing balance (PGW 3502e)

- Compass

- Copper wire sample holder (loop)

- Density bottle (50 ml)

- Digital camera

- Optical microscope

- Bruker XRD D8 Advance (Model V22.0.28)

- A Global Positioning System receiver (Garmin eTrex-10)

- Hammer

- Rubber bucket (50 litres)

- Struers cutting and trimming machine (secotom-10 and Accutom-50)

- Software: Arc GIS 9.3, Surfers-10, GM-SYS, GETECH GETGRID, Google Earth, Oasis Montaj and PetroMod.

3.4 Laboratory work

The laboratory work was concerned with the preparation of thin sections for petrography study (in order to identify the mineralogical composition, texture, nature of cementation, micro structures and authigenic minerals that are present in the rock samples), X-ray diffraction analysis (for mineral components, percentages and crystalline structure in minerals), measurement of density (dry, wet, and grain densities).

CHAPTER FOUR

GEOLOGICAL STUDIES

4.1 Digitized geological map

The geologic maps produced by Council for Geoscience in 1995 were used to generate a detailed digitized geologic map of the study area. The stratigraphic sequence of the Karoo Supergroup in the Eastern Cape Province consists of the Dwyka, Ecca and Beaufort Groups as depicted in Figure 4.1.
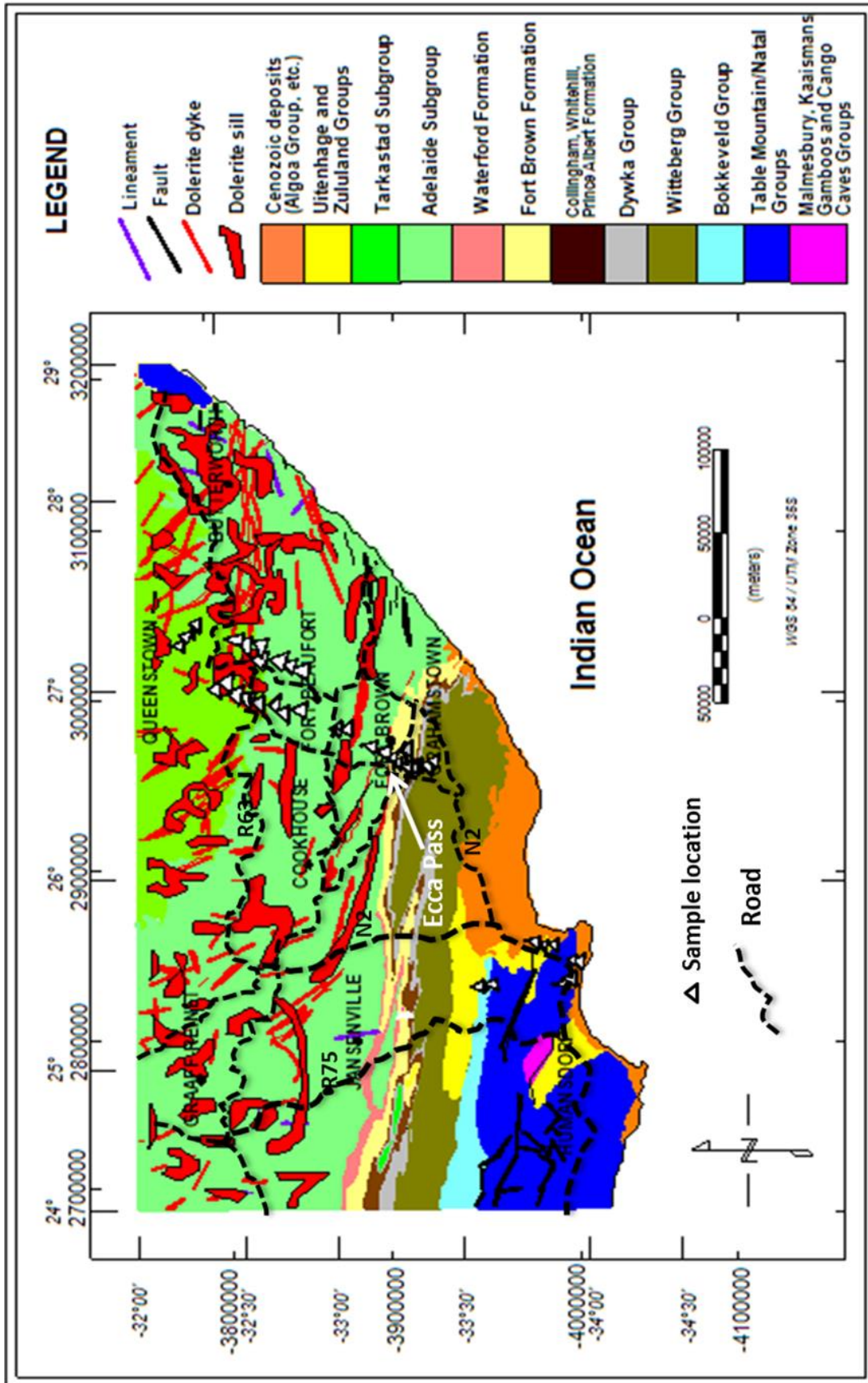
Figure 4.1 Digitized geological map of the study area showing sample location (by author after Council for Geoscience, 1995).

4.2 Dwyka Group

The Dwyka Group diamictites outcrop in the Grahamstown area (Figure 4.1). The diamictite is made up of angular to sub-round granite and quartzite components in the breccias (5 cm to 12 cm in size) with dark fine materials like silt and clay as the matrix (Figure 4.2). The Dwyka facies generally show upward grading sequence into finer-grained clastic rocks signifying deposition from both grounded and floating ice in a glacial environment. Quartz veins were also seen along some joints and faults in the diamictite. The joints which were seen in the Dwyka tillite are extensional in nature, they are clearly seen in the breccias but occur as trace lines in the matrix.
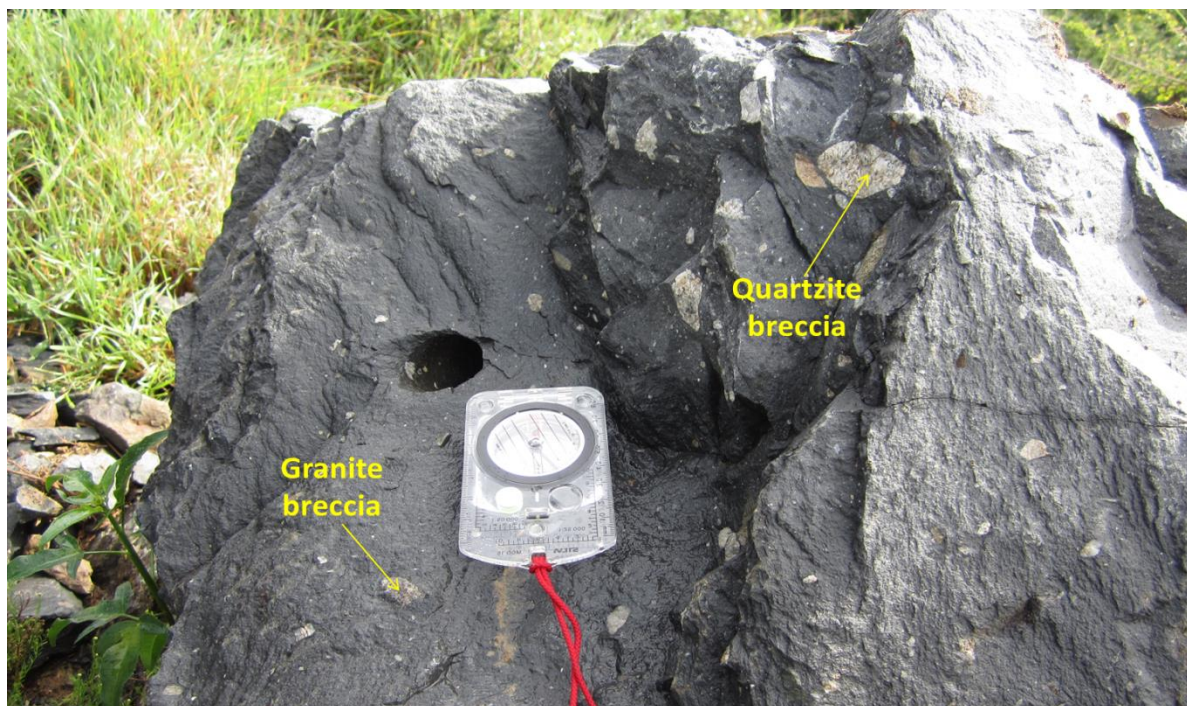
Figure 4.2 Diamictite of the Dwyka Group along the Ecca Pass, north of Grahamstown. The diamictite is made up of angular to sub-round granite and quartzite components in the breccias (5 cm to 12 cm in size) with dark fine materials like silt and clay as the matrix (Elevation: 483 m; Longitude E 26^0 $34'$ $40.4''$; Latitude S 33^0 $18'$ $22.4''$).

Two possible sources of kaolin deposit are seen in the Grahamstown area and they are both road cut exposures. The first deposit is believed to be the main kaolin deposit in the area and the recognised source of this kaolin deposit is the shale of the Witteberg Group in the Cape Supergroup (Figure 4.3). A reverse fault cut across the shale as shown in Figure 4.3.
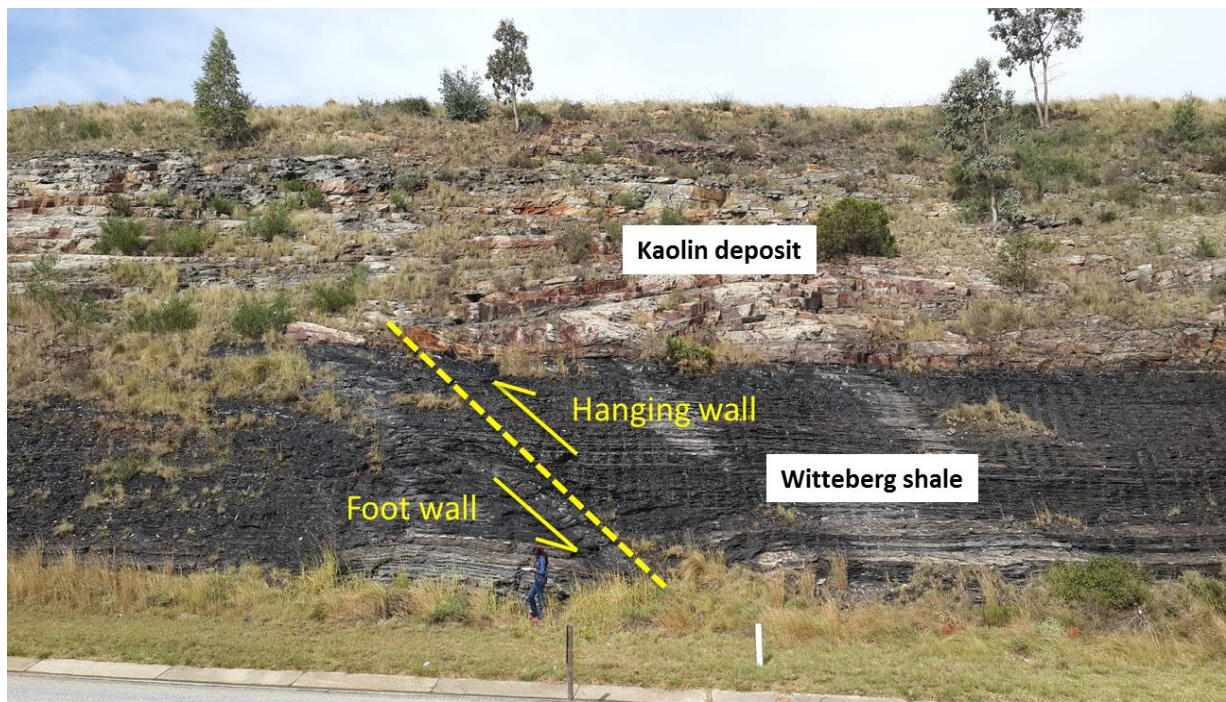
Figure 4.3 Photograph showing road cut exposure of the kaolin deposit possibly sourced from the Witteberg shale.

The second kaolin deposit is related to the Dwyka tillite possibly due to the alteration of feldspar to kaolin (Figure 4.4). Iron-rich nodules, shear-sense indicators and quartz veins are common features on the outcrop (Figure 4.4 a - d). A relatively big quartz vein (about 6 cm in width) cut across the outcrop thus dividing it into two parts; the footwall is the Dwyka tillite whilst the hanging wall is enriched with kaolinised materials (kaolin).
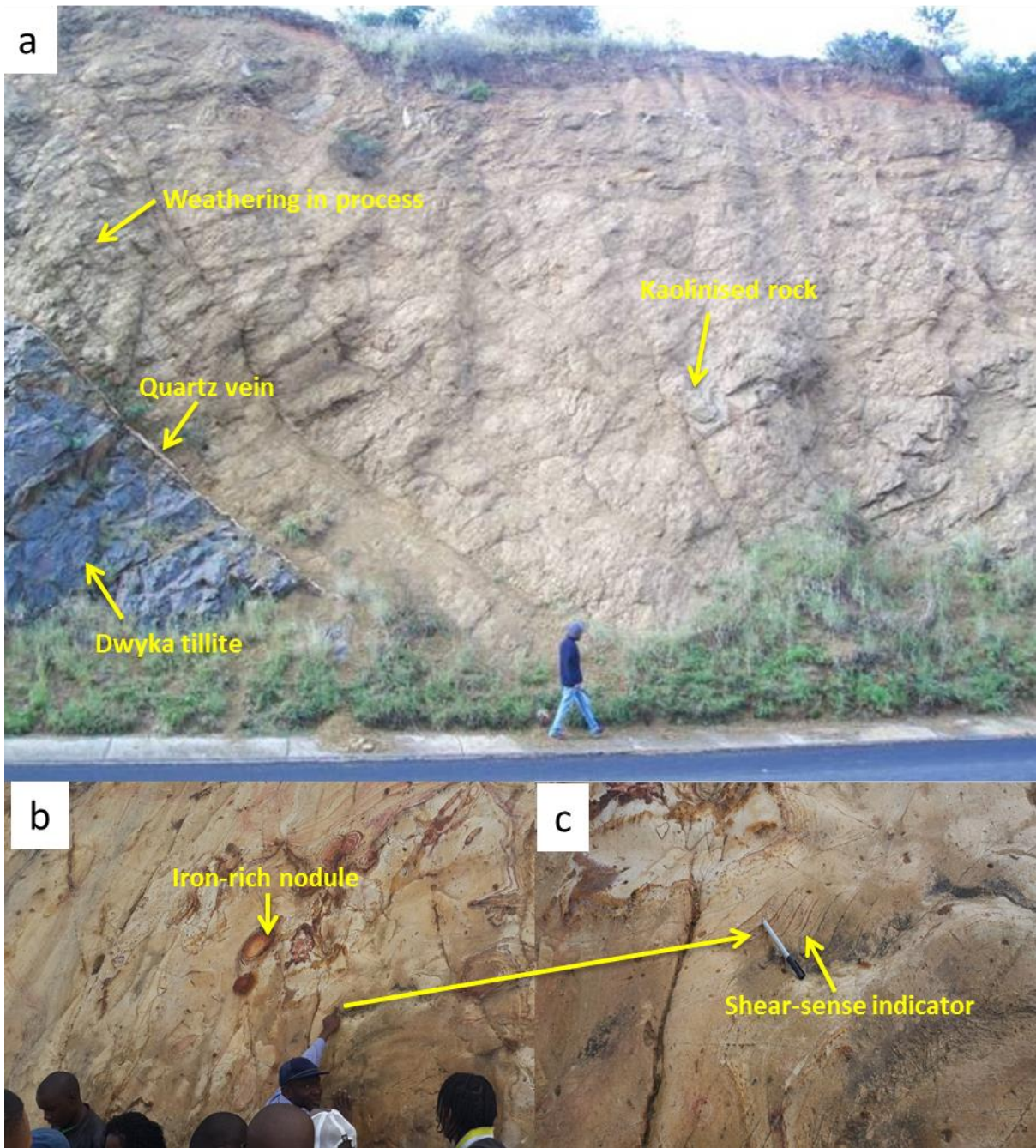
Figure 4.4 Road cut exposure of the kaolin deposit sourced from the Dwyka tillite showing iron-rich nodules, shear-sense indicators and quartz veins.

4.3 Ecca Group

4.3.1 Prince Albert Formation

The Prince Albert Formation, was seen along the Ecca pass and is the basal formation of the Ecca Group, it disconformably overlies the Dwyka Formation and also disconformably overlain by the Whitehill Formation. It is mainly made up of highly weathered greenish-grey shale (Figure 4.5) with some graded silty layers and arenaceous mudstones with measured thickness of about 110 m along road cutting. The strata generally dip at 38° (dip direction of 22°) with the absence of sandstone intercalations and current structures. The mudrock indicate suspension settling of mud in a marine environment whilst the sand and silt were deposited as a result of tractional fall-out from the turbidity current (Haughton *et al*., 2009).

Figure 4.5 Graded silty layers and greenish grey shale of the Prince Albert Formation along the Ecca Pass. (Elevation: 461 m; Longitude E 26^0 37′ 38.4″; Latitude S 33^0 12′ 59.5″).

The shales of the Prince Albert Formation along the Ecca Pass are thin bedded (the beds thickness ranges from 3 cm – 9 cm), well laminated (Figure 4.6) and shows pencil cleavage. Red stained shales were also observed at the top of the formation which could be due to

oxidation of iron elements which was released during the weathering of minerals that are rich in iron such as pyrite, smectite and illite whilst the khaki colour is probably due to tectonic uplift and exposure of the rock to atmospheric conditions leading to the alteration of the original grey-black colour to khaki.
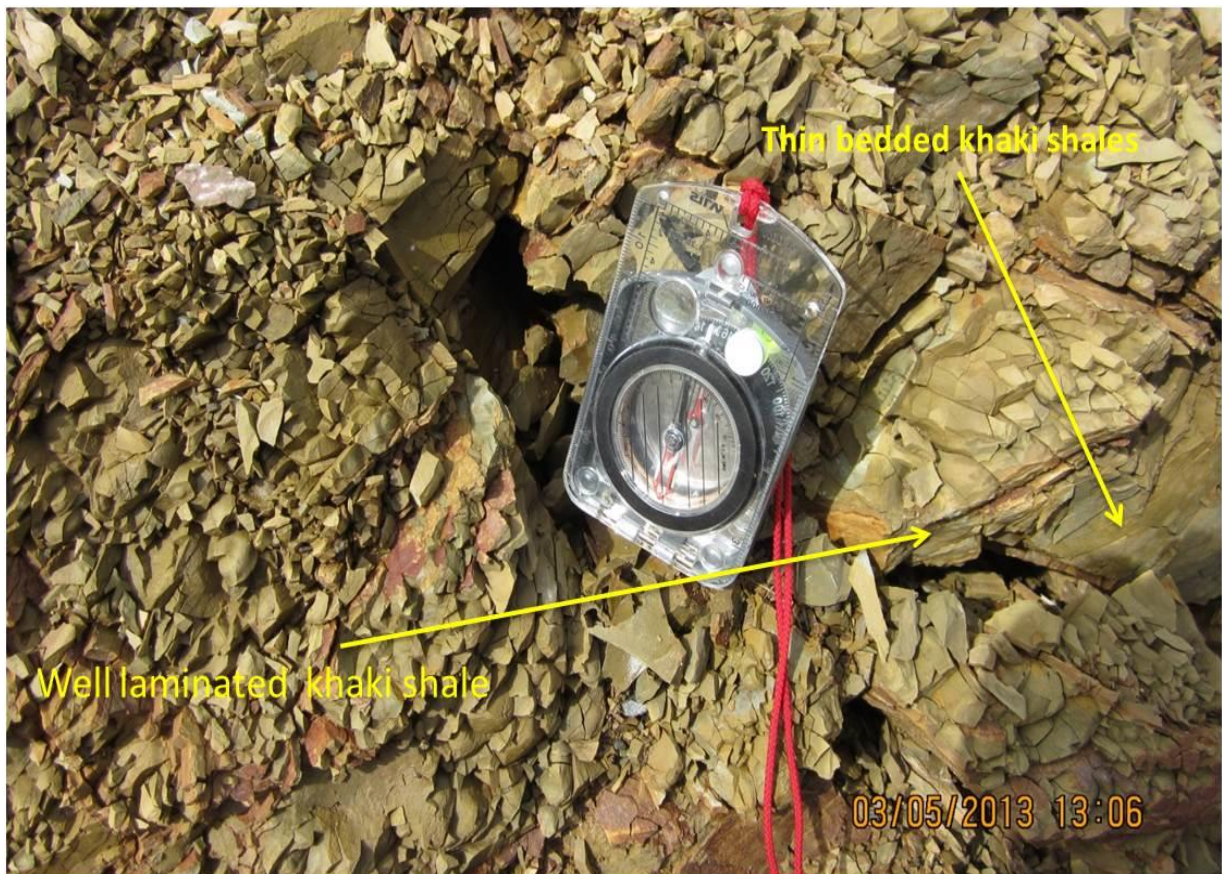
Figure 4.6 Photograph of steep thin bedded and laminated khaki shale along the Ecca Pass. (Elevation: 461 m; Longitude E 26^0 37′ 38.4″; Latitude S 33^0 12′ 59.5″). The khaki colour of the shale was due to the weathering of iron rich minerals, and the original colour of the shale was greyish black.

The arenaceous mudrocks are steep bedded and deformed due to folding, and is believed to be associated with the faulting that cut through the Whitehill Formation. At the bottom of the formation, the mudstones are mostly thin bedded at less than 10 cm for a single layer and sometimes well laminated. The presence of bottom currents probably coarsened the clay grain size of the thin beds. The well-developed lamination as well as the fine grained size of

the sediment indicates a deep water deposition, possibly a reducing (anoxic) environment (when considering the pyrite-rich sediments that possibly indicate a reducing environment). The well-developed lamination and the pyrite-rich sediments may also indicate a slower rate of deposition and possibly a scarce source of supply of sediments when considering the lamination which is between 1 mm and 3 mm in thickness. At the top of the formation, the red stained shales are folded due to structural deformation (Figure 4.7)

Figure 4.7 Folded well laminated red stained shale of the Prince Albert Formation. The red stained shales are folded due to structural deformation   (Elevation: 461 m; Longitude E 26^0 $37'$ $38.4''$; Latitude S 33^0 $12'$ $59.5''$).

4.3.2 Whitehill Formation

The Whitehill Formation rest disconformably on the Prince Albert Formation and is also disconformably overlain by the Collingham Formation. There is a gradational-transitional zone between the Whitehill Formation and the Prince Albert Formation, which is shown by

slight changes in rock colour and lithology for about 1m at the top of the Prince Albert Formation (Figure 4.8).
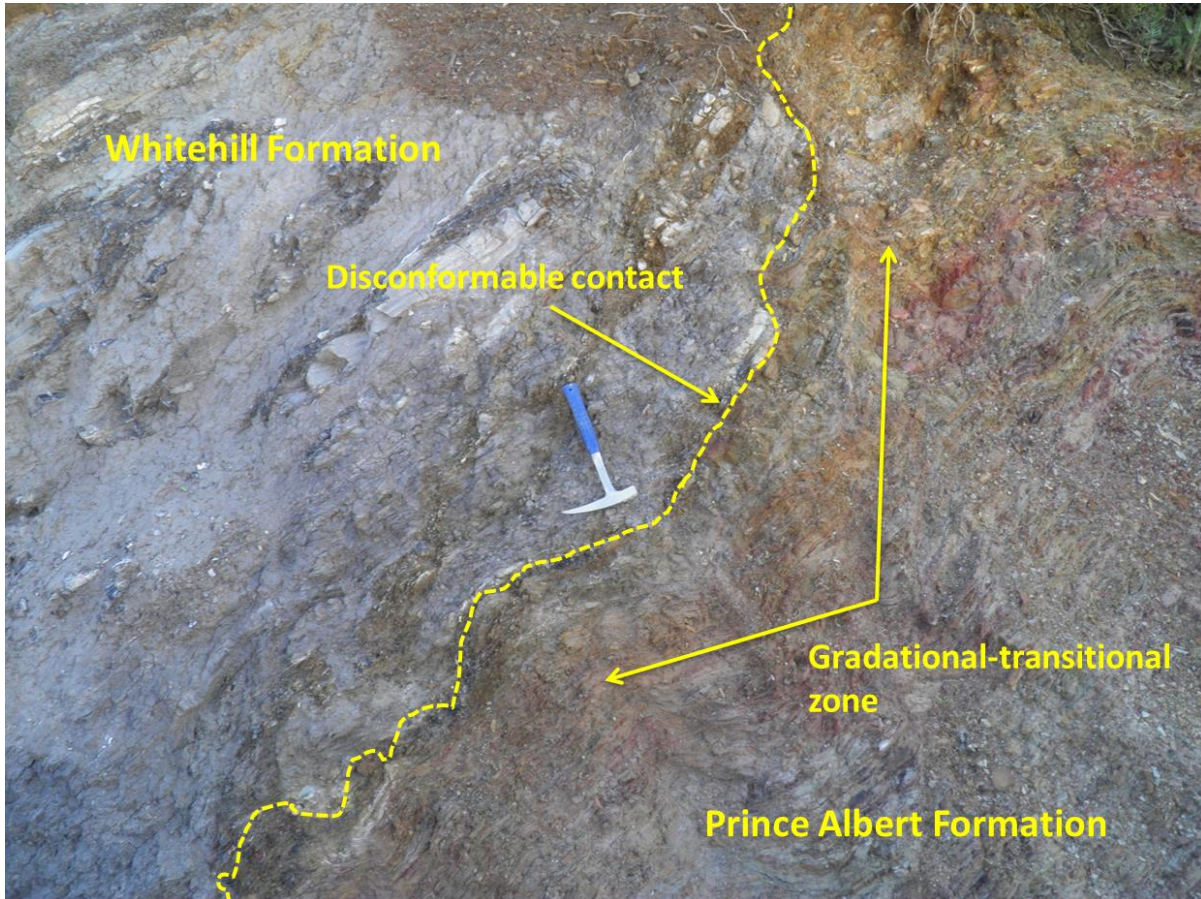
Figure 4.8 Photograph showing gradational-transitional zone and disconformable contact between the Prince Albert Formation and the Whitehill Formation along the Ecca Pass.

The Whitehill Formation is mainly made up of greyish-black, thinly laminated carbonaceous shale with subordinate layers or lenses of chert. The black chert is amorphous silica, which is harder and more resistant to weathering and is darker in colour than the weathered black shale. The co-existence of carbon-rich shale with chert indicates that the silica that forms the chert could have possibly precipitated from the decaying organic materials in the environment. The organic materials as well as the reducing deep sea environment, both contributed to the dark grey colour of the rocks. Some of the silica that precipitated in the

rock sequence was incorporated in the claystones and thus result in the increasing hardness of the rocks. The black carbonaceous shale has been weathered to white shale (Figure 4.9), with patches of red and yellow shades (Figure 4.10) and generally rich in iron sulphides (pyrite). The outcrop is generally extensive and ultra-tabular (about 27 m thick) with a normal fault cutting through the formation (Figure 4.11), thereby dividing it into two layers which lie side by side. The laterally extensive and ultra-tabular nature of the black, laminated, carbonaceous shales indicates deposition in reducing (anoxic) environment.

Figure 4.9 Weathered thinly laminated carbonaceous shale of the Whitehill Formation along the Ecca Pass with subordinate layers or lenses of black chert. The black carbonaceous shale have been weathered to white shale (Elevation: 499 m; Longitude E 26^0 37′ 38.3″; Latitude S 33^0 12′ 58.4″).

Figure 4.10 Weathered thinly laminated shale of the Whitehill Formation with patches of red and yellow shades and generally rich in iron sulphides (pyrite). (Elevation: 499 m; Longitude E 26^0 37′ 38.3″; Latitude S 33^0 12′ 58.4″).
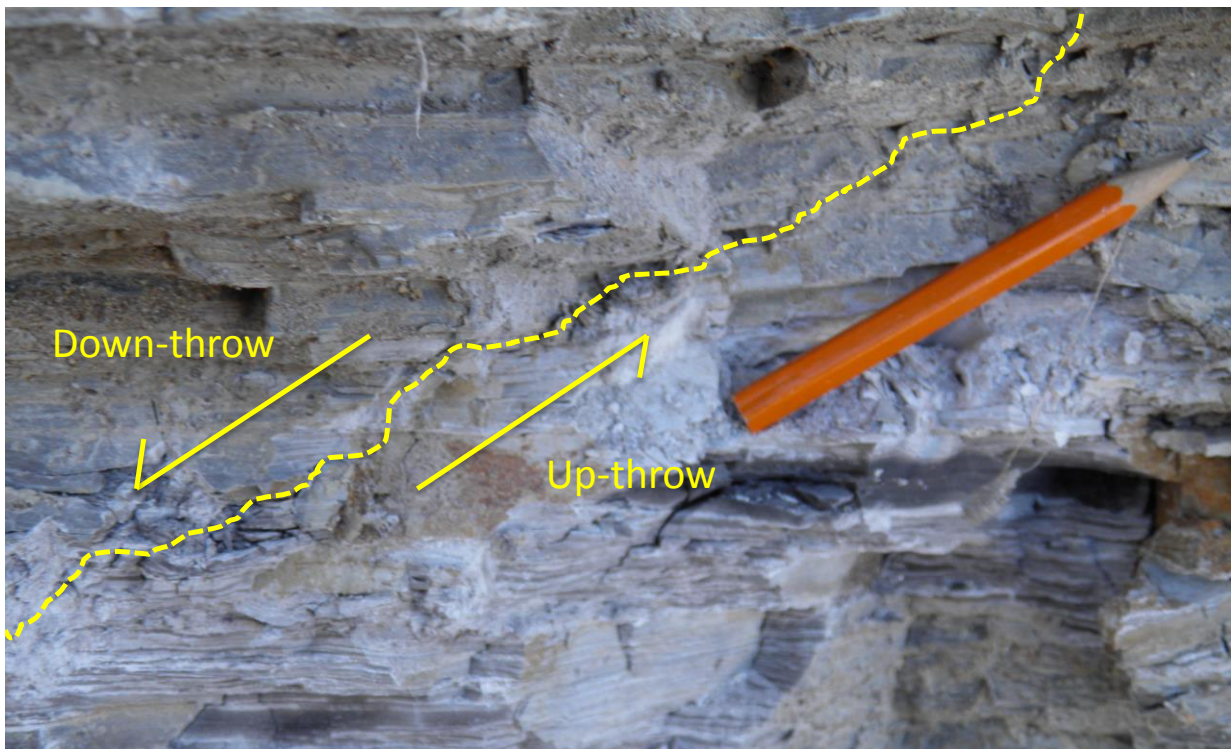
Figure 4.11 Photograph showing a normal fault cutting through the Whitehill Formation, thus dividing it into two layers which lie side by side.

4.3.3 Collingham Formation

The Collingham Formation rests conformably on the Whitehill Formation and is conformably overlain by the Ripon Formation (Figure 4.12). The formation mainly consists of regularly bedded alternation of thin, ultra-tabular, continuous hard beds of (coarse grain), dark-grey siliceous shale and very thin beds of weaker or softer (fine grains) yellowish material that are assumed to be ashfall tuffs that were altered to K-bentonite (Figure 4.13). The yellow layers have an average thickness of 3 cm whilst the interbedded mudrocks has an average thickness of 4.5 cm (Figure 4.13). The formation is divided into two parts by a fault line that runs through it. The footwall has a thickness of about 35.6 m whilst the hanging wall measures up to 21 m. The footwall has thin and tabular mudstones with bedding scale ranging from 1 cm to 11.6 cm in thickness as observed in the field. The mudstones are the hard and dark coloured layers with a relatively coarser grain size; whereas the soft and light coloured layers are claystones, and are relatively fine grained (see Figure 4.14). The hanging wall has much a flat bedded occurrence.
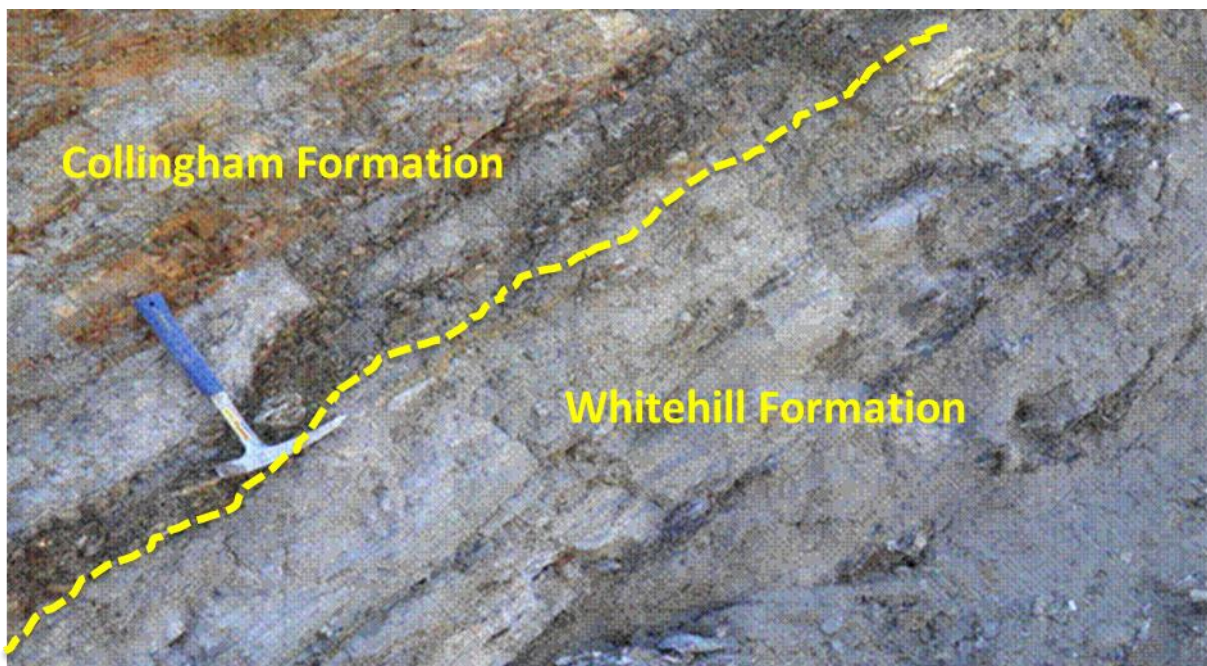
Figure 4.12 Photograph showing conformable contact between the Whitehill Formation and the Collingham Formation along the Ecca Pass.

Figure 4.13 Photograph showing thinly bedded blackish shale of the Collingham Formation along the Ecca Pass, interlayered with yellow material that are assumed to be ashfall tuffs that were altered to K-bentonite. The yellow layers have an average thickness of about 3 cm whilst the thickness of the tabular mudstones varies from 1 cm to 11.6 cm.
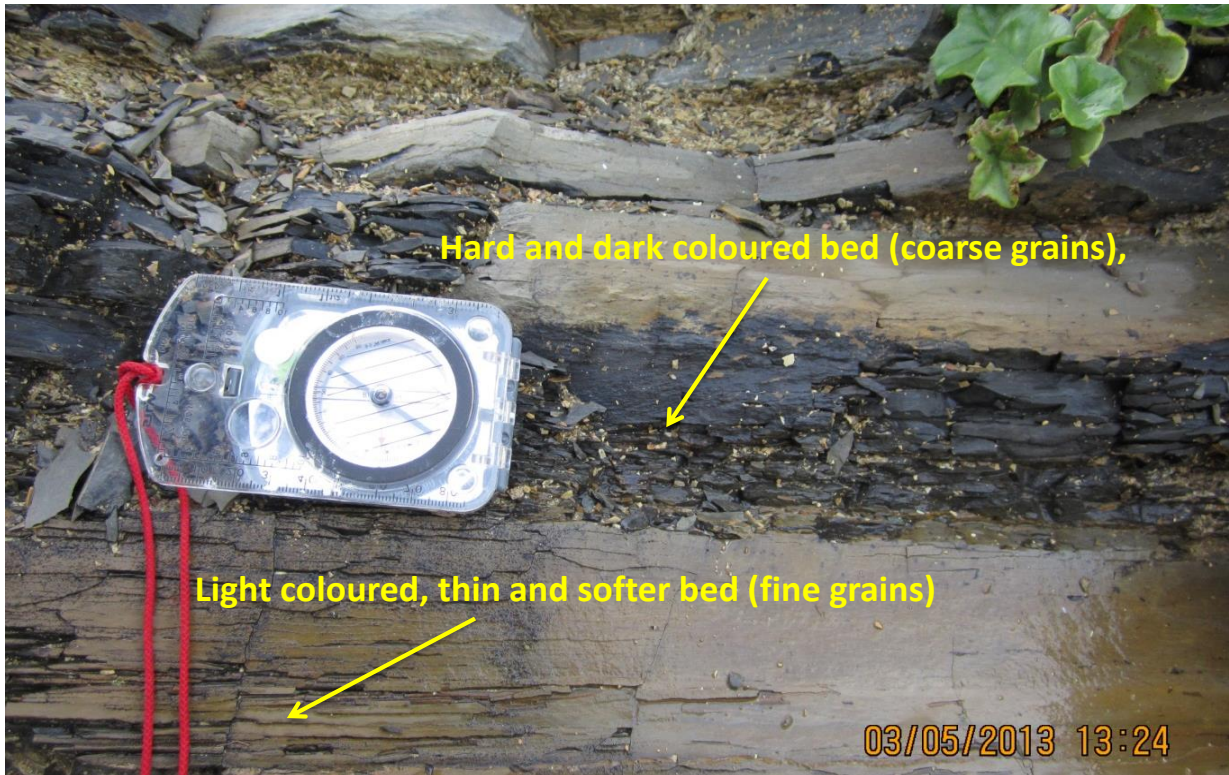
Figure 4.14 Well developed horizontal rhythmite of claystone (soft and light beds) interbedded with the mudstones (hard and dark coloured beds) of the Collingham Formation (Elevation: 471 m; Longitude E 26^0 37′ 35.7″; Latitude S 33^0 12′ 56.0″). The claystone easily crumbles than the mudstones. Lamination structures can be seen in the finer mudstones. Micro-ripple lamination appeared in the relative coarser and thicker mudstone layers, which is a typical sedimentary structure for turbidite sediments.

The soft beds are well laminated with a pure clay mineral composition which result in their flakiness and crumble characteristics. Also, there are micro-ripple laminations and climbing ripple lamination structures in the dark hard mudstone layers, but not found in the soft claystone layers. The alternated layer structure shows typical rhythmite rock features, indicating that the deposits were probably of turbidite sediments in origin and formed in reducing environment. Basically, the purer claystone layers were deposited in relatively quieter water period whereas the hard mudstone layers were formed in a slightly agitated water period, reflecting that the water energy fluctuated during the deposition of sediments. Some of the black shales were weathered and oxidised to brown colour in some part of the outcrop along Ecca Pass.

4.3.4 Ripon Formation

The Ripon Formation disconformably overlies the Collingham Formation (see Figure 4.15). It has an average measured thickness of about 820 m. The strata are well-developed, generally dip at about 36° and were affected by weathering.
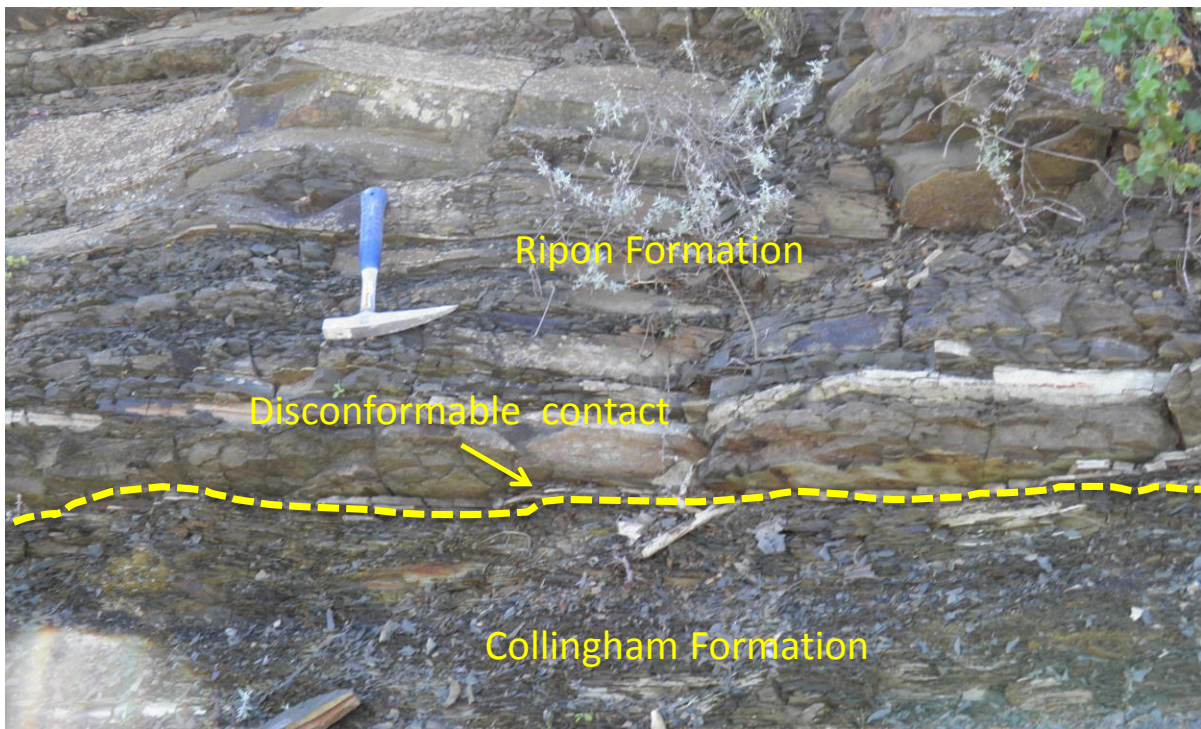
Figure 4.15 Disconformable contact between the Collingham Formation at the bottom and the Ripon Formation at the top. The top beds are slightly inclined compared to the bottom beds, indicating a disconformity or lower angle of unconformity.

Silicification in the Ripon Formation was well-developed than those of the Prince Albert and Whitehill Formations. It consists of poorly sorted, fine to very fine grained sandstones alternating with dark-grey rhythmites and shale units (Figure 4.16). In the Ripon Formation, black shales are separated by grey laminated shale and mudstone as shown in Figure 4.16. The organic content in the black shales increased towards the upper layers as indicated by a much darker colour. Thus, the persistence of the anoxic conditions led to the increase in the organic carbon content of the upper black shale layer. The anoxic conditions probably

suggests that there was an abundance of organic material in the depositional area that depleted oxygen creating conditions under which organic rich sediment was accumulated.
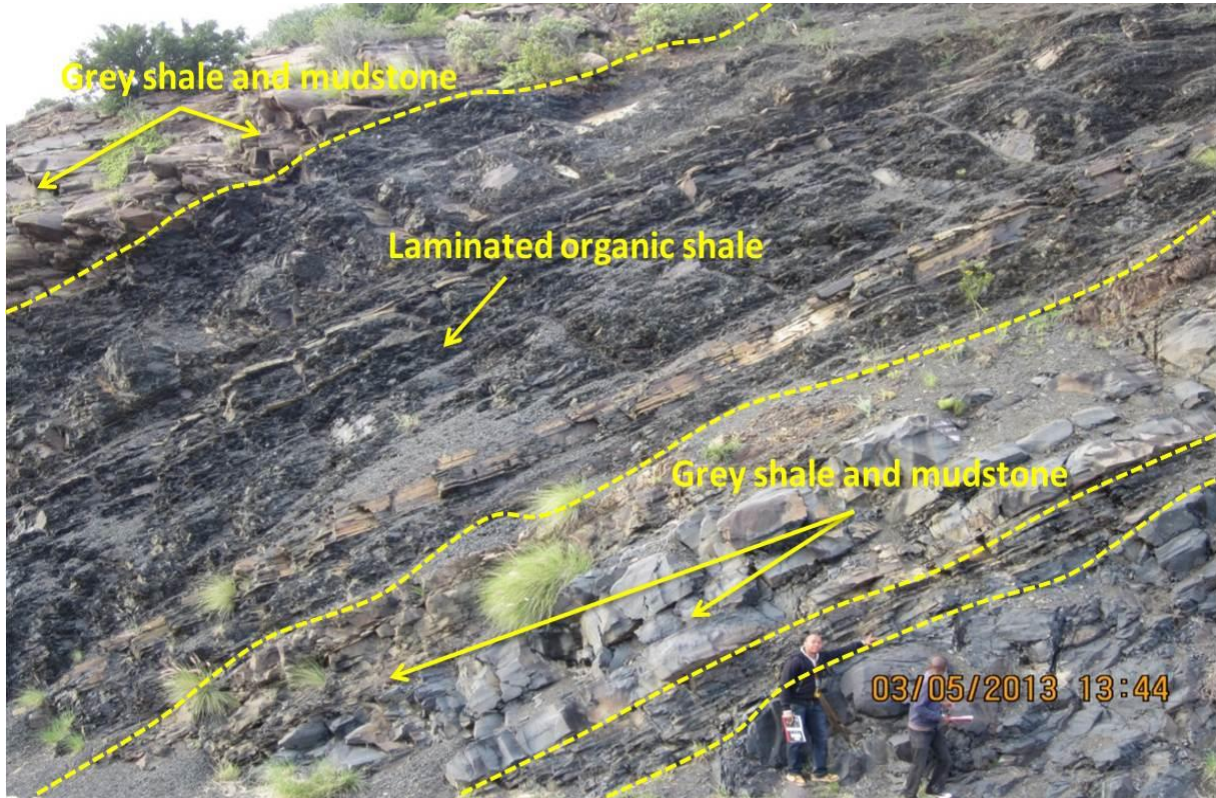
Figure 4.16 Photograph showing laminated organic shale separated by grey shale and mudstone of the Ripon Formation along the Ecca Pass (Elevation: 349 m; Longitude E 26^0 37′ 08.2″; Latitude S 33^0 12′ 09.2″). Most of the sandstones in the lower part (10 m near the base of the formation) of the formation are greywacke which is textually immature.

Typically, the rocks range from thin to thick bedded, ranging from 0.25 m to 48 m in thickness. The thick bedded were mostly affected by turbidity currents showing little or no sedimentary structures. The sediment grains were sub-angular to sub-round and enclosed in clay and matrix minerals. The rocks of the Ripon Formation indicate numerous upward coarsening cycles of well laminated mudstones and sandstones depicted in Figure 4.17.

Figure 4.17 Photograph showing floodplain deposits represented by the alternating sandstones and mudstones.

The sandstones average thickness ranges from 20 cm - 40 cm and they are sharp, tabular with horizontal lamination and occasionally, show upward grading of the thin sandstone beds within the rhythmite (varying from a few mm to a few cm). Typical for all the sandstones, the sediment grains are sub-angular to sub-round and imbedded in clay and matrix minerals that have made the rocks to be very hard. The rocks also have a high percentage of feldspar with matrix minerals that include smectite, illite, chlorite and kaolinite. The sandstones have several horizontal bedding and calcareous concretions (Figure 4.18). Deformational-depositional structures such as convolute bedding, flaser bedding and load casts are common towards the base of the Ripon Formation (see Figure 4.19).
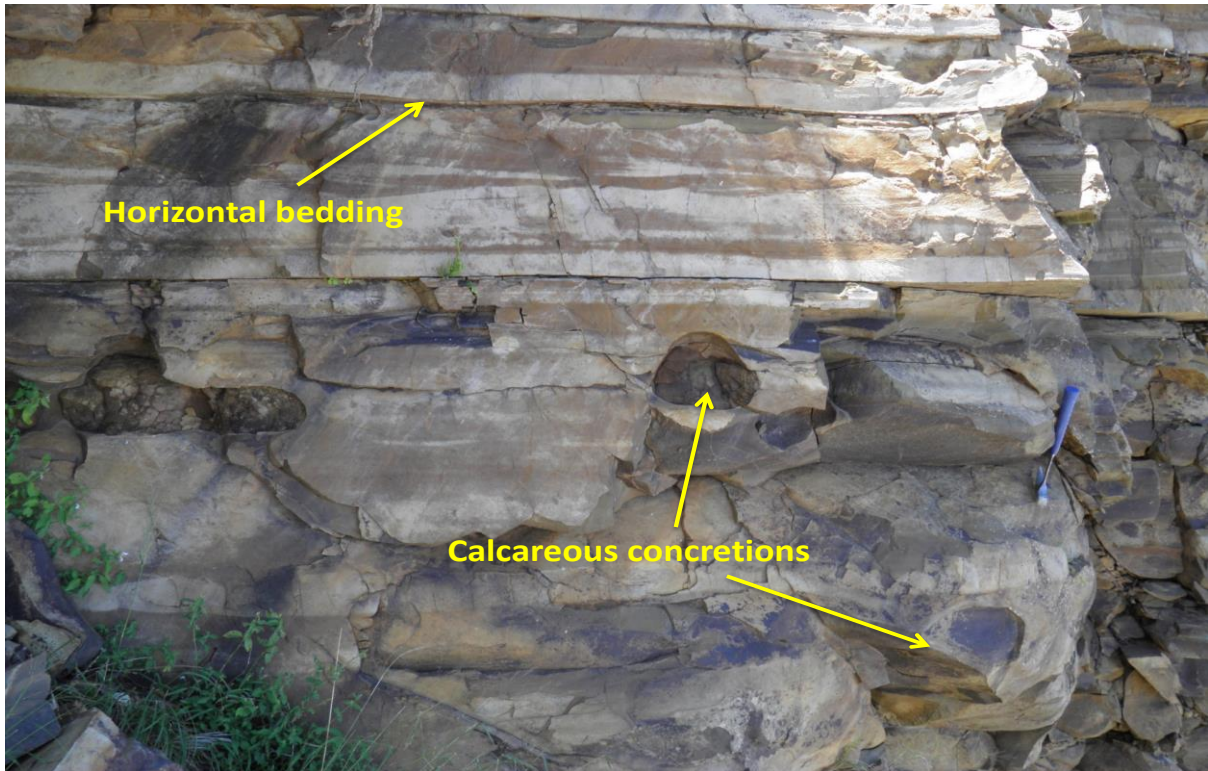
Figure 4.18 Well-developed horizontal bedding, lenticular bedding (upper middle), calcareous concretions, and joints on the greywacke in the basal unit of the Ripon Formation.

Figure 4.19 Photograph showing convolute and flaser bedding of the Ripon Formation. (Elevation: 349 m; Longitude E 26^0 37′ 08.2″; Latitude S 33^0 12′ 09.2″).

4.3.5 Fort Brown Formation

The Fort Brown Formation mainly consists of rhythmite and greenish-grey shale (Figure 4.20) with subordinate sandstone that is seen in the upper part of the outcrop where the grains are coarser (shows upward coarsening). It is believed that the formation was accumulated in a lacustrine environment due to the presence of well-developed varved rhythmite structure and seat-earth layers. The Fort Brown Formation can be divided into two members with a total thickness of 345.2m., the Lower Grey Varve Rhythmite and the Upper Mudstone-Sandstone Member. The Lower Grey Varve Rhythmite are the thin bedded greyish brown and well laminated rhythmites of mudstone, intercalated with a subordinate lenticular sandstone layer of about 12 m length imbedded within the mudstones sequence. The varved rhythmites are represented by light and dark colour varved layers with a thickness of less than 2 mm.

The Upper Mudstone-Sandstone Member had more sandstone beds when compared to the Lower Member. The increase in the sandstone beds indicates the shallowing of the lacustrine environment in which the sediments of the formation accumulated. The shallowing of the basin possibly continued to the overlying Beaufort Group, which is dominated by fluvial sediments. Occasionally, fine horizontally laminated thin bed siltstones occur with some of the interbedded sandstones which either show horizontal lamination or cross/ripple laminations and vary in thickness. In the upper part of the formation, ripples which are associated with wavy bedding are prominent (upper part of the succession) and sometime form starved ripples. Deposition is suggested to be in a regressive shallow reducing environment.
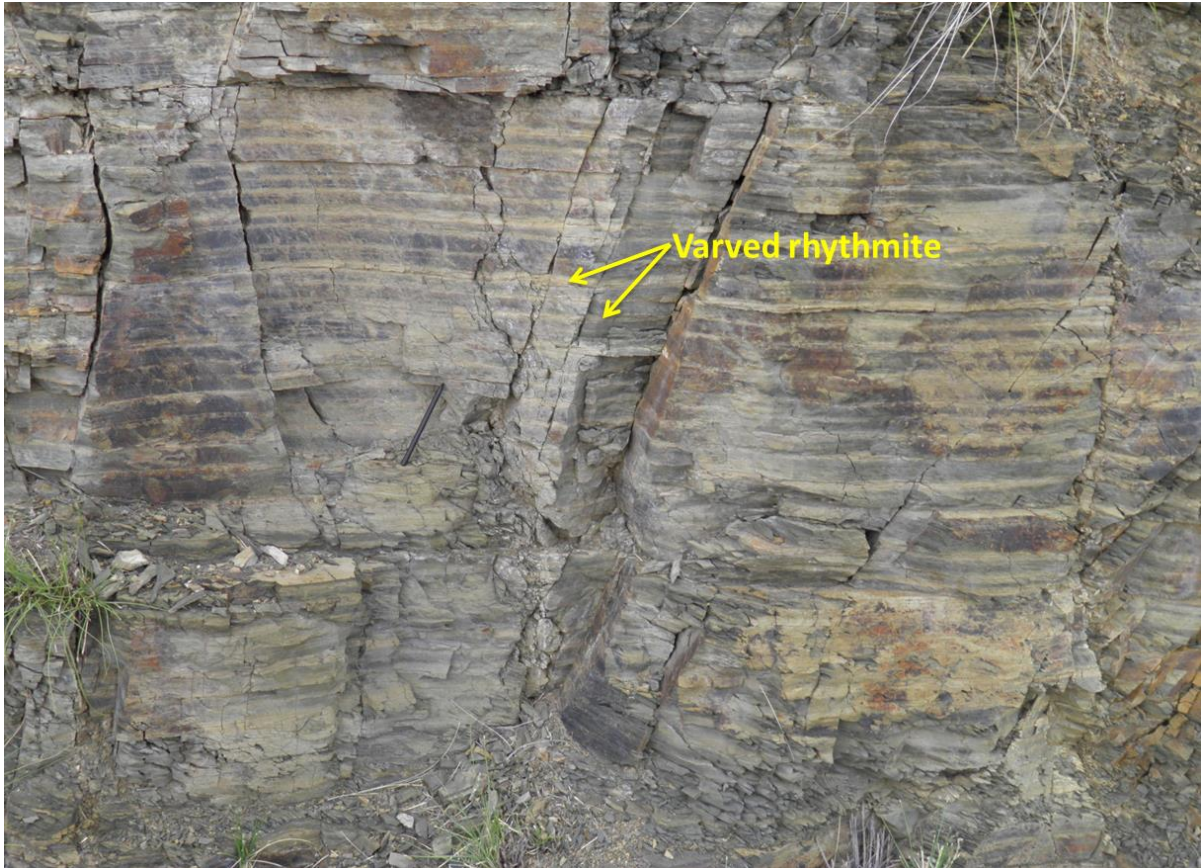
Figure 4.20 Varved rhythmite deposits of the Fort Brown Formation possibly of lacustrine origin. The photograph shows alternating light coloured mudstone and dark coloured mudstone, each with a centimetre thickness. The varves which are another kind of lamination can also be observed and the structures formed in a lacustrine environment with seasonal deposition of sediments. Whenever there was a high inflow of water, coarser sediments were also transported into the basin, whilst the finer sediments were deposited from suspension during periods when the water inflow was low.

The rhythmite facies of the Fort Brown formation consists of alternating light and dark laminae as shown in Figure 4.20. The alternation is possibly due to compositional changes and also the changes in grain size of the sediments. The dark laminae consist mainly of clay minerals whilst the light laminae are silty. The light laminae also reflected low oxygen levels such that small organisms were excluded in the sediments; organic is a contributing factor to the dark colour of sediments. The dark layers are also low energy deposits whilst the light laminae possibly indicate an increase in water strength. The rhythmites are fresh water

lacustrine facies. Overbank flooding of channels brought sand into the lakes for the observed subordinate sandstones in the lower parts of the formation, but as the lake filled up, more sandy materials were deposited in the basin, creating a coarsening up sequence.

4.4 Beaufort Group

The Beaufort Group consist of fine-grained sandstones and mudstones that show fining-upward sequence. The group consists of the Adelaide and Tarkastad Subgroups. The Adelaide Subgroup comprises three formations, namely; Koonap, Middleton and Balfour Formations whilst the Tarkastad is made up of the Katberg and Burgersdorp Formations.

4.4.1 Koonap Formation

The Koonap Formation is predominately made up of greenish silty sandstones and mudstones that show fining upward sequence indicating that deposition occurred in high-energy systems that grade upwards into lower energy systems (Figure 4.21). The sedimentary structures seen on the outcrop includes; trough cross-bedding, flat bedding, ripple marks (occasionally), micro-cross lamination and massive bedding which is very common with the mudstones. Sandstones become more prominent at the upper part of the formation with folded strata.
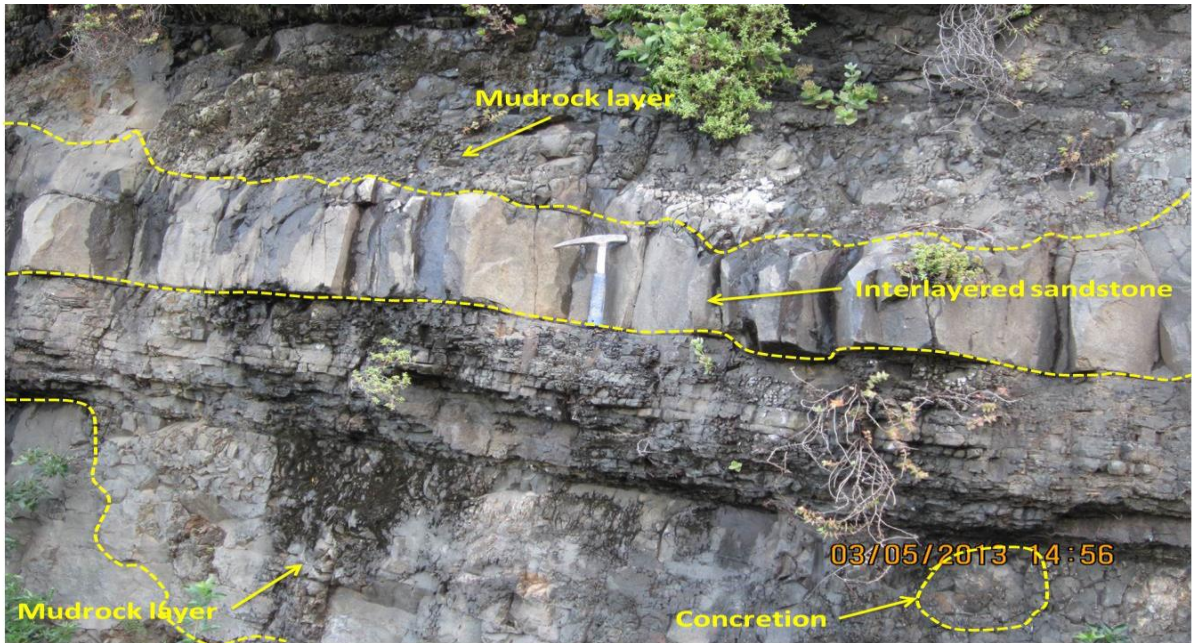
Figure 4.21 Photograph of the Koonap Formation near Fort Beaufort showing sandstone interbedded with mudrock. The sandstones show fining-upward sequence (Elevation: 241 m; Longitude E 26^0 39′ 04.9″; Latitude S 33^0 03′ 24.4″).

4.4.2 Middleton Formation

The Middleton Formation is dominated by red mudstones interbedded with light-grey sandstones (Figure 4.22) that also show fining-upward sequence which is believed to be deposited in low-energy systems such as meandering rivers, channel zones and flood plains. Traces of fossils were found preserved within the rocks of the upper localities of the Middleton formation cropping out along the eastern side of the road R334, approximately 20 km south of Adelaide in the Eastern Cape Province, South Africa. The sedimentary structures seen in the Formation include; trough cross-bedding, flat bedding, massive bedding (common at the base of the Formation) and micro-cross lamination which are associated with fine grained sandstones towards the top of the Formation. Traces of fossils were seen in the upper part of the outcrop.
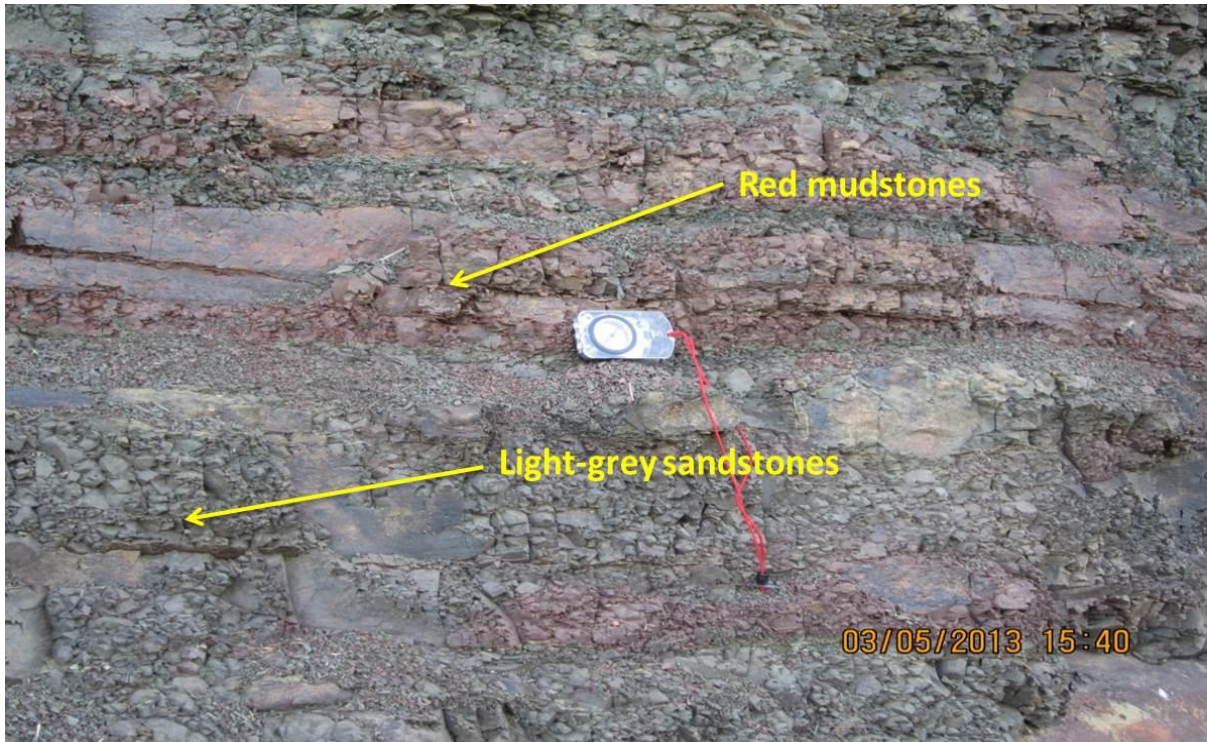
Figure 4.22 Photograph the Middleton Formation around Fort Beaufort showing red mudstones interbedded with light-grey sandstones that show fining-upward sequence believed to be deposited in low-energy systems (Elevation: 463 m; Longitude E 26^0 37′ 58.7″; Latitude S 33^0 51′ 26″).

4.4.3 Balfour Formation

The Balfour Formation is seen around Queenstown and East coast area. It comprises of five members, namely; the Oudeberg, Daggaboersnek, Barberskrans, Elandsberg, and Palingkloof Members. These members are distinguished based on the lithological variation which is dominated and characterised by the alternating sequence of sandstones and mudstones. The Figure below (Figure 4.23) shows the distribution of sediments of the five members that make up the Balfour Formation.
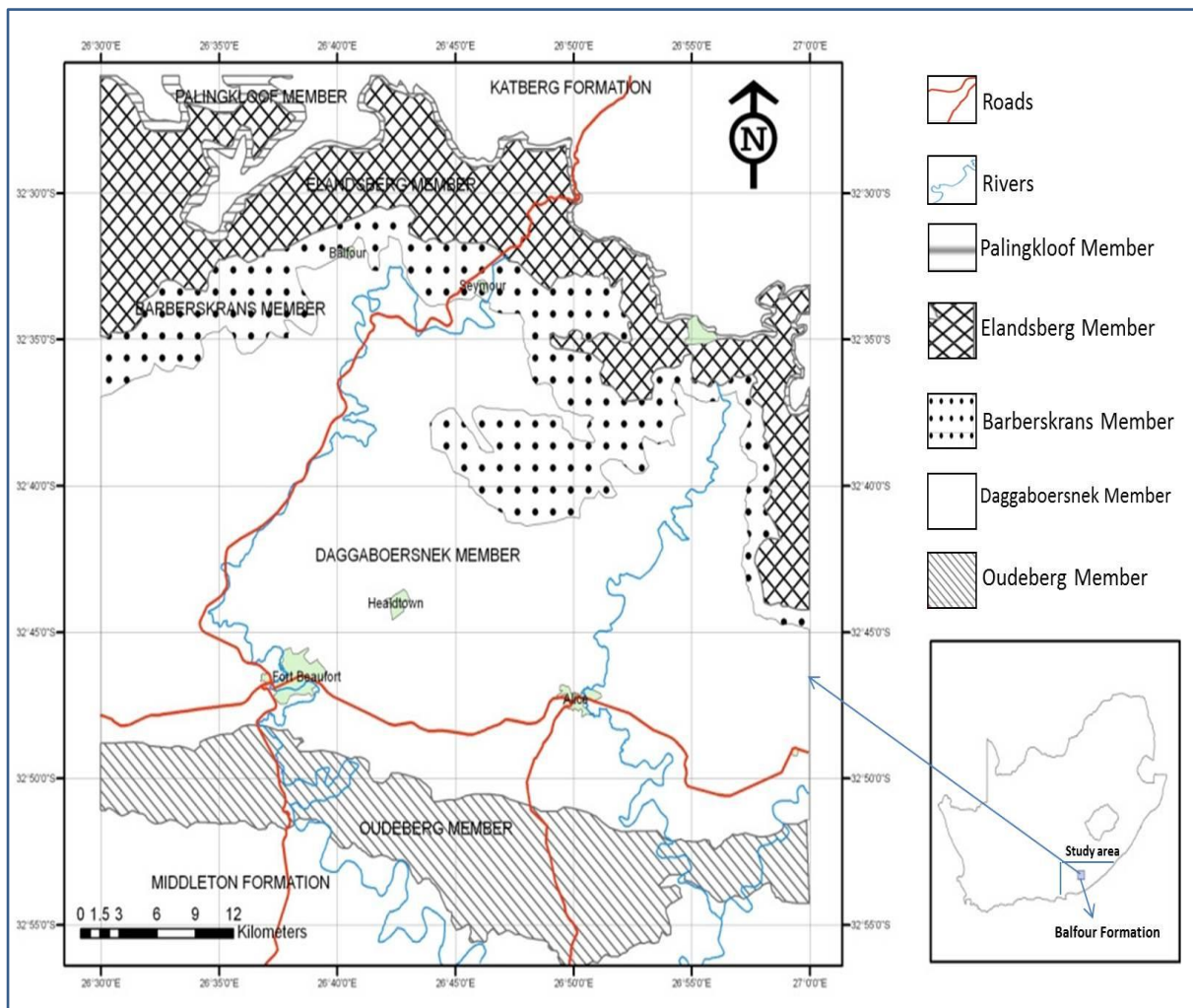
Figure 4.23 Map showing the distribution of sediments of the Oudeberg, Daggaboersnek, Barberskrans, Elandsberg, and Palingkloof Members of the Balfour Formation (Modified by author from Katemaunzanga and Gunter, 2009).

4.4.3.1 Oudeberg Member

The Oudeberg Member is made up of yellowish and light grey sandstones which are occasionally interbedded with mudstones. The thickness varies in the whole succession (from 85 m to about 125 m) due to faulting which results in duplication of strata (Figure 4.24A). They also show fining upward sequence indicating deposition in grading upwards braided rivers instead of meandering rivers (Figure 4.24B). The sandstones at the base of the outcrop are coarse grained and associated with intraformational conglomerates (Figure 4.24C) that grades upward into massive and medium grained sandstones that are up to 3 m in thickness.

The sandstones shows different features such as; tabular cross-bedding, wave-ripple marked surface (Figure 4.24D), weak stratification, ripple cross lamination (Figure 4.24E).
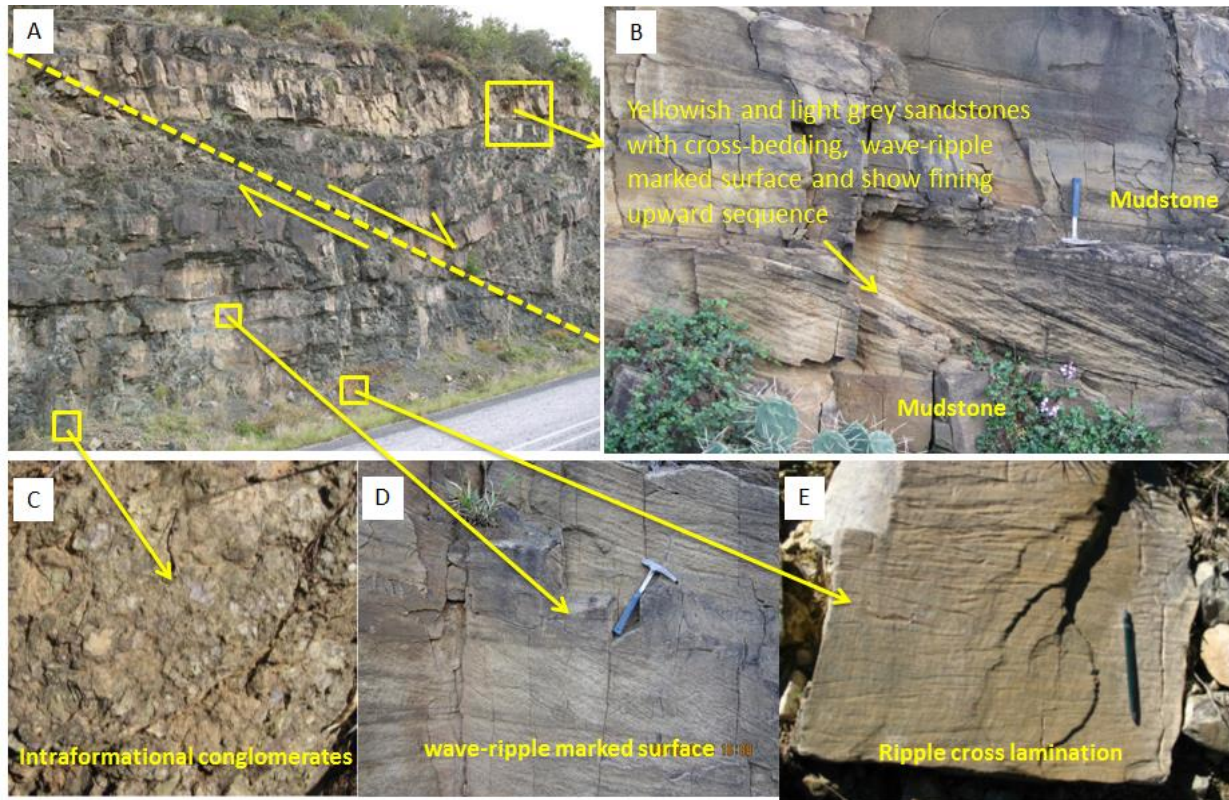
Figure 4.24 Photograph of the Oudeberg Member, north of Fort Beaufort. (A) Faulting that results in duplication of strata. (B) Fining upward sequence indicating deposition in grading upwards braided rivers. (C) intraformational conglomerates. (D) Wave-ripple marked surface. (E) Ripple cross lamination (Elevation: 833 m; Longitude E 26^0 53′ 34.2″; Latitude S 32^0 53′ 38.7″).

4.4.3.2 Daggaboersnek Member

The Daggaboersnek Member is predominantly of light-dark grey mudstones, interbedded with thin tabular sandstones and siltstones (Figure 4.25). The sandstones were deposited as point bars and stained with dark colour due to leaching of the topsoil (organic materials). Intraformational conglomerates were also seen in the Daggaboersnek Member which is made up of mud clasts enclosed in fine-grained sandstone matrix and the fine sandstone shows

fining upward sequence into siltstone and mudstone. Palaeocurrent measurements suggest that the provenance is to the south - southeast (SSE) whilst palaeo-flow direction is north - northwest (NNW) (Katemaunzanga and Gunter, 2009). Horizontal bedding, cross lamination, desiccation cracks, ripple mark, ripple cross-lamination (most common), trough cross-bedding and concretions were seen occasionally in the mudstones. Cubes of the mineral pyrite were also seen on the outcrop and the present day pyrite results in the dark colour stain on the rock.

Figure 4.25 Photograph of Daggaboersnek Member east of Alice showing light-dark grey mudstones interbedded with sandstones. The sandstones are stained with dark colour due to leaching of the topsoil (organic materials) (Elevation: 703 m; Longitude E 26^0 56′ 09.5″; Latitude S 32^0 38′ 23.9″).

4.4.3.3 Barberskrans Member

The Barberskrans Member is a braided river channel deposit that consists predominantly of fine-grained sandstones that show fining upward sequence with occasional horizontal and cross bedding (Figure 4.26). The measured thickness of the whole succession is about 108 m. In some areas, the beds are tilted (inclined) and they show lamination with occasionally parting lineation (Figure 4.27). Trough cross-bedding and current ripple lamination with occasional massive beds were observed in some part (lower portion) of the outcrop. The sandstones are of different facies which includes the massive sandstone and horizontally bedded sandstone. The massive sandstone at the base of the outcrop is fine grained and the thickness ranges from 30 cm – 2 m. The horizontal bedded sandstones were also seen in the field in the lower part of the outcrop in association with the massive sandstone. The horizontal bedded sandstones sometime show stratification intercalated with greenish-grey mudstones and ranges from 20 cm – 10 m thick.

Figure 4.26 Photograph of Barberskrans Member showing fine-grained sandstones with horizontal and cross bedding. The sandstones show fining upward sequence.

Figure 4.27 Khaki sandstone of the Barberskrans Member interbedded with thin laminae of mudrocks, near Hogsback (Elevation: 945 m; Longitude E 25° 50' 34.6"; Latitude S 32° 32' 7.9").

4.4.3.4 Elandsberg Member

The Elandsberg Member is made up of pale grey mudstones, which are interbedded with thin lenticular sandstones just like the Daggaboersnek Member (Figure 4.28). The thickness of the thin lenticular sandstone beds vary from 3 cm to 12 cm whilst the measured thickness of the succession around Cradock area is about 185 m. The mudstones of the Elandsberg Member, which thins in a westerly direction towards and beyond the Cradock area, are of lighter colour than the mudstones of the Daggaboersnek Member which are darker in colour. Cross bedding, cross lamination, ripple marks, ripple cross-bedding (not that common) were seen occasionally in the sandstones. The sandstones lithosomes are both tabular and lenticular and shows trough cross-bedding (common at the base) which grades upwards into cross-lamination. The sandstone at the base of the outcrop is fine grained and the thickness ranges from 20 cm – 2.4 m. Calcareous lenses and concretions are seen concentrated within the mudstone layers. The contact between the Elandsberg Member and the overlying Palingkloof Member is not easily recognized, although it is characterized by the appearance of red-mudstones without an observable hiatus surface.
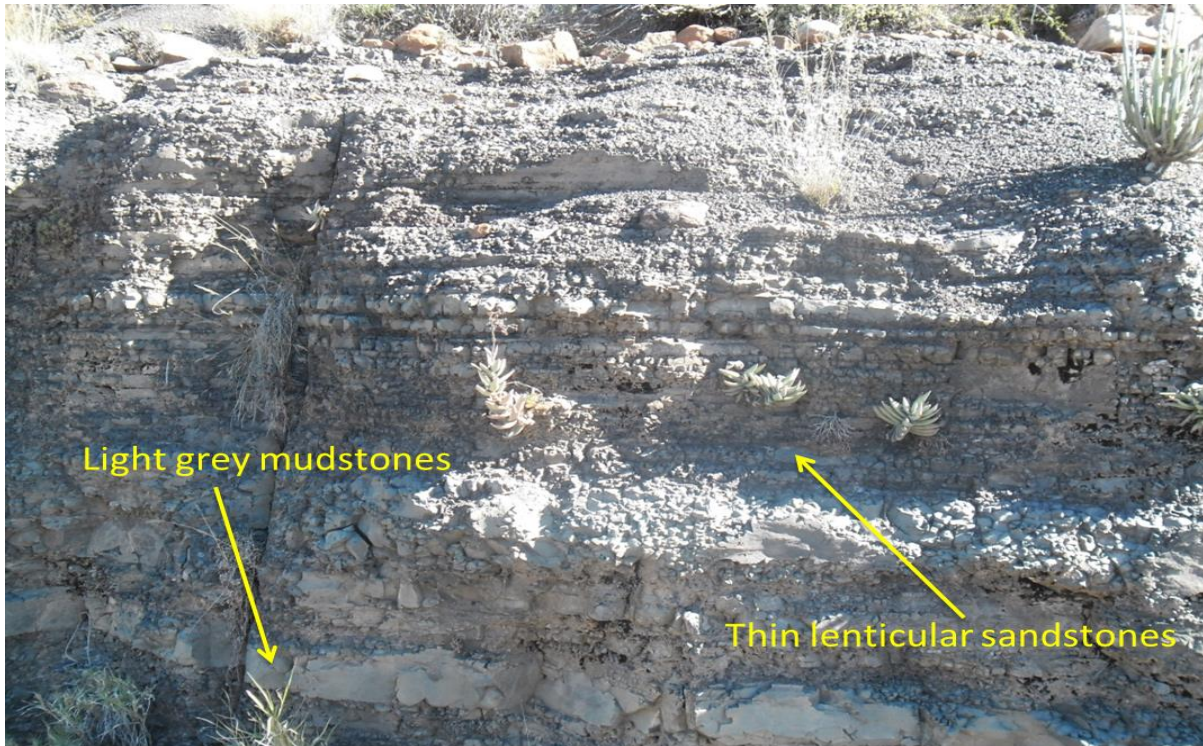
Figure 4.28 Photograph of the Elandsberg Member, near Cradock showing greenish grey mudstones, interbedded with thin lenticular sandstones (Elevation: 930 m; Longitude E 25° 40' 3.3"; Latitude S 32° 12' 49").

4.4.3.5 Palingkloof Member

The Palingkloof Member which overlies the Elandsberg Member is predominantly of red and greyish mudstones with subordinate shale (Figure 4.29). The measured thickness of the whole succession is about 43 m. The beds are thin, ranging between 2 cm to about 15 cm. This member has been the area of interest to many scientists, especially Palaeontologists and Geologists since it covers the historical extinction event that occurred during the Permo-Triassic period. The Permo-Triassic boundary is discernable at the base of the Palingkloof Member along the R61 road between Cradock and Tarkastad towns, where red and grey mudstones are displayed along the road cuttings (Figure 4.30), this placement was based on vertebrate biostratigraphy, with the Permian fauna of the Dicynodon Assemblage Zone occurring in the Elandsberg Member and the overlying Early Triassic Lystrosaurus Assemblage Zone fossils restricted to the Palingkloof Member in the south (Gastaldo *et al*., 2009). The red colour possibly indicates that the environment was oxidized. Dessication cracks, concretions and traces of fossils are very common on the outcrop. Fildani *et al*. (2009)

stated that the P-T boundary in the Skoorsteenberg and Laingsburg Formations can be correlated/or compared with the fluvial-deltaic Palingkloof mudstone of the upper Balfour Formation in the east central Karoo which is the event bed of Smith and Ward (2001). Retallack *et al*. (2006) compared the end-Permian event at about 251 Ma with the end-Dicynodon biozone extinction within this datum. Coney *et al*. (2007) in Fildani *et al*. (2009), allude that this correlation or interpretation is supported at the Commando Drift location by a single grain U-Pb zircon date of 252 Ma ago and paleomagnetic data that record a polarity reversal from R1 to N2 (De Kock and Kirschvink, 2004). Based on the earlier comparison, it was suggested that the marine uppermost Skoorsteenberg and Laingsburg Formations in the Ecca Group are contemporaneous with the fluvial upper Beaufort Group of the east-central Karoo Basin, making the Karoo the only known basin to have a P-T boundary identified in both marine and terrestrial sections (Fildani *et al*., 2009). Fildani *et al*. (2009) concluded that the correlation of the P-T boundary indicates that asymmetric subsidence affected/controlled the style and thickness of sedimentation, resulting in a deep-marine underfilled basin in the southwestern Karoo that is contemporaneous with the fluvial-deltaic overfilled basin in the central-eastern Karoo Basin.
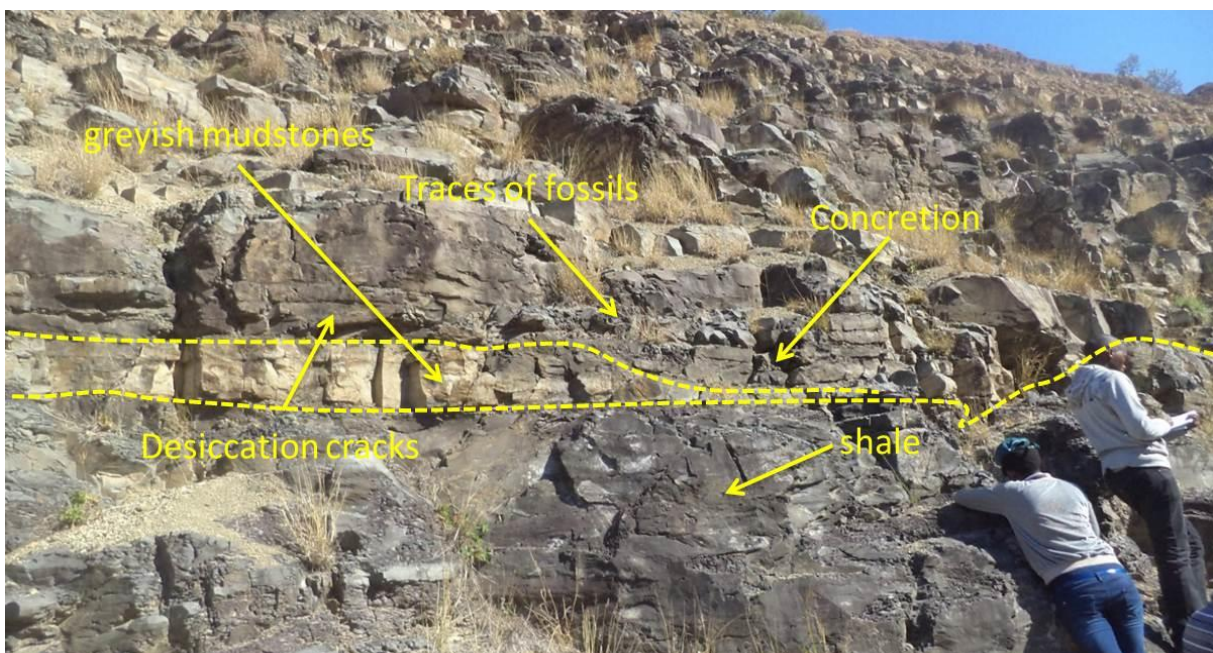
Figure 4.29 Photograph of the Palingkloof Member, near Queenstown showing greyish mudstones with subordinate shale as well as dessication cracks, concretions and traces of fossils (Elevation: 483 m; Longitude E 26° 46' 54.4"; Latitude S 32° 28' 56").
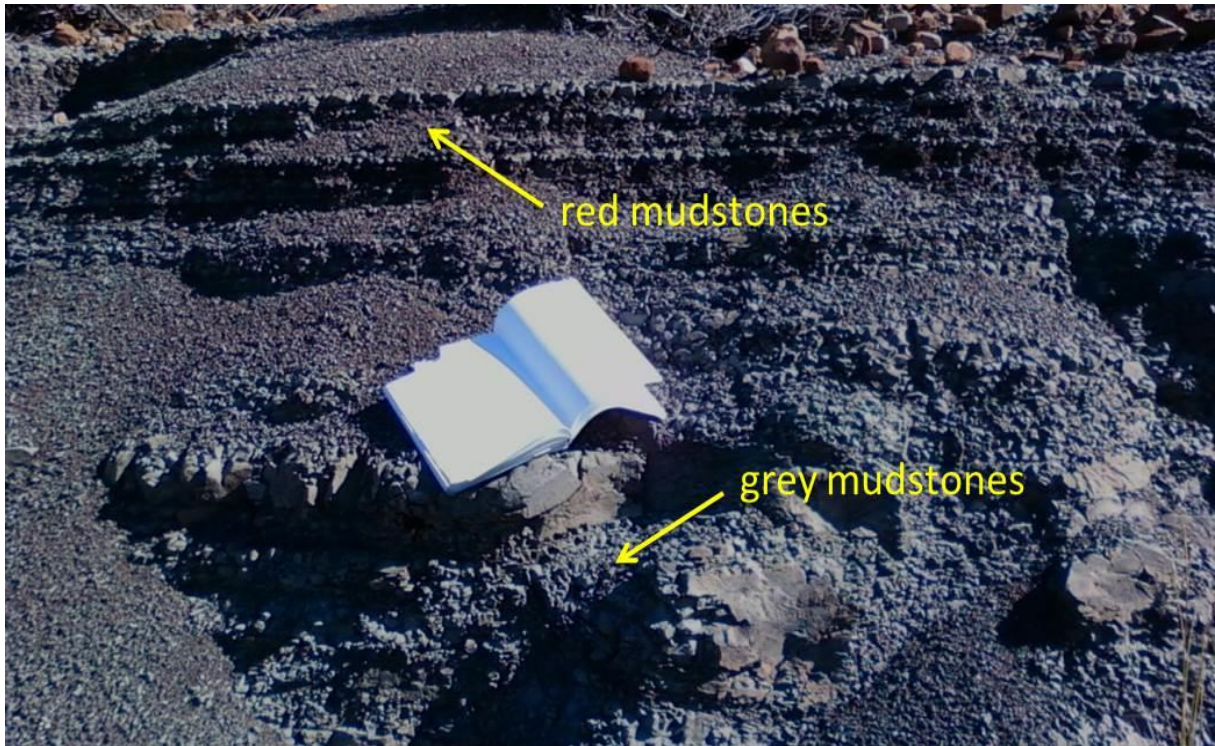
Figure 4.30 Red shales and mudstones at the base of the Palingkloof Member (where the Permo-Triassic boundary is discernable) along the R61 road between Cradock and Tarkastad towns.

4.4.4 Katberg Formation

The Katberg Formation overlies the Palingkloop Member of the Balfour Formation (Figure 4.31a). It is characterised by a high abundance of fine to medium grained, light grey sandstones with subordinate shale and red mudstones. The reddish-yellowish colour with massive bedding indicates oxidizing environment. Sedimentary structures such as tabular cross bedding, massive bedding, joint surfaces, ripple clasts, uneven erosional surfaces (Figure 4.31b), concretions (hematite concretions which are 2 cm - 12 cm in length) (see Figure 4.31c) and lamination with occasional ripple marks (about 0.5 cm in diameter) were seen on the outcrop (common with medium grained sandstones). Trace fossils Lystrosaurus were found (very few). Hollowed spherical bodies (concretions) with white materials that crystallize out due the presence of fluids (zeolite) were seen on the rock surface (Figure 4.31d). The rock fragments are generally very sharp and angular with the presence of minerals such as calcite, quartz and feldspars.

Figure 4.31 Photograph of the Katberg Formation, near Queenstown showing (a) Fine to medium grained, light grey sandstones with subordinate shale.(b) Uneven erosional surfaces. (c) Lamination and concretion (d) Zeolites.

4.4.5 Burgersdorp Formation

The Burgersdorp Formation overlies the Katberg Formation. It is the youngest formation of the Permo-Triassic Beaufort Group. It consists of dark reddish brown mudstones with subordinate red-maroon siltstones and occasionally, fine to medium grained grey sandstones (Figure 4.32). The sedimentary unit shows fining upward sequence which is believed to signify slowly aggrading floodplain deposit drained by meandering river with mixed-load. Smith (1980) envisaged that the strata of the Beaufort Group (Burgersdorp Formation) are predominantly alternating mudstones and siltstones with subordinate lenticular and tabular channel sandstone deposited by a variety of fluvial systems. This resulted in fining-upward sequences of fluvial systems which prograded into the Karoo Basin at the time of basin fill (Smith, 1987; Rubidge, 1995; Smith and Ward, 2001).

The observed mudrocks are massive and occasionally, they contain small calcrete nodule and sand-infilled mudcracks. The base of the sandstone unit is concentrated with matrix-rich mudclast parabreccias sometimes called intraformational mudflake breccio-conglomerates. Sedimentary structures such as cross lamination (common at the top), trough cross bedding and flat bedding were occasionally seen on the outcrop. Almond (2013) also stated that the rocks of the Burgersdorp Formation were laid down within the Main Karoo by northwestwards-flowing meandering rivers during a warm, arid to semi-arid climatic conditions and interpreted the well-laminated reddish mudrock with pedocrete layers (cemented soil) as playa lake deposits.

Figure 4.32 Photograph of the Burgersdorp Formation, near Queenstown showing the brownish mudstones with subordinate red-maroon siltstones and fine to medium grained grey sandstones.

The Beaufort Group is exposed almost over the entire Karoo basin and is extensively intruded by dolerite sills and dykes (at about 180 Ma). Duncan and Marsh (2006) stated that the dolerite intrusions were emplaced during crustal doming and stretching that preceded the break-up of Gondwana at about 180 Ma. The dolerites are not all of the same rock type; they vary from being olivine rich through tholeiitic composition to granophyres. When

considering the minerals within the rocks, they are noted by their differences in colours (Karpeta *et al*., 1979), with the sills showing grading upwards through olivine, hyperite into gabbro. The proportion of the dolerites to the host rock is seen to vary in the formations. Some areas are noted to have more of dolerite than the host rock and in some cases; the dolerite is seen quite less than the host rock. This could be attributed to the fact that some areas experienced much of magmatic activity than other areas. The sediments on the contact of the dolerite intrusions have been indurated or recrystallized, which led to the formation of hornfels as depicted in Figure 4.33.
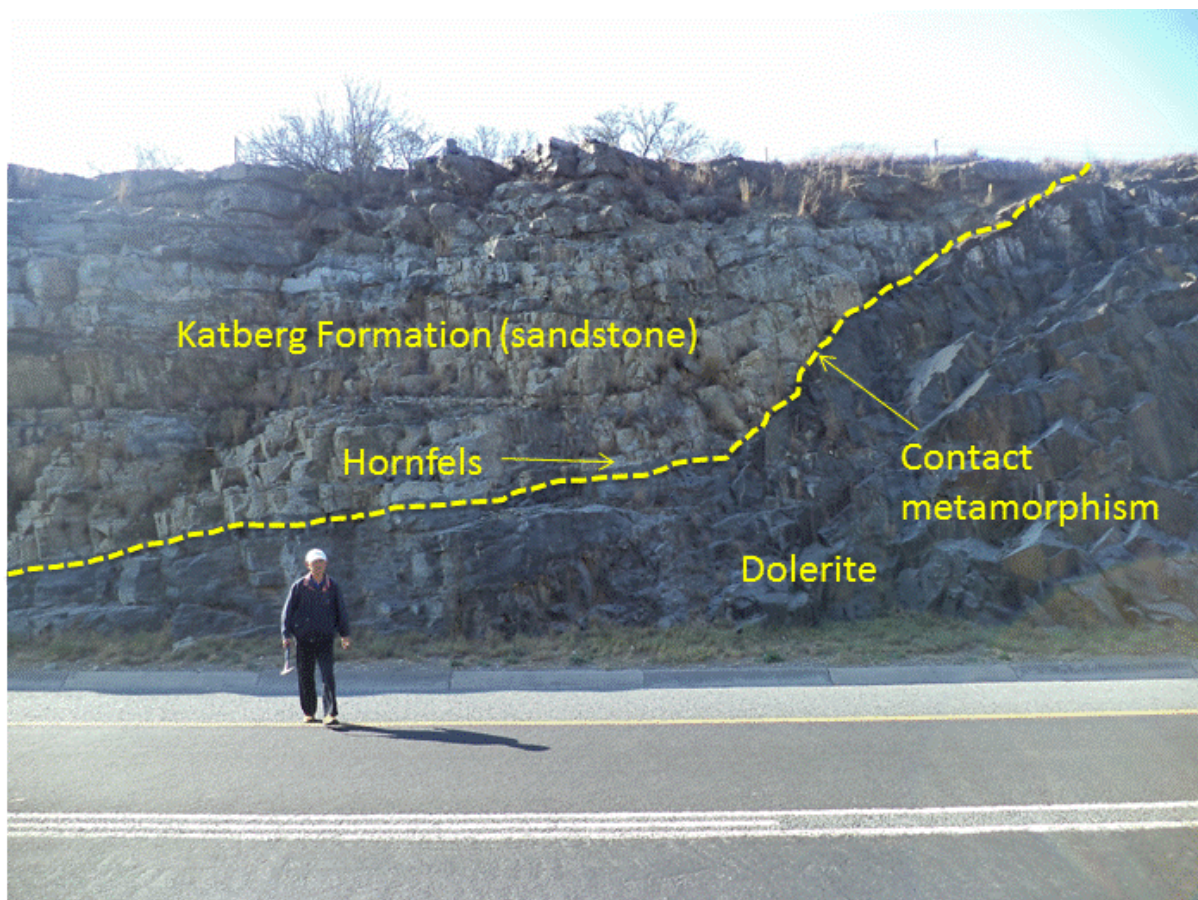
Figure 4.33 Dolerite- baked sandstone contact of the Katberg Formation near Queenstown. The sandstone have been baked or metamorphosed to resistant-weathering Katberg quartzite that is pale grey in colour.
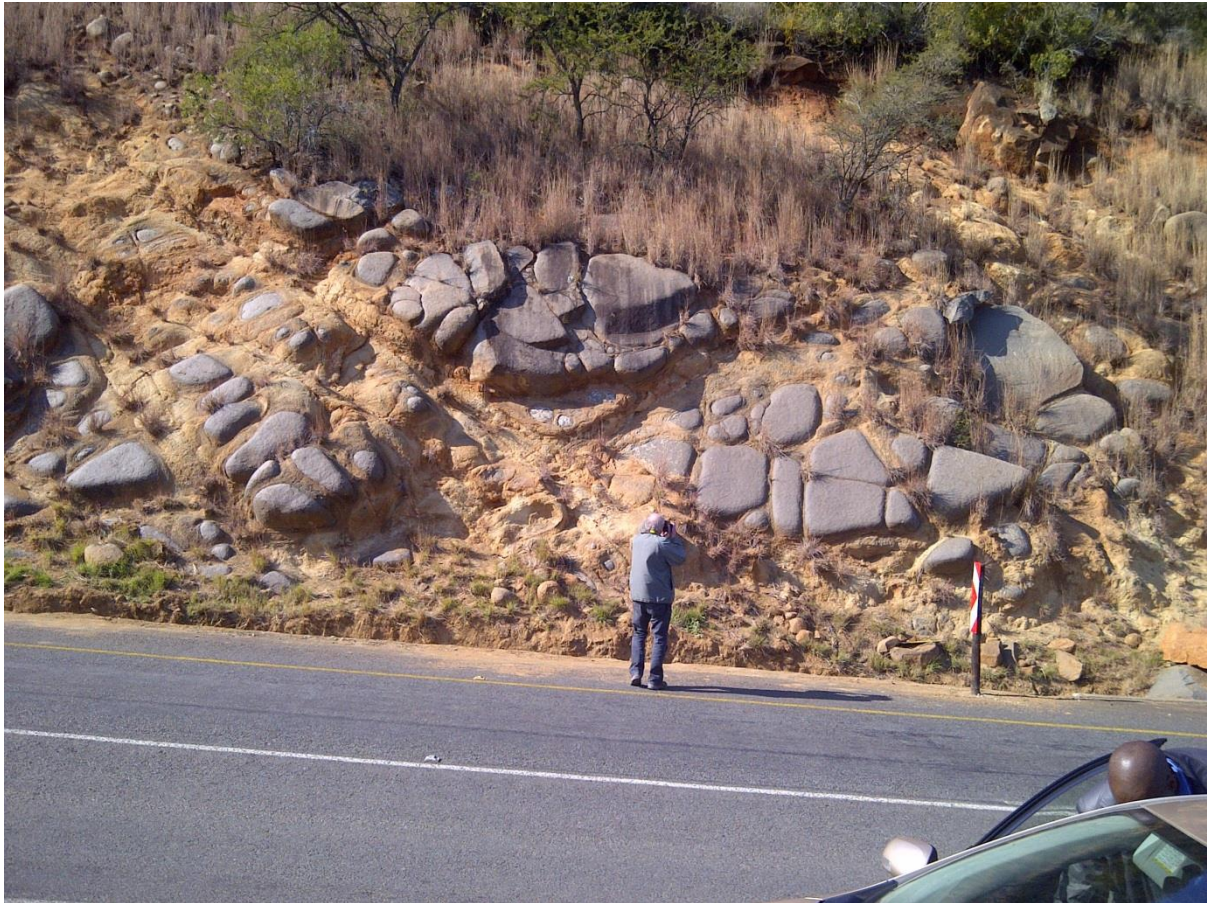
Figure 4.34 Photograph showing weathered dolerite Sabunga boulders and pebbles formed in-situ. Possibly, the boulders have not been transported and it shows evidence of exfoliation or "onion skin" weathering. Note: The "Sabunga" is the South Africa colloquial name for a type of sand and/or gravel, from weatherized dolerite.

The dolerite intrusions (sills and dykes) created the distinctive flat-top hills and mountains in the Karoo, which are the most visible remnant of the dolerite's sill that protect or covers the underlying sandstone from physical processes like weathering and erosion. The dolerite sills and dykes created fractures or cracks in the Karoo that became water reservoir, thus dolerites are used as groundwater localiser in the Karoo (Chevallier *et al*., 2001).

Figure 4.35 Photograph showing a typical Karoo hill, topped with erosion-resistant dolerite.

4.5 Petrographic and mineralogical analyses

4.5.1 Laboratory preparation of thin sections

Thin sections were prepared in the Geology department's thin section laboratory, University of Fort Hare, South Africa. The rock samples were cut into small pieces (rectangular shape) using Struers cutting machine (secotom-10) and ground smooth (frosted) in order to obtain a flat smooth surface without the traces of cutting. This was achieved with the use of a progressive finer abrasive grit (Figure 4.36). The flat, smooth samples were mounted on a 26 mm by 46 mm glass microscope slide using Struers specifix resin mixed with Struers specifix-40 curing agent in the ratio 5:2 by weight (the mounted sample was left for 24 hours). After the sample had been stuck to the microscope slide, it was trimmed using Struers machine (Accutom-50) until its thickness was about 30 µm. The samples were carefully cleaned and vertically stored in thin section boxes.

Figure 4.36 Photograph showing thin sections preparation at the Geology department's thin section laboratory, University of Fort Hare, South Africa.

4.5.2 Petrography and mineralogy

Petrographic studies were conducted under plane and reflected light on the prepared thin sections of rock samples varying from diamictite, mudstones and sandstones. At least two representative thin sections of the Dwyka, Ecca and Beaufort Groups were studied.

4.5.2.1 Petrography of the Dwyka Group diamictites

The microscopic studies of the Dwyka diamictites conducted on thin sections under reflected light shows the presence of sub-rounded - angular granite and minor quartzite components in the breccias of a fine grained clastic matrix which are rich in clay minerals and exhibit stacking (4.37a and 4.37b). Microfractures were seen at some contact between the mineral grains and the matrix that are predominantly made up of coarse mineral fragments (lithic clasts) mainly of quartz and feldspar (albite) with other subordinate fine rocks such as clays and silt (Figure 4.37c and 4.37d).
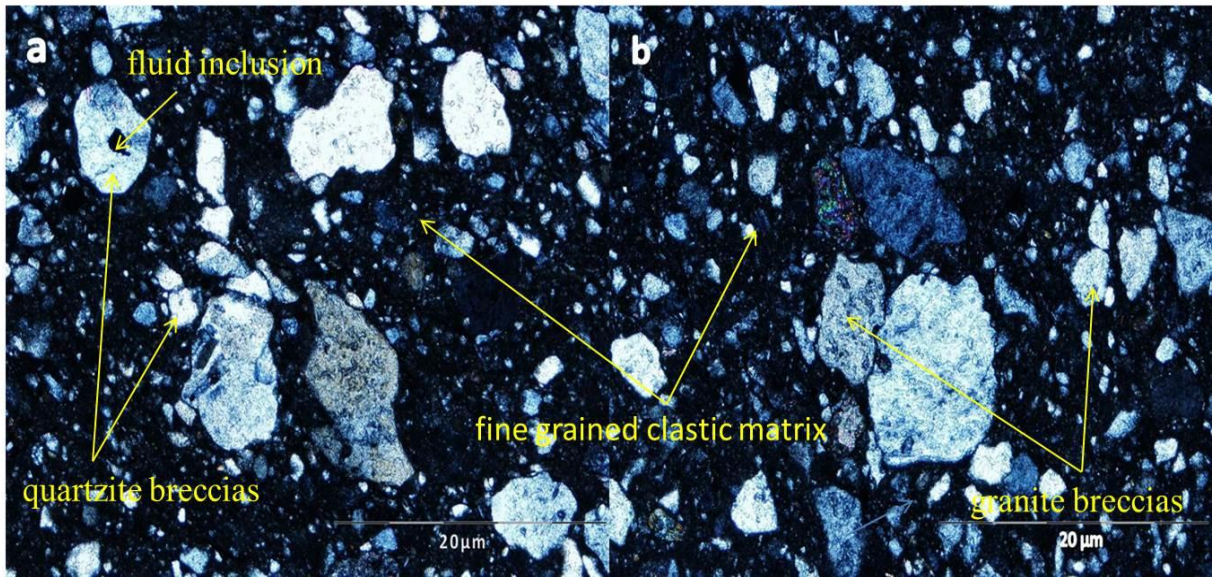
Figure 4.37 Photomicrographs of Dwyka diamictites along the Ecca Pass. (a) Irregular fluid inclusion around sub-angular quartz grains in quartzite clast. (b) Sub-round-angular granite and minor quartzite components in the breccias (fine grained clastic matrix which are rich in clay minerals).
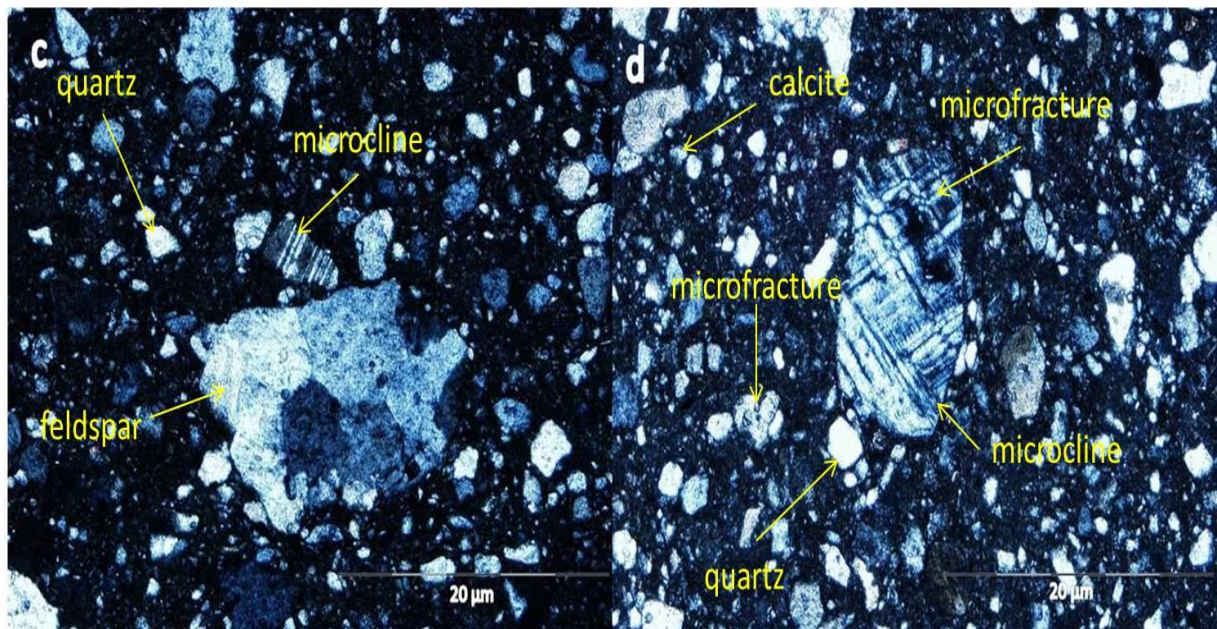
Figure 4.37 (c) Fine- to medium- grained clast population with angular - sub-rounded plagioclase, microcline and quartz. (d) Microfractures at some contact between the mineral grains.

The clast size varies from 20 µm to about 1 cm on the thin section scale. The fine- to medium- grained clast is predominantly of sub-round to sub-angular plagioclase, microcline and quartz. The fine grain matrix consists of mostly of micas (biotite and muscovite), quartz, calcite and opaque minerals although some of the quartz grains exhibit undulatory extinction while few of the feldspar grains show intragranular cataclasis. The composition of the lithic fragments indicates that the source is from granitoids.

4.5.2.2 Petrography of the mudstones of Prince Albert Formation

The mudstones of Prince Albert Formation are folded and consist predominantly of clay minerals with minor detrital grains of quartz, feldspar and muscovite (Figure 4.38). The detrital muscovite have been deformed, recrystallized and chloritised. The deformation of the muscovite is possibly due to compaction of the sediments by the overburden whilst recrystallization of the minerals is due to high temperature as burial depth increases. The relatively low content of hornblende could possibly aid or favours to the formation of hematite around the mineral grains. The observed detrital and authigenic minerals include calcite and sericite with intragranular micropores that are mostly filled with quartz cements. The presence of pyrite indicates reducing environment at the time of deposition. Some of the feldspars have been completely replaced to sericite and calcite with evidence/presence of mineral relicts. Some of the sericite were also recrystallized to muscovite as the diagenetic processes proceeds. The sub-angular to sub-round detrital quartz grains mostly exhibit undulatory extinction while the feldspar grains exhibit twinning although mostly altered to sericite.
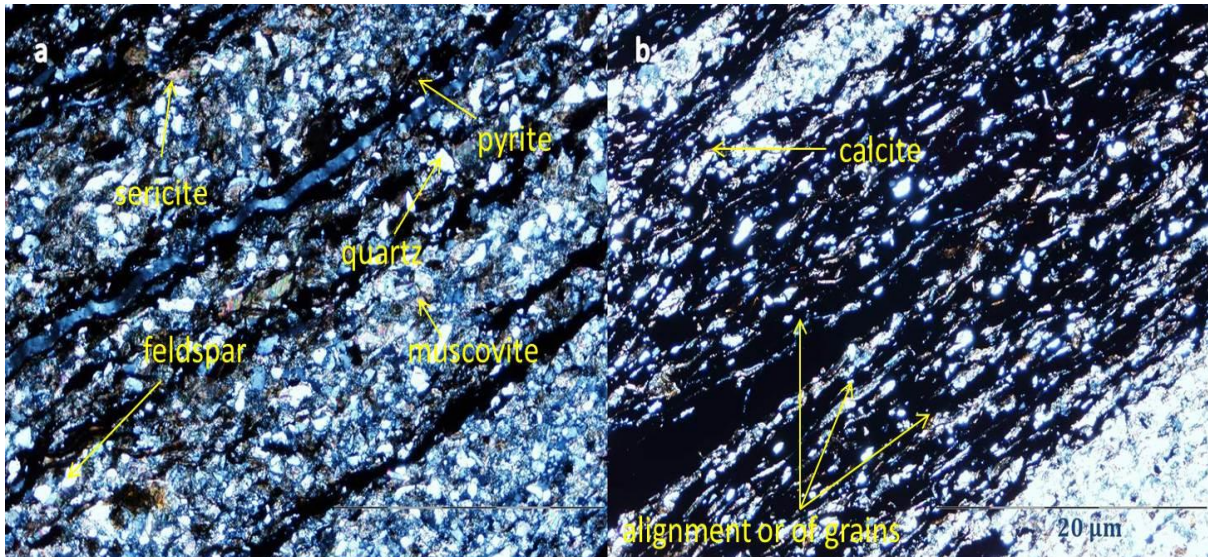
Figure 4.38 Photomicrographs of shales from Prince Albert Formation along the Ecca Pass. (a) Detrital grains of micas (occasionally deformed), quartz, feldspar, sericite (golden colour) and pyrite. (b) Alignment or orientation of grains, recrystallized euhedral calcite (yellowish colour).

4.5.2.3 Petrography of the carbonaceous shale of the Whitehill Formation

Petrographic study of the carbonaceous shale from the Whitehill Formation reveals that the matrix is made up of detrital clay minerals (kaolinite and illite), chlorite and authigenic minerals like pyrite, calcite and quartz (see Figure 4.39) with micropores that are filled with micro-quartz cement and a few quartz overgrowths. Kaolinite is the predominant clay mineral. The observed illite could be due to alteration of smectite to illite. The detrital grain types are mainly silt and sand which are predominantly of quartz and plagioclase feldspar. Carbonaceous fragments are seen as the accessory grains. The dissolution of the carbonate cements creates secondary pores, thereby increasing the overall porosity whilst occasional precipitation of the carbonate cements results in porosity reduction. Intragranular micropores are seen occasionally on the carbonaceous shale. The medium size detrital silt (about 0.04 mm) shows low sphericity and angular grains with sharp edges.
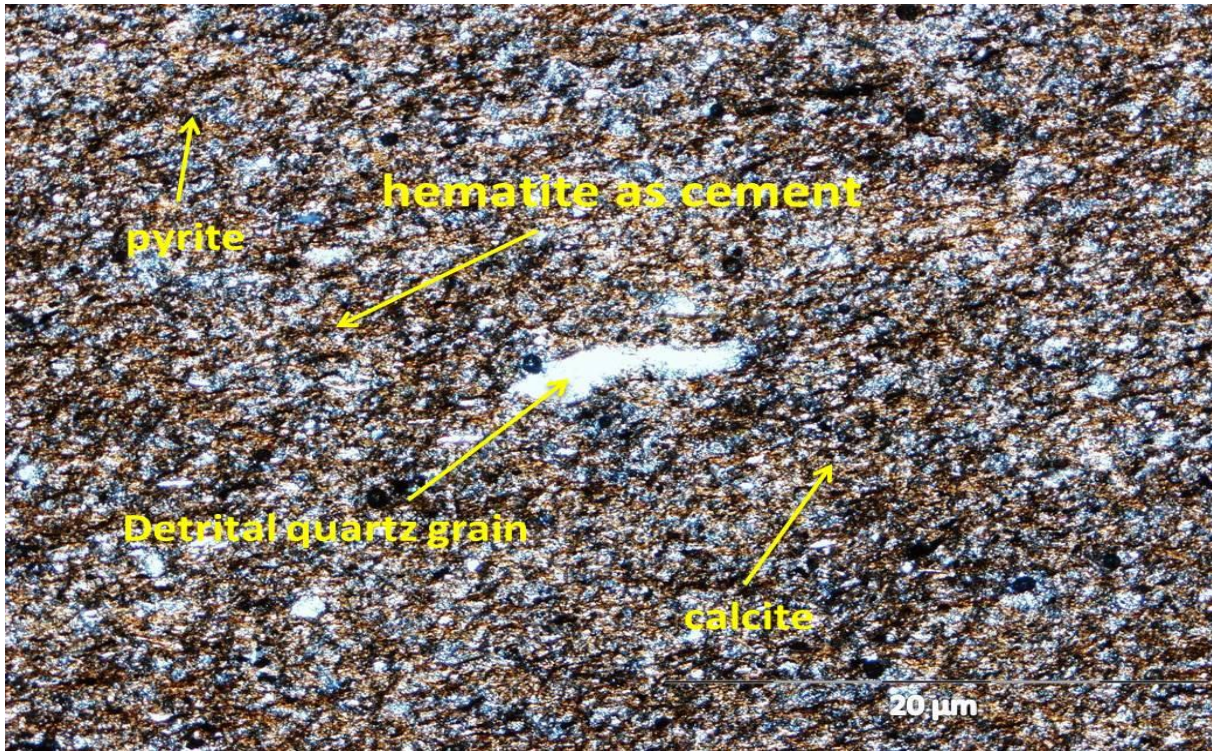
Figure 4.39 Photomicrographs of shales from Whitehill Formation along the Ecca Pass showing calcite (yellowish), pyrite (dark colours), hematite as cement and detrital quartz grain.

4.5.2.4 Petrography of the claystones of Collingham Formation

Microscopic study of the black shale of Collingham Formation also shows minerals quartz, feldspar, micas (biotite and muscovite) and clay minerals similar to those of the Prince Albert Formation. The authigenic minerals seen include quartz, calcite, chlorite, and sericite due to partial or complete recrystallization and alteration of feldspars to sericite or calcite (Figure 4.40a). Calcite and sericite are the most abundant although few of detrital grains of quartz, feldspar and muscovite are seen surrounded by the abundant clay minerals (chlorite). The detrital micas which are sub-angular and sub-round in shapes are also recrystallized and chloritised, some relicts feldspar from which the muscovite was formed was occasionally seen in association with calcite and sericite. Some of the sericite were altered to muscovite. Calcite is the main cement mineral that was identified in the rock and dark lines were also seen which could possibly represent laminations that were observed in the field (Figure 4.40b).
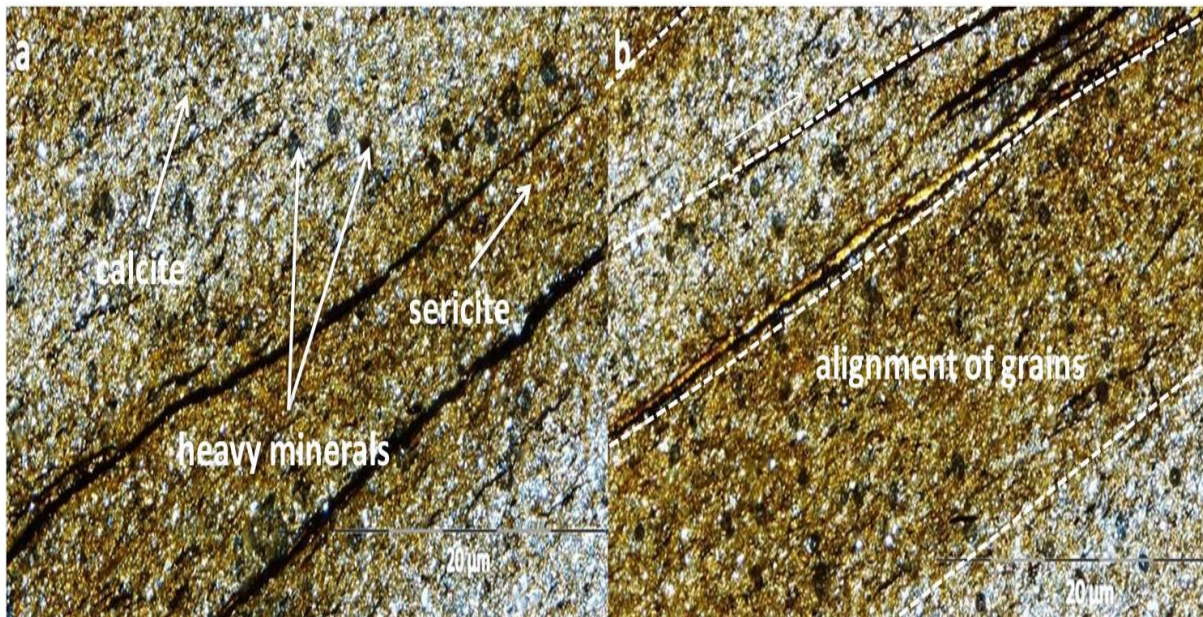
Figure 4.40 Photomicrographs of shales from Collingham Formation along Ecca Pass. (a) Sericite (golden or shiny yellowish colour), calcite (yellowish) and heavy minerals (black colour; parallel to cleavage). (b) Lamination / alignment of grains and presence of mica in the matrix.

4.5.2.5 Petrography of the sandstones of Ripon and Fort Brown Formations

The sandstones of the Ripon and Fort Brown Formations are poorly sorted (immature) and the grain shape is mostly sub-angular which possibly indicates that the sediments were transported over a relatively short distance from the source area (see Figure 4.41). The matrix is predominantly of mixtures of quartz, feldspar, calcite, chlorite, detrital micas and detrital zircon (included in the biotite). The quartz grains are sub-angular to sub-round and mostly exhibit undulatory extinction, while some show uniform extinction (Figure 4.42). Both monocrystalline and polycrystalline quartz were seen in the rock thin sections while few authigenic quartz were also seen with euhedral shape. The presence of polycrystalline quartz grains give clues that quartz rich rocks are present in the source area. The feldspar grains are angular, detrital feldspar (albite, microcline and orthoclase) are seen under the microscope showing low birefringent and interference colour.

83
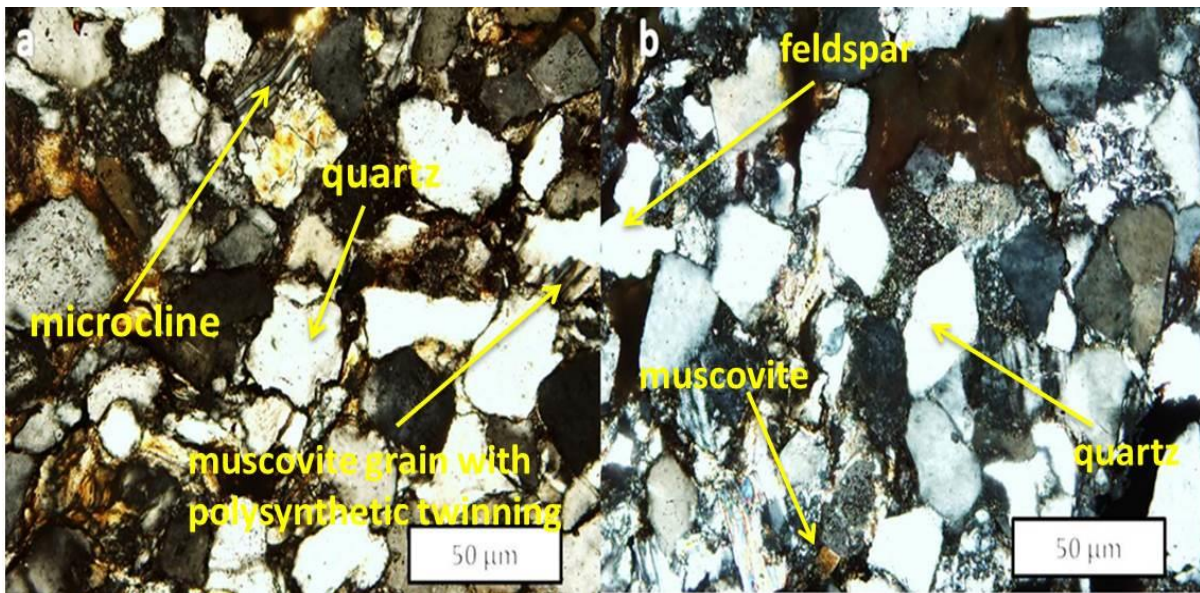
Figure 4.41 Photomicrographs of sandstones from Fort Brown Formation along Ecca Pass. (a) Sub-angular feldspar, microcline, quartz and elongated muscovite grain with polysynthetic twinning. (b) Sub-angular polycrystalline quartz grains and mostly exhibit undulatory extinction.
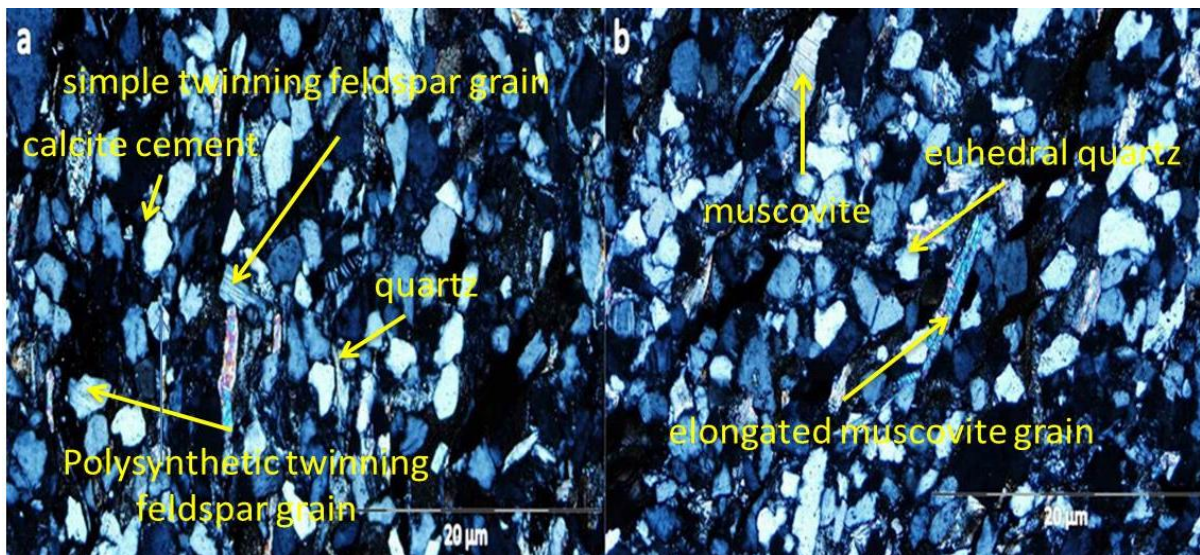
Figure 4.42 Photomicrographs of sandstones from Ripon Formation along Ecca Pass. (a) Calcite cement (dark colour), polysynthetic and simple twinning feldspar grains with zonation. (b) Concave and convex texture within the euhedral quartz grains and elongated muscovite grain with polysynthetic twinning.
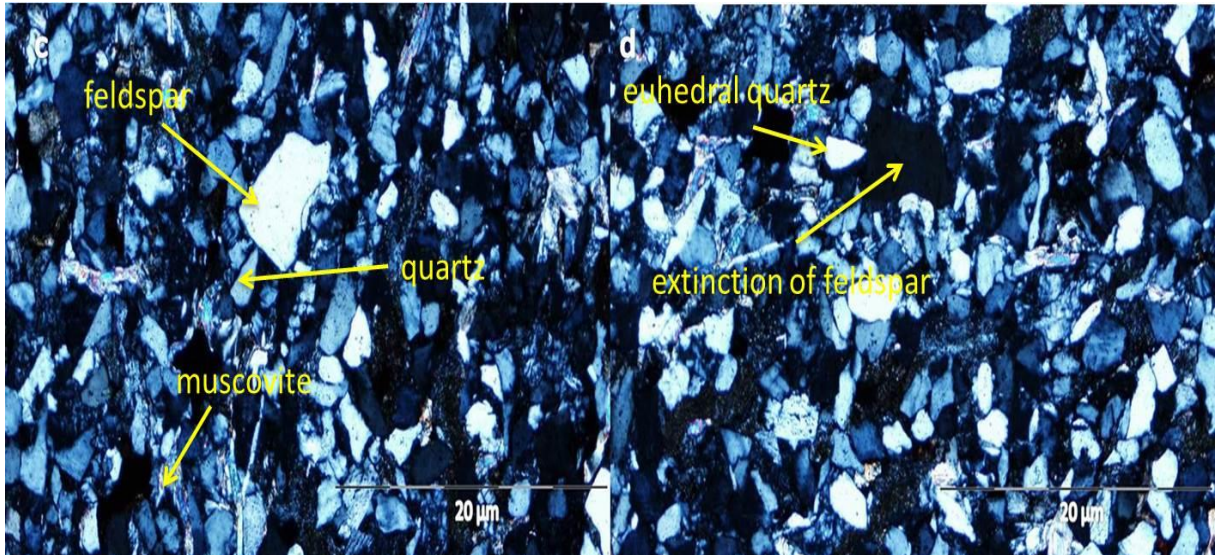
Figure 4.42 (c) Feldspar, quartz and mica as framework grains. (d) Extinction of feldspar (black) with euhedral quartz, poorly sorted with angular to sub-round grains.

4.5.2.6 Petrography of the grey sandstones of Koonap Formation

Petrographic study of sandstones from the Koonap Formation shows that the sandstones are fine - medium grained sandstones (ranging from 0.2 mm up to 1.76 mm in size) which are composed of framework grains of quartz, feldspars, micas, lithic grains and accessory minerals like zircon and garnet (see Figure 4.43). The sandstones are not well sorted and the grains shape varies from sub-angular to sub-round. The main pore filling minerals in the sandstones are calcite, chlorite and few quartz overgrowths. A trace of weathering/alteration was seen in the thin section (possibly the alteration of K-feldspar). The fracturing of the grain results in the formation of secondary porosity (effect of deformation). The quartz also exhibit syntaxial quartz overgrowths at the margin. The detrital are plagioclase and potassium feldspar (microcline) although increase in temperature would have resulted in the albitisation of the plagioclase whilst few occur as authigenic feldspars. It is noted that the sandstones of the Koonap Formation are very different from those of the Ripon (comparing Figure 4.42 and 4.43) possibly going from sandstones to mudstones.
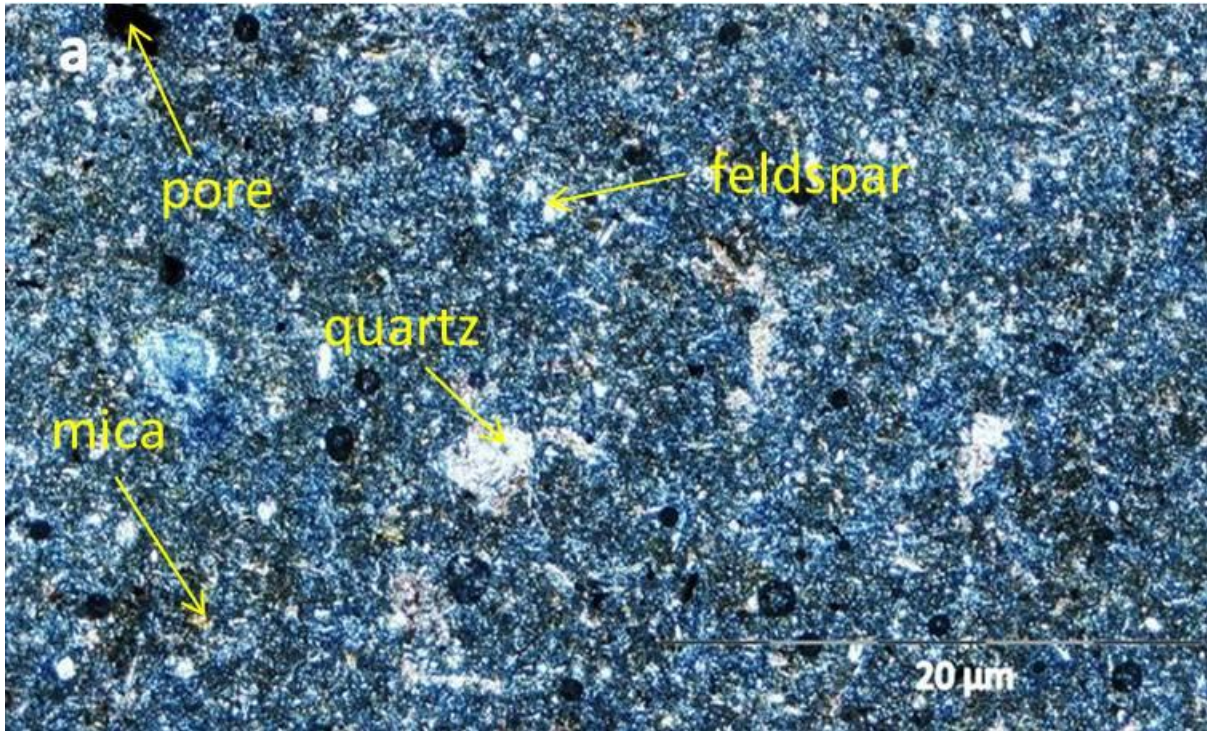
Figure 4.43 Photomicrographs of sandstones from Koonap Formation near Fort Beaufort showing feldspar, quartz, mica and pores.

4.5.2.7 Petrography of the red mudstones of Middleton Formation

The microscopic study of mudstones from the Middleton Formation shows that the clastic texture of the mudstone is dominated by microcrystalline quartz, interstitial clay and authigenic calcite with shape ranging from euhedral to subhedral. Quartz, feldspar and micromicas (with iron oxide) are the detrital grains that were observed (Figure 4.44). Although due to diagenetic recrystallization and replacement, some of the primary structures and grains have been destroyed. The fine mud recrystallized into coarse calcite and muscovite though calcite cement is the dominant secondary cement and the observed microfractures are associated with the recrystallized calcite in the matrix.
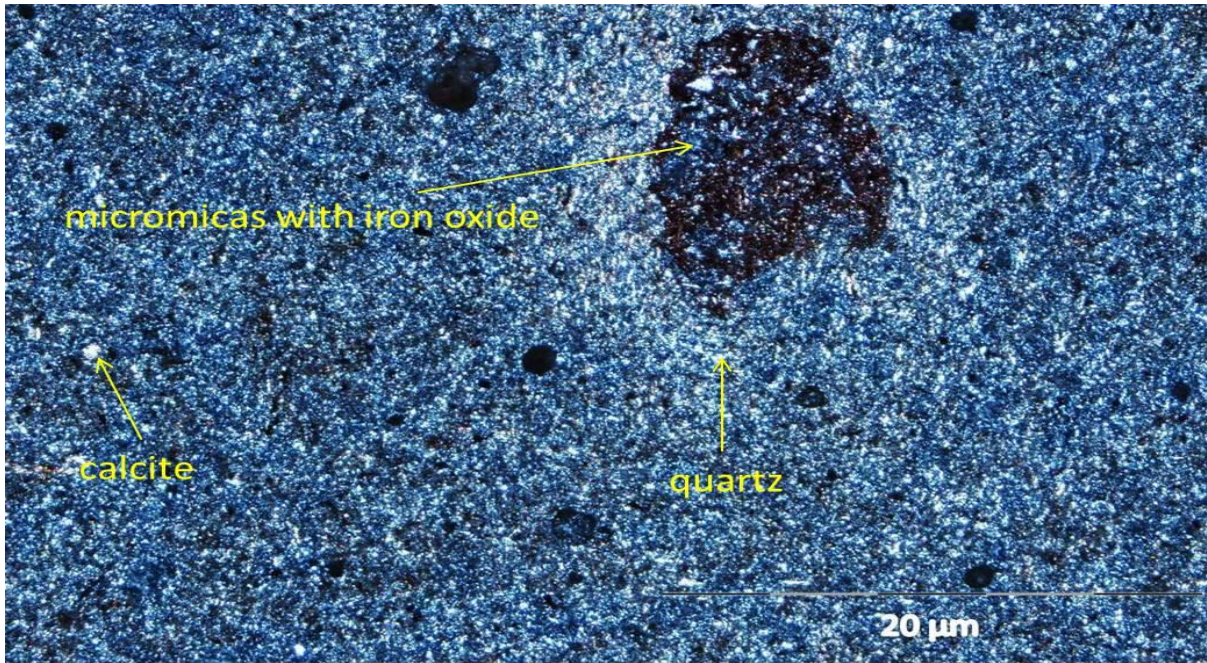
Figure 4.44 Photomicrographs of mudstones from Middleton Formation around Fort Beaufort showing quartz, calcite and micromicas with iron oxide.

4.5.2.8 Petrography of the sandstones of Balfour Formation

Petrographic study of sandstones from the Balfour Formation reveals the presence of detrital material with fine matrix, poorly sorted and sub-round grains with patchy carbonate cement occurring in the interstitial spaces which indicates that the sediments were transported over a relatively short distance from the source area (Figure 4.45a). The framework grains are predominantly of monocrystalline quartz which mostly exhibits uniform extinction, feldspars and other rock fragments (Figure 4.45b). Authigenic cements are mostly of quartz overgrowths with occasional secondary clays. Intergranular pores are the main pore types, although intercrystalline micropores were seen occasionally. Quartz (low quartz) is the most stable detrital mineral in the sandstone. Some of the feldspars show twinning (possibly albite and microcline) which is the basis used to classify the feldspars into twinned and untwined feldspars. The untwined feldspars were differentiated from the quartz in the fine grained samples using strain deformation (as reflected by undulose extinction on framework grains).
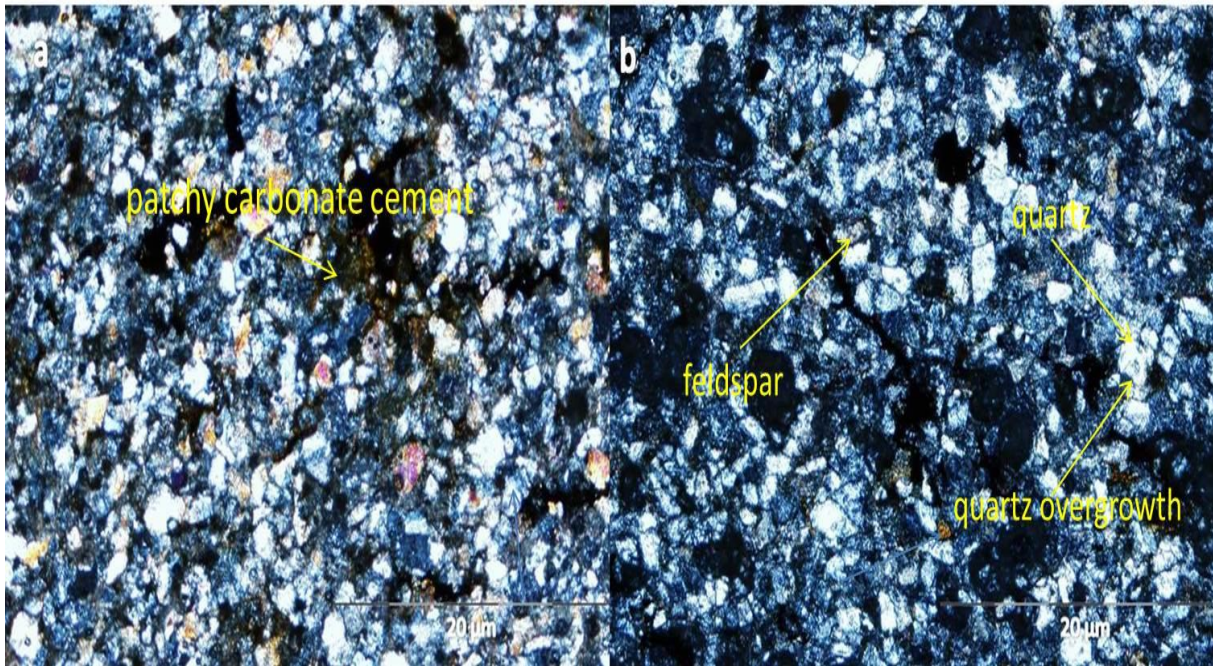
Figure 4.45 Photomicrographs of sandstones from Balfour Formation. (a) fine matrix, poorly sorted and sub-round grains with patchy carbonate cement occurring in the interstitial spaces. (b) Monocrystalline quartz, feldspars and other rock fragments with quartz overgrowths. Note: No significant difference is seen in the sandstones of all the members that make up the Balfour Formation, thus only one section is presented here.

4.5.2.9 Petrography of the sandstones of Katberg Formation

The sandstones are mostly framework supported (grains are in contact); rich in feldspar and lithic grains with minor detrital clay matrix support (Figure 4.46). The fine grained sand is mainly made up of sub-angular to sub-round quartz and plagioclase feldspar as detrital grain types with detrital clay minerals mostly illite. Some of the feldspar grains were altered to sericite and eventually muscovite whilst the others changed to calcite. Accessory grains include carbonaceous fragments and micromicas with authigenic minerals such as pyrite, calcite, and quartz. Microfractures, intragranular and matrix micropores were the major pore types in the sandstone. Secondary quartz cement is the dominant cement with occasional calcite cement.
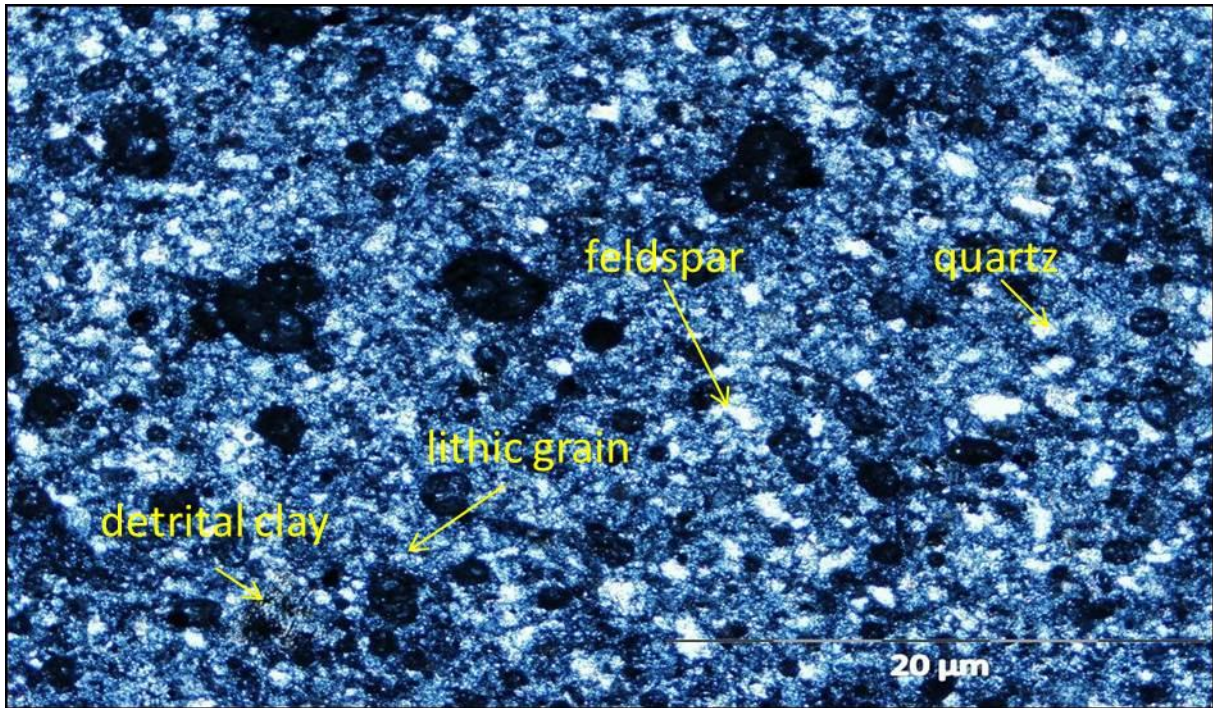
Figure 4.46 Photomicrographs of sandstones from Katberg Formation showing feldspar, quartz, detrital clay and lithic grains.

4.5.2.10 Petrography of the sandstones of Burgersdorp Formation

The sandstones of the Burgersdorp Formation (Figure 4.47) are matrix supported, predominantly of mixtures of clay size quartz, feldspar, chlorite and clay minerals although occasionally mixed with pyrite and carbonates. The sandstone is dominated by detrital microcrystalline quartz and feldspar (mostly alkali feldspar) with particles shape, ranging from sub-angular to sub-round. Some of the feldspar grains are kaolinized with very few grains of microcline and plagioclase whilst some of the quartz grains were fractured and filled with calcite (occasionally muscovite and zircon). Marginal intergrowth between larger grains of quartz and chlorite with the clastic matrix was seen under the cross polarised light. Some of the primary structures and grains of the detrital quartz, feldspar and micas have been recrystallized and replaced due to diagenesis while others were partially destroyed (detrital quartz).
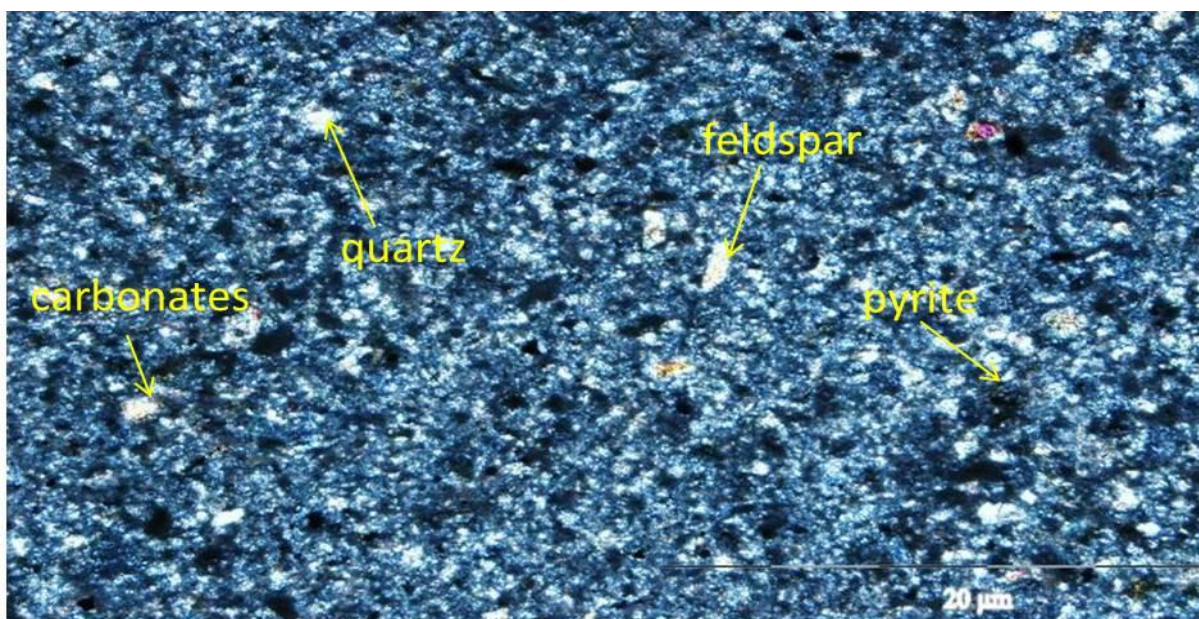
Figure 4.47 Photomicrographs of sandstones from Burgersdorp Formation showing quartz, feldspar, pyrite and carbonates.

4.6 X-ray powder diffraction (XRD)

In order to ascertain the results of the mineralogical investigation, X-ray diffraction analysis was carried out on 11 rock samples that cover the geologic formations in the study area at the Department of Chemistry, University of Fort Hare, South Africa. A representative fraction of the crushed rock samples were ground in an agate mortar that was cleaned with ethanol to less than 45 microns. The ground rock samples were spread on a glass slide and scanned at 2 $^{\circ}$ 2θ per minute from 2 $^{\circ}$ to 70 $^{\circ}$ (wavelength of 1.5406) using Bruker XRD D8 Advance (Model: V22.0.28) at a room temperature of 25°C. The data were measured in reflection mode.

The principles of X-ray powder diffraction, laboratory analysis (e.g. procedure on how the minerals and peaks were searched, displayed as well as the constraints that were used in the analysis) and diffraction patterns are presented in Appendix A. The summary of the minerals identified are tabulated in Tables 4.1 and 4.2.

Table 4.1 Summary of the minerals identified in the rocks of the Dwyka and Ecca Groups.

Minerals	Dwyka (%)	Prince Albert (%)	Whitehill (%)	Collingham (%)	Ripon (%)	Fort Brown (%)
Biotite	18.65	23.86	18.19	25.90	21.38	29.17
Calcite	0.33	0.04	0.25	0.65	2.59	1.91
Chlorite	3.58	2.38	7.65	3.80	2.53	3.84
Feldspar	2.65	0.15	0.34	1.33	0.65	1.30
Garnet	1.17	0.11	1.67	1.11	0.46	0.89
Hematite	0.13	0.02	0.03	0.02	0.12	0.24
Illite	6.03	9.05	12.58	8.42	7.33	4.88
Kaolinite	0.71	0.37	0.77	0.54	0.79	0.85
Muscovite	56.48	47.84	46.48	43.75	50.07	47.00
Quartz	10.01	15.87	11.3	14.03	11.98	5.70
Zeolite	-	-	-	-	1.83	3.98
Zircon	0.26	0.30	0.75	0.45	0.26	0.23
Total	100.00	99.99	100.01	100.00	99.99	99.99

Table 4.2 Summary of the minerals identified in the rocks of the Beaufort Group.

Minerals	Koonap Fm (%)	Middleton Fm (%)	Balfour Fm (%)	Katberg Fm (%)	Burgersdorp Fm (%)
Biotite	21.71	20.70	30.04	12.63	24.90
Calcite	0.11	0.06	0.15	0.24	0.15
Chlorite	3.45	2.68	2.53	3.58	2.35
Feldspar	2.02	1.30	1.58	3.62	1.05
Garnet	0.78	0.37	0.40	0.61	0.27
Hematite	0.14	0.08	0.09	0.09	0.14
Illite	7.29	7.46	5.77	10.58	6.47
Kaolinite	0.92	0.76	0.57	0.73	0.76
Muscovite	53.54	56.82	48.84	46.90	47.75
Quartz	9.62	9.72	8.22	18.48	11.93
Zeolite	-	-	1.53	1.64	3.37
Zircon	0.42	0.06	0.28	0.88	0.85
Total	100.00	100.01	100	99.98	99.99

The XRD result for rocks of the Karoo Supergroup (Table 4.1 and 4.2) shows high percentage of biotite, muscovite, quartz, and relatively low content of feldspar. The heavy mineral assemblages in the rock samples consist predominantly of zircon (0.06 − 0.88 %), garnet (0.11 - 1.67 %) and chlorite (2.38 − 7.65 %). Liu (1999) emphasized that the abundance or concentration of heavy mineral is controlled by complex interactions between different factors such as provenance, depositional environment and the prevailing hydrodynamic condition.

4.7 Discussion

The Dwyka diamictite samples comprise of sub-rounded- angular breccias in fine-grained clastic matrix that are rich in clay minerals. The lateral continuity of the glacial diamictites of the Dwyka Group suggests that deposition by dry based ice sheets, possibly in deeper basement valleys. Almond (2010) alludes that most of the Dwyka sediments were deposited during periods of glacial retreat that are associated with climatic amelioration. Petrographic study of all the thin sections of rocks from the Dwyka Group shows the presence of monocrystalline quartz and granite components in the breccias which possibly signify the existence of granitic and volcanic rocks in the source areas whilst the quartzite components in the breccias suggest metamorphic and tectonically deformed source area.

The lithology of the Ecca Group is dominated by shales, sandstones and siltstones and has a lack of conglomerates in all the formations and this is probably closely linked to the deep water of reducing (anoxic) environment. The sandstones are mostly greywackes, and no arenites are present, which probably indicates that the rocks are textural and mineral immature in nature. The lower part of the Ecca Group (e.g. Prince Albert, Whitehill and Collingham Formations) are dominated by shales and mudstones, whilst the upper part of the group (e.g. Ripon and Fort Brown Formations), sandstones content gradually increases, indicating the water depth of the depositional environment gradually become shallow and changed from deep reducing (anoxic) to deltaic environment, and finally the shallow lacustrine environment.

Feldspar, quartz and micas occur as the major minerals in the rocks with lithics also forming part of the framework grains in the sandstones. Quartz and feldspar grains are both polycrystalline and monocrystalline, indicating that they were not fully separated by long transportation, which is consistent with the immature nature of the rocks. Hematite, garnet, rutile and zircon are the accessory minerals, whilst the clay minerals include; kaolinite, smectite, illite, sericite and chlorite. These minerals possibly exist in the rock either as detrital grains or diagenetic minerals. The detrital nature of the framework grains and the presence of lithic fragments, thus, render the rocks to be terrigenous in origin. From the observed lithics and heavy minerals and the nature of quartz and feldspar minerals, it can be deduced that, the provenances of the sediments were derived mostly from igneous and metamorphic rock sources, rarely from sedimentary rock source.

The presence of mudrock with pyrite in the Prince Albert Formation possibly indicates suspension settling of mud in an anoxic environment since sedimentation of the mudrock took place by suspension settling of mud (e.g. well-laminated shales; Haughton *et al.*, 2009). The organic-rich muds accumulated under anoxic, reducing environment which also agrees with the findings of Catuneanu *et al.* (2005) since a reducing environment is required for the pyrite to be formed. The coarser-grained sand and silt were deposited as a result of tractional fall-out from the turbidity currents in an anoxic environment as depicted by the cross-bedding and ripple lamination. The matrix is mostly composed of iron-rich minerals with red stains that possibly indicate weathering/oxidation of clay minerals. The co-existence of shales and mudstones in the Whitehill Formation indicates that the environment changed from low energy to high energy and vice versa. The turbidity current may also aid the formation of mudstones from the laminated shales.

The brownish sandstone and mudstone of the Ripon and Fort Brown Formations signifies the presence of oxidizing conditions during the time of burial of the sediment whilst the tabular lamination of the shale layers indicates deposition at low rate which is typical of marine environment. The increase in the black shale towards the upper part of the formation indicates that marine conditions and anoxic water were persistent at the deposition time of the formation until brackish conditions returned at the upper part. It is believed that the persistent nature of the anoxic and marine conditions resulted in the increase of the organic content in the upper black shale layer of the Ripon Formation. From bottom to the upper succession (formation) of the Ecca Group, it is noted that the depositional environments gradually changed from deep water environment (Prince Albert, Whitehill and Collingham Formations) to deltaic environment (Ripon Formation) and then to lacustrine environment (Fort Brown Formation), which implies that the sedimentary basin was gradually filling up with sediments and the water depth of the basin was gradually shallowing up. This is also consistent with the evidence that the overlying strata of the Ecca Group, i.e. the Beaufort Group was deposited in a fluvial environment, which was the result of basin water and sea-level continuously retreating or dropping; a reducing environment then shifted to a continental inland environment at last.

The sandstones that were seen in the study area (Ecca and Beaufort) along the Ecca Pass and around Fort Beaufort are greywacke and consist mostly of micas, feldspar, quartz, and rock lithics with heavy minerals. The grain size and shape of the rocks of the Ecca and Beaufort Group are not uniform therefore no concrete evidence can be used to proffer a generalized source area for the rocks (the variation in the grain size and shape depends on the dynamic condition under which the sediments were formed/deposited). Tordiffe (1978) emphasized that the Elandsberg Member which is about 700 m thick and the Palingkloof Member should be lithostratigraphically combined as one Member because the only difference between the Members is the colour difference which is not a criteria for lithostratigraphic subdivision. The slight changes in the paleocurrent and paleoflow direction in the Elandsberg and Pakingkloof Members from SSE and NNW respectively could be due to a change in the paleoslope.

Petrographic studies carried out on the prepared thin sections (Ecca and Beaufort Groups) also support the field observation that the rocks are poorly sorted based on the amount of matrix that was seen both with the naked eye and under the microscope. Maturity in the rocks was based on the degree of sorting of the sediments and the kind of minerals that make up the rock since maturity generally depends on the stability of the minerals in the rock (the more stable the minerals are, the more mature the rock becomes and vice versa). Thus the rocks are immature based on the earlier explanations. The sub-angular and sub-rounded grains with poor sorting (immature) also signify that the sediments might have travelled over a relatively short distance from the source area.

The assemblage of heavy minerals in the rocks of the Karoo Supergroup signifies that the minerals are of granitic or mafic igneous and metamorphic origin as partially seen by the presence of garnet (0.11 - 1.67 %). However, it is possible that sedimentary rock may also contribute to the heavy minerals since heavy mineral like rutile can be formed from pore-solutions and may be derived from the alteration of biotite. The observed cements are primarily quartz and calcite cement whilst the matrix is mostly of muscovite (43.75 − 56.82 %), biotite (12.63 − 29.17 %), calcite (0.04 - 2.59 %), chlorite (2.35 − 7.65 %) and other clay minerals (mostly illite (4.88 − 12.58 %) with uniform patches which indicate that most minerals are of authigenic origin and possibly subjected to very low grade metamorphic conditions. Most of the mica seems to be of authigenic origin with clues indicating that the rock may have been subjected to early metamorphism.

The high percentage of muscovite and biotite in the rock possibly indicate that the sediment source area is near, possibly of igneous and volcanic origin with low weathering/active volcanoes in the source area due to instability of biotite to physical processes like weathering and erosion. The occurrence of quartz cement in the Ecca sandstones under reduce (anoxic) condition possibly signifies the decomposition of biogenic siliceous organisms just after the deposition of the sediments whilst the existence of mica and other heavy minerals indicate that the source area was composed of metamorphic rocks.

The presence of undulatory and non-undulatory quartz have been used to interpret whether the quartz is of igneous or metamorphic origin since non-undulatory quartz are associated or characteristic of volcanic origin whilst the undulatory quartz are of metamorphic origin. Although Pettijohn *et al.* (1987) allude that there are also high percentage of undulatory quartz in volcanic rocks, thus metamorphic origin cannot be ascertained for the rocks based on the proportion of undulatory to non-undulatory quartz.

The presence of monocrystalline quartz, zoned albite and tuffaceous material possibly indicates that granitic and volcanic rocks were also present in the sediment source whilst the high percentage of alkali feldspars which are chemically more stable than the plagioclase signifies that granitic rocks are possibly dominant in the source area. The presence of orthoclase, microcline and polycrystalline quartz with more than five grains possibly indicates metamorphic and igneous origin.

4.8 Conclusions

The relative abundance of monocrystalline quartz and granite breccias in the Dwyka diamictite signify the existence of granitic and volcanic rocks in the source areas whilst the presence of quartzite breccia suggest the presence of metamorphic and tectonically deformed source area.

The presence of mudrock with pyrite in the Prince Albert and Whitehill Formations signify suspension settling of mud in an anoxic environment whilst the brownish sandstone and mudstone of the Ripon and Fort Brown Formations indicate the presence of oxidizing condition during the time of burial of the sediment.

The sandstones that were seen in the study area (Ecca and Beaufort) along the Ecca Pass and around Fort Beaufort are greywacke and consist mostly of micas, feldspar, and quartz. Rock lithics with heavy minerals are also present.

Petrographic studies carried out on the prepared thin section show that the rocks of the Ecca Group (Ripon and Fort Brown Formations) poorly sorted and immature with irregular grain sizes and shapes. The rock lithics gives clues of igneous, metamorphic and volcanic origin, distance from the source area and materials that are present in the source area.

CHAPTER FIVE

MAGNETIC METHOD

5.1 An introduction of the magnetic method

The Earth's outer core is molten, acts like a geodynamo and separates the solid, electrically conducting inner core from the mantle. It is mostly composed of iron. As the Earth slowly cools and iron in the iron-rich fluid alloy solidifies onto the inner core, convection processes in the liquid part of the iron core in the fluid outer core gives rise to the Earth's main field. There is also an external magnetic field arising from charged particles emanating from the sun. Thus the measured magnetic field consists of three parts, i.e. the main field, the magnetic field due to crustal rocks and the external magnetic field (Telford *et al*., 1976; 1990).

The magnetic method in geophysics therefore involves measuring the magnetic field on or above the Earth's surface, and then removing the effects of the main field and external field so that only the effect which is due to crustal rocks remains. This effect generally makes up approximately 1% of the measured field (Reynold, 1997).

The units of measurement for magnetic field are derived in terms of a flow of electric current that is needed in a coil to generate that field (Reynold, 1997). This has units of volt-second per square metre or Weber per square metre (Wb/m^2) or Tesla (T). The magnitude of the Earth's field is of the order of 10^{-5} T. Thus a more convenient SI unit in geophysics is nanotesla ($nT = 10^{-9}$ T), where 1 nT is equal to 1 gamma in c.g.s units (1 nT = 10^{-5} gauss). More information on the magnetic method can be found in Telford *et al*. (1976; 1982; 1990), Blakely (1995), Clark (1997), Reynold (1997), Gunn *et al*. (1997), Mussett *et al*. (2000), Manhanyele *et al*. (2008), and Mahanyele (2010).

5.2 The Earth's geomagnetic field

The geometry and some behaviour of the magnetic field to a first approximation look like that which would be produced if a large bar magnet with two poles (north and south seeking poles) were located in the centre of the Earth inclined at about 11.5^{o} to the geographic axis (see Figure 5.1a). Hence the field is dipolar in nature. It points vertically downward at the

north magnetic pole and vertically upward at the south magnetic pole whilst it is horizontal and pointing north at the equator (Figure 5.1b).
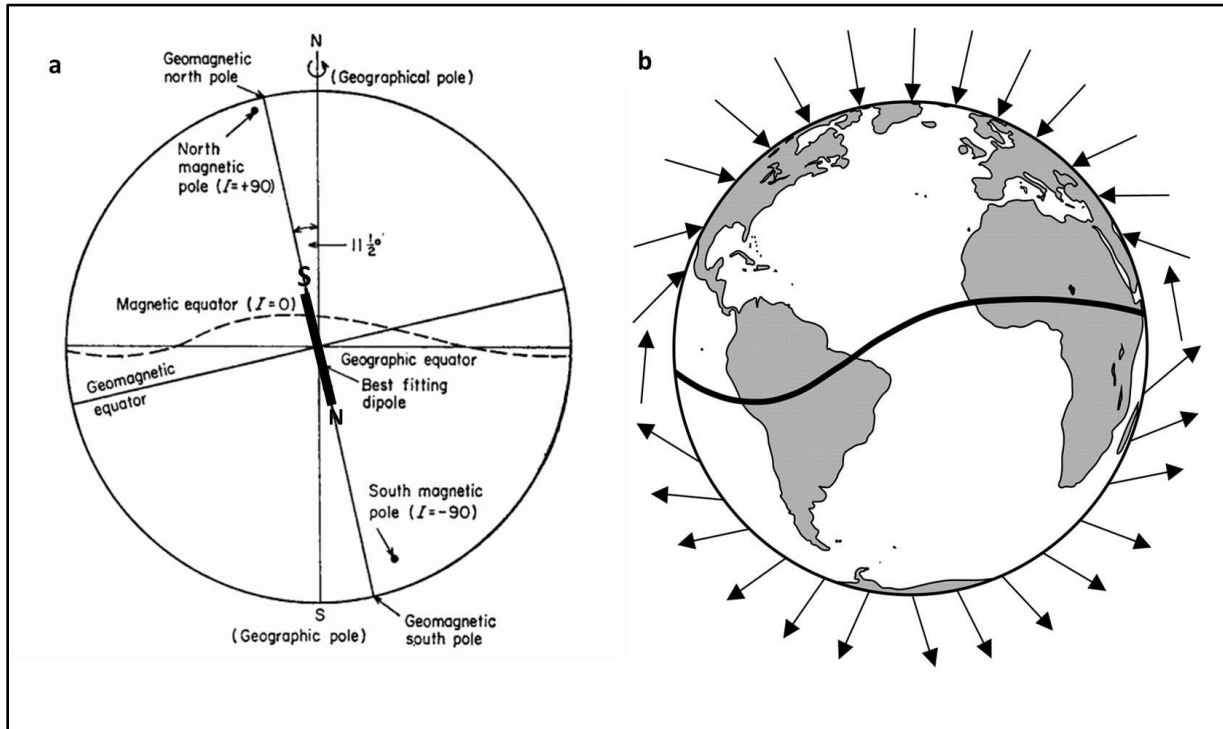
Figure 5.1 The field due to an inclined geocentric dipole and the field lines (Reeves, 2005). Note that the geomagnetic South pole is a magnetic North pole and the geomagnetic North pole is a magnetic south pole.

At random intervals (over hundreds or thousands of years, pole reversal occurs about every 200,000 to 300,000 years, although it has been more than twice that long since the last reversal occurred (Reynolds, 1997)), the Earth's field usually reverses thus leaving a record in rocks which is used for calculating the past motions of continents and ocean floors due to plate tectonics (Reynolds, 1997). According to Telford *et al.* (1990), in sedimentary regions, particularly where the basement depth is greater than 1.5 km, the magnetic contours are normally smooth and variations are small, reflecting the basement features rather than those of the near-surface. Dobrin and Savit (1988) stated that the magnetic relief observed over sedimentary basin areas mostly reflects more the lithology of the basement rather than its topography. However, the areas where igneous and metamorphic rocks are dominant usually

show complex magnetic variations. Deep features are frequently hidden by higher frequency magnetic effects of those of the near surface (Telford *et al*., 1990). The study of how the Earth's magnetic field has changed through geological time is known as paleomagnetism. The use of magnetic reversals to provide global chronometric of geological events is known as magnetostratigraphy (Sharma *et al*., 2005). The elements of the Earth's magnetic field, the main field, crustal field, external field, temporal external variations of the Earth's magnetic field, and magnetic properties of rocks, International Geomagnetic Reference Field (IGRF), magnetic anomalies and instrumentation are presented in Appendix B.

5.3 Data reduction

The total magnetic field ($F_{Observed}$) which is observed in the field is given as:

$$F_{Observed} = F_{Main} + F_{Temporal} + \Delta F_{Crust} \qquad 5.1$$

The field which is due to crustal rocks (magnetic anomaly) is of interest in magnetic surveys, thus:

$$\Delta F_{Crust} = F_{Observed} - F_{Main} - F_{Temporal} \qquad 5.2$$

The F_{Main} is accurately estimated by F_{IGRF} (see Section 7 in Appendix B), $F_{Temporal}$ is monitored during the survey and thus accounted for and removed.

The data from Fugro Airborne Surveys is the $F_{Observed} - F_{Temporal}$. The crustal magnetic field (discussed in Section 3 of Appendix B) was obtained by removing 1975 IGRF from the acquired data (This was done by Fugro Airborne Surveys).

5.4 Data enhancement

The magnetic data enhancements that were used this study include; the downward continuation, vertical derivative, total horizontal derivative, analytical signal, reduction to the pole (RTP) and radially averaged power spectrum (see Section 9 in Appendix B for details).

5.5 Magnetic anomalies and lithologies

Magnetic anomalies are local variations in the Earth's magnetic field due to variation in magnetization of crustal rocks. This is calculated by subtracting the measured values from the model of the Earth's field (IGRF) from the observed magnetic values. A positive or negative magnetic anomaly could be the effect of a single buried magnetic body or sometime may result in both anomalies due to the dipolar nature of magnetism. For example, the induced magnetisation gives rise to dipolar shape (positive and negative lobes) which depend on location, e.g. at the equator, poles or at the same latitude. The remanent magnetisation usually gives rise to negative anomalies. The reduction to the pole (presented in Section 9.4 of Appendix B) can shed light on whether we have induced magnetisation or remanent magnetisation or both.

5.6 Data acquisition, processing and results

Airborne magnetic data were acquired from Fugro Airborne Surveys and Council of Geoscience, South Africa. Fugro Airborne Surveys carried out airborne geophysical surveys over the Eastern Cape Province, South Africa in 1982. A proton precession magnetometer with 0.01 nT resolution was used to acquire the aeromagnetic data. The flight height and line spacing was 60 m and 750 m respectively, whilst sampling along lines was 250 m. The flight line direction was North-South with respect to UTM Zone 35S and tie line direction of East-West. The supplied data in the format of a Geosoft grid was enhanced by both linear and non-linear filtering algorithms in the Montaj MAGMAP filtering system. It processes and enhances gridded datasets by applying two dimensional Fast Fourier Domain filters (FFT filters) in both wavenumber and Fourier domains. The system provides three filtering methods (MAGMAP1-step, step by step and interactive filtering). The interactive filtering method was used to apply the spectral filters such as low-pass, high-pass filters, upward continuation and downward continuation (discussed in Section 9 of Appendix B).

The original space domain grid was prepared for filtering and the Fast Fourier Transform (FFT) was applied to transform the square and periodic space domain to the wavenumber domain, then filters were applied in order to enhance the effects of shallow magnetic sources (such as removal of first-order trend) or enhance deeper magnetic sources. The inverse FFT was applied and enhancements (e.g. vertical derivative, horizontal derivative, analytical

signal and radially averaged spectrum) discussed in Appendix B (Section 9) were calculated and the results are shown in Figure 5.3 – 5.9. The generated maps were superimposed on the simplified geological map of the study area (Figure 5.2) to correlate structures giving rise to the magnetic anomaly.
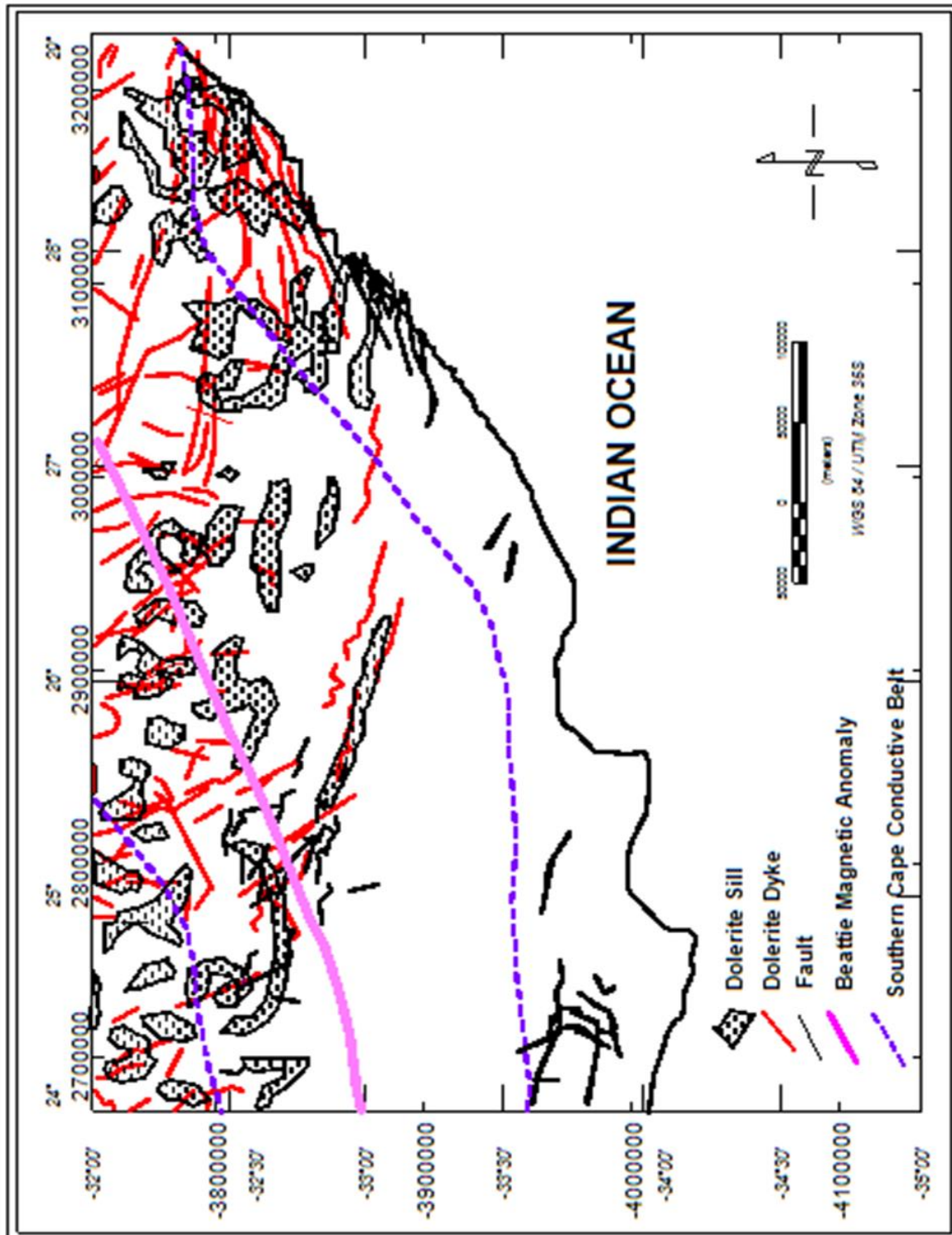
Figure 5.2 Simplified geological map of the study area showing the Southern Cape Conductive Belt (SSCB), part of the Beattie magnetic anomaly (BMA), faults and dolerite intrusions (sills and dykes).
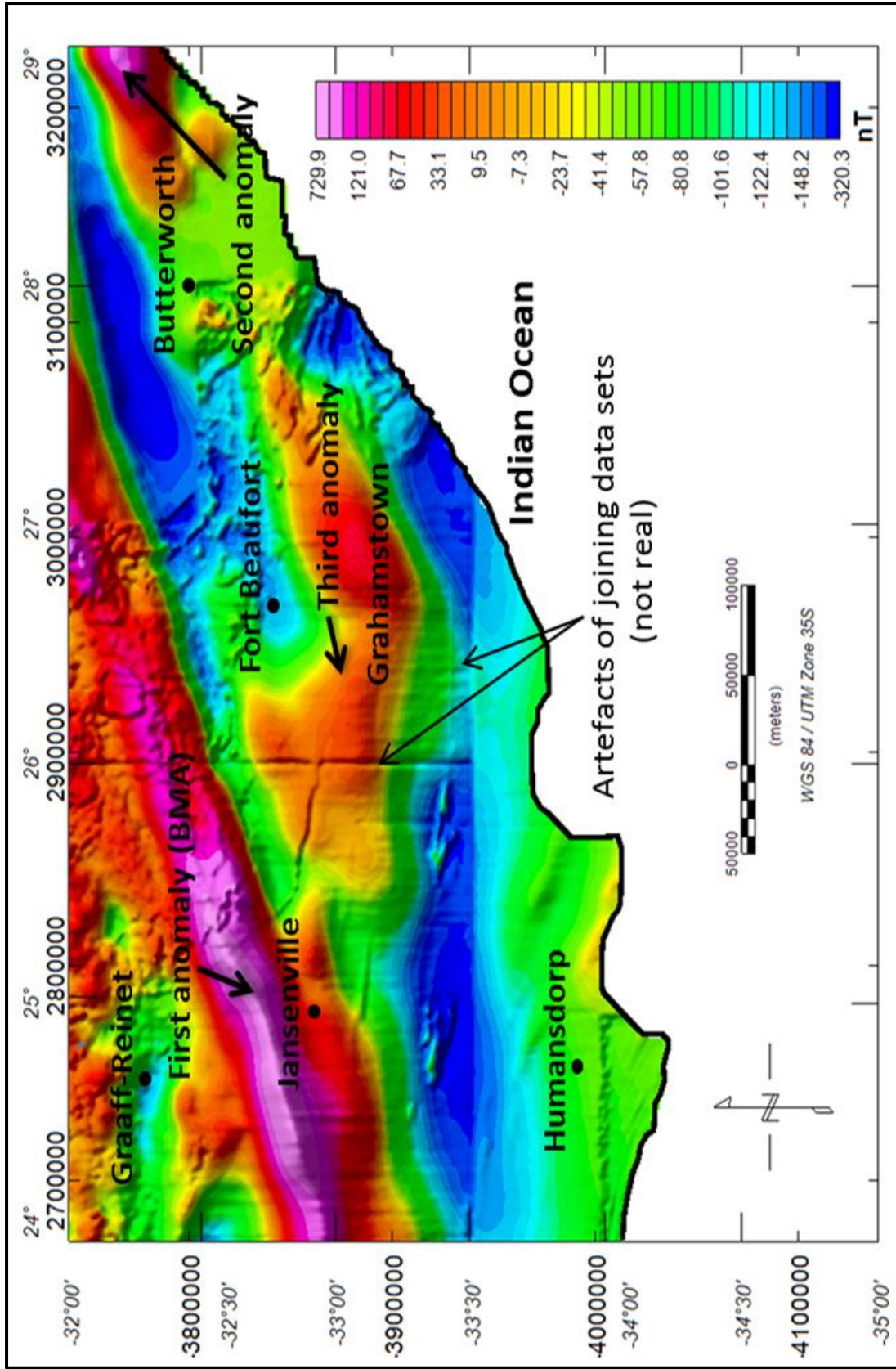
Figure 5.3 Magnetic residual anomaly map (Data courtesy of Fugro Airborne Surveys). The area has three high magnetic zones. The first one which is the main anomaly is part of the Beattie magnetic anomaly and trends in an NE-SW direction. The second anomaly is seen on the northeastern part of the map, while the third anomaly which coincides with a continuous, regional band of high magnetic susceptibility "bean shape" seen in the centre – eastern part of the map.
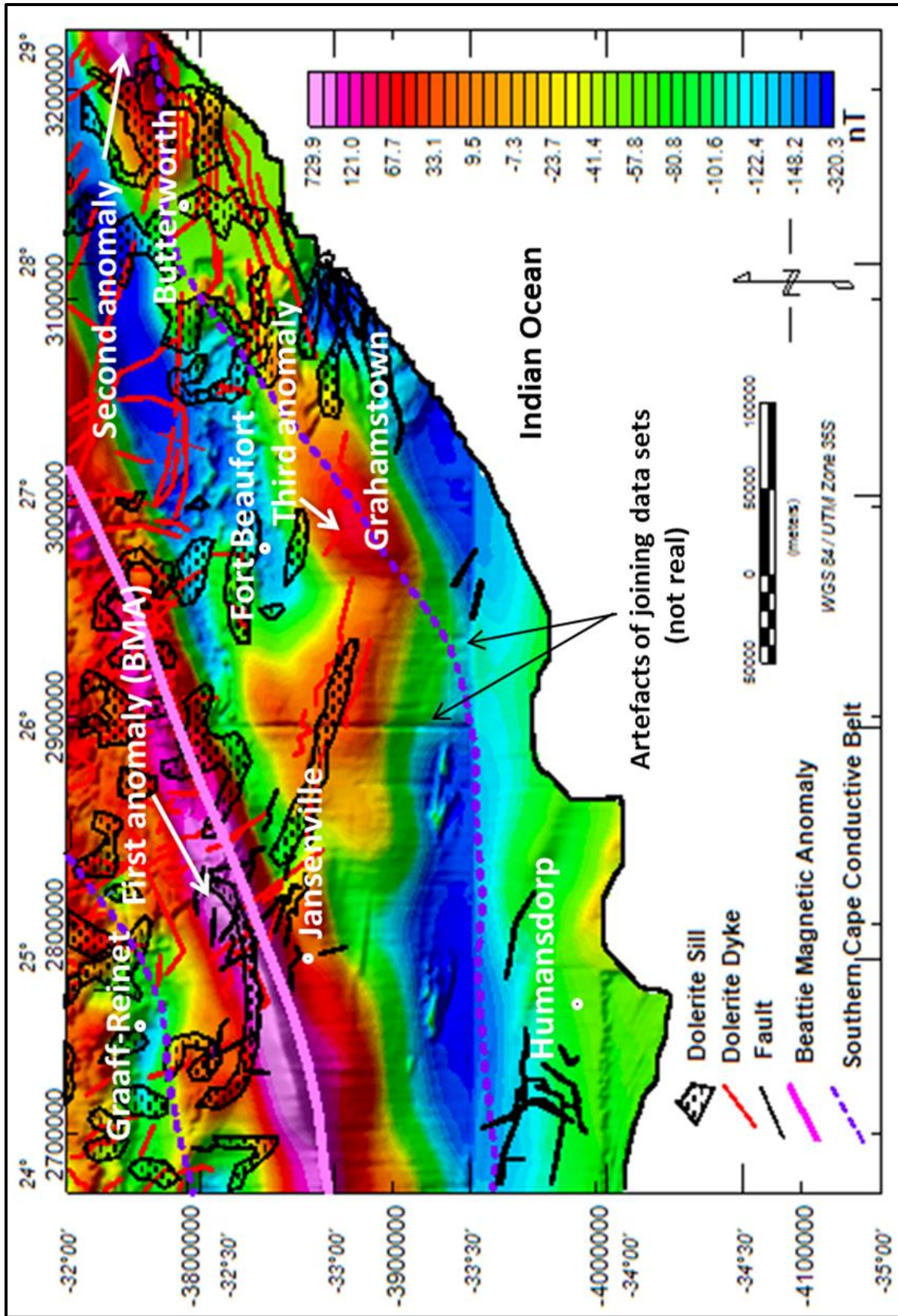
Figure 5.4 Magnetic residual anomaly (reduced to the pole) map overlain on the geology. The map also shows dolerite intrusions (sills and dykes), faults, part of the Beattie magnetic anomaly and the Southern Cape Conductive Belt.

The digitized geological map was overlain on the magnetic map in order to correlate dolerite intrusions (i.e. dykes and sills) with the magnetic anomalies. Figure 5.4 shows three main magnetic anomalies. The first magnetic anomaly of up to 729.9 nT runs from west of Jansenville to north of Fort Beaufort. This anomaly is part of the Beattie magnetic anomaly and could be due to a buried body with high magnetic susceptibility minerals that stretches east - west across the study area. The centre of the first anomaly also shows that the body divides into two, but still trend in the same direction. The second anomaly is seen in the north-eastern part of Butterworth. This anomaly is of relatively small extent with maximum amplitude of about 227.5 nT. It could be due to dolerite intrusions with associated faults that are more prominent in the northeastern part of the map. The third anomaly is the "bean shape anomaly" which is seen between Fort Beaufort and Grahamstown.
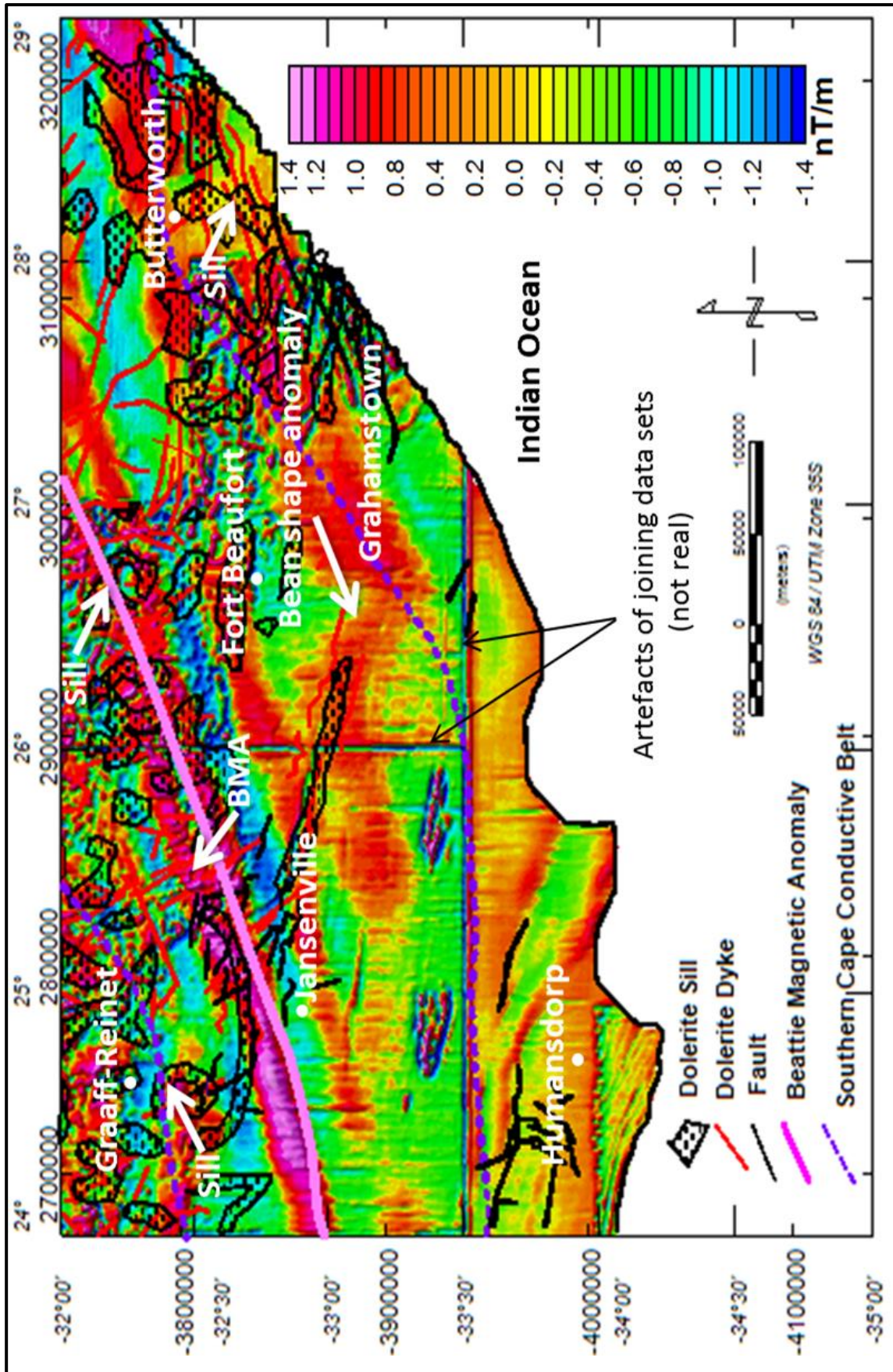
Figure 5.5 Vertical derivative map overlain on the geology. The map also shows dolerite intrusions (sills and dykes), faults, part of the Beattie magnetic anomaly and the Southern Cape Conductive Belt.

The vertical derivative map was overlain on the geological map in order to correlate geologic features (i.e. dykes and sills) with the magnetic signatures. Figure 5.5 shows the first vertical derivative of the magnetic field in Figure 5.3. It enhances near-surface geology (shallow geologic sources in the data), suppress anomalies caused by deeper sources, thereby giving a better resolution of closely-spaced sources. Figure 5.5 shows the main anomaly of amplitude of up to 1.4 nT/m that runs from west of Jansenville to north of Fort Beaufort. It could be due to a shallow buried body and was possibly intruded by dolerite sills and dykes. This anomaly is part of the Beattie magnetic anomaly, and the vertical derivative clearly shows anomalous body is splitting into two anomalies towards the centre of the map (northeast of Jansenville).
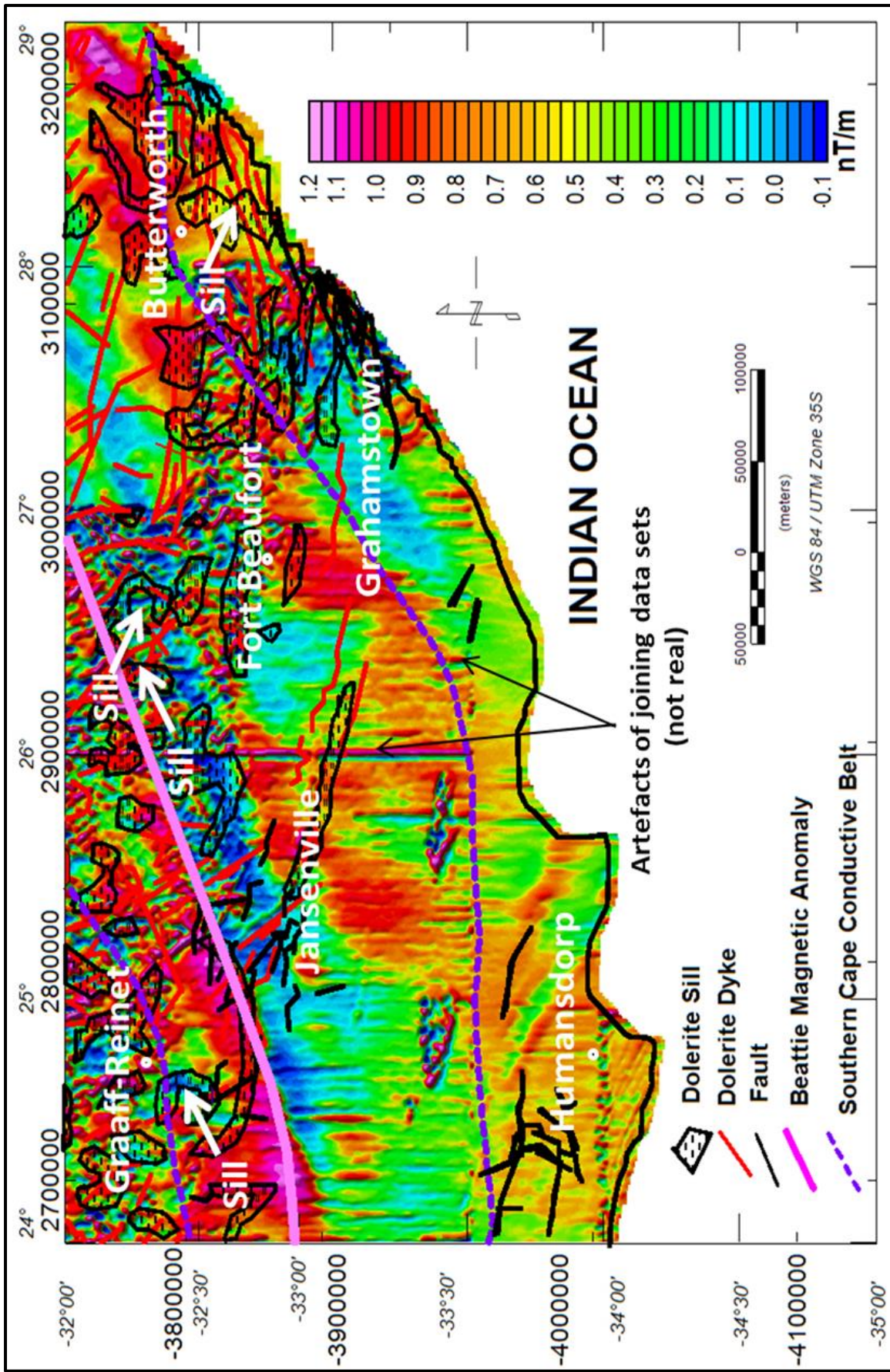
Figure 5.6 Total horizontal derivative map of the magnetic field on the geology. The map also shows dolerite intrusions (sills and dykes), faults, part of the Beattie magnetic anomaly and the Southern Cape Conductive Belt.

The total horizontal derivative map was overlain on the geological map in order to correlate geologic features (i.e. dykes and sills) with the magnetic signatures. Figure 5.6 shows the total horizontal derivative of the magnetic field in Figure 5.3 calculated in the space domain. It gives an indication of the boundary structure and this will be accurate for pole reduced data. The total horizontal derivative map shows interesting features that trend from north of Graaff-Reinet to the northeastern part of Grahamstown, these features also coincide with the dolerite intrusions on the geological map with prominent ring structures (dolerite sills) in the northern part of the map.
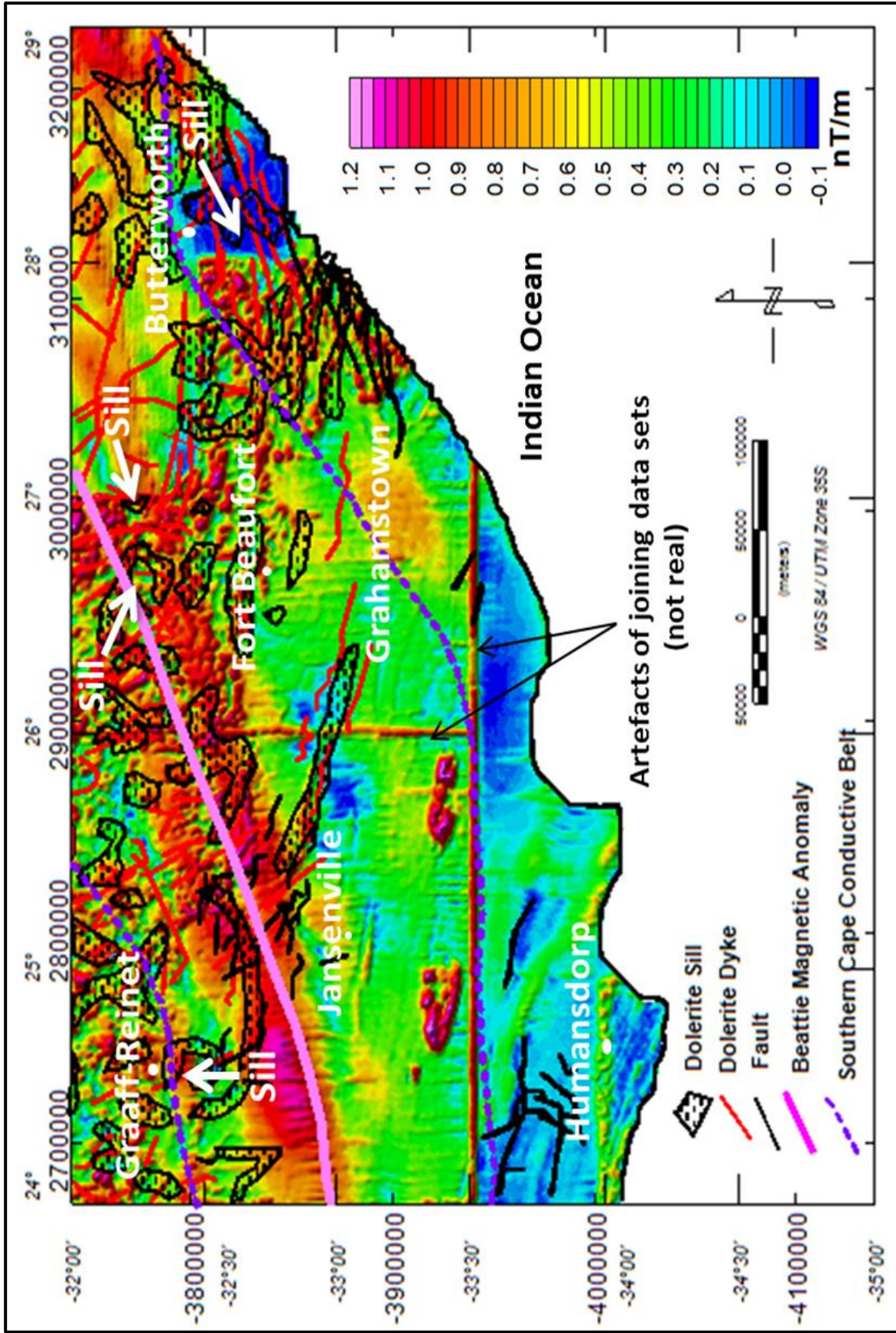
Figure 5.7 Analytical signal map of the study area. The map also shows dolerite intrusions (sills and dykes), faults, part of the Beattie magnetic anomaly and the Southern Cape Conductive Belt.

The analytical signal map was overlain on the geological map in order to correlate geologic features (i.e. dykes and sills) with the magnetic signatures. The analytical signal map (Figure 5.7) was calculated from the horizontal and vertical derivatives of the magnetic field. It helps to identify geologic contact, dolerite intrusions and faults because it is not affected by the direction of source magnetisation, geological dip or ambient magnetic field inclination/declination. It forms ridge maxima over magnetic contacts of any dip. Figure 5.7 shows anomalous highs that clearly outline body (BMA) that was shown in Figure 5.3. A number of faults and dolerite intrusions (e.g. sills, shown with yellow arrows) were outlined on the map which trend in easterly and north-westerly directions. The dolerite intrusions are concentrated in the northern part while most of the faults were observed toward the centre and eastern part (edge) of the map.
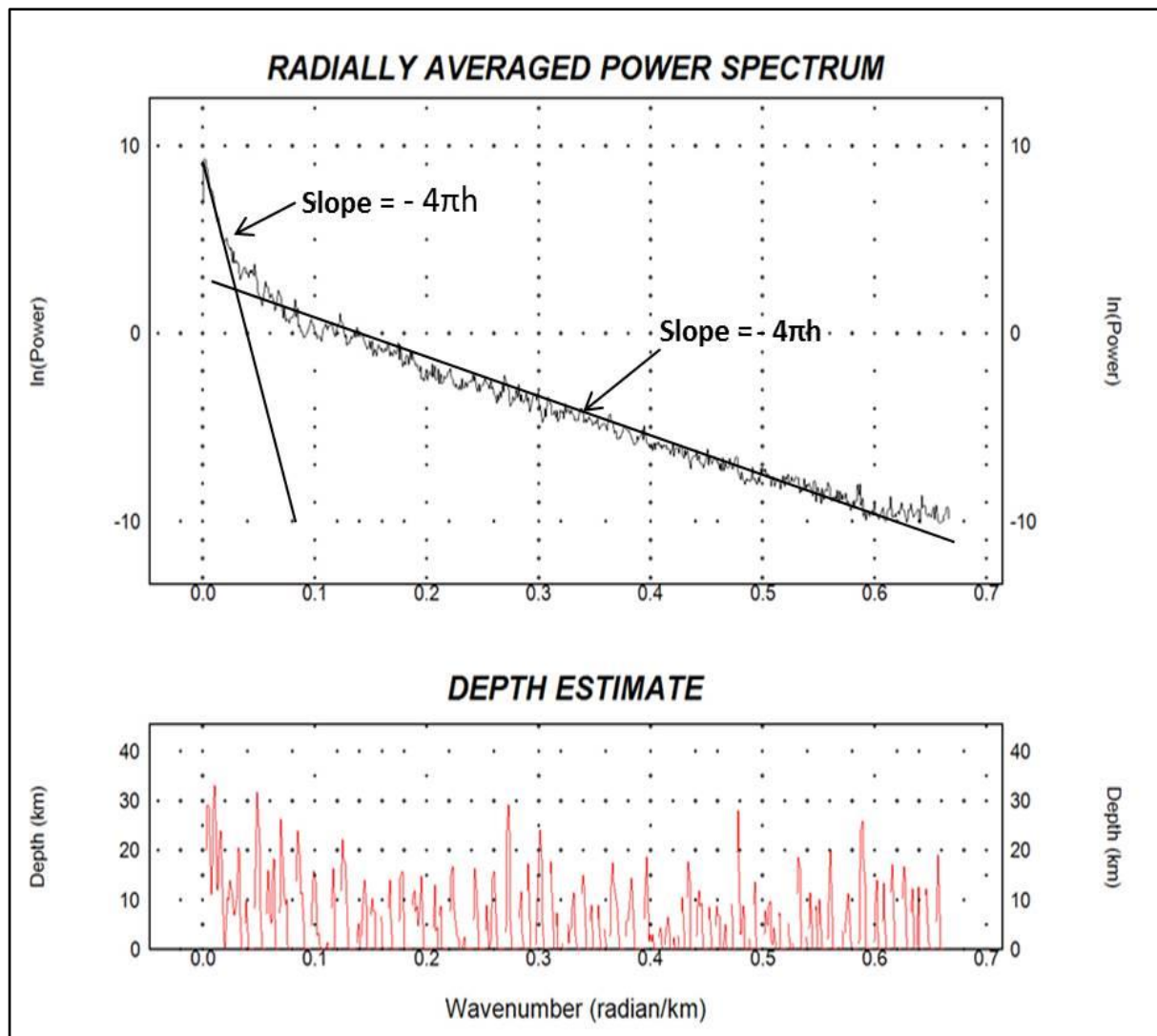
Figure 5.8 Radially averaged power spectrum of the aeromagnetic data of the study area.

111

The radially averaged power spectrum (Figure 5.8) was calculated in the wavenumber domain in order to estimate the depth to magnetic sources. The approximated magnetic depth ($h = \frac{\text{Slope}}{-4\pi}$) of about 0.6 km and up to 15 km were calculated (after subtracting the flight height) from the slope as the average depth to the top of the shallow and deep sources respectively (Figure 5.9).

RADIALLY AVERAGED POWER SPECTRUM

K_{max}

$h = \frac{\text{Slope}}{-4\pi} = 15.071$ km (average depth to deep seated structures)

$h = \frac{\text{Slope}}{-4\pi} = 0.665$ km (average depth to shallow s structures)

In (Power)

Wavenumber (cycle/km)
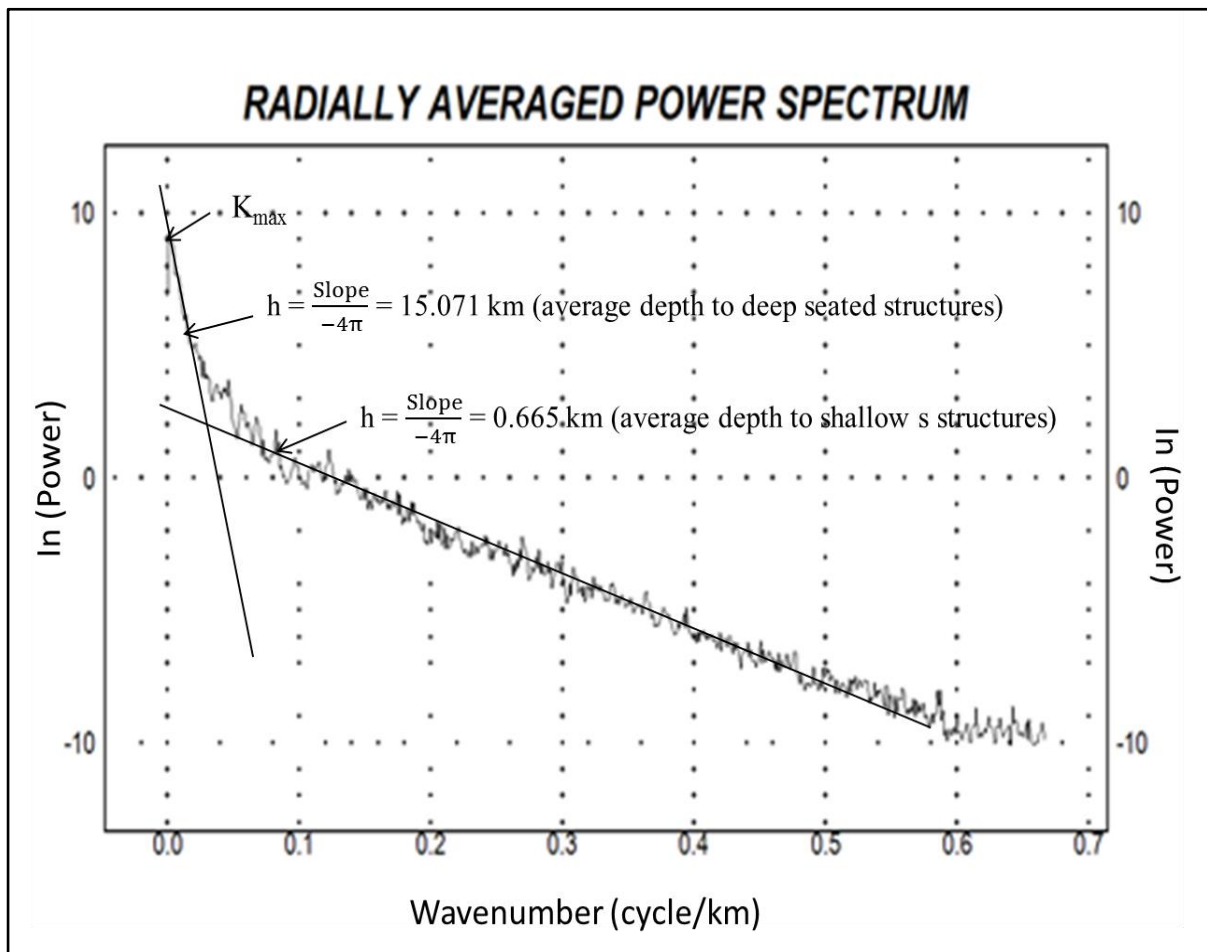
Figure 5.9 Depth estimate from the radially averaged power spectrum.
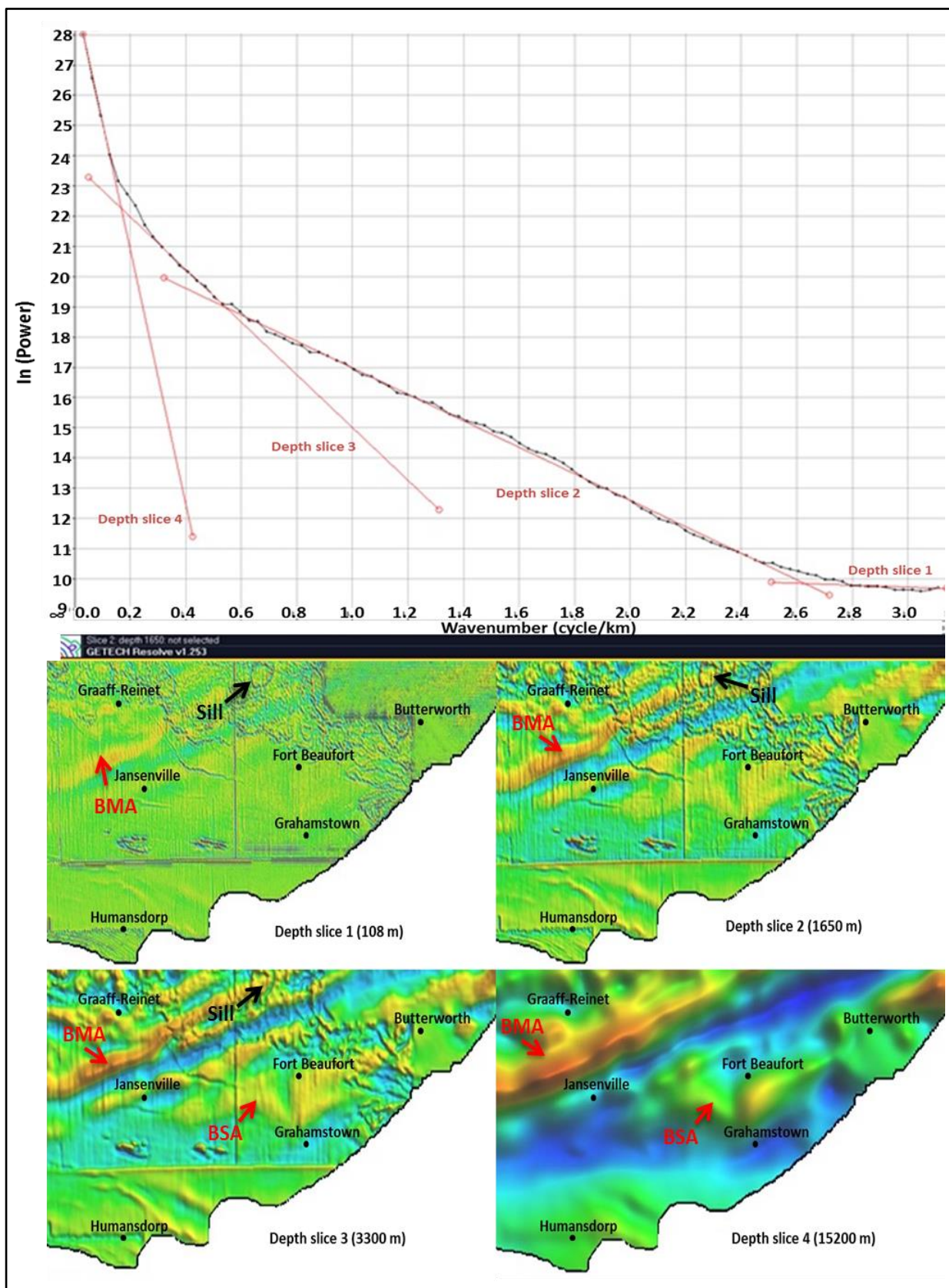
Figure 5.10 Depth slice showing changes in anomaly features with depth. Note: BMA is the Beattie Magnetic anomaly and BSA is the bean shape anomaly.

113

Depth slices (Figure 5.10) were used to compare the anomaly amplitude responses at different depths. Thus the appearance and disappearance of anomalous features at a particular depth can be recognised. Depth slice results (slices 1- 3) clearly show structural trends that coincide with dolerite intrusions on the geological map of the area. It shows that the mapped geologic structures like dolerite intrusions have a response which is clearly visible down to a depth of about 3300 m. The depth slice 4 shows little or no anomalies due to intrusions when compared with the other slices (slice 1- 3). A ring structure (dolerite sill) was seen in the northern part of the map. This sill anomaly becomes more prominent or stronger as the depth increases to about 3300 m but thereafter disappears at a depth of 15200 m.

The BMA appears in all the depth slices (0 - 15200 m) and becomes broader with depth which could be an indication that the source is deeper possibly within the basement. It could be a buried body in the basement (that is possibly intersected by a fault plane dipping in southern direction) or/and a buried massive sulphide-magnetite body within the basement (Lindeque *et al.*, 2007). The bean shape anomaly also behaves in similar manner like the BMA thus it could possibly share the same source(s) with the BMA.

5.7 Conclusions

Based on the data presented in this chapter, the following can be inferred:

- The magnetic map shows a "bean-shape" anomaly (Figure 5.3). From the derivative maps, the anomaly which coincides with the Beattie magnetic anomaly tends to divide into two anomalies and continue to trend in an NE-SW direction could be related to a body that is rich in magnetic minerals and buried within the basement.
- Based on the radially averaged power spectrum, the average depth to the top of the shallow and deep magnetic sources was estimated to be approximately 0.6 km and 15.01 km respectively.
- Based on the depth slice results, it could be deduced that geologic structures like dolerite intrusions are connected and extend to a depth of about 3300 m. The anomaly of the BMA become stronger with depth which could be an indication that the source(s) is deep possibly a buried body in the basement. The bean-shape anomaly that was seen in depth slice 2 – 4 (108 – 15200 m) behaves in a similar manner like the BMA thus it could possibly share the same source(s) with the BMA.

CHAPTER SIX

GAMMA-RAY SPECTROMETRIC METHOD

6.1 An overview of the airborne gamma-ray spectrometric method

Radioactivity is the process by which unstable atomic nuclei spontaneously disintegrate or decay to produce nuclei that are more stable. During radioactive decay, particle and energy are released from the nucleus of a decaying atom. The released particle/energy is called radiation. A material (e.g. element) that spontaneously releases this kind of radiation is said to be radioactive (e.g. radioactive element). Coetzee (2008) stated that each radioactive element emits or releases its own characteristic form of radiation. The different types of ionizing radiation that are released from the nucleus of a decaying atom include alpha particles (i.e. an ionised helium atom), beta particles (i.e., an electron) and gamma rays (electromagnetic radiation).

Radioactivity can either be natural (natural radioactivity) or induced (induced radioactivity). The induced radioactivity is produced artificially from nuclides (e.g. in a reactor). The half-life of a radioactive isotope is the amount of time required for one half of the radioactive nuclei to undergo decay. Unstable atomic nuclei (parent) do not always decay to produce nuclei (daughter) that are more stable. At times the daughter is unstable and decays with its own half-life which can involve many steps in a radioactive chain before a stable daughter is finally produced (Minty, 1997).

Radioactive potassium-40 (^{40}K) is only about 0.012 % of the naturally occurring potassium. The three main naturally occurring radioactive series decay chains are thorium-232 chain (^{232}Th), uranium-238 chain (^{238}U) and uranium-235 chain (^{235}U). The abundance of potassium is determined as gamma-rays are released when potassium-40 decays to argon whilst the abundance of uranium and thorium are measured indirectly from the emission peaks that are associated with ^{208}Tl and ^{214}Bi (Stevenson *et al.*, 2004). Natural radioactivity due to potassium, thorium and uranium (^{238}U is measured because ^{235}U is a minor constituent) are measured during radiometric survey (Stevenson *et al.*, 2004). The decay of ^{238}U to stable ^{206}Pb involves 14 intermediate decays, therefore resulting in a large effect on the total radiation (see Figure 6.1).
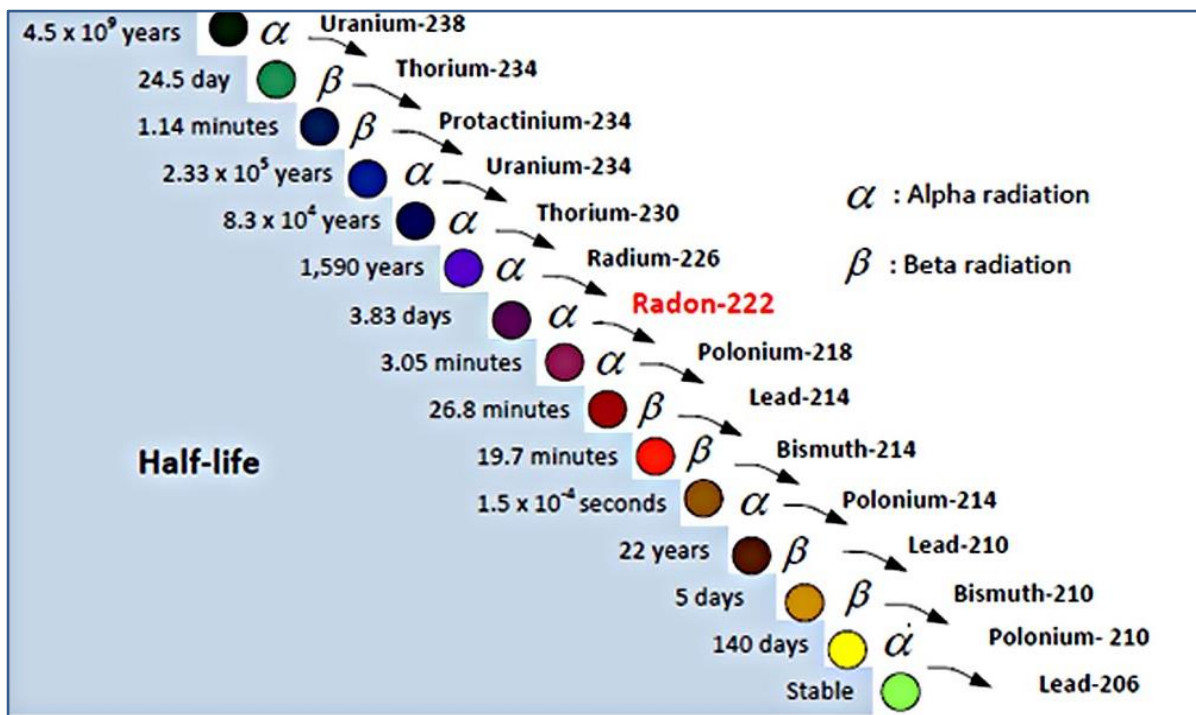
Figure 6.1 Half-life for the decay of uranium-238 to stable lead-206 (Stevenson et al., 2004).

Most radioactivity surveys detect gamma ray because alpha and beta particles are stopped by soil/rock and about 90 % of the measured radioactive response comes from the upper 20 – 35 cm of the surface of soils and rocks which is penetrated by gamma ray. According to Killeen (1979), the three main processes by which gamma rays interact with matter are photoelectric effect, Compton scattering and pair production (see Figure 6.2).
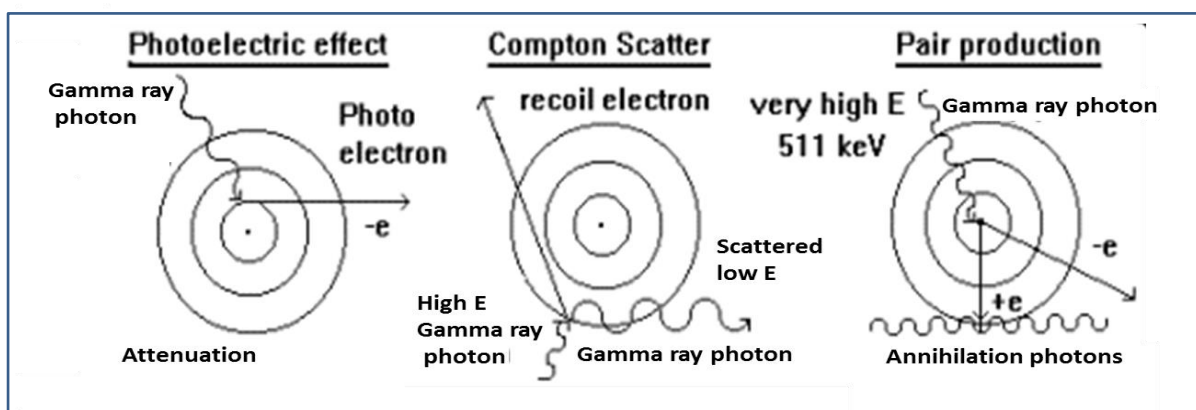
Figure 6.2 Interaction of gamma rays with matter (Killeen, 1979).

The unit for measuring gamma ray energy is electron-volt (eV) usually expressed in keV or MeV (k = 10^3; M = 10^6). The measurement of gamma rays of all energy is known as total count which is measured in counts per second (cps).

Table 6.1 Radioelement concentrations in different rock types (Killeen, 1979).

Rock type	K (%)	U (ppm)	Th (ppm)
Acidic	0.1 - 8	0.1 - 30	0.1 - 250
Basic	0.02 - 3	0.01 - 6	0.03 - 15
Ultrabasic	0 - 1	0 - 1.6	0 - 8
Sedimentary	0.01 - 10	0.1 - 80	0.2 - 350
Metamorphic	0.01 - 6	0.1 - 150	0.1 - 100

Airborne gamma-ray surveys are usually flown at constant height above the ground level (between 50 m and 100 m) with regular grid along parallel lines (flight lines). The flight line spacing is mostly between 50 m and 400 m with measurement taken every 50 - 60 m along the flight line and the tie line (tie line is perpendicular to the flight line) spacing is approximately 5 times that of the flight line spacing (usually 500 - 1000 m) depending on the survey purpose. The speed of the aircraft is relatively slow at about 50 - 60 m/s for fixed-wing surveys and 25 - 30 m/s for helicopter surveys.

Gamma ray surveys are mostly used for geological, geochemical, environmental mapping and for mineral exploration such as exploring for ores of uranium and thorium. The instrumentation, gamma ray data acquisition, calibration and processing are presented in Appendix B (Section 9.7 – 9.9). More details on radioactivity surveying can be found in Minty (1997), Coetzee (2008) and Stevenson *et al*. (2004).

The gamma ray survey datasets were displayed as map and profiles (Figure 6.3 - 6.8). The total gamma radiation count map was superimposed on the digitized geological map of the area to correlate geologic features giving rise to the high total gamma radiation count.

The blanks in the dataset (spots with white colour in Figure 6.4) are locations or areas without the total gamma radiation count (no data were collected) which could be due to urban development. Also, there is a site or mine (shown with a thick black arrow in Figure 6.4) where uranium was previously mined. This mine was probably not well managed and has been closed due to environmental pollution, thus physical processes like weathering and erosion could have acted on the site and washed down the detrital materials that contain radioactive elements like uranium, thorium and potassium.

The supplied data have only total count, but no individual channel count (e.g. U, Th and K) thus it was only used as a mapping tool. Assuming the individual channels were supplied with the data, then it would have been possible to determine the amount of individual radioelement (in ppm, cpm and %) in the ground as well as plotting ternary diagram and sum-normalization (i.e. $K/(K+U+Th)$, $U/(K+U+Th)$, $Th/(K+U+Th)$) in order to determine the relative abundance of the radioelements.

6.2 Radiometric results
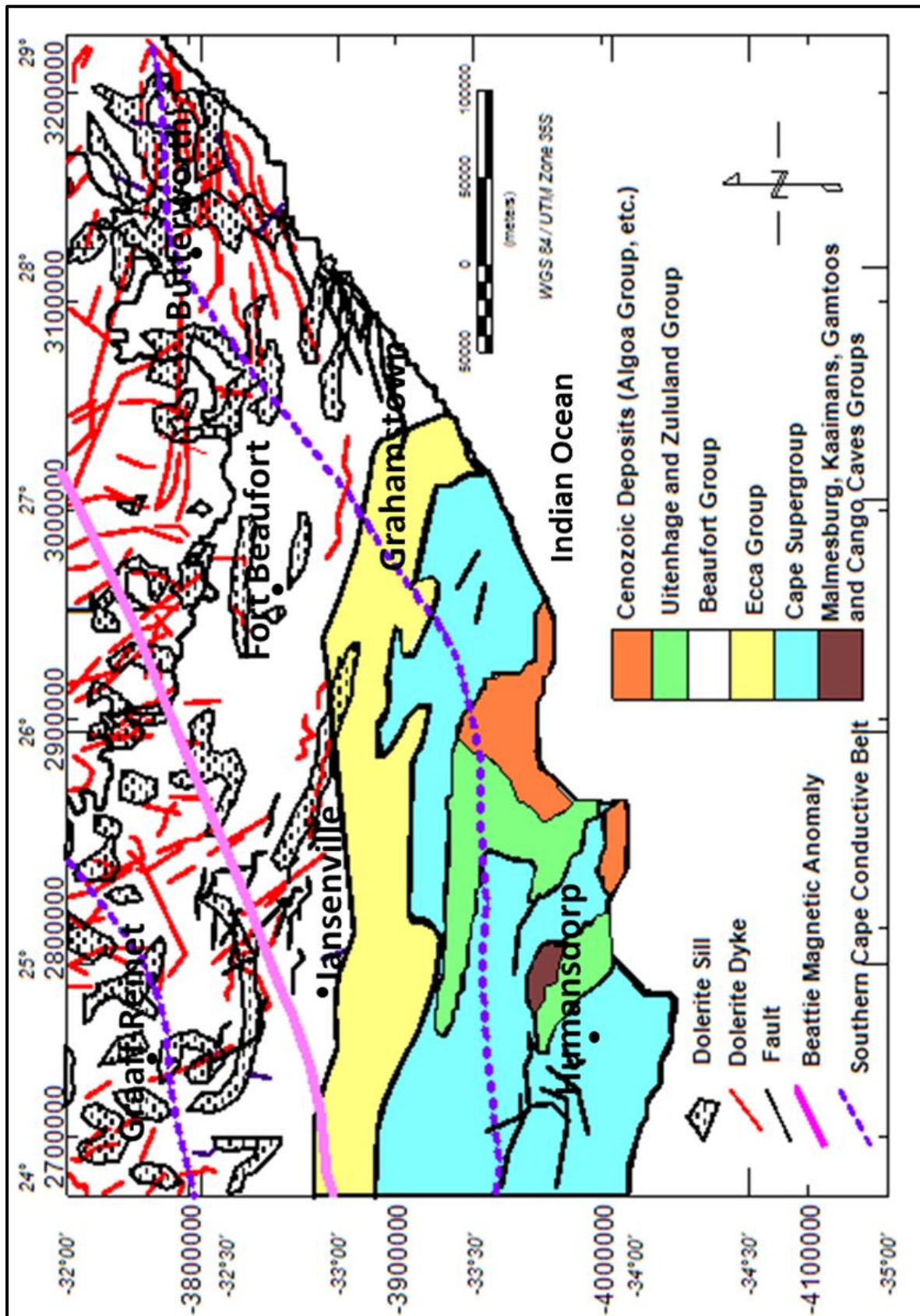
Figure 6.3 Simplified geological map of the study area showing geologic groups/supergroup, part of the Beattie magnetic anomaly (BMA), Southern Cape Conductive Belt (SSCB), faults and dolerite intrusions (sills and dykes).

119
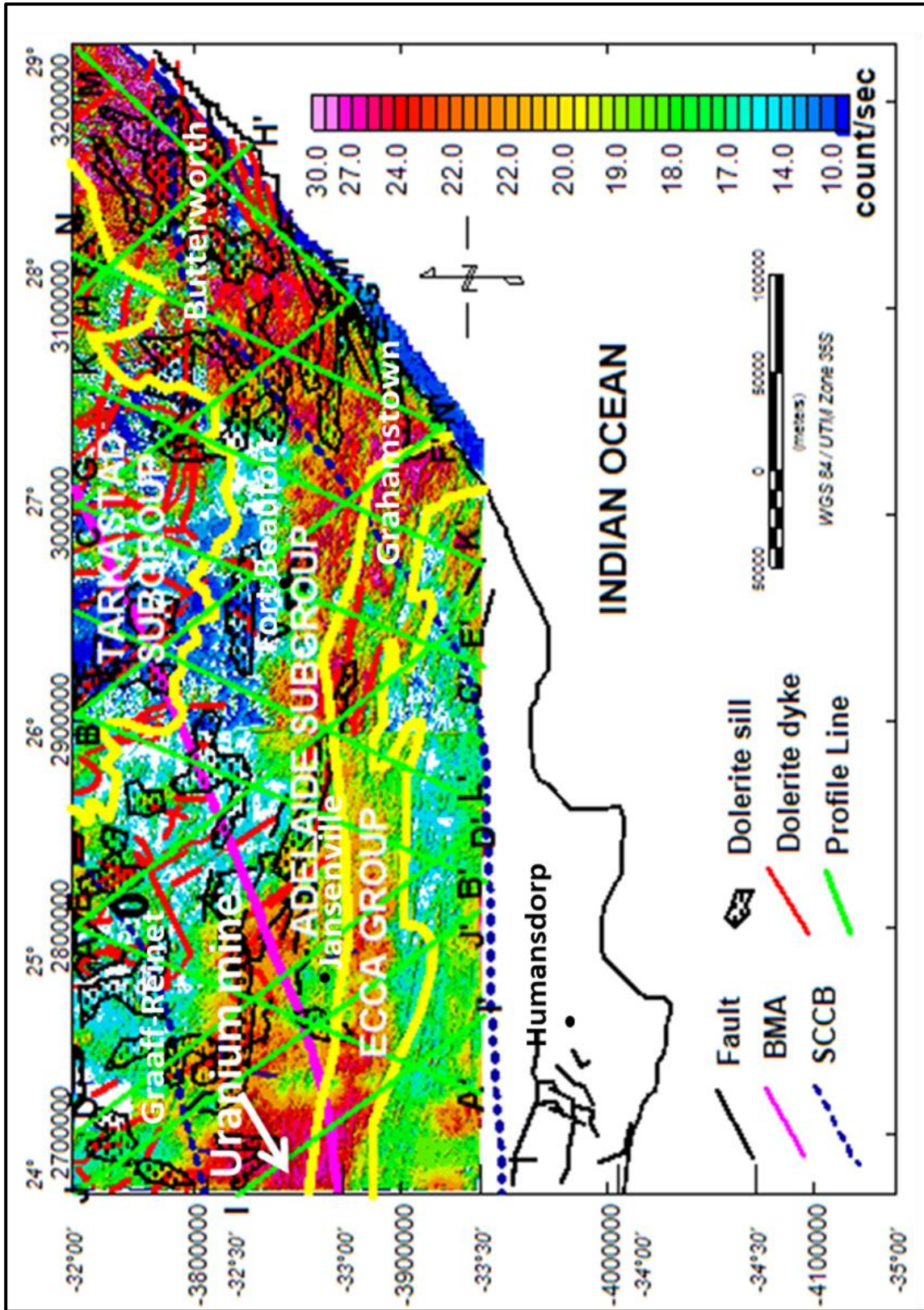
Figure 6.4 Total gamma radiation count map of the study area (Data courtesy of Council for Geoscience). Note: The map also shows dolerite intrusions (sills and dykes), faults, part of the Beattie magnetic anomaly and the Southern Cape Conductive Belt. The site where uranium was previously mined is shown by the white arrow (west of Jansenville), the yellow colour shows the geologic boundary between the Ecca and Beaufort (Adelaide and Tarkastad Subgroups) Groups.

Figure 6.4 shows high concentrations of total gamma radiation counts in the northeast part of the map. The right top corner of the map (northeast of Butterworth) shows the highest radiation counts/sec. The western part of Jansenville (site where uranium was previously mined (known as uramine) shown with black arrow) also indicates relatively high total counts of about 26 counts/sec. Generally, the igneous rocks of the Karoo strata have relatively low counts (blue to green colour) but it is fascinating to note that there is a high total radiation count in the Adelaide Subgroup and this could be due to the uranium and thorium in the detrital materials, as well as the enrichment of feldspars (k-feldspar) with calcite, quartz, zircon and clay minerals in the fluvial channel sandstones.

Uranium deposits in the Karoo Supergroup are confined to fluvially-deposited sandstones in the Adelaide Subgroup. Cole and Wipplinger (2001) stated that the absence of uranium in lithologies of similar disposition in terms of depositional environment (paleoclimate and palaeoenvironments) is probably due to the absence or lack of a suitable uranium source at the time of metallogenesis. Basement granite and volcanic ash have been proposed as possible uranium sources for the Adelaide Subgroup. The warm, semi-arid paleoclimate of all these stratigraphic units (Beaufort Group) signifies an oxidising environment, which is required for the leaching and mobilisation of uranium from the above sources. Uranium-bearing solutions probably migrated through the sand bodies with precipitation occurring in relatively sparse reduced zones that contained carbonaceous debris.

The uranium that was locally mined (Figure 6.4) was probably sourced from granitic terrane located west of the study area (Karoo Uranium Province, in the Western Cape Province of South Africa). Clastic material containing this uranium was probably transported into the basin by entrainment within fluvial sediments; also, some of the volcanic ash may have been transported and deposited. The stream or river that flows in the study area, especially around the mining site could also have transported a proportion of the metals (naturally occurring radioactive uranium and thorium as well as their decay products (e.g. radon and radium)) either in solution and/or adsorbed by clay minerals and organic detritus.

Cole and Wipplinger (2001) stated that the metals were dispersed in both flood basin mud and fluvial sand before being later mobilised and transported in slightly oxidised and alkaline solutions. The presence of calcite in the fluvial sandstones of the Adelaide Subgroup indicates that the uranium was probably transported in solution as uranyl carbonate

complexes. Uraniferous ore-forming fluids presumably derived either from volcanic tuff fragments, which were laid down contemporaneously with the fluvial sediments and/or from the detrital materials transported from a granitic provenance. There remains much speculation as to which of the two processes are more plausible.
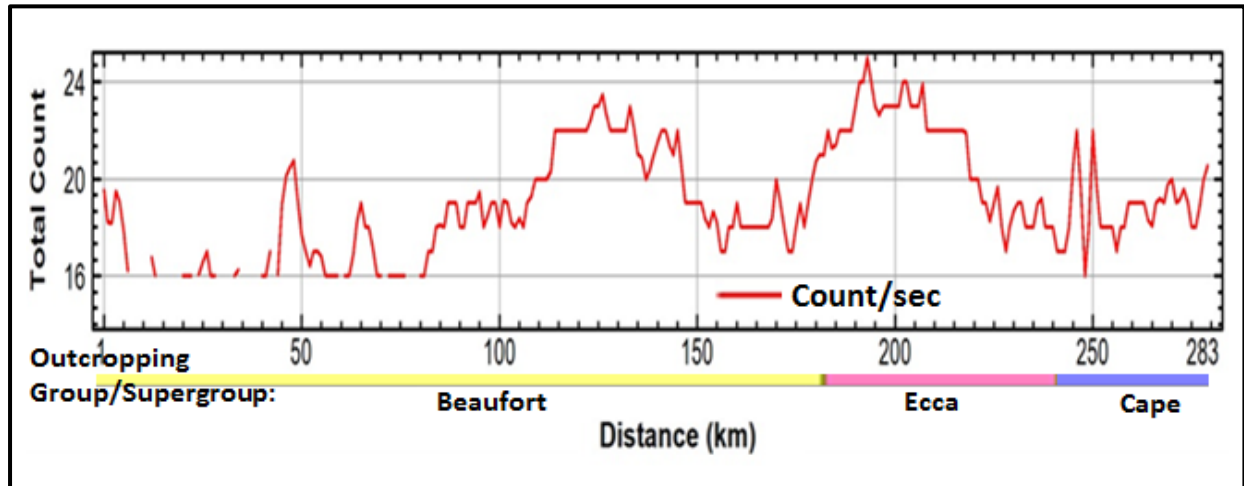
Figure 6.5 Profile for total gamma radiation count rate along Line A - A'.

There are two areas along profile A - A' with relatively high total count rate. The first area with high total radiation count rate has values that range from 18 - 23 counts/sec between the distances of about 75 - 155 km. The second area with high radiation count rate has values that range from 17.5 - 25 count/sec between distances 180 - 230 km. These high radiation count rates could be due to the enrichment of uranium and thorium in the detrital material, as well as the feldspars that are present in the fluvial sandstones.
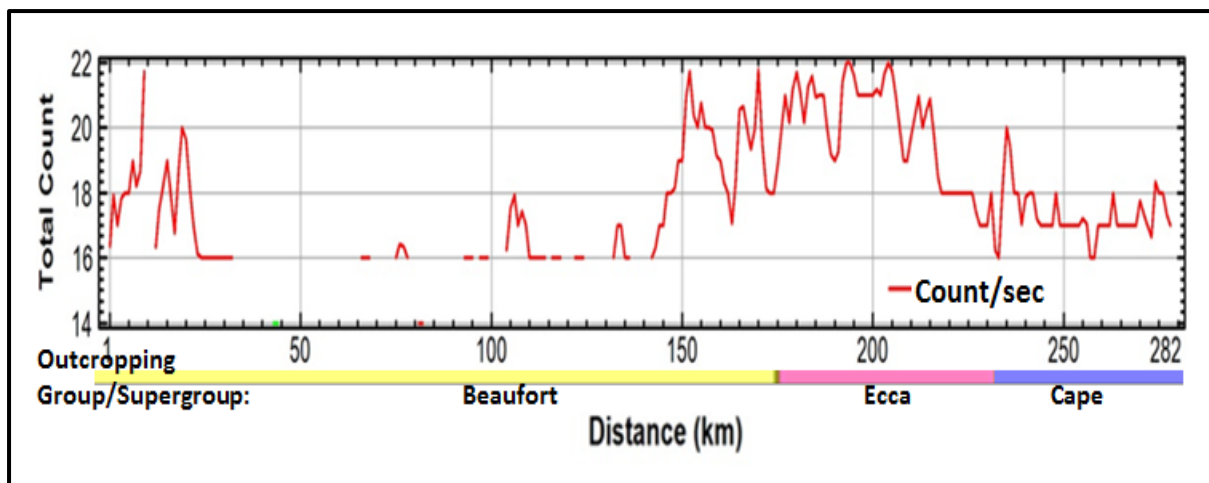
Figure 6.6 Profile for total gamma radiation count rate along Line B - B'.

The area with high total count rates whose values range from 16 - 22 counts/sec is seen between distances of 140 – 230 km. This high radiation count rate could also be due to the uranium and thorium in the detrital materials as well as the enrichment of radioelements in the feldspars (k-feldspar), zircon and clay minerals, which are present in the fluvial channel sandstones at shallow depth (within 0.45 m from the surface).
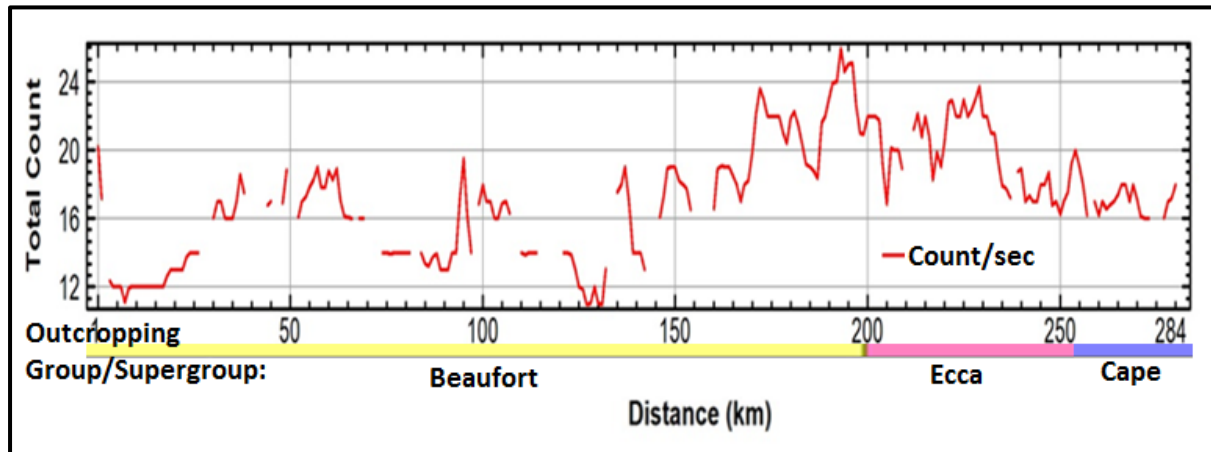
Figure 6.7 Profile for total gamma radiation count rate along Line C - C'.

The first area along this profile with high total count rate of about 18 – 30 count/sec falls within distances of 150 – 260 km. The second area with relatively high total radiation count rate of about 14 - 18.5 count/sec falls within the distance of 30 – 85 km. These high total count rates could be attributed to the uranium and thorium in the detrital materials as well as the enrichment of radioelements in the feldspars (k-feldspar), zircon and clay minerals.

123
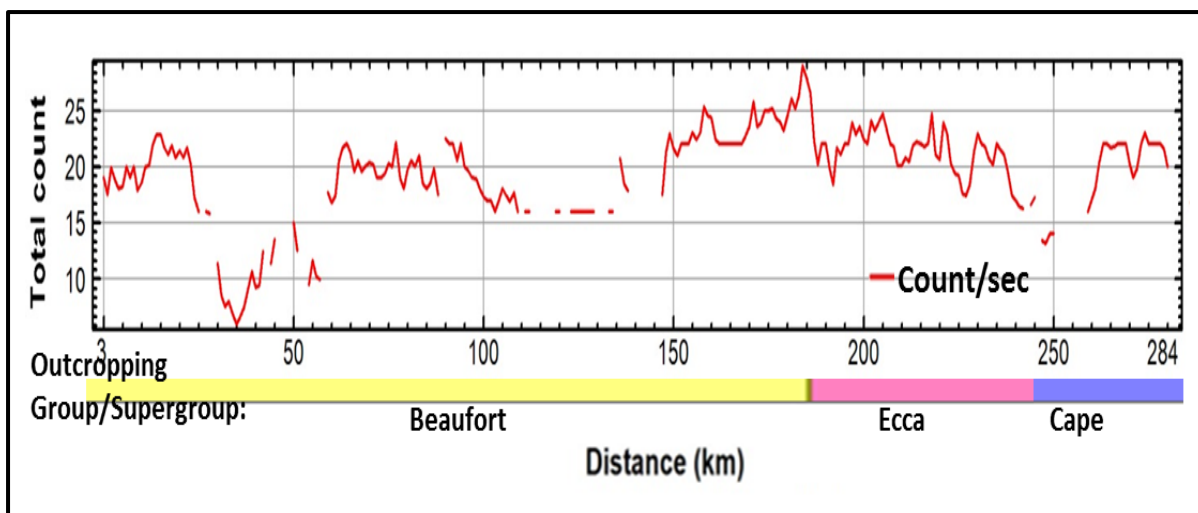
Figure 6.8 Profile for total gamma radiation count rate along Line K - K'.

There are two areas with high total radiation count rate along Line K-K'. The first area with relatively high total count rate of about 16 – 22.5 count/sec falls within distances of 80 – 155 km with the peak total count rate of 22.5 counts/sec at of about 125 km. The second area with high total radiation count rate that range from 16.5 - 24.5 count/sec falls within the distance of 160 – 230 km. These high radiation count rates could also be due to the uranium and thorium in the detrital material, as well as the feldspars that are enriched in the fluvial sandstones.

6.3 Conclusions

The gamma ray survey datasets were displayed as map and profiles. From the total gamma radiation count map and profiles, it could be deduced that region with high gamma radiation count could be due to the uranium and thorium in the detrital material, as well as the accumulation of radioelements in the sediments of the Adelaide Subgroup that are rich in feldspars (k-feldspar) with calcite, quartz and clay minerals and possibly intruded by dolerites (about 180 Ma) and faulted. The radioactive elements (e.g. uranium) could possibly be sourced from the volcanic fragments in the host fluvial sandstone, from the surrounding shales and probably the Precambrian basement granites that shielded the detritus to the depositional basin.

CHAPTER SEVEN

GRAVITY METHOD

7.1 An overview of the gravity method

Gravity surveys measure variations in the Earth's gravitational field due to the density contrast of sub-surface rocks. The measured variations in the Earth's gravitational field can be processed and interpreted using different approaches such as analytical and computational methods. Interpretation of gravity data is centred on the forces of attraction experienced between two bodies of different masses either in motion or under the influence of gravity which were explained by Newton's laws.

Newton derived two laws relating to gravity, namely; Newton's Universal Law of gravitation and Newton's second law of motion. Newton's Universal Law of gravitation states that "the force of attraction between two bodies of known masses is directly proportional to the product of the two masses and inversely proportional to the square of the distance between them". Thus the magnitude of the force (F) is given as:

$$F = \frac{G \times M \times m}{R^2} \qquad 7.1$$

where M and m are the masses of the two bodies, R is the distance separating them, and $G = 6.67 \times 10^{-11} \, N \, m^2 \, kg^{-2}$ is the gravitational constant.

Newton's law of motion states that "the force (F) is equal to mass (m) multiply by the acceleration due to gravity (g)" (see equation 7.2).

$$F = m \times g \qquad 7.2$$

$$F = m \times g = \frac{G \times M \times m}{R^2}$$

Thus;

$$g = \frac{G \times M}{R^2} \qquad 7.3$$

The Earth's acceleration due to gravity, herein referred to as gravity (g), is directly proportional to the mass (M) of the Earth and inversely proportional to the square of the Earth's radius (R). The mass (M) is a function of the density of subsurface rocks in the area of the measuring station. This implies that the Earth's gravitational field anomalies are due to differences in the density of subsurface rocks and the distance to these subsurface rocks from the gravimeter.

Gravity measurements are usually taken along traverses that cut across the location of the target (high gravity anomaly which is a function of density contrast). In order to accurately pick or detect a target such as fault or a dense body, the projected size of the target will aid in estimating the distance between stations during the survey. Large station separations are used for large target whilst small station separations are applied to small targets.

The unit of gravity is $m\,s^{-2}$, this is too big in gravity surveys and a preferred smaller unit is in $\mu m\,s^{-2}$ which is gravity unit (g.u.), i.e. 1 g.u. $= 1 \times 10^{-6} m\,s^{-2} = 0.1$ mGal. The mGal is mostly used in this study since the supplied data was in mGal (0.1 mGal $= 1$ g. u.).

7.2 Gravity measurement (instrumentation)

The instrument used to measure gravity is called a gravity meter or gravimeter. Gravity measurements can be subdivided into absolute and relative measurements. The absolute gravity can be measured using a falling body and swinging pendulum. Relative changes in gravity between two points or locations are measured in exploration with the use is of a relative gravimeter. There are different types of gravimeters used for relative measurements ranging from stable to unstable gravimeters depending on the purpose of the survey either for mineral/hydrocarbon exploration or regional geological studies. The stable gravimeter has a sensing system which returns to its original position when it is disturbed (e.g. Askania, Boliden and Gulf gravimeters). The unstable gravimeter has a system which moves further away from its original position when it is disturbed (e.g. Lacoste-Romberg, Worden and Sodin gravimeters).

In a survey where relative gravity values are measured, they can be converted to absolute gravity values by tying a base station in the survey to an International Gravity Standardisation

Net 1971 (IGSN 71) network and thus all the acquired relative gravity values at all stations can be reduced relative to absolute gravity values.

7.3 Gravity data reduction

The measured or observed gravity value depends on the time, latitude, elevation/height, topography and rock densities. Thus, these effects must be removed except the last one (rock densities) so that only effects of geological features remain. The process of removing the effects is called gravity data reduction and this is presented in Appendix C (Section 1). The difference between the observed gravity value and that derived from using the shape/figure of the Earth is known as the gravity anomaly.

7.4 Data enhancement

The enhancements that were carried out on the magnetic data in Appendix B (Section 9) are also applicable to the gravity data. See section 9 in Appendix B for details.

7.5 Rock densities

Density is expressed as the mass of a substance per unit volume or as the ratio of mass in air of a unit volume of a sample at a given temperature. The bulk density of rock samples is a function of individual grains, porosity and pore-fluid (fluid that fills the pore spaces). Density varies in different rock types due to differences in mineralogy and degree of consolidation. Generally, density increases in igneous rocks with decreasing silica content, and increases in metamorphic rocks with decreasing acidity (the same as silica content) and with increasing metamorphic grade (Reynolds, 1997). Density of sedimentary rocks is a function of composition, age and depth of burial, cementation, porosity, tectonic processes and pore-fluid type (Reynolds, 1997).

Density can be subdivided into three main types namely; dry density (when the pore space is empty), wet density (when the pores are filled with fluids such as water) and grain or particle density (Reynolds, 1997). Density of rock samples can be determined in the laboratory by a number of methods such as direct volume measurement (i.e., graduated cylinder), buoyancy

determined volume and gas pycnometer (Reynolds, 1997). In this study, the density of rock samples was determined using the buoyancy determined volume (see Section 2 in Appendix C), which uses Archimedes' principle because of the easy accessibility to the measuring equipment, relatively much cheaper, simple to perform with high rate of accuracy and minimal or no error due to parallax when taking the readings compared to volume measurement (i.e., graduated cylinder). The three main types of rock sample densities can be illustrated as shown in Appendix C (Sections 2).

7.6 Sample descriptions

Two hundred and fifty-eight (258) rock samples were collected from road cut outcrops of several formations of the Karoo and Cape Supergroups. The samples range from diamictite, shale, sandstone, mudstone, quartzite, limestone, chert, schist, and conglomerate (Pre-Cape). The samples were labelled with a permanent marker and the location was recorded using a GPS (Garmin eTrex-10) receiver in the field. The rock samples are generally fine-medium grained. Most of the samples are relatively fresh and a small number have been exposed to weathering and erosion. Efforts were made to ensure that all the samples collected are fresh samples, but due to the degree of weathering in the study area, even some samples collected at depth were still slightly affected by weathering. The calculated density of the weathered rock samples might not be a representation of the sample density at great depth.

7.7 Procedures for measuring density of rock samples

An Adam electronic weighing balance, model PGW-3502e with serial number AE434L456, maximum capacity of 3500 g, 0.01 g readability, full tare range, 0.01 g repeatability, $\pm$ 0.01 g readout accuracy, $\pm$ 0.02 g linearity, bi-directional RS-232 (standard) interface and an external calibration (only) was used to measure rock densities in the laboratory. The device can measure seventeen (17) different measuring units, including gram, kilogram, carat, grain, newton, pound and ounce. There is an adjustable feet and spirit level at the rear of the balance and an under hook point at the base where the sample holder could be attached.

The PGW-3502e electronic balance provides outstanding precision and valuable features such as controlling fluctuations while measurement is in progress. The animal/dynamic

weighing mode on the balance helps to take accurate readings when the environment or application is disturbed by influences like vibrations, oscillation or movement of objects on the platform, or air movements.

The balance was located on a laboratory bench that is free from vibration. The four (4) pan supports and stainless steel were gently placed on the weighing platform. The hook point was placed over a strategically located hole in the laboratory bench. A sample holder (loop) was created with the use of thin copper wire such that the rock sample rests comfortably on the loop side while the other side is placed on the hook at the base of the balance. A bucket partially filled with water was placed under the laboratory bench such that the constructed loop is immersed in the water without making contact with the bottom and edges of the bucket (see Figure 7.1). The balance was levelled using the adjustable feet and spirit level at the rear of the balance until the bubble in the spirit level is centred. The balance was connected to a power source and balanced at zero mark. The balance was allowed to warm up for about twenty (20) minutes. The battery level, weighing unit, and stability were checked and certified before measurement commenced.
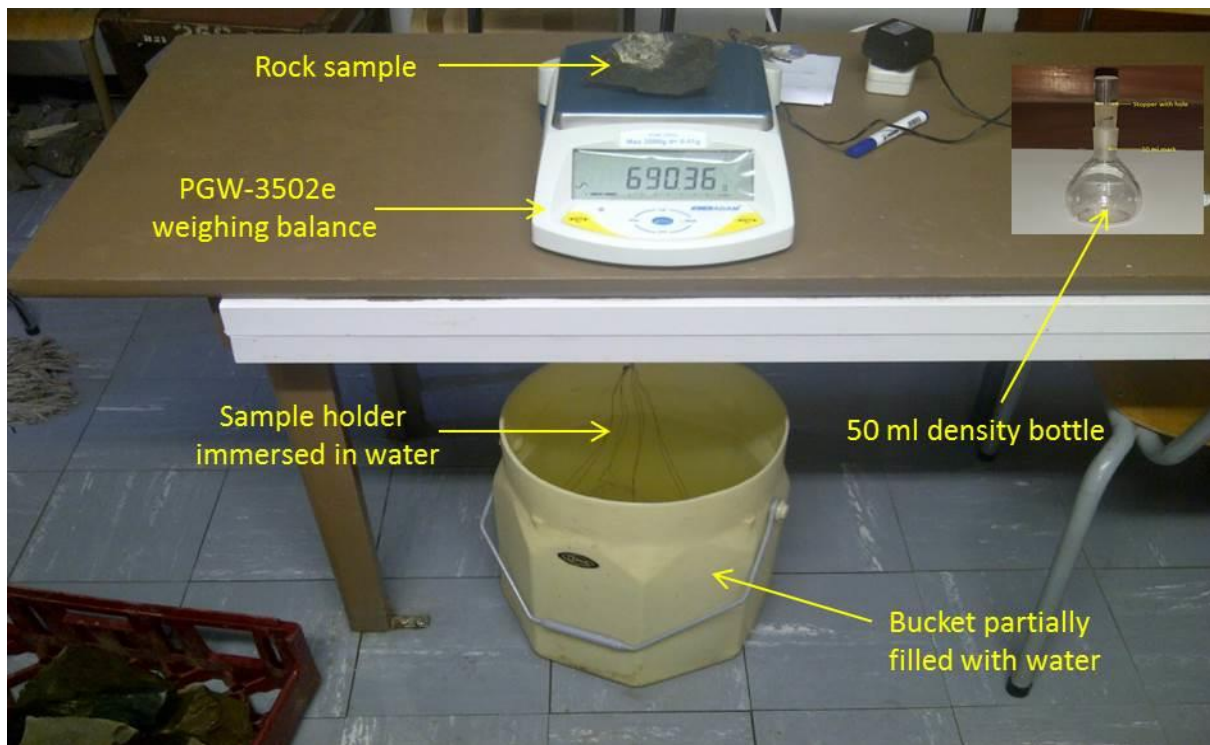
Figure 7.1 Photograph showing how the mass of rock samples were measured in the laboratory using Archimedes' principle.

To determine dry densities for the samples, the rock samples were sun dried for days instead of oven drying the samples to avoid damaging (cooking) of rock samples like shale. The dry sample was placed on the weighing balance and the mass in the air was recorded as M_a. The same sample was placed on the loop that was immersed in the water and the reading was quickly taken and recorded as M_b. This procedure was repeated for all the other dry samples.

To determine the particle density, the samples were soaked for at least 24 hours in a container filled with water to ensure that the pore spaces are completely filled or saturated with water. The soaked sample was quickly transferred from the bath of water and placed on the loop that was immersed in the water in the bucket and the reading was taken and recorded as M_c. This procedure was repeated for all the other soaked rock samples.

The formulae for dry, wet and particle densities require the density of water and without this the expressions are simply specific densities. In order to meet this requirement, a 50 ml density bottle was used to determine the water density. The density bottle is of accurately known volume and has a ground glass tight sealing stopper with a capillary tube that allows gas and excess water to escape (see Figure 7.1). The density bottle was weighed empty on the Adam PGW-3502e electronic weighing balance and the mass recorded, and then it was completely filled with water, tightly sealed with the stopper and weighed. The mass of the water was determined and the density was calculated. This was repeated every hour throughout the course of weighing samples. The result of the hourly measurements of water density is presented in Table 7.1.

An average water density of 1.022 g/cm^3 was obtained and applied when calculating the densities and porosities of the rock samples. The water density values depend on its temperature and pressure, i.e. decrease in temperature results in the water molecules to be well and closely packed together, thereby leading to increase in the density of water and vice versa, but this relationship is not linear. It was observed that the effect of temperature and pressure on the water density is negligible because the hourly densities of water are almost constant throughout the experiment. It could be inferred that the temperature and pressure were fairly constant throughout the experiment period.

Table 7.1 Hourly measurements of water density using a 50 ml density bottle.

Week	Day/date	Time	Density (g/cm^3)	Daily average density (g/cm^3)	Weekly average density (g/cm^3)
week 1	Monday 8/07/2013	09:00	1.022	1.022	1.022
		10:00	1.022		
		11:00	1.022		
		12:00	1.022		
		13:00	1.022		
	Tuesday 9/07/2013	09:00	1.022	1.022	
		10:00	1.021		
		11:00	1.022		
		12:00	1.022		
		13:00	1.023		
	Wednesday 10/07/2013	09:00	1.022	1.022	
		10:00	1.022		
		11:00	1.022		
		12:00	1.022		
		13:00	1.022		
	Thursday 11/07/2013	09:00	1.022	1.022	
		10:00	1.021		
		11:00	1.021		
		12:00	1.023		
		13:00	1.023		
Week 2	Monday 15/07/2013	09:00	1.022	1.022	1.022
		10:00	1.022		
		11:00	1.021		
		12:00	1.023		
		13:00	1.022		
	Tuesday 16/07/2013	09:00	1.023	1.022	
		10:00	1.023		
		11:00	1.021		
		12:00	1.021		
		13:00	1.022		
	Wednesday 17/07/2013	09:00	1.022	1.022	
		10:00	1.022		
		11:00	1.022		
		12:00	1.022		
		13:00	1.022		
	Thursday 18/07/2013	09:00	1.023	1.022	
		10:00	1.022		
		11:00	1.022		
		12:00	1.022		
		13:00	1.021		

7.8 Density and porosity results

The dry density, wet density, particle density and porosity of all the rock samples were calculated in Microsoft Excel spreadsheet by applying the appropriate formulae. The results are tabulated in Table 7.2.

Table 7.2 Average dry, wet and particle densities and porosity of all the rock samples for the several formations in the Karoo and Cape Supergroups.

FORMATION / INTRUSION	LITHOLOGY	NUMBER OF SAMPLES	AVERAGE DRY DENSITY (g/cm^3)	AVERAGE WET DENSITY (g/cm^3)	AVERAGE PARTICLE DENSITY (g/cm^3)	AVERAGE POROSITY (%)
Intrusions	Dolerite	15	2.7556	2.7577	2.7612	0.2033
Burgersdorp	Sandstone	6	2.7407	2.7480	2.7604	0.7119
Katberg	Sandstone	10	2.7430	2.7514	2.7659	0.8282
Palingkloof	Sandstone	17	2.7163	2.7277	2.7469	1.1150
Elandsberg	Sandstone	18	2.6740	2.6867	2.7075	1.2413
Barberskrans	Sandstone	14	2.6831	2.6927	2.7084	0.9357
Daggaboersnek	Sandstone	15	2.6985	2.7083	2.7244	0.9562
Oudeberg	Sandstone	17	2.7723	2.7840	2.8044	1.1442
Middleton	Mudstone	13	2.7316	2.7547	2.7949	2.2670
Koonap	Sandstone	12	2.7708	2.7913	2.8277	2.0127
Fort Brown	Shale	8	2.7564	2.7663	2.7835	0.9744
Ripon	Shale	8	2.7615	2.7707	2.7867	0.9053
Collingham	Shale / tuff	12	2.6978	2.7122	2.7363	1.4075
Whitehill	Black shale	23	2.5258	2.5596	2.6102	3.3095
Prince Albert	Khaki shale	15	2.6411	2.6540	2.6748	1.2601
Dwyka	Diamictite	11	2.6621	2.6671	2.6753	0.4931
Witteberg	Sandstone	10	2.7078	2.7217	2.7451	1.3569
Bokkeveld	Siltstone	10	2.6333	2.6479	2.6714	1.4257
Table Mountain	Conglomerate	12	2.7128	2.7275	2.7523	1.4355
Pre Cape	Chert	12	2.7508	2.7634	2.7851	1.2311
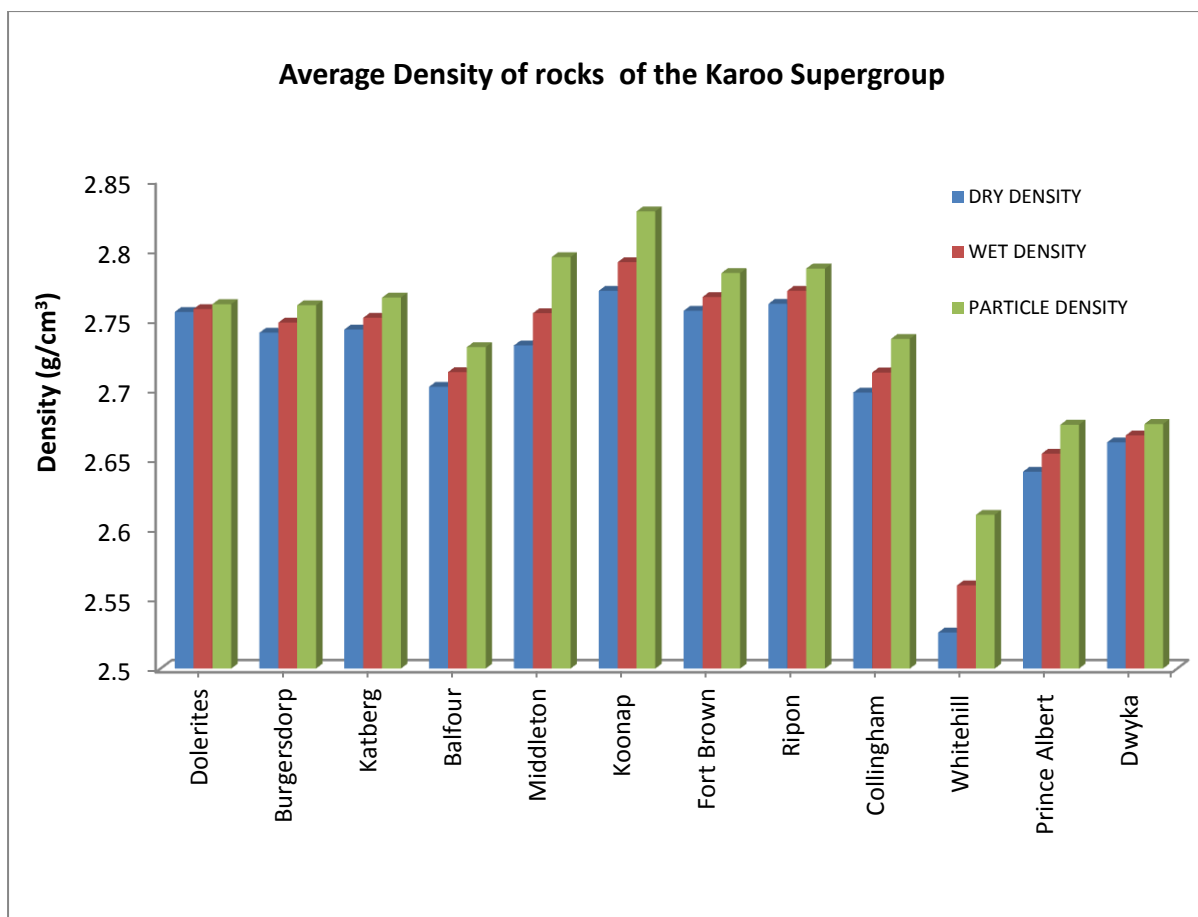
Figure 7.2 Bar chart of average densities of rock samples from the Karoo Supergroup and the dolerite intrusions.

Figure 7.2 shows that the average dry, wet and particle density values range from 2.5258 - 2.7723 g/cm^3, 2.5596 - 2.7913 g/cm^3 and 2.6102 - 2.8277 g/cm^3, respectively. The carbonaceous shale of the Whitehill Formation had the lowest average dry, wet and particle densities of 2.5258 g/cm^3, 2.5596 g/cm^3 and 2.6102 g/cm^3, respectively. The sandstones of the Balfour Formation had the highest average dry density of 2.7723 g/cm^3 whilst the sandstones of the Koonap Formation had the highest average wet and particle densities of about 2.7913 g/cm^3 and 2.8277 g/cm^3, respectively. The observed low density values for the carbonaceous shale may lead one to infer relatively high porosities for the formation since density is inversely proportional to porosity. These low density values could be due to weathering which altered the black carbonaceous shale to white shale. The dolerite intrusions (mostly sill) have an average dry, wet and particle densities of 2.7556 g/cm^3, 2.7577 g/cm^3 and 2.7612 g/cm^3, respectively.
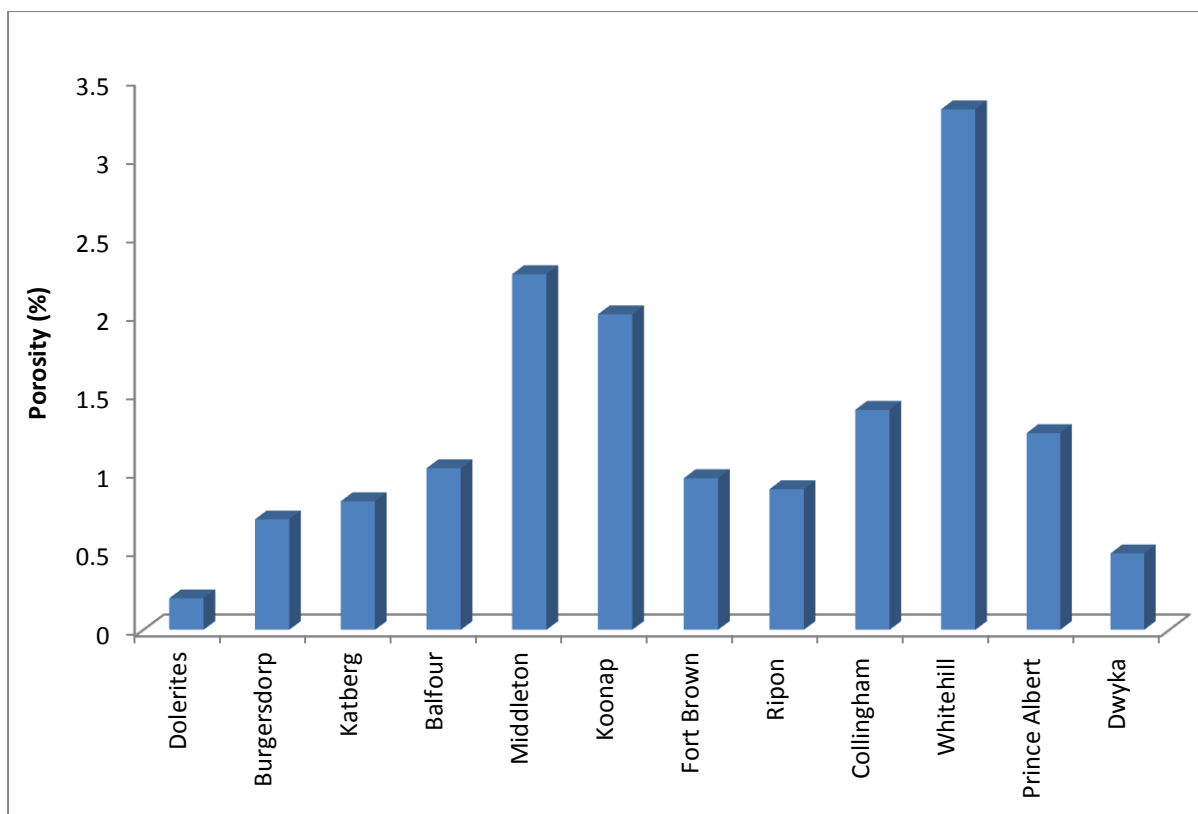
Figure 7.3 Bar chart of average porosity of rock samples from the Karoo Supergroup and the dolerite intrusions.

Figure 7.3 shows that the calculated average porosity of rock samples from various formations of the Karoo Supergroup. The values range from 0.4931 – 3.3095 %. The weathered black carbonaceous shale of the Whitehill Formation had the highest average porosity of up to 3.31 %, followed by the mudstones of the Middleton Formation with a porosity of 2.267 %. The dolerite intrusions (sills and dykes) have the lowest average porosity of about 0.20 %, followed by the diamictite of the Dwyka Formation with average porosity of about 0. 49 %.

7.8.1 Density - porosity relationship

The relationship between density and porosity was determined by plotting a graph of dry density against porosity and a least squares best line fitted through the data using Microsoft Excel (see Section 3 in Appendix C). The correlation coefficient (R) and coefficient of determination which is also known as the square of Pearson Product Moment Correlation

Coefficient (R^2) was calculated and tabulated as shown in Table 7.3. Note: The densities and porosities results (bar charts, density-porosity graphs and data) for each geologic formation are presented in Section 3 (Appendix C).

Table 7.3 Dry density - porosity relationship of rocks from the Karoo Supergroup.

Formation / Member	Number of Samples	Coefficient of Determination (R^2)	Correlation coefficient (R)	Linear Relationship
Burgersdorp	6	0.9007	0.9841	Closely related
Katberg	10	0.9896	0.9943	Closely related
Palingkloof	17	0.9888	0.9982	Closely related
Elandsberg	18	0.9778	0.9885	Closely related
Barberskrans	14	0.9926	0.9916	Closely related
Daggaboersnek	15	0.9517	0.9963	Closely related
Oudeberg	17	0.9674	0.9933	Closely related
Middleton	13	0.9886	0.9943	Closely related
Koonap	12	0.9867	0.9836	Closely related
Fort Brown	8	0.9926	0.9756	Closely related
Ripon	8	0.9833	0.9963	Closely related
Collingham	12	0.9970	0.9888	Closely related
Whitehill	23	0.9965	0.9944	Closely Related
Prince Albert	15	0.9886	0.9948	Closely related
Dwyka	11	0.9685	0.9491	Closely related

The correlation coefficient (R) in Table 7.3 is the statistical method which shows how strongly pairs of values are related. The standard values for the correlation coefficient (R) ranges from -1 to +1. The closer the correlation coefficient (R) value to either positive (+1) or negative (-1), the closer the variables are related.

The study of the relationship between dry density and porosity of rocks from Karoo Supergroup generally indicates an inverse relationship i.e. a negative correlation between the two parameters. The correlation coefficient values R range from 0.9491 - 0.9982. Due to the high correlation coefficient values for the parameters, the regression equation could also be used to determine the porosity since the dry density was practically determined from the laboratory. From the plot of dry density against porosity (section 3 in Appendix C: negative regression), the regression equation for the Burgersdorp Formation for example, is given as:

$$Y = -0.1364X + 1.0852 \qquad\qquad 7.4$$

This mathematical equation can also be expressed as:

$$\Phi = -0.1364\rho_d + 1.0852 \qquad\qquad 7.5$$

where Φ is the porosity and ρ_d is the dry density that was determined in the laboratory.

The expression (equation 7.5) is the relationship between dry density and porosity. The regression equations for all the formations were calculated and tabulated in Table 7.4. The calculated porosity values from the linear regression were compared with the values obtained from the laboratory.

Table 7.4 Correlation between the porosity values estimated from the regression equations and those determined in the laboratory.

Formation/Member	Regression equation	ρ_d (g/cm^3)	Φ (%)	Φ_L (%)
Burgersdorp	$\Phi = -0.1364\rho_d + 1.0852$	2.7407	0.7114	0.7119
Katberg	$\Phi = -1.069\rho_d + 3.7596$	2.7430	0.8273	0.8282
Palingkloof	$\Phi = -0.0797\rho_d + 1.3309$	2.7163	1.1144	1.1150
Elandsberg	$\Phi = -0.2338\rho_d + 1.8654$	2.6740	1.2402	1.2413
Barberskrans	$\Phi = -0.1126\rho_d + 1.2360$	2.6831	0.9339	0.9357
Daggaboersnek	$\Phi = -0.2001\rho_d + 1.4937$	2.6985	0.9537	0.9562
Oudeberg	$\Phi = -0.093\rho_d + 1.3963$	2.7723	1.1385	1.1442
Middleton	$\Phi = -0.0219\rho_d + 2.3239$	2.7316	2.2641	2.2670
Koonap	$\Phi = -0.0128\rho_d + 2.0482$	2.7708	2.0127	2.0127
Fort Brown	$\Phi = -0.0731\rho_d + 1.1728$	2.7564	0.9713	0.9744
Ripon	$\Phi = -0.1319\rho_d + 1.2695$	2.7615	0.9053	0.9053
Collingham	$\Phi = -0.0163\rho_d + 1.4513$	2.6978	1.4073	1.4075
Whitehill	$\Phi = -0.0701\rho_d + 3.4862$	2.5258	3.3091	3.3095
Prince Albert	$\Phi = -0.0788\rho_d + 1.4636$	2.6411	1.2555	1.2601
Dwyka	$\Phi = -0.0816\rho_d + 0.7424$	2.7521	0.5178	0.5198

Note that Φ is the porosity of rock calculated from the regression equation, Φ_L is the porosity that was determined in the laboratory; and ρ_d is the dry density of rock that was also determined in the laboratory.

7.9 Gravity results
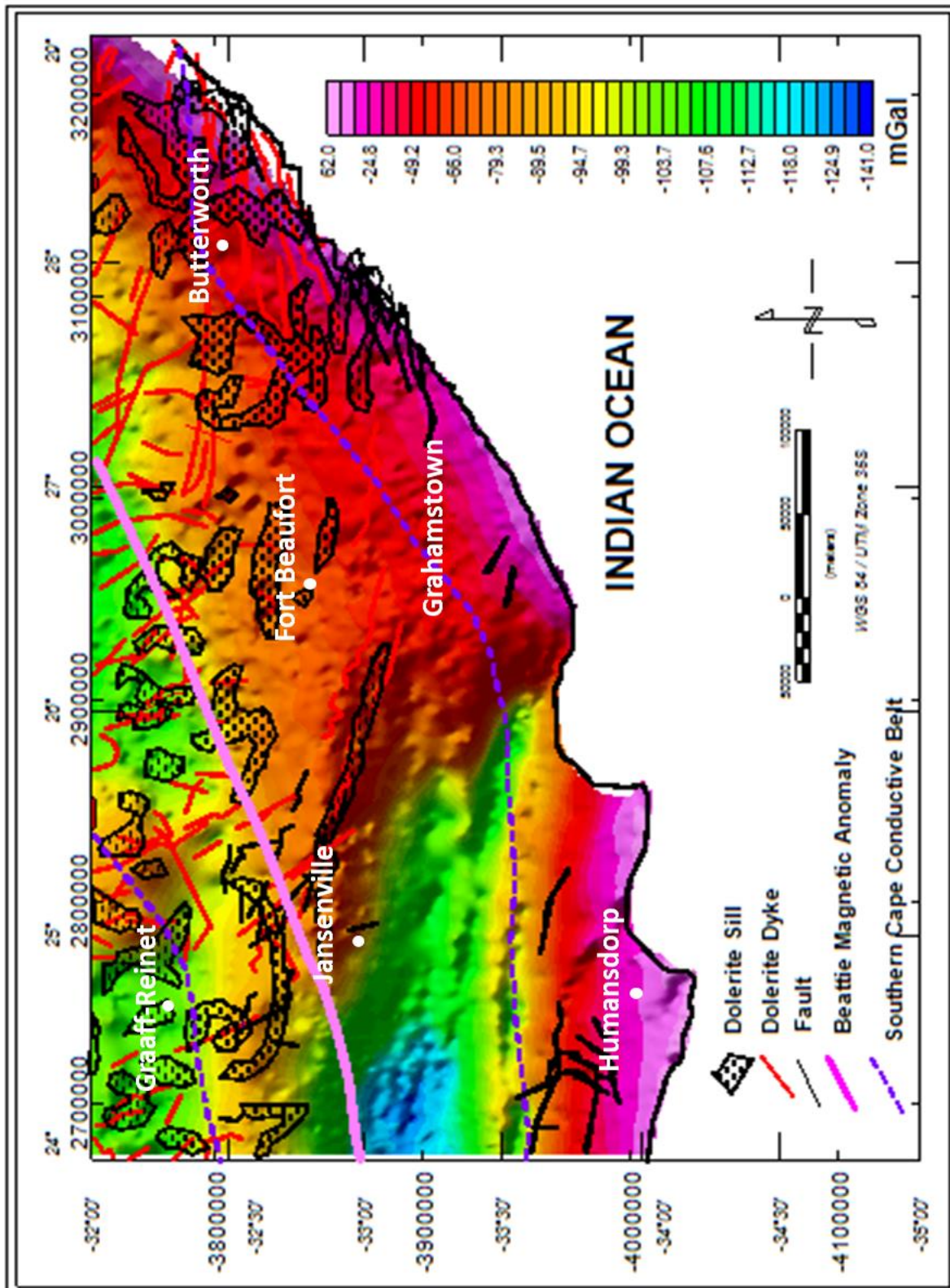
Figure 7.4 Bouguer anomaly map of the study area (Data courtesy of Council for Geoscience). The map also shows dolerite intrusions (sills and dykes), fault, part of the Beattie magnetic anomaly and the Southern Cape Conductive Belt.
Note: 1 mGal = 10 g.u.

The Bouguer anomaly map (Figure 7.4) shows an increase in gravity values, of long wavelength, from around -140.7 mGal inland (southwestern and northern side of Jansenville) to high gravity values of up to 60.1 mGal in coastal areas (western part of Humansdorp and continue to the northeast of Butterworth along the coastline). This dominant gravity variation is possibly due to a deeper source/interface inland that shallows southward towards the coast e.g. the basement and/or Moho (this is seen on models presented in Chapter 8).

7.10 Conclusions

Two hundred and fifty-eight (258) rock samples were collected from road cut outcrops of several formations of the Karoo and Cape Supergroups. The average densities of rocks from the Karoo Supergroup range from 2.5258 - 2.8277 g/cm^3. The average porosities range from 0.4931 – 3.3095 %. The relationship between the dry densities and porosities of the rocks indicate high correlation coefficient values (R) that range from 0.9491 - 0.9982. This implies that the variables (dry density and porosity) are closely related. The average densities of dolerite intrusions range from 2.7556 - 2.7612 g/cm^3 whilst the average porosity is about 0.20 %. The Bouguer anomaly map shows a dominant gravity variation of long wavelength that is inferred to be due to a deeper basement and/or Moho that get shallower from inland towards the coast.

CHAPTER EIGHT

MODELLING

8.1 Gravity profile modelling

The gravity profiles were modelled using the GM-SYS in Geosoft Oasis Montaj. This provides an easy interface for interactively creating, modifying and plotting models to fit the observed gravity profile. This uses the algorithms described in Talwani and Heirtzler (1964), and Won and Bevis (1987). Given a starting model, the GM-SYS inversion modelling (optimization) makes use of the Marqardt inversion algorithm (described in Marqardt, 1963) to linearize and invert the calculations by reversing the procedures in order to automatically obtain the optimal fit of the geologic model to the gravity profile. Different Earth models can produce the same gravity response because gravity models are not unique. Therefore obtained models may not be geologically realistic and one needs to provide suitable constraints to get meaningful models.

8.1.1 2½ D gravity profile modelling

GM-SYS version 7.3 (18) was used to produce forward models from fourteen gravity profiles labelled (A - N) that traverses the study area. Four profiles (A - D) were originally selected to cut across the formations of the Karoo Supergroup as well as the Beattie magnetic anomaly, then another four profiles (E - H) were added in a way that they all intersect profiles A - D at almost right angles, thus increasing the coverage area. Finally, six more profiles (I - N) were added to have full or total coverage of the study area (Figure 8. 1) as well as controlling most of the features on the elevation map (Figure 8. 2) in order to avoid aliasing. Fourteen (14) profiles (A - N) were modelled and for each profile three (3) models were produced using the minimum, average and maximum density values giving a total of fifty two (52) models that were analysed to get the geologic group (sequence) thicknesses and their sensitivity to density changes.

A geologic model for a selected gravity profile was created and real-time calculation of the gravity response of a specific Earth model was performed. The modelling was constrained by the thickness, elevation and average dry density of rocks (see Section 7.8) from various formations of the Karoo Supergroup that outcrop in the study area.
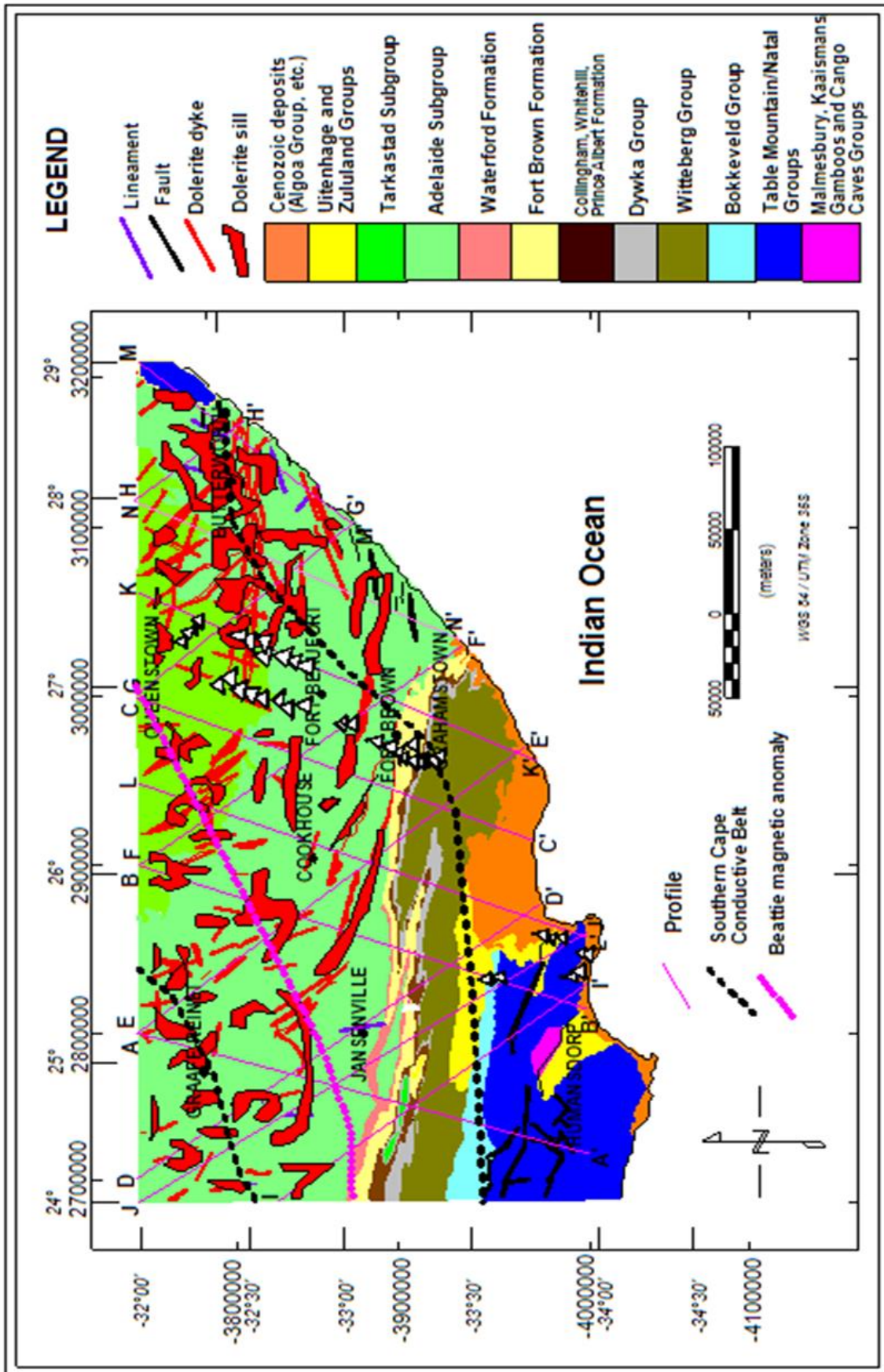
Figure 8.1 Digitized geological map of the study area showing profiles (A – N). The map also shows geologic formations, dolerite intrusions (sills and dykes), faults, part of the Beattie magnetic anomaly and the Southern Cape Conductive Belt.
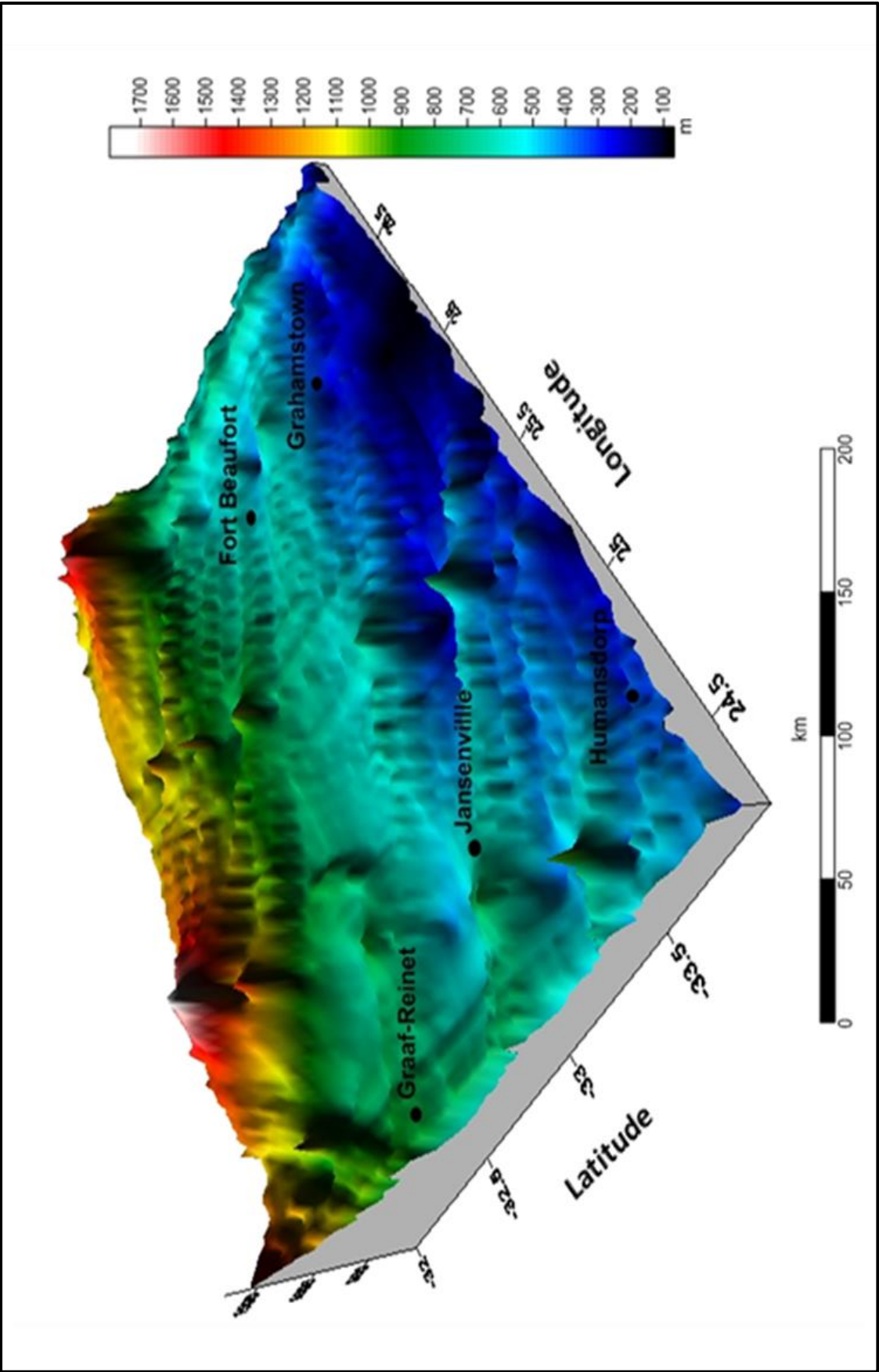
Figure 8.2 3D view of the current elevation map (Data extracted from Google Earth and displayed using Surfer-10)

The measured density values in Section 7.3 were used to get the average density value for each geologic group. Average densities of 2.520 g/cm^3, 2.565 g/cm^3, 2.662 g/cm^3, 2.675 g/cm^3 and 2.772 g/cm^3 were assigned to Beaufort Group, Ecca Group, Dwyka Group, Cape Supergroup, and Basement, respectively, based on the density information. The measured density for the Cenozoic and Uitenhage/Zululand Groups ranges from 2.365 – 2.498 g/cm^3. The average dry density for each geologic group falls within the range (2.300 – 2.800 g/cm^3) that was stated by several researchers, e.g. Maxwell (1964), Van der Voort, (2001) and Johnson *et al*. (2006) that investigated the Karoo Basin in South Africa. The dry densities of rocks in the upper mantle (below the Moho) were extracted from literatures (Hynes and Snyder, 1995; Cook *et al*., 2010; Mjelde, *et al*., 2013; Thybo and Artemieva, 2014) and the density values range from 3.140 – 3.400 g/cm^3. The highest, lowest and average dry density values that were used in the models for the geologic groups are presented in Table 8.1.

Table 8.1 Rock density values used for gravity profile modelling.

	Beaufort	Ecca	Dwyka	Cape	Dolerite Intrusions	Basement	Below the Moho (Mantle)
Highest Density (g/cm^3)	2.765	2.781	2.678	2.719	2.829	2.820	3.400
Lowest Density (g/cm^3)	2.274	2.349	2.585	2.630	2.710	2.723	3.140
Average Density (g/cm^3)	2.520	2.565	2.662	2.675	2.766	2.772	3.270

The geological map of the study area was used to measure the actual profile lengths and positions along the profiles to each geologic group outcrop within the study area (Figure 8.1) and at infinity (outside the study area but along the profile). This was done in order to set constraints to the model such that the model will perfectly fit or agree with what is obtained in the real-world. A starting GM-SYS model was created from a map profile (e.g. A - A') by importing the gravity grid and elevation grid (Figure 8.2). The estimated thickness (length) and position of each group from the geological map were used to develop the starting model (Figure 8.3). Each starting model was extended to infinity at both ends (i.e., a long distance say ± 500 km in this case) to eliminate edge-effects. A constant or DC shift was assigned and subtracted from the calculated gravity data in order for the calculated gravity data (black line) to match the observed data (black dots). This was done because the calculated value is an absolute gravity calculation of the model extending to 500 km in the ±X directions.

Geologic boundaries that cross the profile were located in the starting models using the control points (red points) with respect to the measurements. These control points remain fixed whilst any other points can be moved or adjusted. The model was prepared for inversion by assigning names, densities, dimensions (length of blocks in +Y and −Y strike direction) to the blocks representing the various rock units. After preparing the model for inversion, the actual inversion process was initiated such that the calculated curves are updated in the anomaly panes, leaving dotted lines as the previous calculated curve which automatically changes the original model when accepted. The inversion process was repeated until the final model had an acceptable minimum root mean square (RMS) error (red line) between the calculated and observed gravity. The final model was inspected to see if it was geologically reasonable. The simple gravity models are presented in Figure 8.4 - 8.17.

Note: The Mohorovicic discontinuity (also known as Moho) is the boundary between the crust and the mantle in the Earth. Moho depth is a depth where seismic waves change velocity and marks a change in chemical composition (still open to debate; Sixsmith *et al*., 2004). Several authors like James *et al*. (2003), Tedla *et al*. (2011), Stankiewicz and de Wit (2013) have indicated a Moho depth in the range of 44 - 50 km, 40 - 50 km, and 40 - 45 km, respectively. In order to cover the depth envisaged for the Moho by the authors, the depth to the Moho was originally set at 35 km (see Figure 8.3) and left to vary during the modelling process, such that the model will establish the best fit depth for the Moho. The thickness of the dolerite intrusions was estimated from literatures (i.e. Chevallier and Woodford, 1999; Chevallier et al., 2001) and they were calculated from the Soekor well (SP1/69, between East London and Bisho). The thickness of the dolerite intrusions were used in the models. The modelled dolerite sills and dykes were originally set in horizontal and vertical positions, respectively and allow varying or changing during the modelling process in order to have the best fit model (Figure 8.3). The difference in density between the basement rocks and the dolerite intrusions is very small, such that for modelling purpose, intrusions in the basement were taken to be part of the basement. Thus, although the intrusions appear to terminate at the top of the basement, they do extend into the basement. In order to test the sensitivity of the models to density changes, the highest and lowest density values in Table 8.1 were also used to get alternative models for all the profiles. Since a total of 52 models were obtained, only those of the average density values are presented in this chapter. The alternative models were used to check the sensitivity of the gravity models, which is presented in Section 8.2.5.
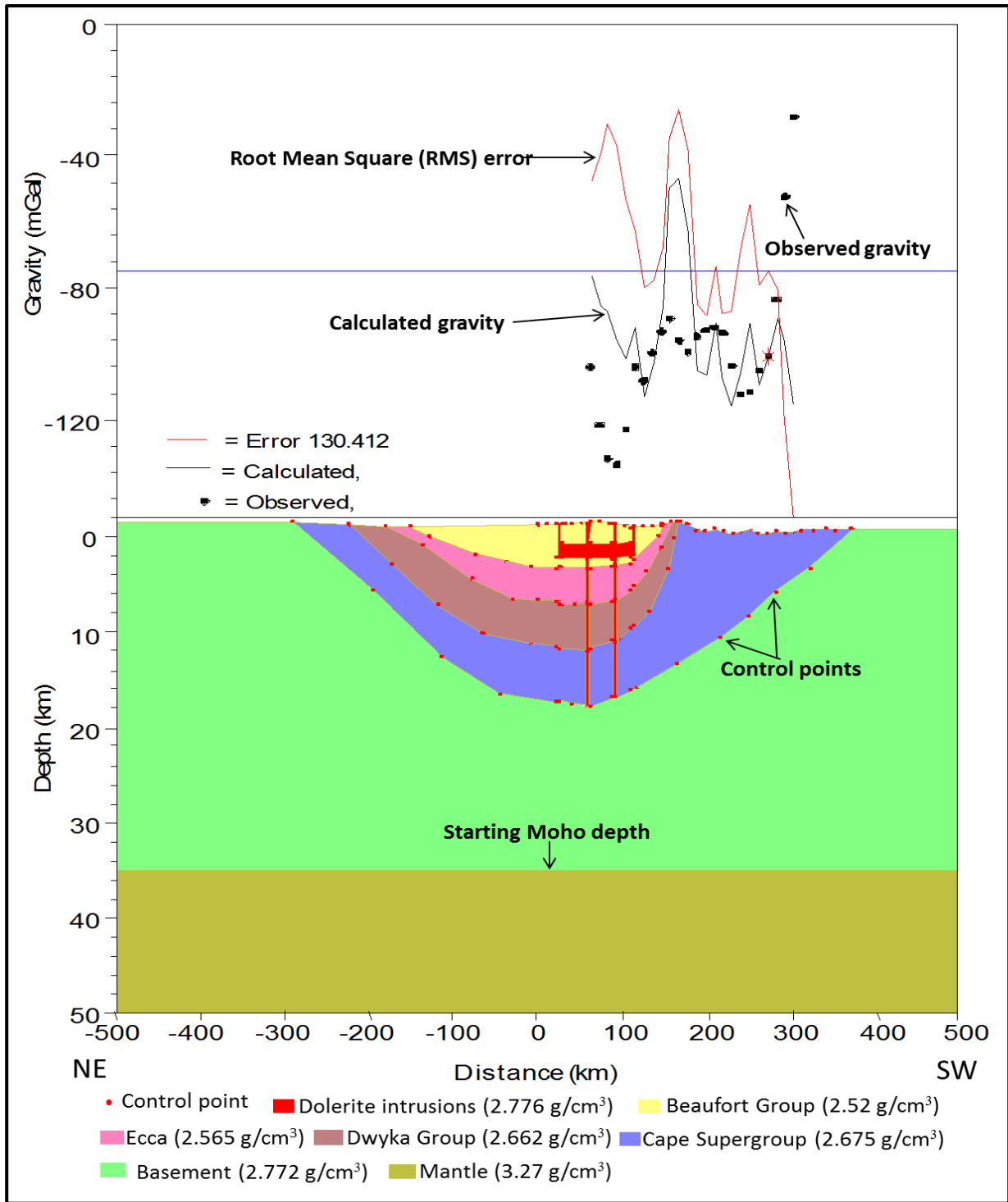
Figure 8.3 Starting model for profile A - A'. Vertical exaggeration (VE) = 5.75, Initial root mean square (RMS) error = 130.412 Note: When the black line/curve (calculated gravity) matches with the black dots (observed gravity), it indicates a perfect fit with minimum error. The modelled dolerite sills and dykes (presented in Figure 8.4 – 8.17) were originally set in horizontal and vertical positions, respectively and allowed to vary or change during the modelling process in order to have the best fit model.
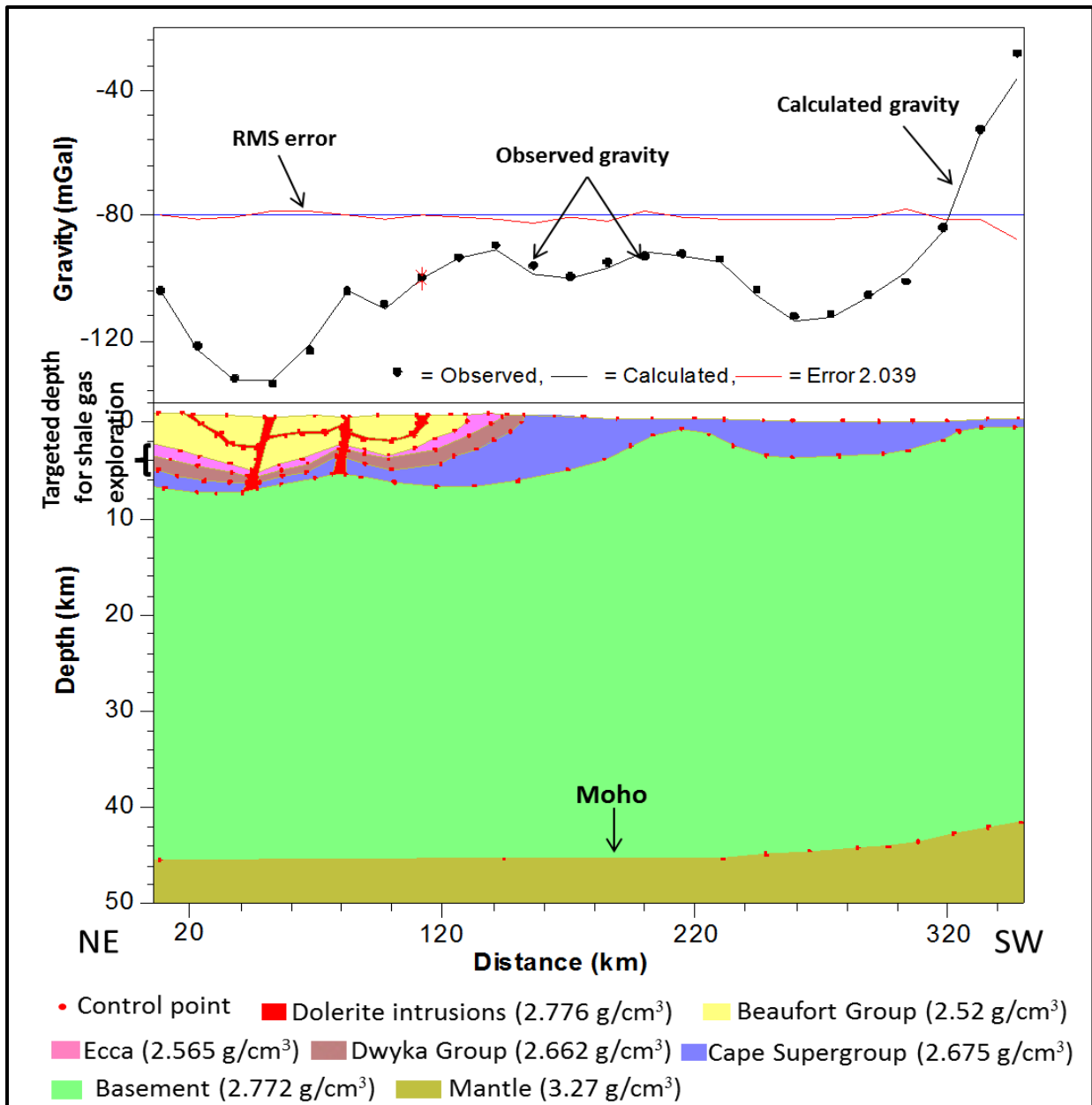
Figure 8.4 Gravity modelling of profile A - A'. Vertical exaggeration (VE) = 2.12, Initial and final RMS errors are 95.481 and 2.039, respectively.

Profile A - A' (see Figure 8.1) starts in the Karoo Basin and ends at the coast. The model of profile A - A' is shown in Figure 8.4. Along this profile, the minimum gravity value is -112.9 mGal inside the Karoo Basin and the maximum gravity value of about - 22.5 mGal at the coast. The thickness of the Beaufort, Ecca and Dwyka Groups varies along this profile due to deformation as shown in the model by undulating surfaces. The Karoo (Dwyka, Ecca and Beaufort Groups) and Cape Supergroups (Witteberg, Bokkeveld and Table Mountain Group) have been intruded by dolerites (about 180 Ma) as shown in Figure 8.4. The dolerite dykes probably served as feeders to the sills that are seen in the Beaufort Group.
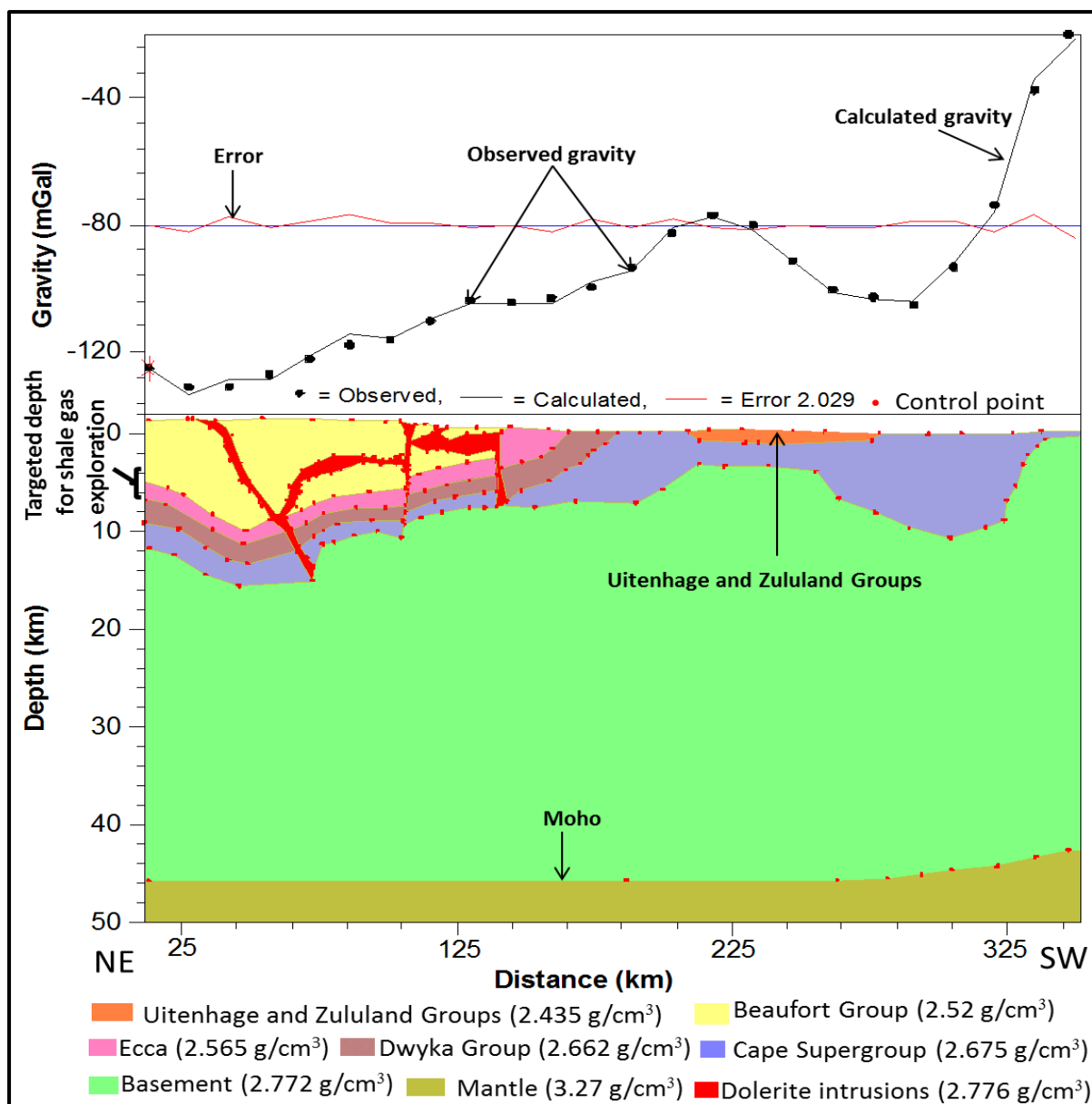
Figure 8.5 Gravity modelling of profile B – B'. VE = 1.98, Initial and final RMS errors are 61.705 and 2.029, respectively. Note: When the black curve (calculated gravity) matches with the black dots (observed gravity), it indicates a perfect fit with minimum error.

Figure 8.5 shows the gravity modelling of profile B - B' which starts in the Karoo Basin and ends at the coast. The minimum gravity value along this profile is -102.6 mGal whilst the maximum value is up to -22.6 mGal. The layers in the model have been intruded by dolerites (about 180 Ma) and show undulations which are inferred to be due to deformation. Evidence of faulting (lateral displacement) is also seen in the model between distances of about 40 km to 170 km. Along this profile, the Uitenhage and Zululand Groups are seen between the distance of about 200 km to 270 km and their thicknesses also vary along the profile due to deformation.

147
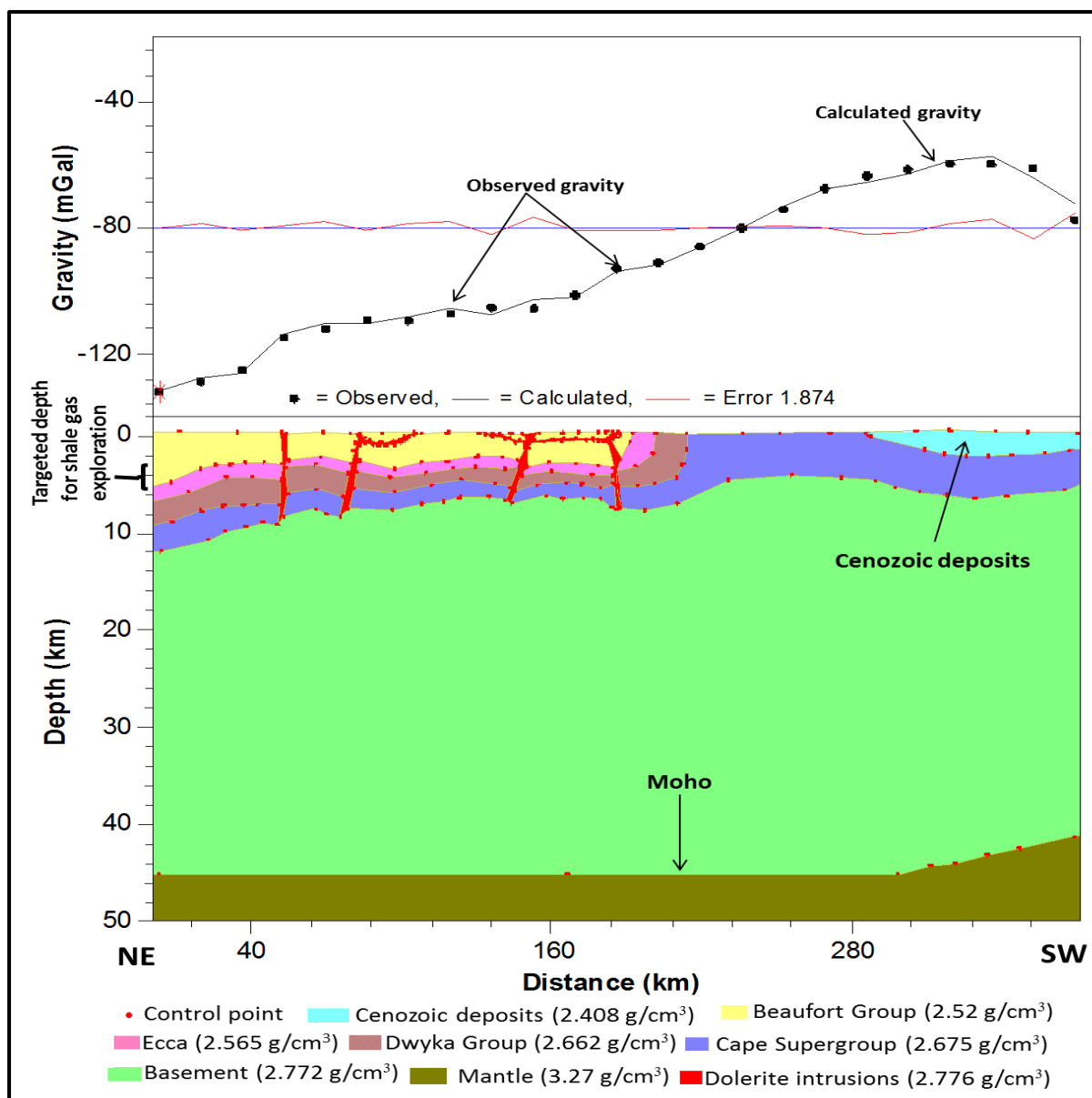
Figure 8.6 Gravity modelling of profile C - C'. VE = 1.82, Initial and final RMS errors are 82.623 and 1.874, respectively. Note: When the black curve (calculated gravity) matches with the black dots (observed gravity), it indicates a perfect fit with minimum error.

Figure 8.6 shows the gravity modelling of profile C - C' that has increasing gravity values from the northeast to southwest direction of the map. The gravity values increases from about -107.8 mGal in the Karoo Basin to around -21.4 mGal at the coast. The thickness of the layers also varies along this profile due to deformation. The Karoo (Dwyka, Ecca and Beaufort Groups) and Cape Supergroup (Witteberg, Bokkeveld and Table Mountain Group) have been intruded by dolerites in the form of dykes and sills with associated faulting as depicted in Figure 8.6. The Cenozoic deposits (outcropping on the surface) are encountered along this profile between the distances of about 280 km to 360 km as shown in Figure 8.6.

148

Figure 8.7 Gravity modelling of profile D - D'. VE = 1.36, Initial and final RMS errors are 110.014 and 1.155, respectively.

Figure 8.7 shows the gravity modelling of profile D - D' that passes through an area of relatively low gravity values in the northwestern – southeastern part of the map. The layers (Dwyka, Ecca and Beaufort Groups, as well as the Cape Supergroup) in the model also show undulations as result of deformation that are evidenced in the model. Also, the geologic sequence has been intruded by dolerites in the form of dykes and sills. The dykes probably served as feeders to the sills that outcrop on the surface. The Cenozoic deposits as well as the Uitenhage and Zululand Groups were seen along the profile (between the distance of 190 km to about 240 km) and their thicknesses also varies across the profile due to deformation.

Figure 8.8 Gravity modelling of profile E - E'. VE = 1.53, Initial and final RMS errors are 65.381 and 1.201 respectively.

Figure 8.8 shows the gravity modelling results of profile E - E' that has increasing of gravity values from the northwestern – southeastern direction of the map. The thickness of the Beaufort, Ecca and Dwyka and Cape Supergroup varies along this profile due to deformation as shown in the model. The dolerite intrusions that outcrop on the surface are seen in the model extending to depth cutting through the Cape, Dwyka, Ecca, and Beaufort sequence in the form of dykes and sills (Figure 8.8). Lateral displacement (faulting) is also seen cutting through the Cape, Dwyka and Ecca Groups between distances of about 20 - 100 km.
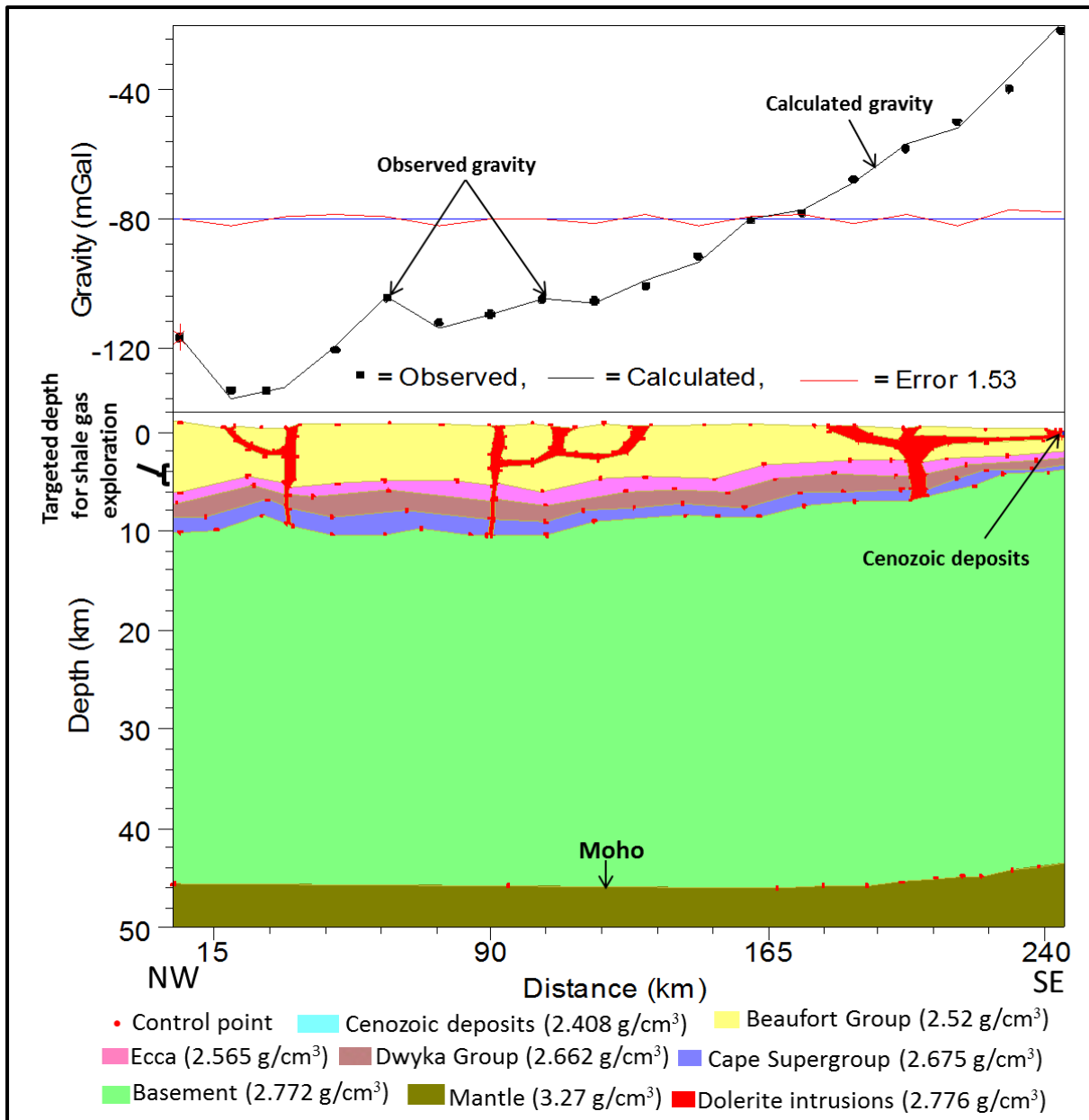
Figure 8.9 Gravity modelling of profile F - F'. VE = 1.89, Initial and final RMS errors are 48.268 and 1.53, respectively. The modelled dolerite sills and dykes were originally set in horizontal and vertical positions, respectively and allowed to vary or change during the modelling process in order to have the best fit model.

The model of profile F - F' is shown in Figure 8.9. The minimum gravity value along this profile is -110.3 mGal whilst the maximum gravity value is -22.1 mGal. Generally, the thickness of the Karoo (Beaufort, Ecca and Dwyka Groups) and Cape (Witteberg, Bokkeveld and Table Mountain Groups) Supergroups varies along this profile as a result of deformation as depicted in the model by undulating surfaces. The geologic sequence has been intruded by dolerite sills and dykes (about 180 Ma) extending to depth as shown in Figure 8.9.
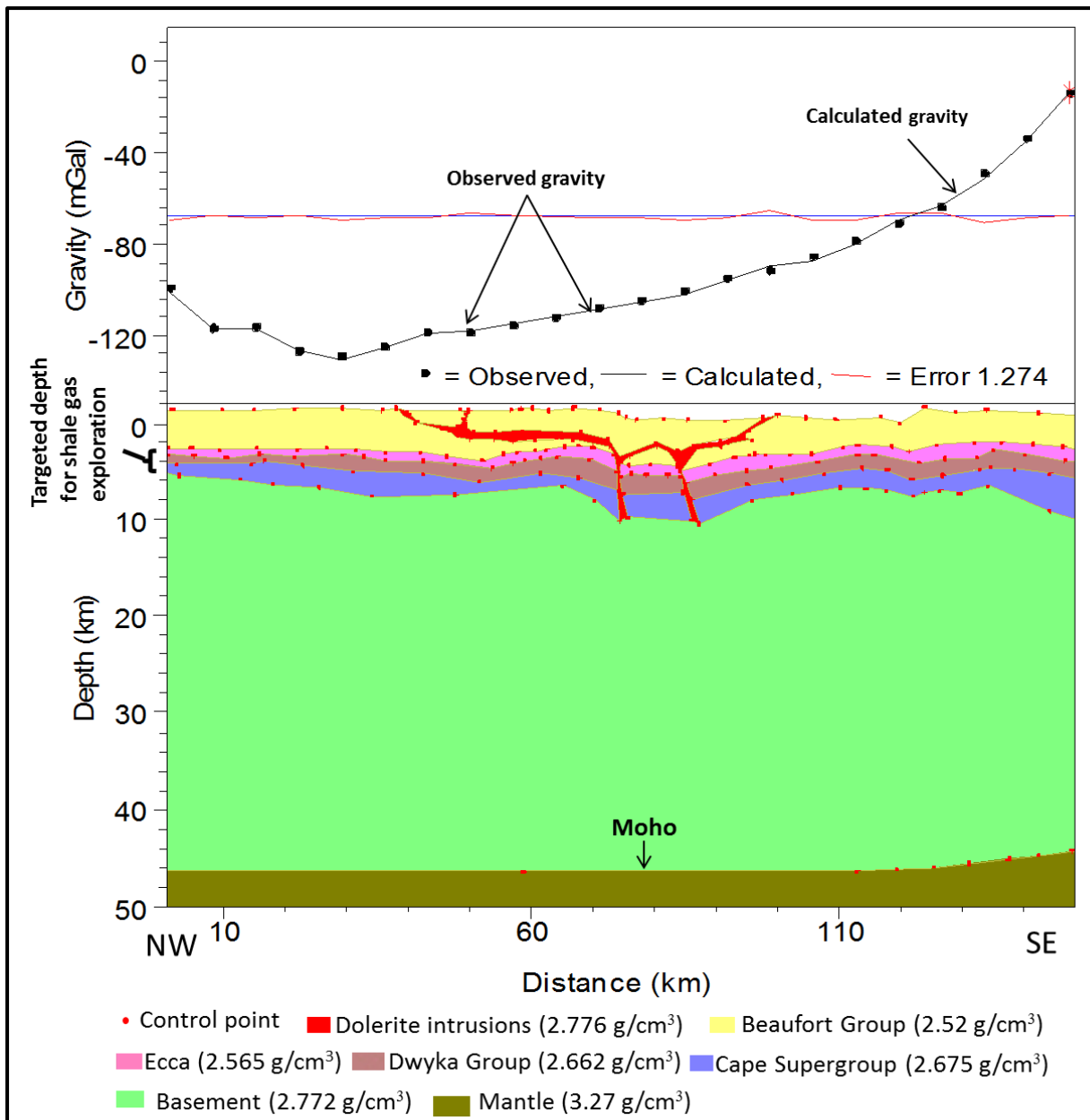
Figure 8.10 Gravity modelling of profile G – G'. VE = 1.09, Initial and final RMS errors are 61.843 and 1.274, respectively.

The model of profile G - G' is shown in Figure 8.10. Along this profile, the thickness of the layers varies due to deformation as shown in the model. At the start of the profile, the layers are relatively flat or horizontal (distance of about 1 km – 44 km) and show undulating surfaces from a distance of about 45 km until the end of the profile. The Karoo (Dwyka, Ecca and Beaufort Groups) and Cape Supergroups (Witteberg, Bokkeveld and Table Mountain Group) have been intruded by dolerites (about 180 Ma) as shown in Figure 8.10. The dolerite dykes probably served as feeders to the sills that are seen in the Beaufort Group as well as outcropping on the surface.
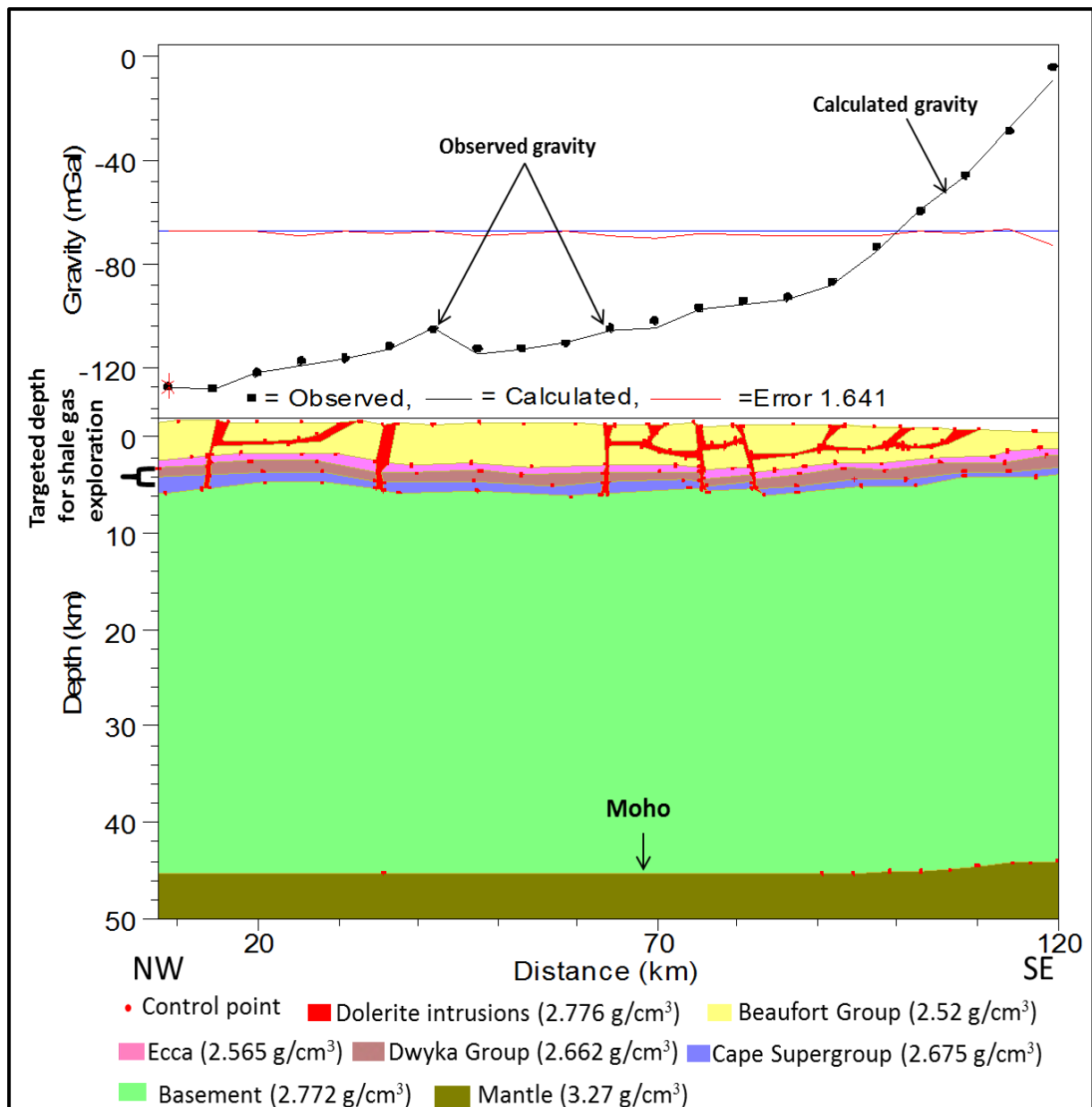
Figure 8.11 Gravity modelling of profile H - H'. VE = 2.19, Initial and final RMS errors are 61.675 and 1.641, respectively. Note: The modelled dolerite sills and dykes were originally set in horizontal and vertical positions, respectively and allowed to vary or change during the modelling process in order to have the best fit model.

Figure 8.11 shows the gravity modelling of profile H-H' that has increasing gravity values from the northwest to southeast direction of the map. The thickness of the layers also varies along this profile due to deformation. The dolerite intrusions that outcrop on the surface are seen in the model extending to depth cutting through the Beaufort, Ecca, Dwyka and Cape Supergroup in the form of dykes and sills with associated faulting as depicted in Figure 8.11.
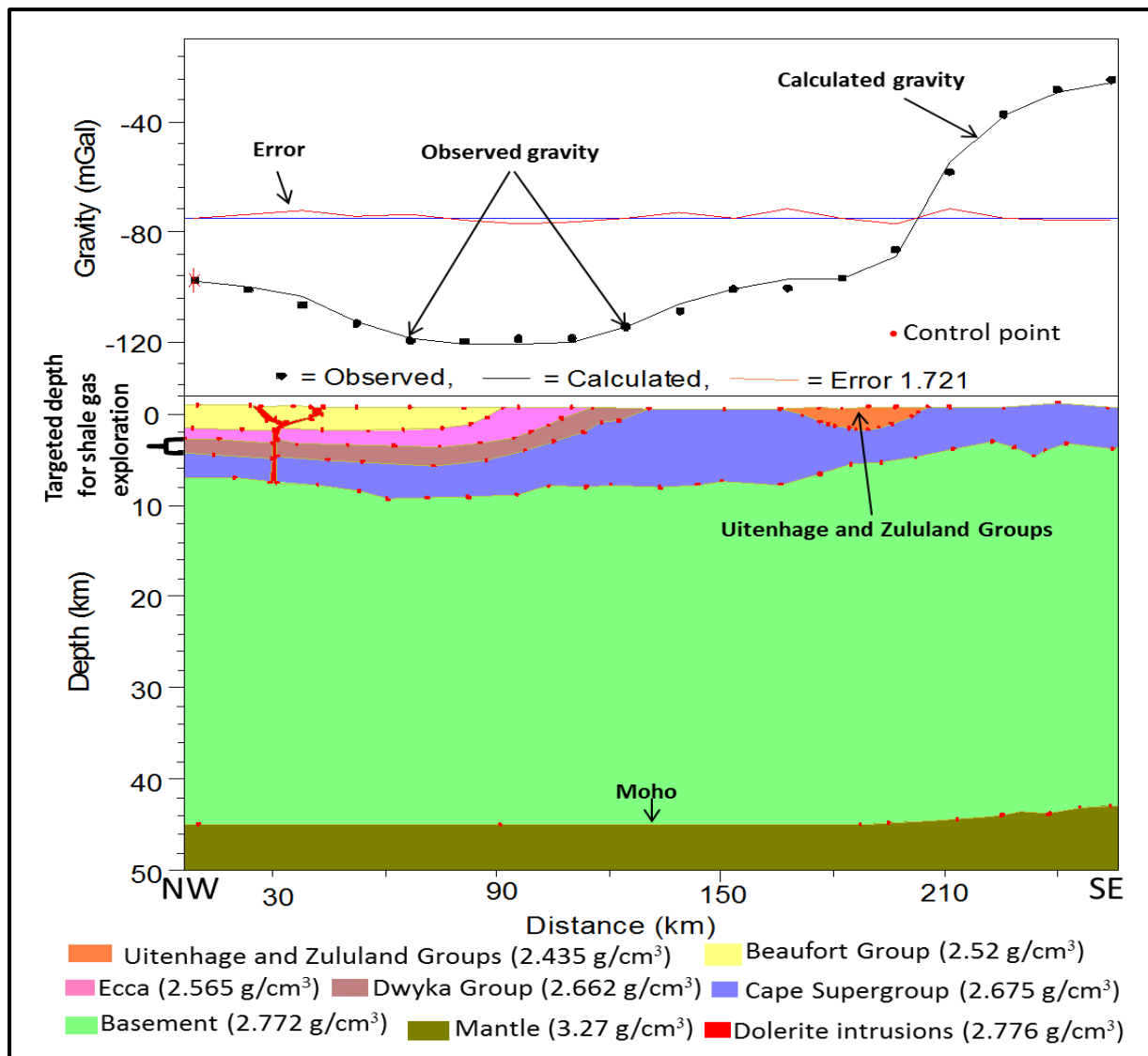
Figure 8.12 Gravity modelling of profile I – I'. VE = 0.80, Initial and final RMS errors are 64.389 and 1.721, respectively.

Gravity modelling results of profile I - I' are shown in Figure 8.12. The profile passes through an area of relatively low gravity values in the northwestern – southeastern part of the map. The minimum gravity value along this profile is about -122.5 mGal whilst the maximum value is -16.6 mGal. The thickness of the Beaufort, Ecca and Dwyka Groups varies along this profile due to deformation. The Karoo (Dwyka, Ecca and Beaufort Groups) and Cape Supergroup (Witteberg, Bokkeveld and Table Mountain Group) have been intruded by a dolerite dyke (about 180 Ma) as shown in Figure 8.12 which probably served as feeder to the sill that is seen in the Beaufort Group as well as outcropping on the surface. The Uitenhage and Zululand Groups (outcropping on the surface) are encountered along this profile between the distances of about 160 km to 200 km as depicted in Figure 8.12.
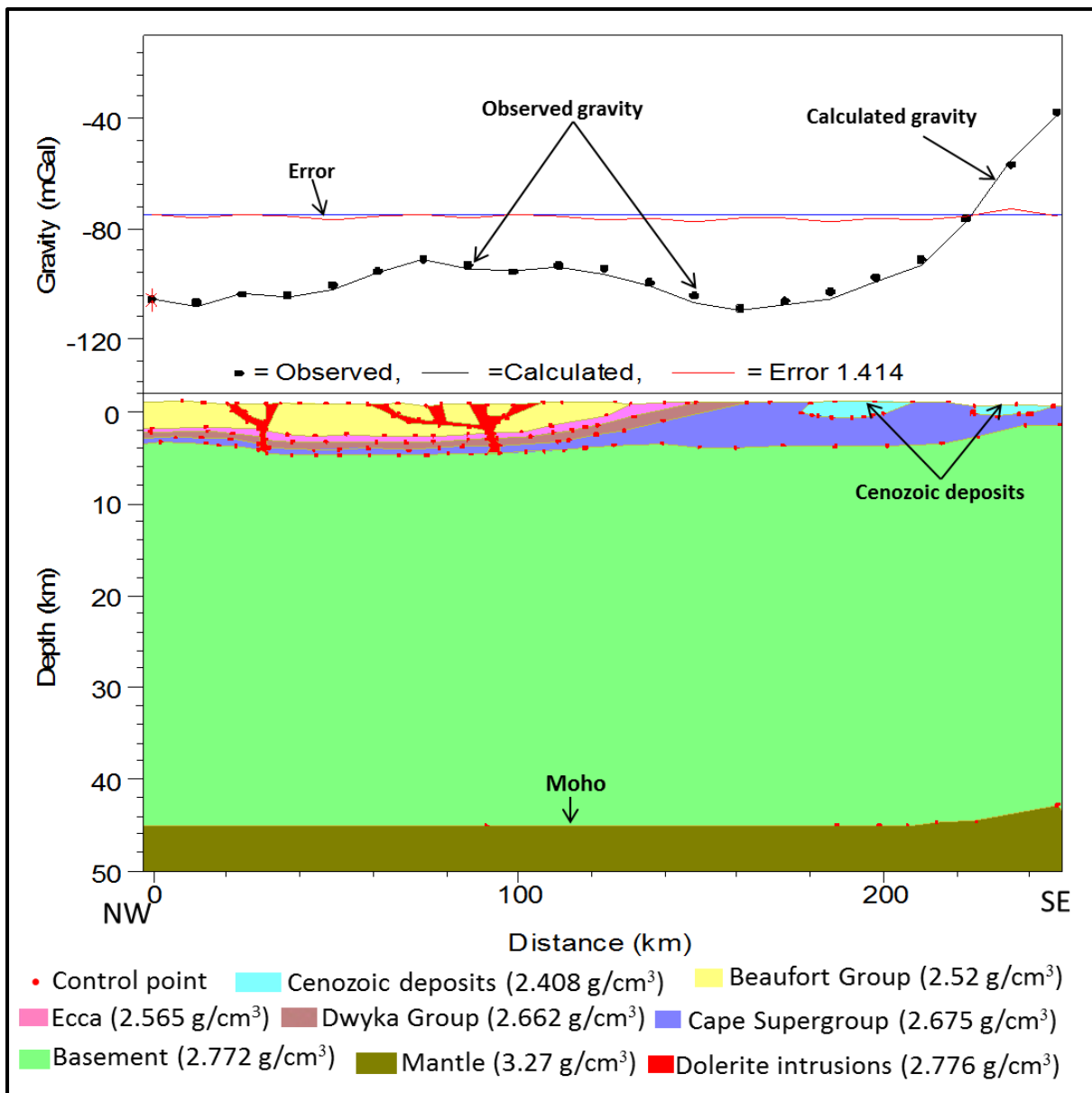
Figure 8.13 Gravity modelling of profile J - J'. VE = 0.93, Initial and final RMS errors are 48.483 and 1.414, respectively. Note: When the black curve (calculated gravity) matches with the black dots (observed gravity), it indicates a perfect fit with minimum error.

Figure 8.13 shows the gravity modelling of profile J - J' that starts in the Karoo Basin and ends at the coast. The thickness of the Beaufort, Ecca, Dwyka and Cape Supergroup varies along this profile due to deformation as shown in the model. The dolerite intrusions that outcrop on the surface are seen in the model extending to depth cutting through the Beaufort, Ecca, Dwyka and Cape Supergroup in the form of dykes and sills (Figure 8.13). The Uitenhage and Zululand Groups (outcropping on the surface) are encountered along this profile as shown in Figure 8.13.
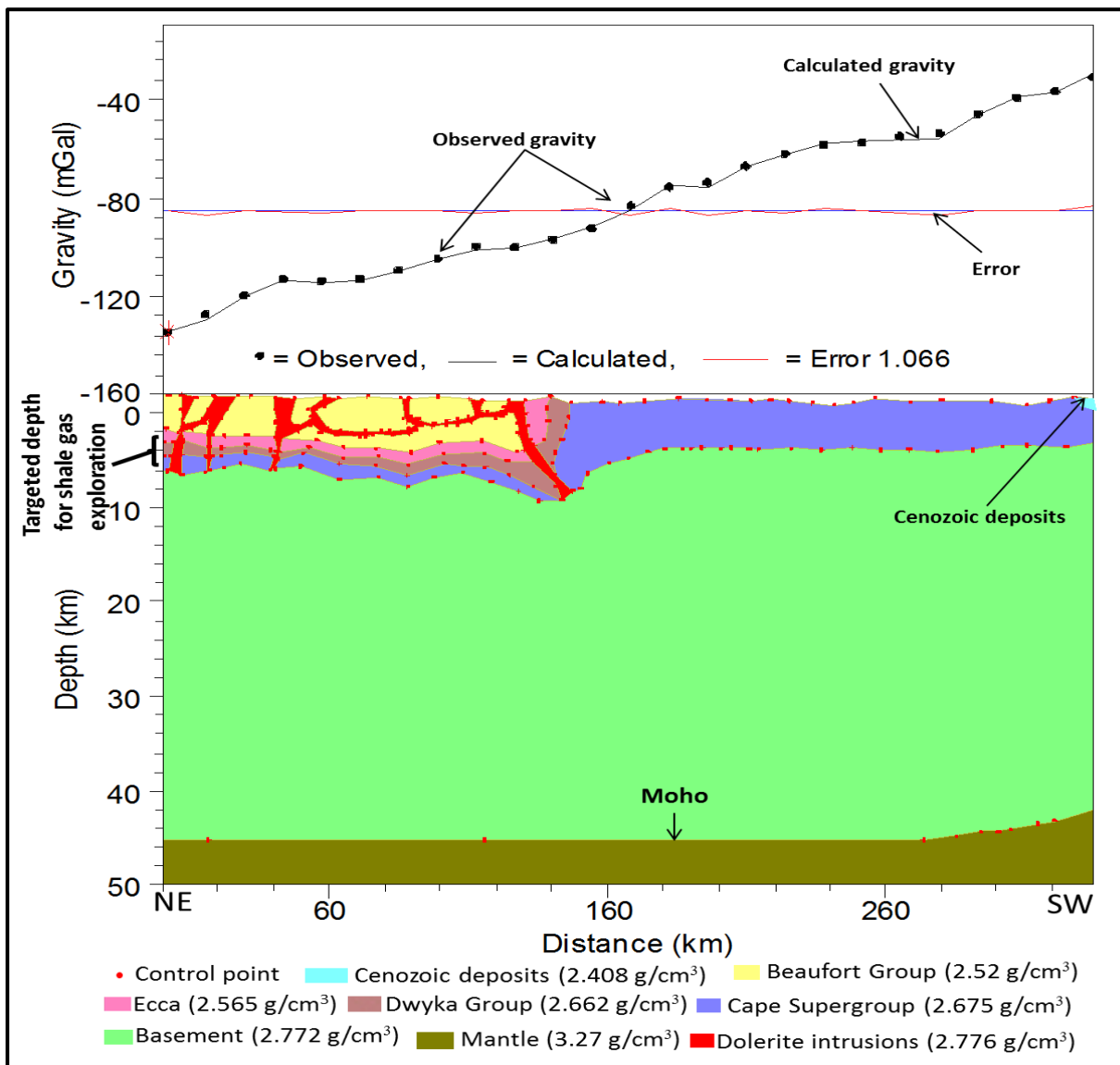
Figure 8.14 Gravity modelling of profile K - K'. VE = 1.97, Initial and final RMS errors are 58.466 and 1.066, respectively. Note: The modelled dolerite sills and dykes were originally set in horizontal and vertical positions, respectively and allowed to vary or change during the modelling process in order to have the best fit model.

Figure 8.14 shows the gravity modelling of profile K - K'. This has increasing gravity values from the northeastern – southwestern direction of the map. The layers in the model have been intruded by dolerites (about 180 Ma) and show undulations which are inferred to due to deformation, evidence of associated faults (lateral displacement) is also seen in the model between the distance of about 130 - 170 km. The dolerite intrusions that outcrop on the surface are seen in the model extending to depth cutting through the Beaufort, Ecca, Dwyka and Cape Supergroup in the form of dykes and sills. These dykes served as feeders to the sills that are outcropping on the surface (Figure 8.14).
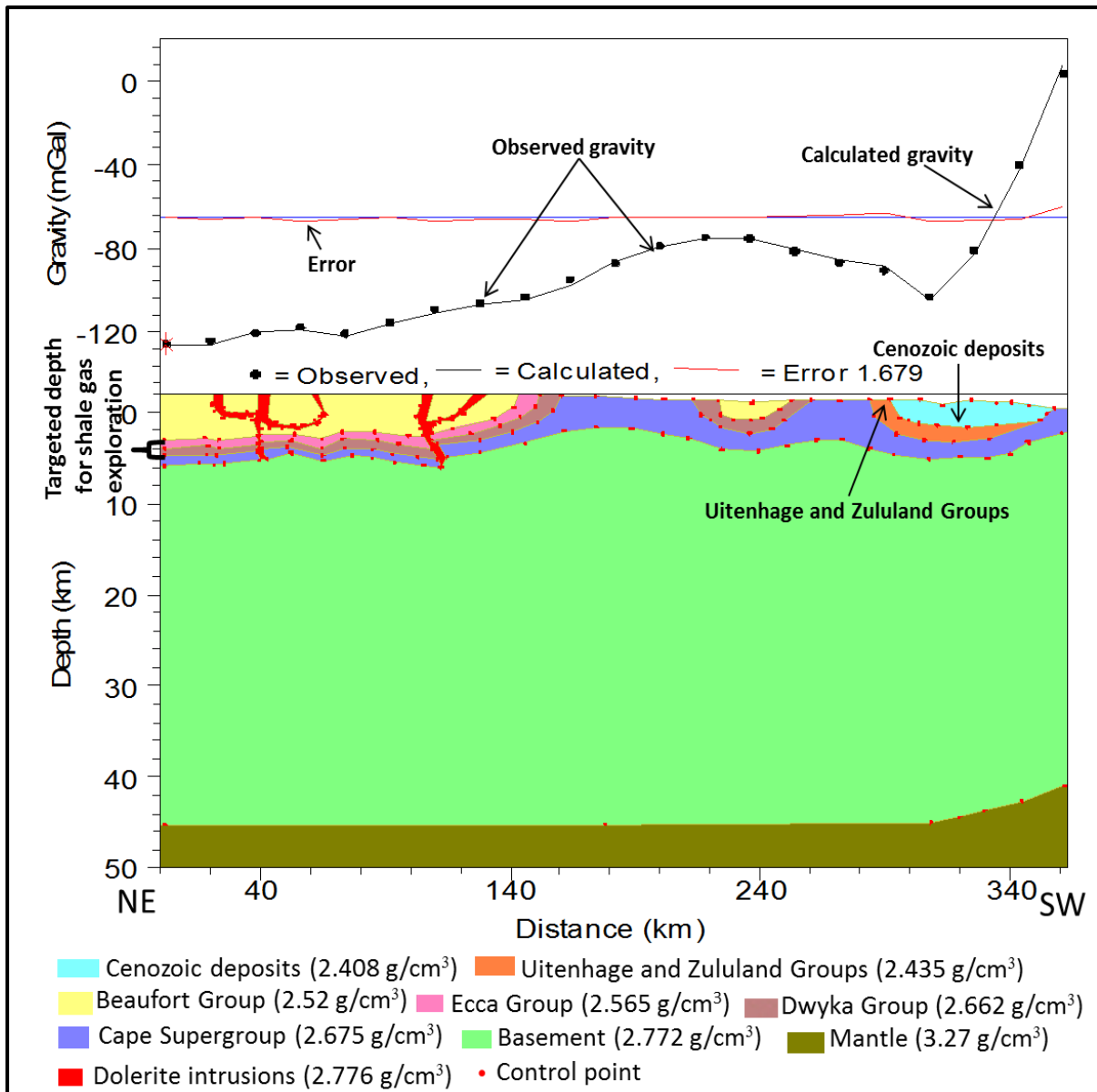
Figure 8.15 Gravity modelling of profile L – L'. VE = 2.27, Initial and final RMS errors are 148.036 and 1.679, respectively.

Figure 8.15 shows the gravity modelling of profile L - L'. The minimum gravity value along this profile is about -108.4 mGal inside the basin, whilst the maximum value is about 7.9 mGal at the coast. The geologic sequence in the model also shows undulations as a result of deformation. The sequence has been intruded by dolerites in the form of dykes and sills and they extend to depth. The observed faults are associated with the dolerite intrusion. The Uitenhage and Zululand Groups (outcropping on the surface) are seen along this profile between the distances of about 285 km to 350 km as depicted in Figure 8.15.

157
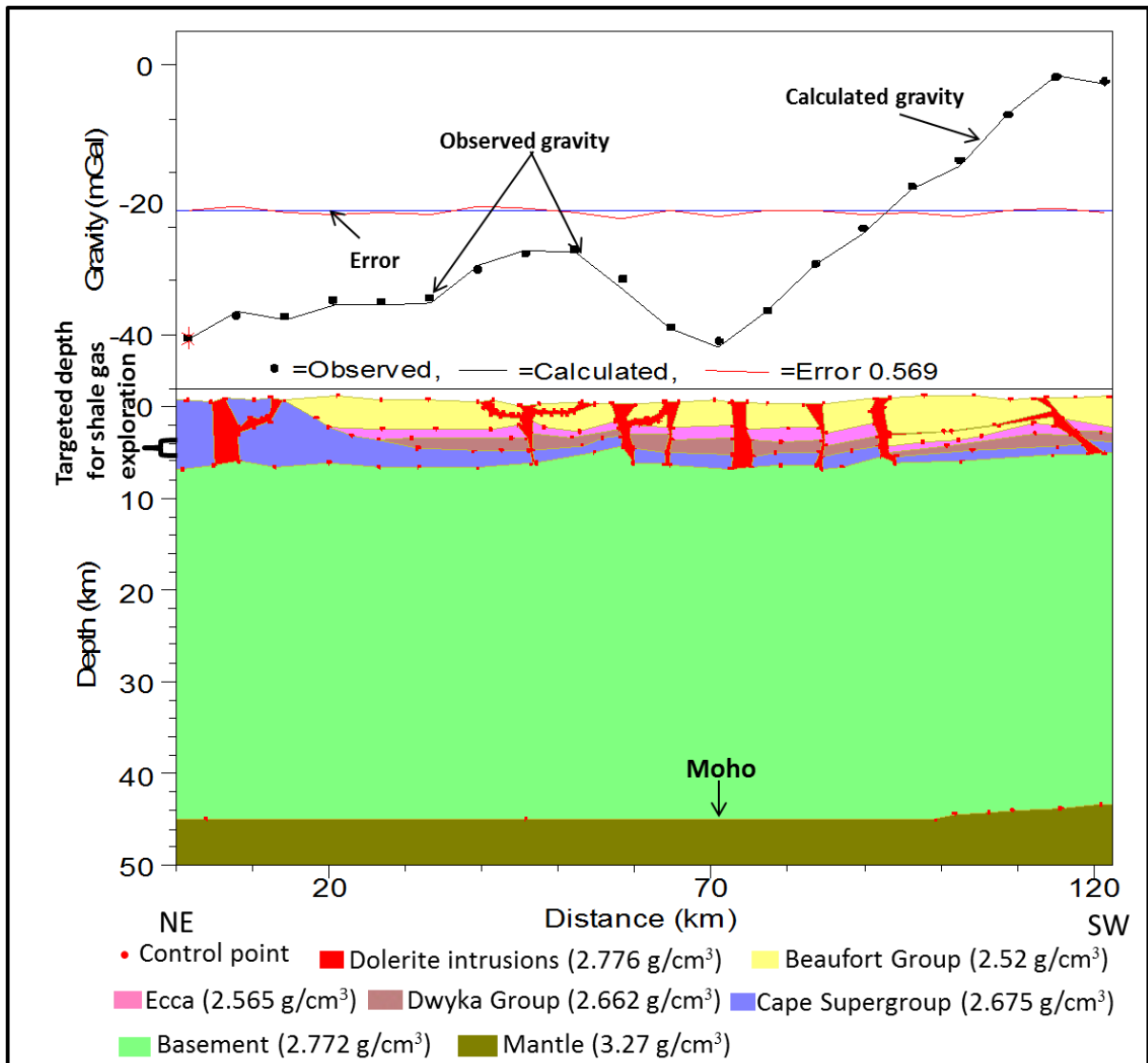
Figure 8.16 Gravity modelling of profile M – M'. Vertical exaggeration = 0.9, Initial and final RMS errors are 74.381 and 0.569, respectively. Note: When the black curve (calculated gravity) joins/matches with the black dots (observed gravity), it indicates a perfect fit with minimum error.

The model of profile M - M' is shown in Figure 8.16. The Cape Supergroup outcrop at the start of the profile (a distance of 1-10 km) and have been intruded by dolerites (about 180 Ma). The thickness of the Beaufort, Ecca and Dwyka Groups varies along this profile due to deformation as shown in the model. Generally, the Karoo (Dwyka, Ecca and Beaufort Groups) and Cape Supergroup (Witteberg, Bokkeveld and Table Mountain Groups) have been intruded by dolerite sills and dykes with associated faults (lateral displacement of the layers) as shown in Figure 8.16.
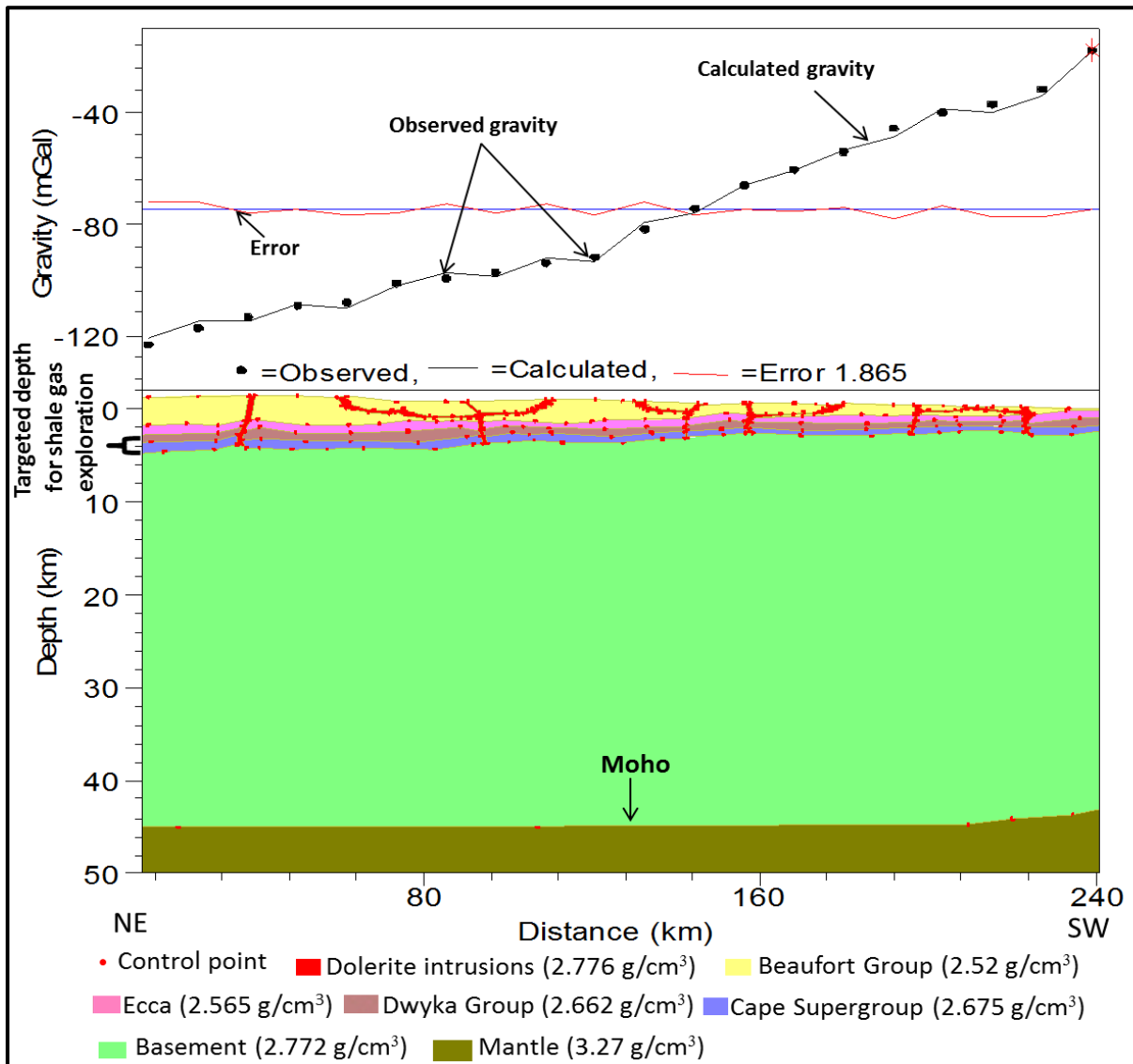
Figure 8.17 Gravity modelling of profile N – N'. Vertical exaggeration = 3.11, Initial and final RMS errors are 84.381 and 1.865, respectively. Note: The modelled dolerite sills and dykes were originally set in horizontal and vertical positions, respectively and allowed to vary or change during the modelling process in order to have the best fit model. When the black curve (calculated gravity) joins/matches with the black dots (observed gravity), it indicates a perfect fit with minimum error.

Figure 8.17 shows the gravity modelling of profile N - N' that has increasing gravity values from the northeastern – southwestern direction of the map. The layers in the model are approximately horizontal, although they show small undulations and are intruded by dolerites (sills and dykes). The dolerite intrusions cut through the Cape and Karoo sequence as well as outcrop on the surface. Evidence of associated faulting (lateral displacement) is also seen in the model.

In the study area, the Moho is generally horizontal at a depth of about 45 km inland and rises to about 42 km at the coastal area with a slope of about 3°. The depth of the Moho shallows towards the ocean and this usually results in an increase in the gravity values which is of long wavelength. Thus the depth to the Moho in all the gravity profile models falls within 40 - 45 km which agrees with the depth envisaged by Tedla *et al.* (2011) as well as Stankiewicz and de Wit (2013) that the Moho depth is at 40 – 45 km beneath the inland sections.

8.2 Elevation and thickness estimate from GM-SYS models

The gravity modelling results from GM-SYS were exported in real-world coordinates as a Geosoft xyz file for each surface (horizon) for all the profiles in order to estimate the vertical thickness of each geologic group. The first surface (Beaufort top) for all the profiles was exported from the fourteen (14) models and imported into a single database using the "merge append" such that all the xyz files for the Beaufort top surface is displayed. The data were gridded at a grid cell size of 10 km. The same procedure was carried out for the remaining four surfaces (Beaufort bottom, Ecca bottom, Dwyka bottom and Cape bottom, respectively) for all the profiles. The "grid math" was used to calculate the vertical thickness of each group e.g. Current Beaufort isochore thickness = Beaufort top grid – Beaufort bottom grid. The output was displayed as another grid. The following were deduced from the gravity model and used to estimate the thickness of each group/supergroup.

- Beaufort bottom grid = Ecca top grid
- Ecca bottom grid = Dwyka top grid
- Dwyka bottom grid = Cape top grid

Therefore:

- Cape top grid – Cape bottom grid = Current Cape isochore thickness (Figure 8.19)
- Dwyka top grid – Dwyka bottom grid = Current Dwyka isochore thickness (Figure 8.21)
- Ecca top grid – Ecca bottom grid = Current Ecca isochore thickness (Figure 8.23)
- Beaufort top grid – Beaufort bottom grid = Current Beaufort isochore thickness (Figure 8.25)

The current elevations are the remaining elevation after subsidence, deformation, and physical processes acted on the geologic sequence during and after deposition. This current elevation of all the groups/supergroups were recovered by extracting each surface (horizon) for all the profiles in real world coordinates. The single excel data sheet for Beaufort top along all the profiles was reduced relative to the sea level. Most of the profiles end on the coastline with average minimum elevation value of 8.31 m. The lowest value (averaging 8.31 m) which is equal to zero sea level are at B', C', D', E', F', G', H', I', K', M' and N', respectively was subtracted from each depth accordingly. Coordinates were assigned and the data were gridded using the same grid parameter that was used for all the maps. The same procedure was applied to the other surfaces (Ecca top, Dwyka top and Cape top, respectively) for all the profiles and the lowest point (8.31 m) was also removed in order to reduce each surface relative to the sea level. The extracted data in excel format was imported in Geosoft and displayed as shown in Figures 8.18 - 8.25.

8.2.1 Cape Supergroup elevation/depth below sea level and isochore thickness map
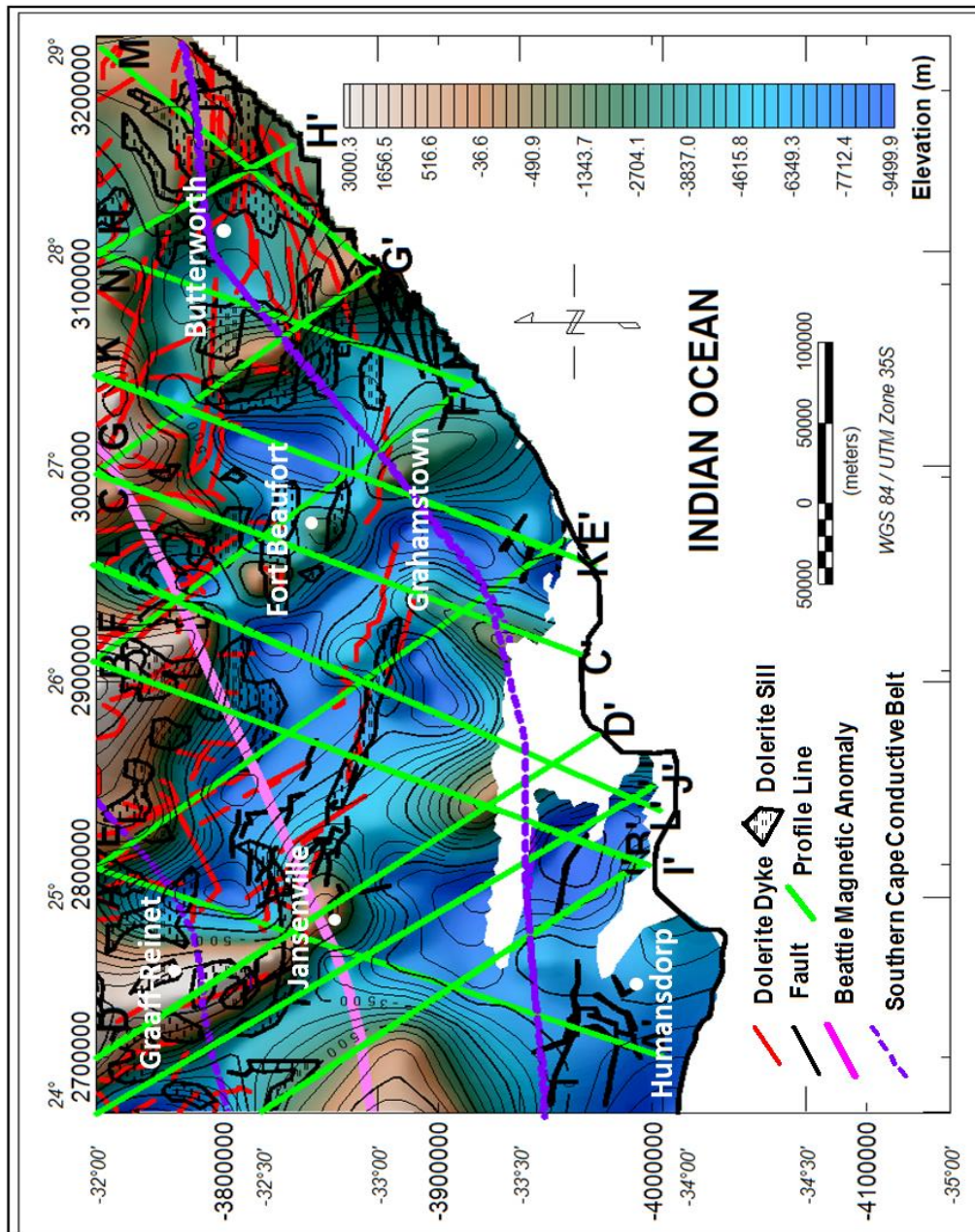
Figure 8.18 Superimposed elevation map of the Cape Supergroup as deduced from gravity profile models using GM-SYS. The map also shows dolerite intrusions (sills and dykes), faults, part of the Beattie magnetic anomaly and the Southern Cape Conductive Belt.

Figure 8.18 shows the current elevation map of the Cape Supergroup relative to the sea level (the negative sign in the elevation values denotes elevation below the sea level). The dark – light brown coloured areas on the map with high elevation (greater than -490 m) are structural or basement high areas with a peak elevation of up to 3000 m above the sea level. The areas with the blue colour (less than -7000 m) are the basement low areas with a minimum elevation or depth of about 9500 m below the sea level.
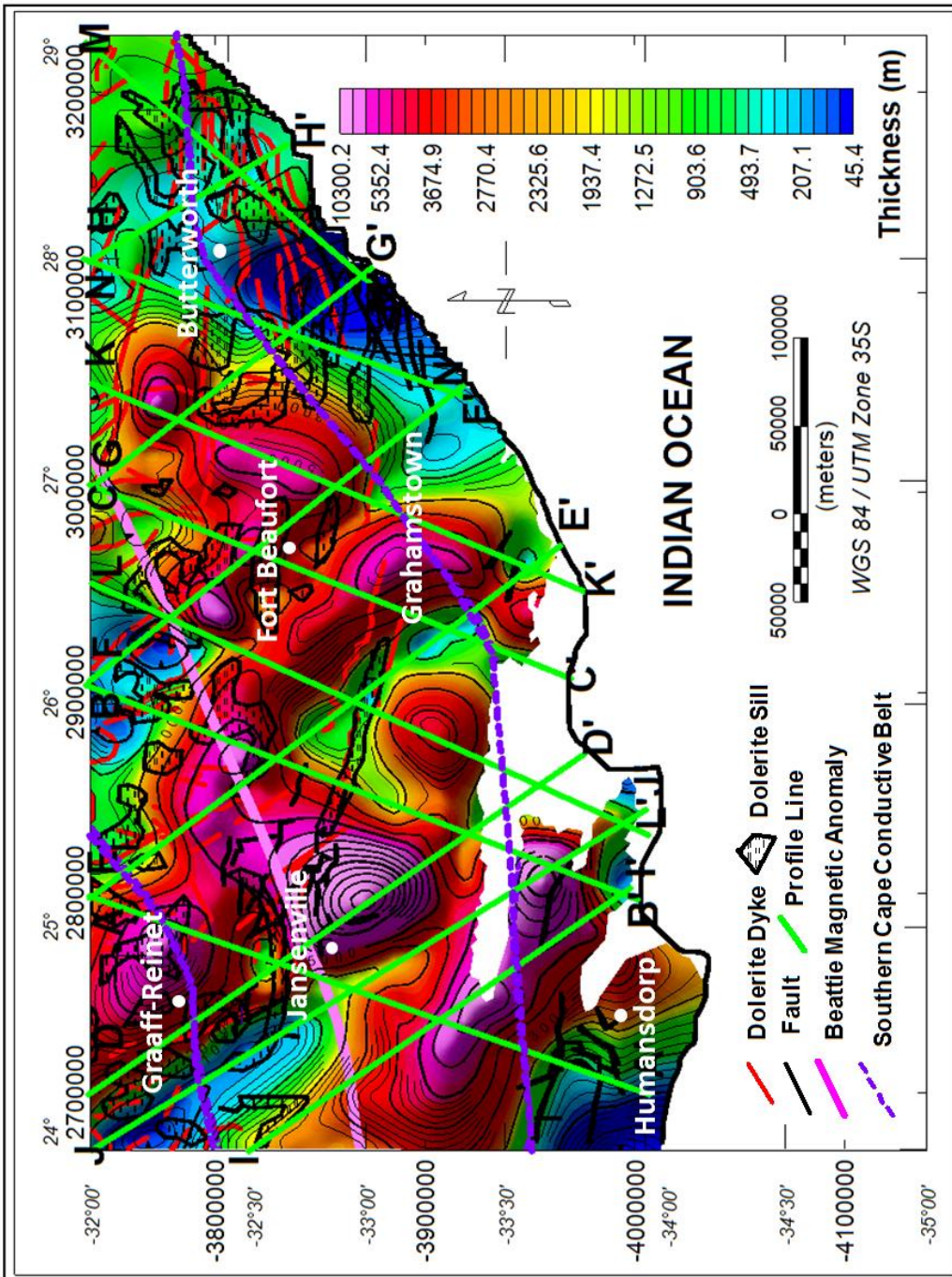
Figure 8.19 Superimposed isochore (true vertical) thickness map of the Cape Supergroup as deduced from gravity profile models using GM-SYS. The map also shows dolerite intrusions (sills and dykes), faults, part of the Beattie magnetic anomaly and the Southern Cape Conductive Belt.

Figure 8.19 is an isochore (true vertical) thickness map of the Cape Supergroup. The red - purple colour areas in the map have current vertical thicknesses that range from 3400 m – 10300 m. The blue - green colour areas in the map show areas with vertical thicknesses that range from about 45 - 1500 m thick. Note: The derived thickness map is an isochore thickness map that shows/connects lines of equal thickness in a layer where the thicknesses are measured vertically as explained in Section 8.2.

8.2.2 Dwyka Group current elevation/depth below sea level and isochore thickness map
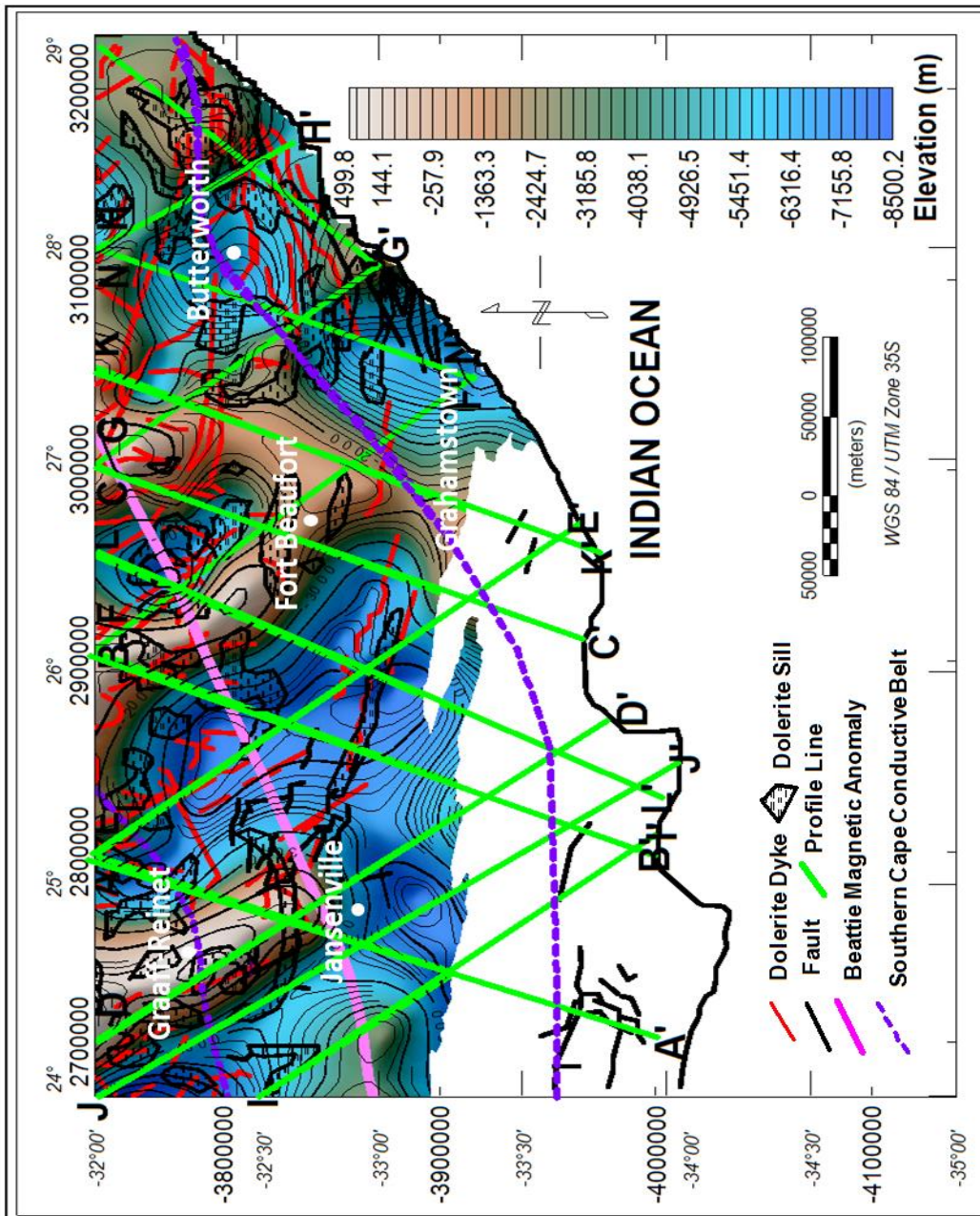
Figure 8.20 Superimposed elevation map of the Dwyka Group as deduced from gravity profile models using GM-SYS. The map also shows dolerite intrusions (sills and dykes), faults, part of the Beattie magnetic anomaly and the Southern Cape Conductive Belt.

Figure 8.20 shows the elevation map of the Dwyka Group relative to the sea level. The dark – light brown colour area on the map with high elevation (greater than -2400 m contour level) are said to be structural or basement highs with a peak elevation of about 500 m above the sea level. The blue colours in the elevation map (less than -5000 m contour level) are the basement low areas with a minimum elevation or depth of around 8500 m below the sea level.
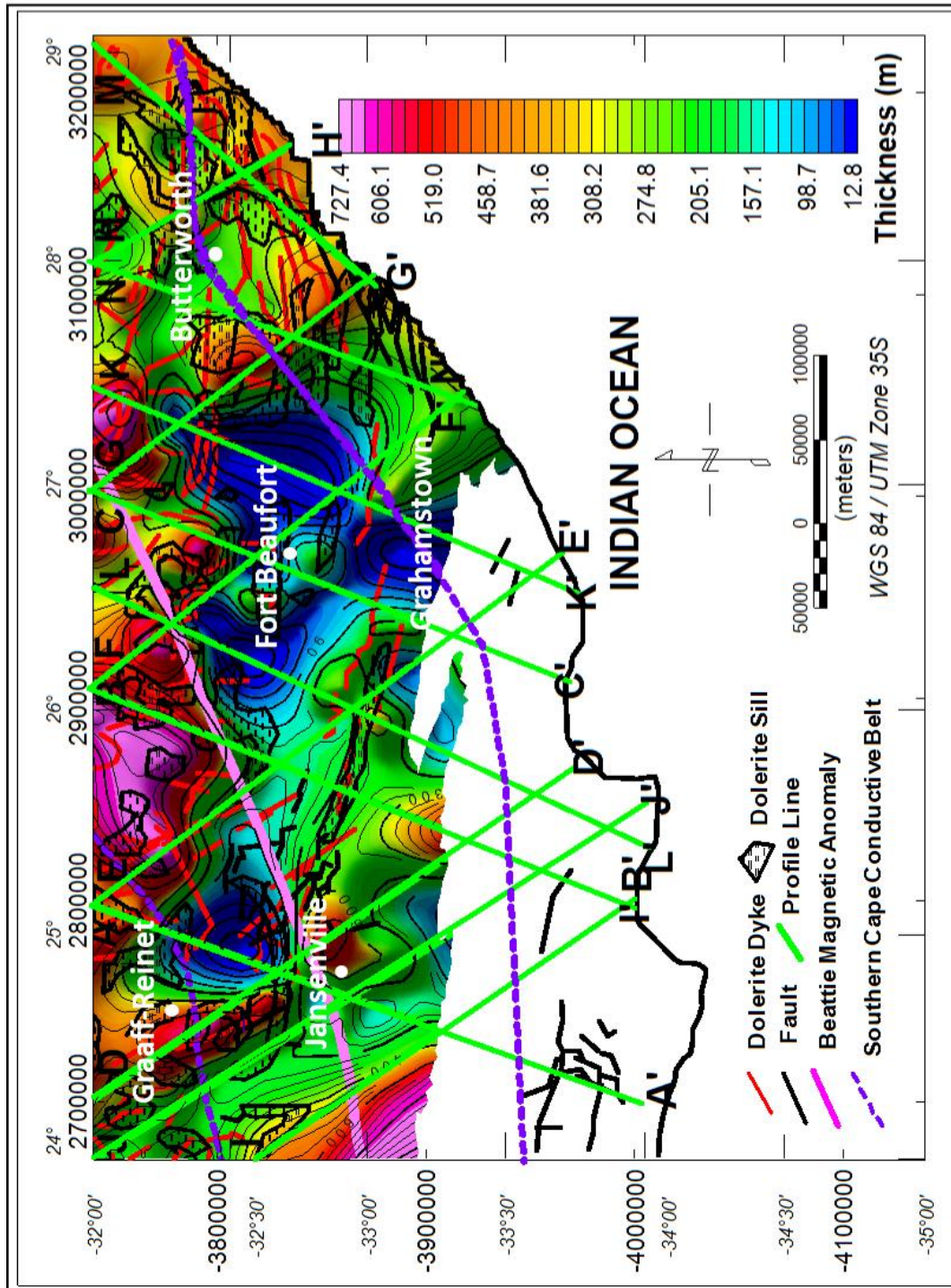
Figure 8.21 Superimposed isochore (true vertical) thickness map of the Dwyka Group as deduced from gravity profile models using GM-SYS. The map also shows dolerite intrusions (sills and dykes), faults, part of the Beattie magnetic anomaly and the Southern Cape Conductive Belt.

The red - purple colour on the map (Figure 8.21) denotes areas with a vertical thickness that range from about 480 - 727 m, whilst areas with deep – light blue colour indicate areas with vertical thickness below 180 m thick. Note: The derived thickness map is an isochore thickness map that shows/connects lines of equal thickness in a layer where the thicknesses are measured vertically.

165

8.2.3 Ecca Group current elevation/depth below sea level and isochore thickness map
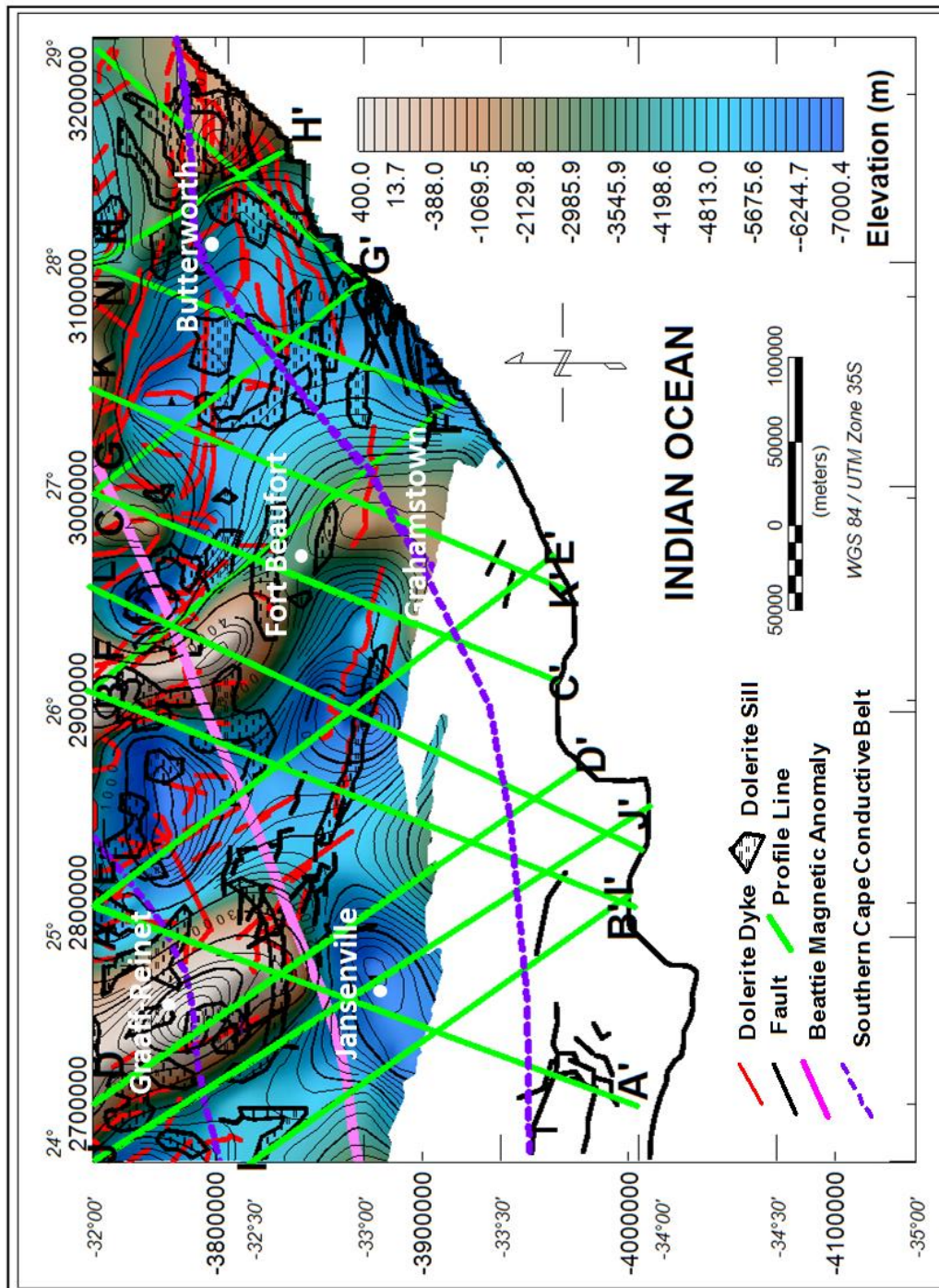
Figure 8.22 Superimposed elevation map of the Ecca Group as deduced from gravity profile models using GM-SYS. The map also shows dolerite intrusions (sills and dykes), faults, part of the Beattie magnetic anomaly and the Southern Cape Conductive Belt.

The dark – light brown colour areas on the map with high elevation (greater than -2000 m) are structural or basement high areas with a peak elevation of about 400 m above the sea level. The areas with the blue colours (less than -3500 m) are the basement low areas with a minimum elevation or depth of about 7000 m below the sea level.
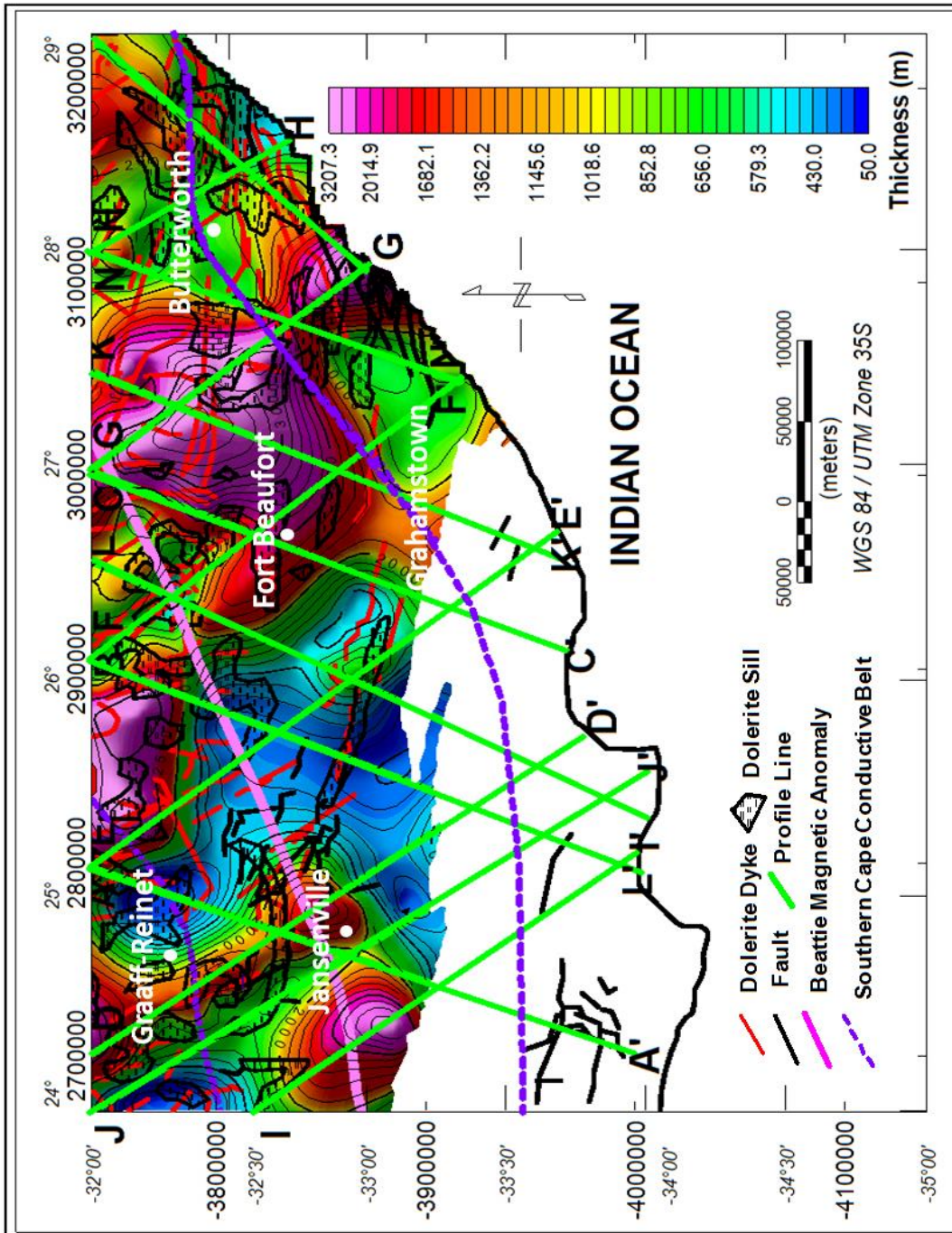
Figure 8.23 Superimposed isochore (true vertical) thickness map of the Ecca Group as deduced from gravity profile models using GM-SYS. The map also shows dolerite intrusions (sills and dykes), faults, part of the Beattie magnetic anomaly and the Southern Cape Conductive Belt.

Figure 8.23 shows an isochore (true vertical) thickness map of the Ecca. The red - purple colour areas on the map show areas with a vertical thickness that range from about 1500 - 3207 m. The blue - green colour areas on the map show areas with vertical thicknesses that range from about 50 - 850 m thick. Note: The derived thickness map is an isochore thickness map which shows/connects lines of equal thickness in a layer where the thicknesses are measured vertically.

167

8.2.4 Beaufort Group elevation/depth below sea level and isochore thickness map
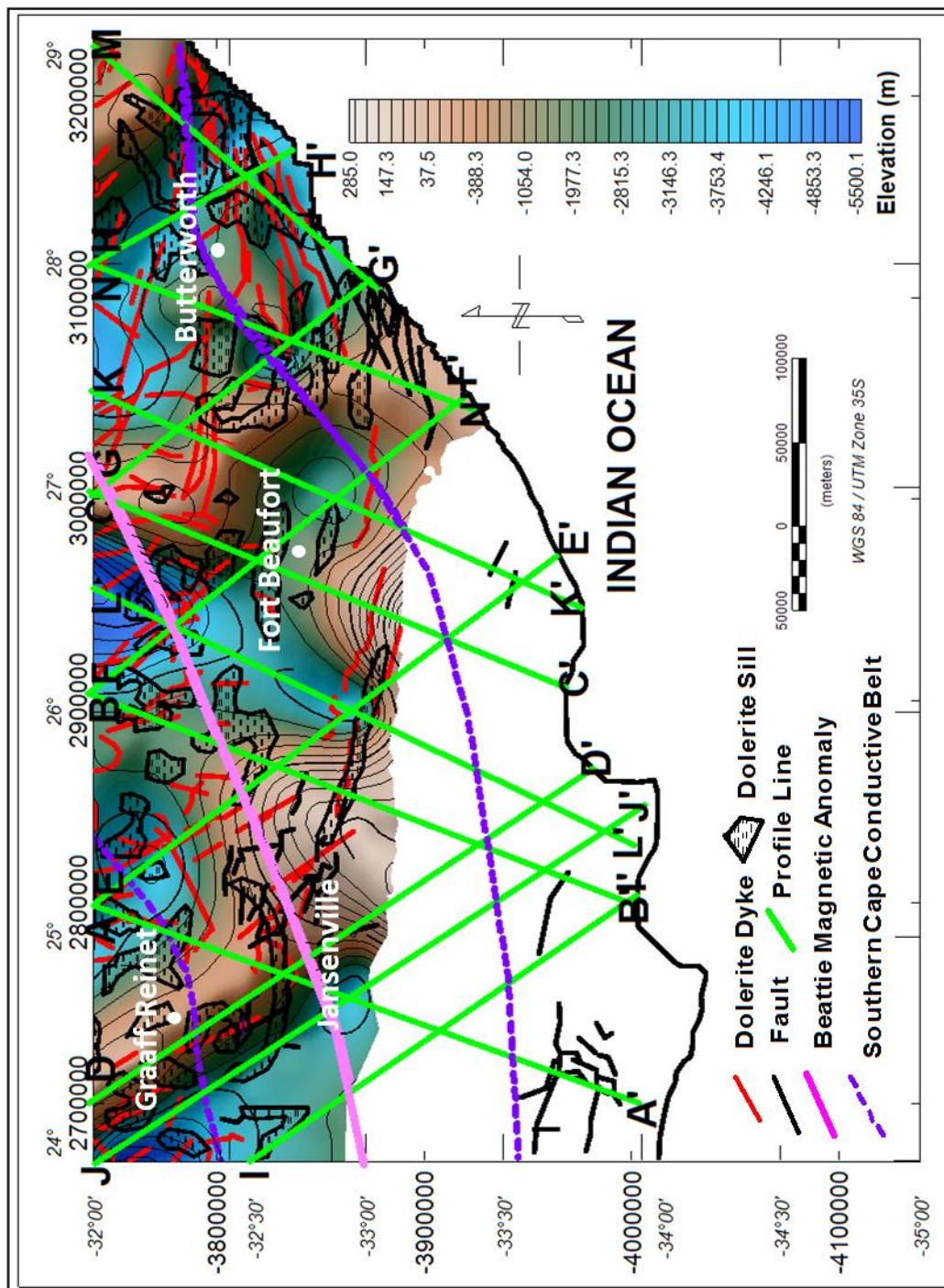
Figure 8.24 Superimposed elevation map of the Beaufort Group as deduced from gravity profile models using GM-SYS. The map also shows dolerite intrusions (sills and dykes), faults, part of the Beattie magnetic anomaly and the Southern Cape Conductive Belt.

The dark – light brown colour areas on the map (Figure 8.24) with high elevation (greater than -1100 m) are said to be structural or basement high areas with a peak elevation of up to 285 m above the sea level. The areas with the blue colours (less than -3500 m) are the basement low areas with a minimum elevation or depth of about 5500 m below the sea level.
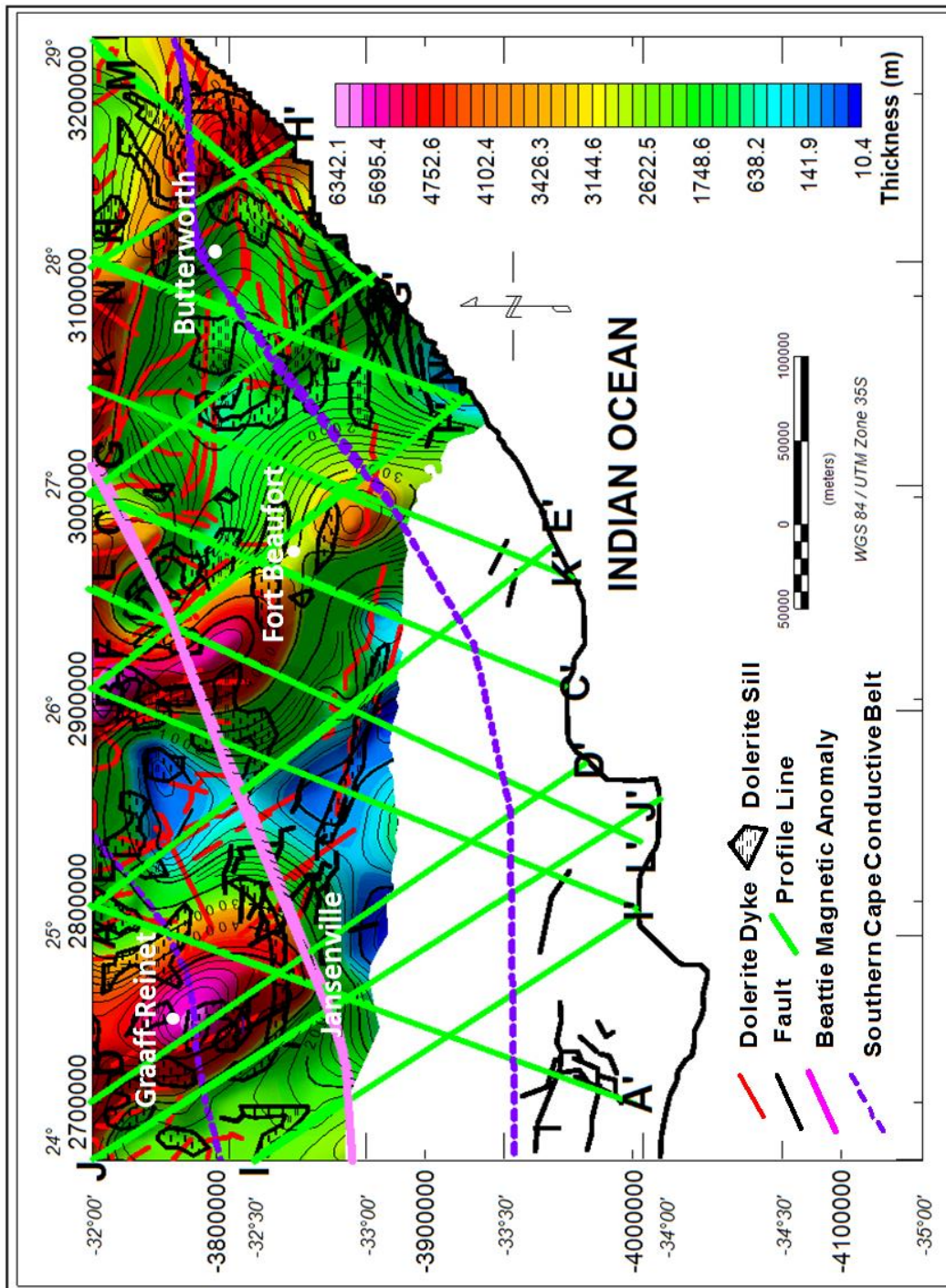
Figure 8.25 Superimposed isochore (true vertical) thickness map of the Beaufort Group as deduced from gravity profile models using GM-SYS. The map also shows dolerite intrusions (sills and dykes), faults, part of the Beattie magnetic anomaly and the Southern Cape Conductive Belt.

The red - purple colour areas on the map (Figure 8.25) show areas with vertical thickness that range from about 4400 - 6342 m, while the blue - green colour areas on the map show areas with vertical thicknesses that range from about 10 - 650 m thick. Note: The derived thickness map is an isochore thickness map which shows/connects lines of equal thickness in a layer where the thicknesses are measured vertically as explained in Section 8.2.

169

8.2.5 Sensitivity of the gravity profile models to change in density

In order to test the depth and isochore thicknesses derived from the sections more convincingly, the highest and lowest density values (measured) were also used to model all the profiles and the extracted depth from all the models were compared to check for variations in depth as the density changes. The sensitivity of the gravity models were also tested by comparing the variation in the derived isochore thicknesses at every grid point (201 $\times$ 118) in the model (i.e. total of about 23718 grid points) , as the density values assigned to the groups/supergroup (blocks) changes from average density value, to maximum and finally minimum values (Table 8.2).

Table 8.2 Sensitivity of the isochore thicknesses derived from the model to density changes.

Group/ Supergroup	Av. ρ (kg/m^3)	$\Delta\rho$ (kg/m^3)	Min. ΔH (m)	Max. ΔH (m)	Av. ΔH (m)	Error (m)
Beaufort	2520	+ 245	103.02	486.18	294.60	$\pm$ 295.21
		- 246	103.54	488.07	295.81	
Ecca	2565	+ 216	93.69	432.91	263.30	$\pm$ 262.92
		- 216	94.35	430.71	262.53	
Dwyka	2662	+ 16	9.28	36.37	22.83	$\pm$ 24.74
		- 21	12.04	41.26	26.65	
Cape	2675	+ 57	25.62	103.88	64.75	$\pm$ 63.63
		- 45	28.19	96.82	62.51	
Basement	2772	+ 48	21.69	100.74	61.22	$\pm$ 62.40
		- 49	24.73	102.43	63.58	

Note: Av. ρ = Average dry density values used in the model; $\Delta\rho$ = Change in dry density values used in the model (the positive sign denotes change/increase in density from average density value to maximum density value in the model i.e. Δ ρ = Maximum density value - Average dry density value, while the negative sign denotes change/decrease in density from average density to minimum density i.e. Minimum density value - Average density values); Min. ΔH = Minimum change in vertical thickness due to density change; Max. ΔH = Maximum change in vertical thickness due to density change; Av. ΔH = Average change in vertical thickness due to density change; Error (average change in isochore thickness) = sensitivity of the model to density change.

8.2.6 Discussion and summary of the depositional history/results

The current sediment isochore thickness (also known as true vertical thickness; Figure 8.19; 8.21; 8.23; 8.25), was determined by subtracting the depth of the bottom surface from the depth of the top surface and extrapolated vertically using GM-SYS (discussed in Section 8.2). The incoming sediments (Cape Supergroup) covering the basement relief as well as the sediments of the Karoo Supergroup show variation in current vertical thickness across the study area. For instance, the current vertical thickness of the Cape Supergroup varies from about 45 – 10300 m, whilst the Dwyka Group, Ecca Group and Beaufort Group varies from about 13 – 727 m, 50 – 3207 m and 10 – 6342 m, respectively. These variations in the current vertical thickness across the study area are possibly due to deformations that cause some of the beds/layers to be folded. The deformations are evidenced in the gravity profile models presented in Figure 8.4 - 8.17. This deformation and processes that led to the development of the basin (depositional history of the groups) are discussed below.

Several researchers (e.g. Tankard *et al*., 1982; de Wit and Ransome, 1992; Hälbich, 1993; Paton, 2006) documented that the tectonic evolution of southern South Africa involves series of compressional and extensional deformation episodes over the last 650 Ma. Thomas *et al*. (1993) in Paton (2006) envisaged that the Namaqua-Natal Belt that developed as a result of compression of the passive margin at the southern edge of the Kaapvaal Craton during the Namaqua-Natal Orogeny (950 - 900 Ma) is one of the main factors that controls the development of the region. Tankard *et al*. (1982) allude that, after the termination/end of compression, a series of east-west trending extensional basins developed from about 900 - 600 Ma, within which the sediments of the Pre-Cape Group were deposited, these basins were later overturned during the Pan African Orogeny (600 - 450 Ma).

According to McCarthy and Rubidge (2005), at about 500 million years ago, the supercontinent Gondwana had consolidated and the mountains ranges that developed along its suture were being eroded, thus exposing the Pan-African metamorphic rocks that had formed deep below the surface. By 450 million years ago, rifting began across what is today the southern Cape (probably as a result of internal tension experienced by the supercontinent), causing thinning of the crust and invasion by the sea. Rivers were said to have diverted into the rift and began to deposit its sediment (mainly sand and gravel) to form the Klipheuwel Group (McCarthy and Rubidge, 2005).

171

A major rift was created by the continued stretching of the present deeply eroded Pan-African belts. McCarthy and Rubidge (2005) stated that this rifting extended eastward across the southern part of South Africa to beyond the present position of Port Elizabeth (Figure 8.1). The north-easterly part of the rifting extends into the present-day KwaZulu-Natal (Figure 1.1). The rift was flooded rapidly by the sea and thus resulted in the formation of a seaway across the southern Cape (called the Agulhas Sea; see Figure 8.26A) as the crust thinned and subsided. The rocks of the Klipheuwel Group and the eroded Pan-African rocks (Cape granites and associated metamorphosed sedimentary rocks of the Malmesbury, Kango and the Kaaimans Groups; Figure 8.1) floored the sea in the west and east, respectively.
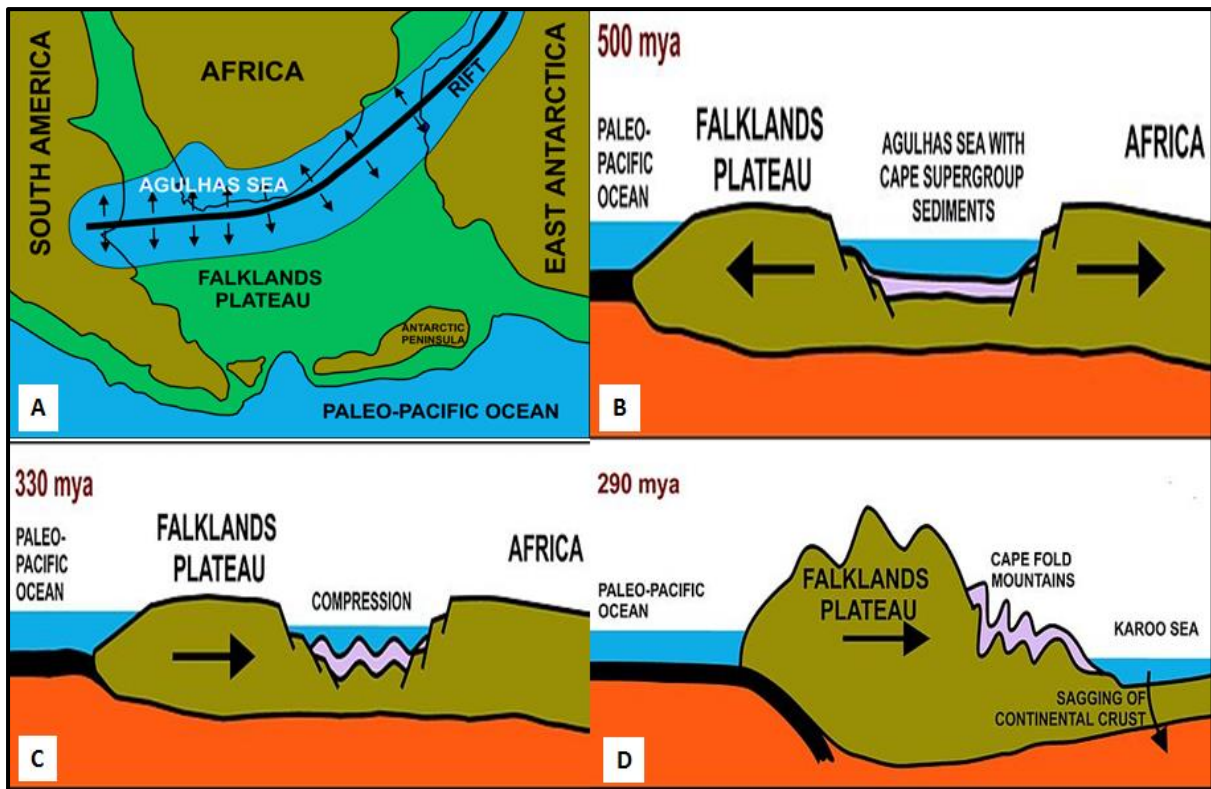
Figure 8.26 Events that led to the development of the Karoo basin (Karoo Period of sediment deposition) in Southern Africa. (A) Southern Gondwana during the Cambrian-Ordovician Periods. The olive-green colour depicts today's continents into which the supercontinent finally broke up. (B) The geology about 500 Ma, with the sediments that would later form the Cape Supergroup settling in the Agulhas Sea. (C) The drifting of the Falkland Plateau northwards once again to close the Agulhas Sea. This drifting caused the Cape Supergroup to be deformed and resulted in a series of folds. (D) The subduction of the paleo-Pacific Oceanic plate beneath the Falkland Plateau, during the Early Permian period, resulted in a massive range of mountains. These mountains were later eroded into the Karoo Sea, forming, especially, the Beaufort Group of the Karoo Supergroup (http://en.wikipedia.org/wiki/Karoo_Supergroup). Note: In Figure 8.26 (B - D), the continental plates are represented by the olive-green structures, the paleo-Pacific - Oceanic plate is shown with the thick black layer on the left, while the orange and blue colour shows the upper mantle and the flooded areas or ocean, respectively.

As the rifting continued, the depression (basement lows) widened and more sediments were transported and deposited in the depressions forming the Cape Supergroup (Figure 8.18). The current maximum vertical thickness of the Cape Supergroup rocks as derived from the models is about 10300 ± 64 m in the study area (Figure 8.19; Table 8.2). Deposition during the initial phases of the Cape basin subsidence has been interpreted as being tectonically controlled by faulting of the basement (Tankard *et al*., 2009; Figure 8.4 - 8.17). The rocks of the Cape Supergroup can be subdivided into three groups (the Witteberg Group, Bokkeveld Group and the Table Mountain Group) of varying age, depositional environment and fossil content. The top of the Witteberg Group signifies the end of sedimentation in the Agulhas Sea. McCarthy and Rubidge (2005) further explained that the end of sedimentation in the Agulhas Sea is noted by a change from an environment of stretching, thinning and subsidence of the crust, to an environment of compression, crustal shortening and thickening. Generally, the rocks of the Cape Supergroup were deposited over a period ranging from the Ordovician to the Carboniferous (about 500 Ma to 330 Ma). The Cape Supergroup is believed to have been deposited in a passive margin basin after "the Late Precambrian to Early Cambrian Saldanian orogeny and Pan-African depositional cycles had completed in the Gondwana" due to extensional processes (Catuneanu, 2004; Figure 8.26).

At about 310 million years ago, McCarthy and Rubidge (2005) allude that, a subduction zone developed along the southern margin of Gondwana due to closure of the rift valley that started at about 330 million years ago, and the internal part of the supercontinent began to experience compression (Figure 8.26C). This caused the sedimentary rocks of the Cape Supergroup to begin to fold or buckle (as evidenced in the models presented in Figure 8.4 - 8.17), the crust thickened, forming a mountain range in the place where the Agulhas Sea formerly existed. Thus, the earlier known Agulhas Sea became the Cape Mountains. Due to the load (weight) of this mountain range, the continental crust of Southern Africa began to sag, resulting in a basin development or depression (lows) on the northern flanks, into which the sediments of the Karoo Supergroup were deposited over a period that span from the Late Carboniferous to the Middle Jurassic (about 310 Ma to 182 Ma). Paton (2006) stated that the development of the Gondwanian orogeny in the Permian led to the termination of Cape Supergroup deposition. Deformation of the Cape Supergroup margin deposits into the Cape Fold Belt as well as the formation of the Karoo foreland basin to the north are manifestation of the compression in South Africa (Veevers *et al*., 1994 in Paton 2006). Paton (2006)

concluded that the Cape Fold Belt cannot be classified as a thin skinned nor thick-skinned tectonic end-member but their deformation can be said to be controlled by a south dipping mega-decollement that shows features of both end-members.

With time, much of the Cape Supergroup rocks became buried under the Karoo deposits, but later re-surfaced as mountains during the upliftment of the subcontinent at about 180 million years ago (coincides with the intrusion of dolerites depicted in the models; Figure 8.4 - 8.13), and again at about 20 million years ago, initiated an episode of continuous erosion that removed some of the surface deposits from Southern Africa. According to Wopfner (2002) in Catuneanu *et al*. (2005), the tectonic regime during Karoo time was defined by compression and accretion along the southern margin of Gondwana coeval with extension proliferating into the supercontinent from its Tethyan margin. From the start of the Late Carboniferous, tensional stresses propagated gradually to the south from the Tethyan margin, controlling the deposition of Karoo sediments in grabens and subsequent rift structures. Tankard *et al*. (2012) allude that the Cape and Karoo basins represent two main periods of intermittent subsidence and sedimentation within the internal part of Gondwana. They further envisaged that the Cape basin developed by extensional processes in an episutural setting and after about 30 Ma of hiatus, the Karoo basin developed as a tabular cratonic cover.

According to McCarthy and Rubidge (2005), at the time of formation of the Cape Mountain, South Africa was believed to be located over the South Pole due to the steady northward drifting of Gondwana (Figure 2.2). The ice sheet that covered the southern Gondwana (e.g. Africa) was probably of several kilometres thick. The glacial deposits from the ice sheet were the first of the sediments to be deposited in the developing Karoo depression (Figure 8.20), thus making the Dwyka Group as the earliest and lowermost of the sedimentary deposits of the Karoo Supergroup (Figure 8.4 – 8.17). The basin in which the sediments were deposited was deepest in the south along the Cape Mountain front, thus the ice sheet floated on an inland lake, also known as the Karoo inland sea (McCarthy and Rubidge, 2005; Figure 8.26). Subsequently, the glaciers that emerged from the mountains floated out of the sea as icebergs, they seasonally melted and retreated leaving an enormous quantities of unsorted mud and large fragments of rock that characterised the Dwyka Group (see Figure 4.2). The current maximum vertical thickness for the Dwyka Group deposits in the study area is about 727 $\pm$ 25 m (Figure 8.21; Table 8.2). The deduced current vertical thickness of the Dwyka Group falls within the range estimated by several researches (e.g. Du Toit, 1954; Smith, 1990;

Johnson *et al*., 2006) that the thickness of the group increases southwards and the maximum thickness varies from about 500 - 800 m in the south but decreases northwards (1 - 600 m).

Catuneanu (2004) speculated that the earliest Karoo sedimentary rocks (about 330 - 300 Ma) must have been over-thrusted, "cannibalized" and included within the structures of the Cape Fold Belt. This can also be linked to the similarities in structures/beddings of the Dwyka and Cape Supergroup in Figure 8.4 – 8.17. According to Tankard *et al*. (2009), the Cape orogeny is pre-dated by the dynamic phase of subsidence experienced by the early Karoo basin during the Permian. They suggested rapid rate of collapse of the Carboniferous high plateau due to the lack of marked transition to the Dwyka basement high and platform facies associations. Vertical displacement of rigid basement blocks decoupled along crustal-scale boundary was the main subsidence that occurred which is revealed in the distribution of the Dwyka Facies associations (Tankard *et al*., 2009). The rate of subsidence of the Namaqua and Natal blocks exceeded the rate in which sediment were supplied, and thus led to the underfilled basin of the platform facies association. The different types of glacial deposits in the Dwyka Group are attributed to the several episodes of advance and retreat of the ice sheets (McCarthy and Rubidge, 2005).

Continued northward drifting of the Gondwana away from the polar region, caused all the ice to melt, after all the ice had melted (disappeared), a vast inland water body (inland sea) remained, this water body extended across South Africa and the neighbouring regions of Gondwana. According to McCarthy and Rubidge (2005), this inland sea might have had an opening to the ocean but with a lesser or small tidal effects (probably, it is similar to the Black Sea). The Cargonian Highlands that formed the high ground, north of the sea, and the rivers draining the mountains that are north of the Karoo Sea deposited their sediments along the northern shoreline, forming large swampy deltas. However, some of the sediments were derived from the south (Cape Mountain; Figure 8.18) and deposited into the Karoo Sea. These deposits are called the Ecca Group of the Karoo Supergroup, they consist mostly of shales and there current maximum vertical thickness in the study area is about 3207 ± 263 m (Figure 8.23; Table 8.2). Tankard *et al*. (2012) allude that the style of subsidence in the Dwyka Group continued into the Ecca Group which is an underfilled basin, dominated by argillaceous sedimentation. The transition from the Dwyka glacially affected sedimentation in the post-glacial early Ecca.

During the Ecca time, the Falklands Plateau collided and was later fused/joined with the Southern Africa (Figure 8.26), resulting in the range of mountains that is seen south of the Cape Fold Belt. The rocks of the Ecca Group are important because of their fossils content (McCarthy and Rubidge, 2005). Tankard *et al*. (2009) allude that the Karoo basin subsidence resulted from mantle flow but becomes complex due to variable degrees of foundering of the basement blocks. These basement blocks are coincident with the Hex River area oroclinal bend in the present day Cape Fold Belt and possibly behaved as a buried basin boundary during the Ecca Group time, probably influencing the position of the shelf edge in a way that is similar to a passive margin (Tankard *et al*., 2009). With the continued accumulation or deposition of sediments into the Karoo Sea as well as formation of the Falkland Plateau and Cape Fold Mountain ranges, the Karoo Sea gradually got filled with sediments that were mostly derived from the Cape Mountains in the south (by this time, the highlands that were formed, north of the Karoo Sea had been probably levelled by erosion and subsequently buried beneath the newer sediments), and the Mississippi-like rivers flowed over the filled-up Karoo Basin from the south, providing new habitats for a variety of flora and fauna. These sediments form the Beaufort Group have the current maximum vertical thickness of about 6342 ± 295 m (Figure 8.25; Table 8.2) in the study area is.

Johnson *et al*. (2006) envisaged that by Beaufort time, the climate had warmed sufficiently to become semi-arid such that the Ecca seaway regressed. This led to the establishment of a fully non-marine environment and resulted in the accumulation of the fluvio-lacustrine Beaufort Group (Beaufort sediments; Figure 8.25). The Karoo Sea later became a lake with time (McCarthy and Rubidge, 2005). This transition into the terrestrial marine environments marks the boundary between the Ecca Group and the Beaufort Group which occurred over a period of about 250 million years ago. Johnson *et al*. (2006) also stated that subsequent orogenic activity at the beginning of the Triassic with associated uplift resulted in the influx of Beaufort sediments which extended throughout the basin. The effect of basin morphology and local structural relief is revealed by significant lateral changes in thickness (Figure 8.25).

Weckmann *et al*. (2012) stated that the main deformation that took place in the Cape Fold Belt at about ca 250 Ma affected the Proterozoic metasediments, as well as the overlying Paleozoic cover. The Karoo Basin was first referred to as a passive margin (Smith, 1995). Subsequently, it was generally referred to as a retroarc-foreland basin (Dickinson 1974 in Johnson *et al*., 2006; Johnson and Beaumont, 1995 in Catuneanu *et al*., 1998), with fills in

front of the Cape Fold Belt situated in southwestern Gondwana. The rocks of the Cape Supergroup are more resistant to erosion when compared to the softer rocks of the Karoo Supergroup. Tankard *et al*. (2009; 2012) stated that the sedimentary fill of the Karoo Basin are result of crustal uplift, fault-controlled subsidence, and long periods of regional subsidence during which faulting was subordinate (Figure 8.4 - 8.17). Hälbich (1993) envisaged that the lower units of the Karoo Basin, as well as the Cape Supergroup rocks were deformed at about 250 Ma, with the formation of north-vergent asymmetric or overturned folds and thrust faults. The development of the Cape Fold Belt during the deposition of sediments within the Karoo Basin greatly influenced the depositional environments within the basin and is in turn considered as the major source of detritus to the Karoo Supergroup. The intense deformation of the Cape Supergroup strata along with some lower units of the Karoo Supergroup along the southern margin of the basin is considered to be a direct consequence of the orogeny (Johnson *et al*., 2006; Figure 8.19; 8.21; 8.23).

Tankard *et al*. (2012) stated that regional thickness and stratigraphic variation in the Cape and Karoo basin (Figure 8.19; 8.21; 8.23; 8.25) reveals the control of first-order crustal faults and asymmetric subsidence of the intervening basement blocks. They further speculated that the Ecca subsidence between these crustal faults was uniformed and without the characteristics diagnostic of significant upper-plate extension, such as normal basin-forming faults, syn-rift sedimentary wedges or unconformities. Tectonic interpretation of the Karoo Basin has usually been centred on a uniform foreland basin model and regional stratigraphic relationships that indicate an Early to Middle Permian age for the whole of Ecca Group (Johnson *et al*., 2006). Provenance studies by some researches (e.g. Johnson, 1991; Andersson *et al*., 2004) show that there was no contribution from the Cape Fold Belt until deposition of the upper Beaufort Group.

Catuneanu *et al*. (2005) stated that tectonism was the main control on accommodation in the Karoo basin, with subsidence mechanisms ranging from flexural in the south, in relation to processes of subduction and orogenesis along the paleo-Pacific margin, to extensional in the north, propagating southwards from the divergent Tethyan margin. The Karoo Basin responded to eight tectonic events related to the Panthalassan (paleo-Pacific) plate beneath Gondwana from the time of deposition of the Dwyka through to the Elliot Formation. These tectonic events produced variation in the depositional sedimentary successions within the

Karoo setting (Catuneanu *et al*., 1998) and indicate changes in climate over time. Within this time span, the Karoo Basin is seen to contain the thickest stratigraphic megasequence of several deposition episodes (Catuneanu and Elango, 2001; Figure 8.21; 8.23; 8.25). The source of the sedimentary fill in the Karoo Basin is related to the mountain belt in the paleo-Pacific southwestern Gondwana when rifting of the Gondwana supercontinent began, also referred to as the flexural subsidence stage (Johnson, 1991; Cole, 1992 in Bordy *et al*., 2005; Duncan *et al*., 1997 in Catuneanu *et al*., 1998; 2005). The Karoo succession was intruded by dolerite sills and dykes (at about 180 Ma) as depicted in the gravity models (Figure 8.4 - 8.17). The extrusive equivalents of these dolerites are present as an erosional remnant of continental flood basalt to the northeast of the study area (Figure 4.35).

Table 8.3 Comparison of current maximum thicknesses for the Karoo Supergroup from different authors.

Group	This study	Johnson *et al*. (2006)	Johnson (1976)
	Current isochore thickness	Stratigraphic thickness	Stratigraphic thickness
	Max. Thickness (m)	Max. Thickness (m)	Max thickness (m)
Beaufort	6342 ± 295	6850	6000
Ecca	3207 ± 263	3400	3000
Dwyka	727 ± 25	750	700

Note: The value given for the error or sensitivity (e.g. ± 295) is the average value for the variation in the isochore thickness when the density changed from average density to maximum density and when the density values changed from average density to minimum density values as depicted in Table 8.2.

Generally, as the density of the Karoo sedimentary succession changes, the thickness also changes. Based on the data presented in Table 8.3, it can be inferred that the Beaufort Group (Koonap, Middleton, Balfour, Katberg and Burgersdorp Formations) with current maximum vertical thickness of up to 6342 ± 295 m is the thickest group within the Karoo Supergroup. The Ecca Group (Prince Albert, Whitehill, Collingham, Ripon, Fort Brown and Waterford Formations) has a current maximum vertical thickness of about 3207 ± 263 m while the Dwyka Group has a maximum vertical thickness of approximately 727 ± 25 m. The

maximum vertical thicknesses obtained for each group (Karoo Supergroup) from the GM-SYS model are close the maximum thicknesses calculated for the groups by several authors (e.g. Johnson 1976; Johnson *et al.*, 2006; Alao and Mikes, 2011). There are very slight differences in the maximum thickness values as shown in Table 8.3 which could be due to the fact that the vertical thicknesses were obtained in this study rather than stratigraphic thickness.

8.3 1D PetroMod modelling

Geological record shows that most of the non-renewable fuel and ground water resources in the world are hosted by sedimentary rocks. Therefore, detailed knowledge and/or understanding of the geological relationships between these resources and the host sedimentary strata are required for basin modelling. This will assist in the exploration and exploitation of the available resources. The Karoo Basin hosts thick sediments (Figure 8.21, 8.23 and 8.25) that give insight into the depositional history of the basin from the time of formation to the time of deposition. The lower Ecca Group (Prince Albert, Collingham and Whitehill Formations) is the focus of interest for shale gas exploration in the Karoo Basin since they are considered as important repositories for hydrocarbon accumulation.

According to Advanced Resources International (2013), the three main source rocks for hydrocarbon (shale gas) in the Karoo Basin are the Prince Albert shale (type III), Whitehill shale (type II) and Collingham shale (type II). The lower Ecca Group was estimated to contain 1559 trillion cubic feet (Tcf) risked gas in place (GIP) and 399.6 trillion cubic feet (Tcf) as the risked recoverable.

Petroleum system modelling was carried out using the PetroMod 1D software (Version 2012.2) supplied by Schlumberger. It combines seismic, well, and geological information to model the evolution of a sedimentary basin. The PetroMod works on the principles of actualism and fundamental physical laws. Actualism is used by geologists to interpret geologic records and natural processes that lead to their formation whilst incorporating the concept of uniformitarianism, relate natural processes affecting the geologic record today to processes in the past. It also elucidates that the general natural rates of geologic processes like volcanic eruption, weathering, erosion and deposition are constant through time. The present-day data was used when modelling using PetroMod, thus the geologic history of the basin can

be restored as well as make predictions about unknown or uncertain regions of a basin where little or no direct data is available although the present-day situation must be fully understood as possible. However, the quality of the input data determines the reliability of the model. The better the calibration of the model, the more predictive and useful it is for exploration purposes. More information on the working principle of PetroMod can be found in McKenzie (1978), Shea (1982), Henke (2011) and Schlumberger Information Solutions (2013).

The petroleum modelling aid in investigating the degree, timing of generation, migration and accumulation of hydrocarbon which are related and used in understanding the burial depth of the Karoo Basin sediments (see Figure 8.27). The stratigraphy, deposition age, lithology and output parameters (thickness and depth) that were exported from the GM-SYS profiles model were loaded into the 1D PetroMod work environment which form the basis of the petroleum system input model. The petroleum system elements (PSE) were defined for the lithologies whilst the total organic carbon (TOC) and kinetics were assigned to the source rock from the PetroMod database access cells to generate petroleum from kerogen.
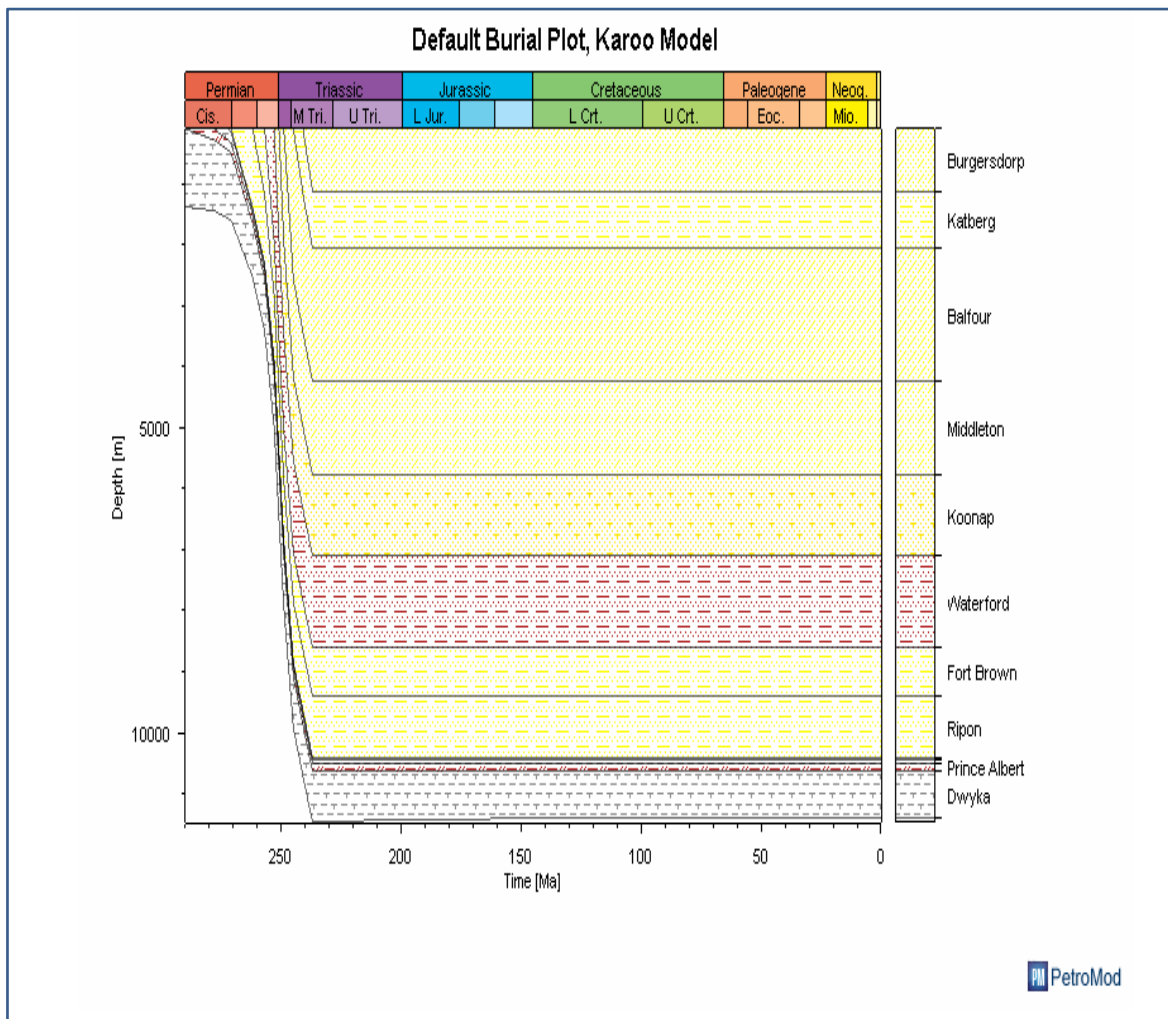
Figure 8.27 Burial history plot of the southeastern Karoo Basin.

The boundary condition such as the paleo water depth (PWD) for the Karoo Basin was extracted from Visser and Loock (1978) and assigned to the model (Table 8.4). The global mean surface temperature (based on Wygrala, 1989; Figure 8.28) and the assigned PWD were used to automatically calculate the sediment - water interface temperature (SWIT). The heat flow was modelled using a McKenzie-type lithospheric stretching model (McKenzie, 1978). The result of the boundary conditions is tabulated in Table 8.4 and the boundary conditions plot of the southeastern Karoo Basin was displayed as shown in Figure 8.29.
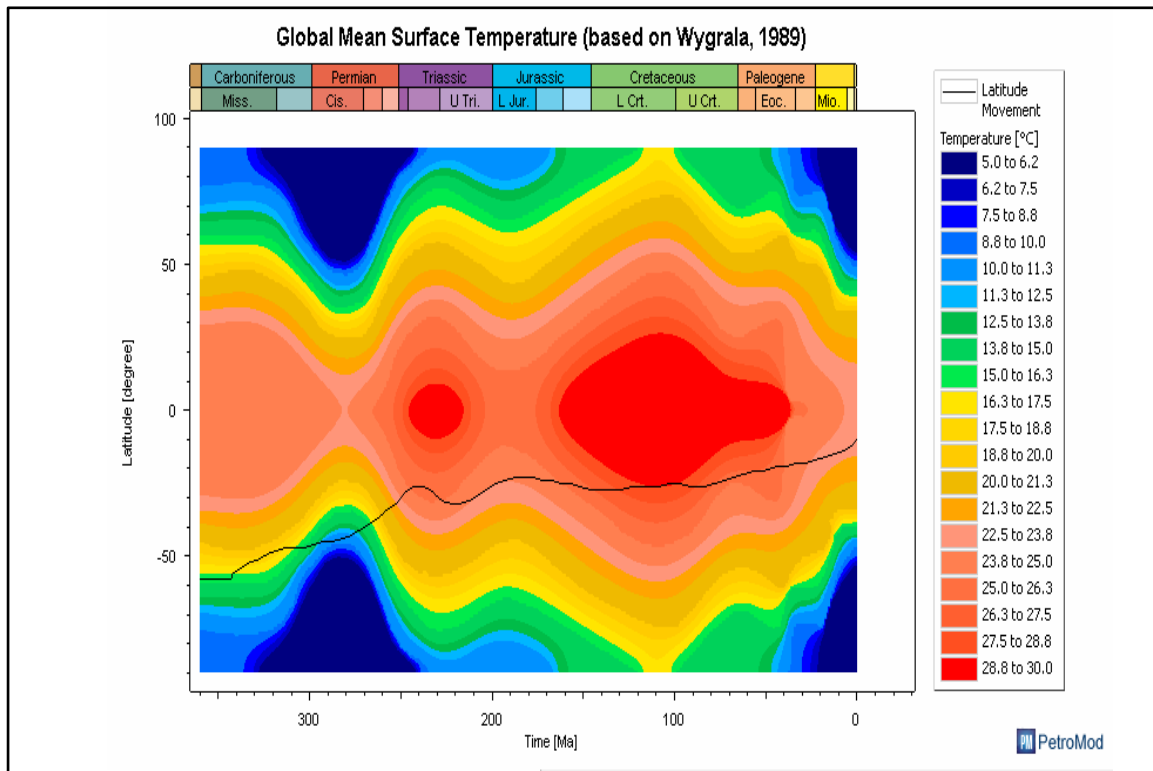
Figure 8.28 Global mean surface temperature (based on Wygrala, 1989).

Table 8.4 Paleo water depth (PWD), sediment - water interface temperature (SWIT) and heat flow (HF) for the Karoo Basin.

	Visser and Loock, (1978)	From PetroMod	Based on McKenzie, 1978
Age (Ma)	**PWD (m)**	**SWIT** (°C)	**HF (mW/m^2)**
0	120	20.08	64.10
50	120	23.17	68.60
120	80	26.53	76.30
280	65	8.55	80.10
290	35	9.00	83.20
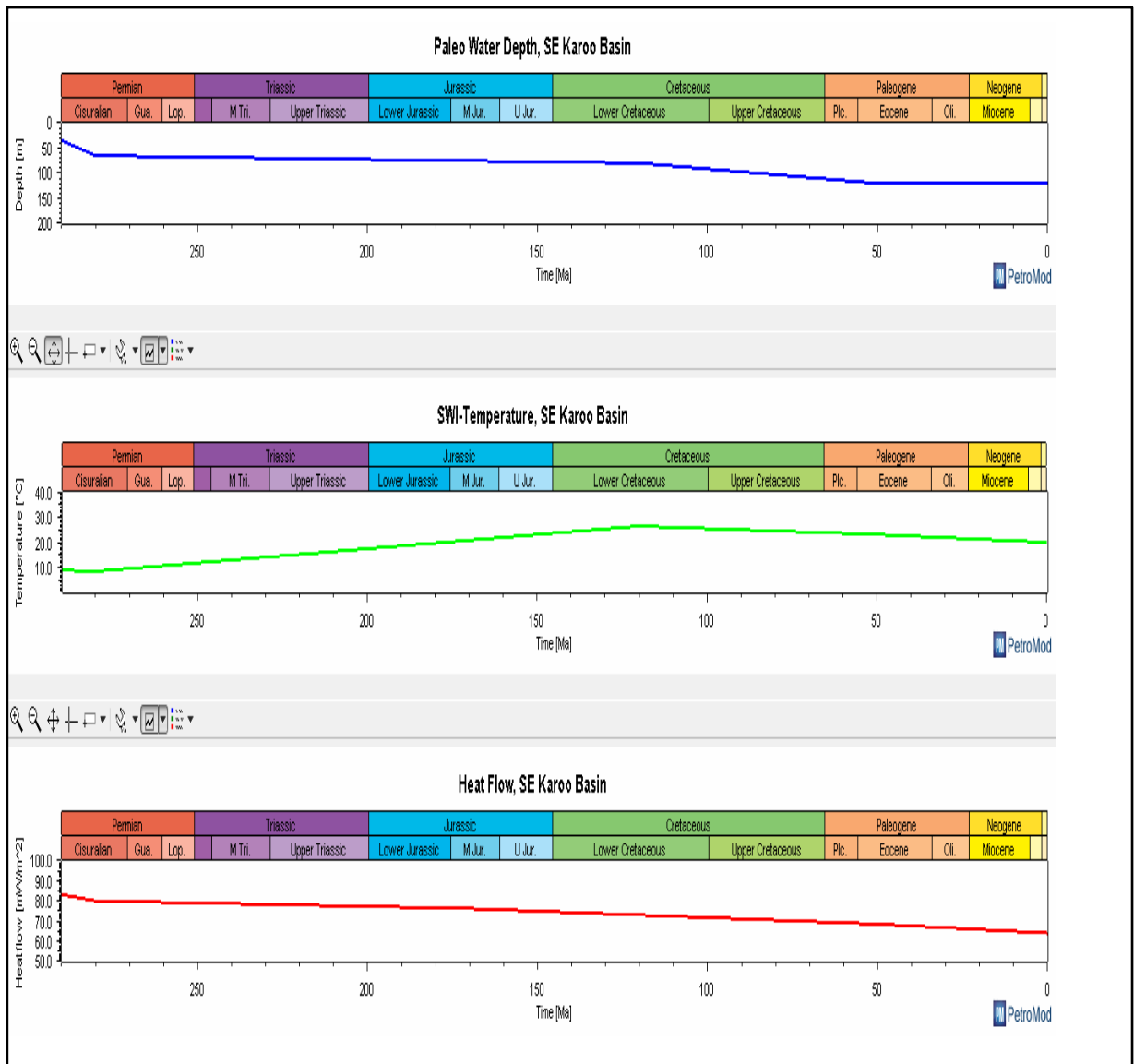
Figure 8.29 Boundary conditions plot of the southeastern Karoo Basin.

The depth, paleotemperature and vitrinite reflectance values were extracted from Aarnes *et al*. (2011) and used to calibrate the model (see Table 8.5).

Table 8.5 Borehole data used for calibrating the lower Ecca Group (Aarnes *et al.*, 2011).

Depth (m)	Paleotemperature (°F)	Vitrinite Reflectance (%)
36	438.64	4.50
43	447.73	4.70
66	472.73	4.90
75	487.27	5.60
86	503.64	5.70
95	514.55	5.80
105	525.45	6.00
126	549.09	6.50
135	560.00	7.00

The data were entered into the model using the "Well Editor" menu and calibrating models in order to refine the model by running simulation such that the observed temperature and vitrinite reflectance curves in the 1D PSM output (depth plots, time plots and burial histories) coincides or fits with the calibrated data. The (paleo) heat flow through time and erosional surface were redefined in order for the paleotemperature and vitrinite reflectance curves to fit better to the calibrated data respectively (Figure 8.30). The depth, total organic carbon (TOC) and maximum temperature (T_{max}) were also extracted from the depth profiles and chemostratigraphy across 135 m of core from SFT2 in Geel *et al.* (2013) (Table 8.6)
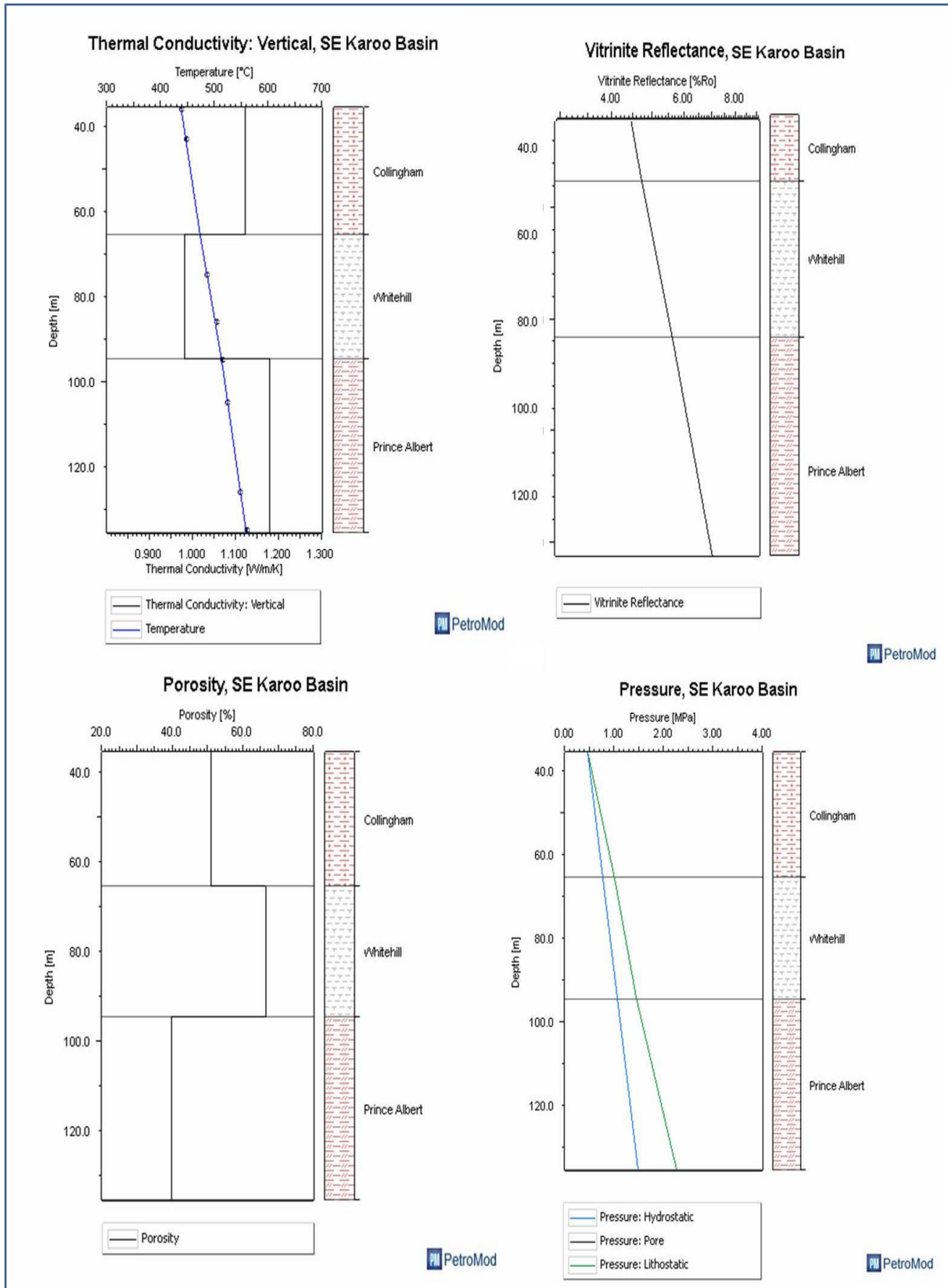
Figure 8.30 Depth plots of the southeastern Karoo Basin. Note: The hydrostatic pressure coincides with the pore pressure.

186

Table 8.6 Estimated data extracted from depth profiles and chemostratigraphy across 135 m of core from SFT2 (Taken directly from Geel *et al*., 2013).

Depth (m)	TOC (%)	T_{max} (°C)	Formation
173	1.20	600	Collingham
182.5	1.21	410	Collingham
191.25	1.20	420	Collingham
200	8.00	590	Whitehill
208.75	6.00	570	Whitehill
217.5	2.80	580	Whitehill
226.25	0.20	560	Prince Albert
235	0.10	570	Prince Albert
243.75	0.25	600	Prince Albert
252.5	0.50	600	Prince Albert
261.25	0.28	600	Prince Albert

Table 8.7 Level of thermal maturity of oil (Peters and Cassa, 1994).

Level of Thermal Maturity						
	Maturation				Generation	
	R_o	T_{max}	Thermal Alteration Index (TAI)	Bitumen/TOC	Bitumen	Production Index
Stage of Thermal Maturity for Oil	(%)	°C			(mg/g rock)	[$S_1/(S_1 + S_2)$]
Immature	0.2-0.6	<435	1.5-2.6	<0.05	<50	<0.10
Mature						
Early	0.6-0.65	435-445	2.6-2.7	0.05-0.10	50-100	0.10-0.15
Peak	0.65-0.9	445-450	2.7-2.9	0.15-0.25	150-250	0.25-0.40
Late	0.9-1.35	450-470	2.9-3.3	---	---	>0.40
Postmature	>1.35	>470	>3.3	---	---	---
From Peters and Cassa, 1994						

The study of the model (Figure 8.27) and the data extracted from Geel *et al*. (2013) shows potential source of hydrocarbon generation in the Late Carboniferous - Middle Permian sequences in the Karoo Basin with respect to the stratigraphic evolution of the successions. According to Peter and Cassa (1994), rocks with vitrinite reflectance greater than 1.35 % and temperature greater than 470 ℃ are termed post matured (see Table 8.7). Vitrinite maturation is not greatly affected by pressure but mostly by temperature and the conversion of organics to hydrocarbon depends on the temperature which the organics experienced during burial. Also, the kerogen type during diagenesis and early catagenesis is temperature dependent, therefore it can be inferred that the rocks of the lower Ecca Group are post matured based on the average vitrinite reflectance and temperature values of 5.63 % and 499.99 ℃ respectively.
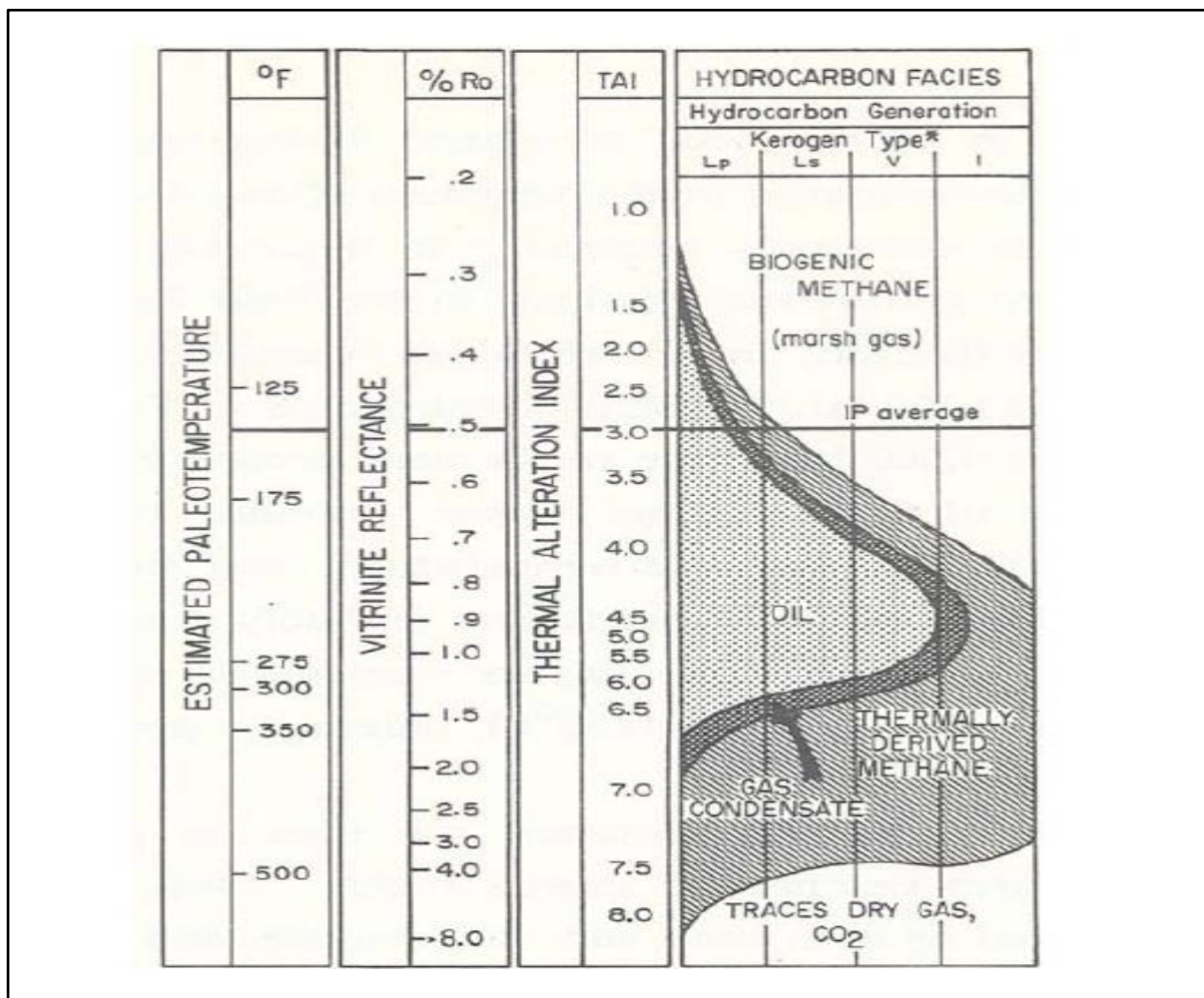
Figure 8.31 Relationship between depth, vitrinite reflectance and hydrocarbon facies (After Pusey, 1973).

According to Pussey (1973) in Tissot *et al*. (1984), vitrinite reflectance values of hydrocarbon source rock that falls between 0.4 % and 1.3 % denote that the source rock is within the oil generation window whilst source rock with values less than 0.5 % are considered thermally immature. Source rocks with vitrinite reflectance greater than 1.3 % suggest gas window maturity. Based on the Pussey (1973) classification (Figure 8.30), it can be inferred that the rocks of the lower Ecca Group belong to the dry gas window since the average vitrinite reflectance value is 5.63 %. Therefore, they are thermally mature for hydrocarbon (shale gas) generation. However, the reliability of the data cannot be ascertained and realistic migration could not be performed in the 1D model because the model lacks the essential dimensions that are required for petroleum accumulation and migration prediction, so it should only be considered as a possibility or likelihood.

8.4 Conclusions

Based on the data presented in this chapter, the following can be deduced:

- Based on the isochore (true vertical) thickness map, it could be inferred that the Beaufort Group is the thickest of all the groups that make up the Karoo Supergroup with maximum thickness of up to 6342 ± 295 m, followed by the Ecca and Dwyka Groups with maximum thicknesses of about 3207 ± 263 m and 727 ± 25 m, respectively.

- Based on the PetroMod 1D modelling, it can be deduced that the rocks of the lower Ecca Group (Prince Albert, Whitehill and Collingham Formations) possess source rock potential for significant hydrocarbon generations (i.e., shale gas) that can merit gas exploration in the Karoo Basin. This is supported by the vitrinite reflectance and temperature values, although the yield could not be ascertained.

CHAPTER NINE

DISCUSSION, CONCLUSIONS AND RECOMMENDATIONS

9.1 Discussion

This study used existing aeromagnetic, gravity and radiometric data to generate geophysical maps and models for the southeastern Karoo Basin. Petrographic and mineralogical studies were also undertaken to investigate sedimentary structures, mineral compositions and proffer sediment source area. The geophysical and geological investigation of the southeastern Karoo Basin revealed information about the magnetic, gravity and radiometric anomalies, sedimentary structures, mineralogy, depositional environments, thicknesses and the geological processes.

Petrographic studies on the Dwyka diamictite indicate the presence of monocrystalline quartz and granite components in the breccias which possibly indicate the existence of granitic and volcanic rocks in the source areas while the presence of quartzite components in the breccia suggest the presence of metamorphic and tectonically deformed source area. The lithology of the Ecca Group is dominated by shales, sandstones and siltstones and has a lack of conglomerates in all the formations and this is probably closely linked to the deep water of reducing (anoxic) environment.

Feldspar, quartz and micas occur as the major minerals in the rocks with lithics also forming part of the framework grains in the sandstones. Quartz and feldspar grains are both polycrystalline and monocrystalline, indicating that they were not fully separated by long transportation, which is consistent with the immature nature of the rocks. Hematite, garnet, rutile and zircon are the accessory minerals, whilst the clay minerals include; kaolinite, smectite, illite, sericite and chlorite. These minerals possibly exist in the rock either as detrital grains or diagenetic minerals. The detrital nature of the framework grains and the presence of lithic fragments, thus, render the rocks to be terrigenous in origin. From the observed lithics and heavy minerals and the nature of quartz and feldspar minerals, it can be deduced that, the provenances of the sediments were derived mostly from igneous and metamorphic rock sources, rarely from sedimentary rock source.

Based on the laterally extensive, ultra-tabular nature of the shales of the Whitehill and Collingham Formations, several authors (e.g. Johnson, 1976; Williamson, 1996; Catuneanu *et al*., 2005) suggested that the sediments were deposited in deep water and reducing environment while the co-existence of shales and mudstones in the Whitehill Formation suggest that the environment changed from low energy to high energy. The relative abundance of monocrystalline quartz, zoned albite and tuffaceous material in the Collingham Formation possibly indicates that granitic and volcanic rocks were also present in the sediment source area while the high percentage of alkali feldspars which are chemically more stable than the plagioclase signifies that granitic rocks are possibly dominant in the source area.

The brownish sandstone and mudstone of the Ripon and Fort Brown Formations signifies the presence of oxidizing condition during the time of burial of the sediment whilst the tabular lamination of the shale layers indicates deposition at low rate which is typical of marine environment. Petrographic studies on the sandstones of the Ecca and Beaufort Groups along the Ecca Pass and around Fort Beaufort show that the sandstones are poorly sorted and immature with irregular grain sizes and shapes and consist mostly of micas, feldspar, quartz and rock lithics with heavy minerals. The rock lithics give clues of igneous, metamorphic and volcanic origin, distance from source area and materials that are present in the source area. The assemblage of heavy minerals in the rocks of the Karoo Supergroup signify that the minerals are of granitic or mafic igneous and metamorphic origin due to the presence of ilmenite (0.03 – 0.52 %) and garnet (0.1 – 1.49 %). These findings are supported by several authors like Johnson *et al*. (2006) and Katemaunzanga and Gunter (2009) that the sediments of the Ecca and Beaufort Groups are from igneous, volcanic and metamorphic source area.

The observed cements are primarily quartz and calcite cement whilst the matrix is mostly of muscovite, biotite, calcite, chlorite and other clay minerals (mostly illite) with uniform patches which indicates that the rock is of authigenic origin and possibly subjected to very low grade metamorphic conditions. The fine-grained nature of the matrix suggests a detrital origin instead of authigenic origin. The lower part of the Ecca Group (e.g. Prince Albert, Whitehill and Collingham Formations) are dominated by shales and mudstones, whilst the upper part of the group (e.g. Ripon and Fort Brown Formations), sandstones content gradually increases, indicating the water depth of the depositional environment gradually

became shallow and changed from deep reducing (anoxic) to deltaic environment, and finally to the shallow lacustrine environment.

The average magnetic depths of about 0.6 km and 15 km were determined from the radially averaged power spectrum as the depths to the top of the shallow and deep sources respectively. The Beattie magnetic anomaly is one of the largest crustal anomalies in the world and trends northeast to southwest of the study area. It is suggested to be due to deeper source(s) possibly within the basement which agrees with the findings of Weckmann *et al*. (2007a). The anomaly which coincides with the "bean shape" anomaly (Figure 5.3) could possibly have the same source(s) with the BMA based on the depth slicing results.

Figure 6.3 shows high total gamma radiation count rate in the northeast part of the map. The relative high gamma radiation count rate of up to 26 count/sec in the western part of the study area could possibly be an extension of the uranium-rich belt that is associated with the shale and sandstones of the Karoo Supergroup in the Western Cape Province (Figure 1.1). The peak of the total radiation count rate (30 count/sec) seen in the northeast of Butterworth which is anomalous could also be an extension of the Karoo uranium province. This area (west of Jansenville in Figure 6.3) was previously mined for uranium (the depth is generally less than 30 m from the surface) and should be seriously checked or monitored when considering fracturing of the Karoo for shale gas. Generally, the igneous rocks of the Karoo strata are connected with relatively low total gamma radiation count rate, but it is fascinating to note that the concentration of high total radiation count rate in the Ecca and lower Beaufort Groups could be due to uranium and thorium in the detrital materials as well as the enrichment of radioelements in the feldspars (k-feldspar), calcite, quartz, zircon and clay minerals in the fluvial channel sandstones. This explanation (also given by Exxon) for the high radiation count rate in the Ecca and lower Beaufort Groups is evidenced in the XRD analysis results (Table 4.1and 4.2) and supported by several researchers like Johnson (1976 and 1991); Beaukes (1970); Grasty and Shives (1997); Cole and Wipplinger (2001). Basement granite and volcanic ash have been proposed as possible uranium sources for the Adelaide Subgroup and granite for the Molteno and Elliot formations. Clastic material containing uranium was probably transported into the basin by entrainment within fluvial sediments; also, some volcanic ash may have been transported and deposited. The stream or river that flows in the study area, especially around the mining site could also have transported a proportion of the radioelements (naturally occurring radioactive uranium and

thorium as well as their decay products (e.g. radon and radium) either in solution and/or adsorbed by clay minerals and organic detritus.

The density and porosity results show that the carbonaceous shale of the Whitehill Formation had the lowest average dry, wet and particle densities of 2.5258 g/cm^3, 2.5596 g/cm^3 and 2.6102 g/cm^3, respectively. The sandstones of the Oudeberg Member (Balfour Formation) had the highest average dry density of 2.7723 g/cm^3 whilst the sandstones of the Koonap Formation had the highest average wet and particle densities of 2.7913 g/cm^3 and 2.8277 g/cm^3 respectively. The weathered black carbonaceous shale of the Whitehill Formation had the highest average porosity of up to 3.31 %, followed by the mudstones of the Middleton Formation with a porosity of about 2.267 %. The diamictite of the Dwyka Formation have the lowest average porosity of about 0. 49 %. The study of the relationship between dry density and porosity of rocks from Karoo Supergroup generally shows linear relationships with high correlation values that are close to -1. Thus, it can be inferred that the parameters are closely related. The negative correlation implies that the lower the density, the higher the porosity and vice-versa, which agrees with the finding of various researchers (Gates and West, 2008; Adameso *et al*., 2012) that density increases with decrease in porosity. This was observed in the shales of the Whitehill Formation with highest average porosity (about 3.31 %) and lowest dry density (2.5258 g/cm^3).

The Bouguer anomaly map (Figure 7.4) shows an increase in gravity values from inland (southwestern and northern side of Jansenville) with the low gravity values of around -140.7 mGal to coastal areas with high gravity values of up to 60.1 mGal. The Bouguer anomaly map (Figure 7.4) give indications that the dominant gravity variation is of long wavelength, thus it is possibly due to a deeper source/interface inland that shallows towards the coast e.g. basement and/or Moho. This is seen on the gravity models presented in Figure 8.4 – 8.17. The Moho is at a depth of about 45 km inland and rises to about 42 km depth at the coast.

Based on the isochore thickness map results, it could be inferred that the Beaufort Group is the thickest of all the groups that make up the Karoo Supergroup with maximum thickness of up to 6342 $\pm$ 295 m, followed by the Ecca and Dwyka Groups with maximum thicknesses of about 3207 $\pm$ 263 m and 727 $\pm$ 25 m, respectively. The models in Figure 8.4 – 8.17 show undulations of the geologic sequence (group) which are consistent with deformation. Catuneanu *et al*. (2005) stated that tectonism was the main control on accommodation in the

Karoo basin, with subsidence mechanisms ranging from flexural in the south, in relation to processes of subduction and orogenesis along the paleo-Pacific margin, to extensional in the north, propagating southwards from the divergent Tethyan margin. The Karoo Basin responded to eight tectonic events related to the Panthalassan (paleo-Pacific) plate beneath Gondwana from the time of deposition of the Dwyka through to the Elliot Formation. These tectonic events produced variation in the depositional sedimentary successions within the Karoo setting (Catuneanu *et al*., 1998; Figure 8.21; 8.23; 8.25). According to Tankard *et al*. (2012) first-order faults and the rigid blocks of the basement between them controlled the basin style of subsidence as well as sedimentation. The thicknesses values are close those calculated by several authors (e.g. Johnson 1976; Johnson *et al*., 2006; Alao and Mikes, 2011) as shown in Table 8.3. The correlation of the isochore thickness map (Figure 8.23) with the depositional surface (elevation) map (Figure 8.22) for the Ecca Group shows that the sedimentary cover is thick in the western part and towards the northeastern parts of the map. Therefore, it is likely to favour hydrocarbon accumulation when other conditions necessary for hydrocarbon formation are present.

Based on the PetroMod 1D modelling, it can be deduce that the rocks of the lower Ecca Group (Prince Albert, Whitehill and Collingham Formations) possess source rock potential for significant hydrocarbon generations (i.e., shale gas) that can merit gas exploration in the Karoo Basin. This is supported by the vitrinite reflectance and temperature values and other authors (e.g. Cole and McLachlan, 1994; Schmidt, 2004; Geel *et al*., 2013), although the yield could not be ascertained.

Based on the structural control of deposition (sedimentation) in the southeastern Karoo Basin, it can be inferred that dolerite intrusions which are more prominent in the study area are interconnected as depicted in the models (Figure 8.4 - 8.17). This could possibly affect the quality of the shale resources and probably pose threat by increasing the risk of fracking the Karoo for shale gas exploration. The targeted depth for unconventional shale gas exploration in the Karoo Basin falls between 3000 to 5000 m below the ground surface (shown in Figure 8.14 – 8.17) and hydrogeological investigation of Karoo aquifers are limited to shallow depths of up to 500 m. Thus the interconnectivity of geologic structures like dolerite intrusions (mostly sills) at depth could pose a serious threat to fracking of the Karoo for shale gas as well as the excessive water that is required for fracking (about 25 million litres of water is required to frack a well which is equivalent to the average water consumption of a

Karoo town (e.g. Beaufort West, for approximately 3 days) and the possible environmental implications especially in area of high gamma radiation counts such as locations within the study area with high total gamma radiation count.

9.2 Conclusions

Based on the results presented in this study, the following conclusions are made:

- The sandstones of the Ecca and Beaufort Groups along the Ecca Pass and around Fort Beaufort are poorly sorted and immature. The sediment source area is close and is of igneous (granitic or mafic), metamorphic and volcanic origin.

- The average magnetic depths to shallow and deep sources are about 0.6 km and up to 15 km respectively.

- The magnetic signature (BMA) gets stronger with depth (seen up to 15 km) which could be an indication that the source is deeper. The bean-shape anomaly behaves in a similar manner.

- The high total gamma radiation count rate in the Ecca and lower Beaufort Groups are due uranium and thorium in the detrital material, as well as the enrichment of radioelements in the feldspars (k-feldspar), calcite, quartz, zircon and clay minerals in the fluvial channel sandstones.

- The density and porosity results show that the sandstones of the Oudeberg Member (Balfour Formation) had the highest average dry density of 2.7723 g/cm^3 whilst the sandstones of the Koonap Formation had the highest average wet and particle densities of 2.7913 g/cm^3 and 2.8277 g/cm^3 respectively. The weathered black carbonaceous shale of the Whitehill Formation had the highest average porosity of about to 3.31 %.

- The dominant gravity signatures in the study area is of long wavelength which is possibly due to a deep source/interface inland that shallows towards the coast e.g. basement and/or Moho. The Moho is at about 45 km depth inland and shallows to about 42 km at the coast.

- The Beaufort Group is the thickest of all the groups that make up the Karoo Supergroup with maximum vertical thickness of about 6342 ± 295 m. followed by the Ecca and Dwyka Groups with maximum vertical thicknesses of up to 3207 ± 263 m

and 727 ± 25 m, respectively. The variation in the derived vertical thickness is due to deformation.

- The rocks of the lower Ecca Group (Prince Albert, Whitehill and Collingham Formations) possess source rock potential for significant hydrocarbon generation (i.e., shale gas) that can merit gas exploration in the Karoo Basin.

This research study has contributed to the improvement of information or knowledge on the southeastern Karoo Basin. The project:

- Has determined the average depth to the top of the shallow and deep magnetic sources using the radially averaged power spectrum.
- Has suggested that the source of the Beattie magnetic anomaly appears to get stronger with depth which could be an indication of deep source(s).
- Has elucidated sedimentary layering and true-vertical thicknesses by building simple models from gravity profiles that traverse the southeastern Karoo Basin.
- The 2½ D modelling has revealed the configuration of the southeastern Karoo Basin and the thickness of the various formations. The modelling results have been used to show the isochore thickness and the depositional surfaces.
- Has performed 1D petroleum system modelling which gives a preliminary insight into assessing the potential of accumulation of oil and gas in the southeastern Karoo Basin.

This study has shown that the applications of geophysical surveys combined with geological investigations provide a powerful tool in delineating the lithological and structural setting that may influence or control the mineralization and hydrocarbon generation in southeastern Karoo Basin.

9.3 Recommendations

This project will possibly serve as a basis for future basin history models of the southeastern Karoo Basin. It is recommended that further investigation be carried out in the southeastern Karoo Basin by the same geophysical methods with high resolution data and finally drilling. This will assist in confirming the presence, exact location and inter-relationship between geological structures at depth which will help in assessing the risks of fracking the Karoo for shale gas. It is also strongly recommended that realistic gas migration should be performed in 2D and 3D PetroMod migration models because the 1D model lacks the essential dimensions that are required for petroleum accumulation and migration prediction.

REFERENCES

Aarnes, I., Svensen, H., Polteau, S. and Planke, S., (2011). Contact metamorphic devolatization of shales in the Karoo Basin, South Africa and the effects of multiple sill intrusions. Chemical Geology, vol. 281, p 181-194.

Adameso, O.A., Adekoya, J.A., and Olaleye, B.M., (2012). The inter-relationship of bulk density and porosity of some crystalline basement complex rocks: A case study of some rock type in South-western Nigeria. ISOR Journal of Engineering, vol. 2 (4), p 555 -562.

Advance Resource International, (2013). Shale gas and oil assessment in Karoo Basin, South Africa. In:EIA/ARI World Shale Gas and Shale Oil Resource Assessment. p1-14. http://www.adv-res.com/pdf/19_XIX_EIA_ARI__S%20Africa_June_2013.pdf

Akande, S.O., Ojo, O.J., Erdtmann, B.D. and Hetenyi, M., (1998). Paleoenvironments, source rock potential and thermal maturity of the Upper Benue rift basins, Nigeria: implications for hydrocarbon exploration. Organic Geochemistry, vol. 29, No 1–3, p 531–542.

Alao, A.O. and Mikes, D., (2011). Subsidence analysis of the Permian Tanqua depocentre, Southwestern Karoo Basin, South Africa. South Africa Journal of Geology, vol. 114, p 325-328.

Almond, J.E. (2010). Proposed iNca Energy wind facility on the farms Cathcarts Gift 311 and Latham 205 near Queenstown, Eastern Cape Province. Palaeontological impact assessment: combined desktop and scoping study, 30 pp. Natura Viva cc, Cape Town.

Almond, J.E., (2013). Palaeontological Heritage Study: Combined desktop and field based Assessment. Natura Viva cc, Cape Town, 33pp.

Anderson, P.O.D., Worden, R.H., Hodson, D.M. and Flint, S., (2004). Provenance evolution and chemostratigraphy of a Palaeozoic submarine fan-complex: Tanqua Karoo Basin, South Africa. Marine and Petroleum Geology, vol. 21, p 555-577.

Bajus, M., (2014). Shale gas and tight oil, unconventional fossil fuels. Petroleum and Coal, 56(3), 206-221. www.vurup.sk/petroleum-coal

Bamford, M.K., (2000). Fossil wood of Karoo age deposits in South Africa and Namibia as aid in biostratigraphical correlation. J. Afr. Earth Sci. 31, 119-132.

Bamford, M.K. (2004). Diversity of woody vegetation of Gondwanan southern Africa. Gondwana Research 7, 153-164.

Beattie, J.C., (1909). Report of a magnetic survey of South Africa. Royal Society of London Publication, Cambridge University Press, United Kingdom.

Beukes, N.J., (1970). Stratigraphy and sedimentology of the Cave Sandstone Stage, Karoo System. In: S.H. Haughton (Editor). Proceedings 2nd IUGS Symposium on Gondwana Stratigraphy and Palaeontology, CSIR, Pretoria, South Africa, p 321–341.

Bhattacharrya, B.K., (1966). Continuous spectrum of the total magnetic field anomaly due to a rectangular prismatic body. Geophysics vol 31 pp 97-121.

Bhattacharyya, B. K., and Lei-Kuang Leu., (1975). Spectral Analysis of gravity and magnetic anomalies due to two dimensional structures: Geophysics, vol. 40, pp. 993-1013.

Birkholz, M., Genzel, C. and Jung, T., (2004). X-ray diffraction study on residual stress and preferred orientation in thin titanium films subjected to a high ion f lux during deposition, J. Appl. Phys. vol. 96, 172pp.

Blakely, R.J., Langeheim, V.E., Ponce, D.A. and Dixon, G.L., (2000). Aeromagnetic survey of the Amargosa desert, Nevada and California: A tool for understanding near-surface Geology and hydrology. U.S. Geological Survey Open-File Report 00-188, 39pp.

Blakely, R.J., (1995). Potential theory in Gravity and Magnetic Applications: Cambridge University Press, Cambridge, UK, 441pp.

Bordy, E.M., Hancox, P.J. and Rubidge, B., (2005). The contact of the Molteno and Elliot Formations through the main Karoo Basin, South Africa: A second- sequence boundary. South Africa Journal of Geology, vol. 108, p 351-364.

Botha, J., And Smith, R.M.H., (2006). Rapid vertebrate recuperation in the Karoo Basin of South Africa following the End-Permian extinction: Journal of African Earth Science, v. 45, p. 502–514.

Bott, M. H. P., (1959). The use of electronic digital computers for the evaluation of gravimetric terrain corrections. Geophysical Prospecting 7, p46–54.

Bott, M. P. H., (1960). The use of rapid digital computing methods for direct gravity interpretation of sedimentary basins. Geophysical Journal, vol. 3, p63-67.

Bott, M. P. H., (1962). A simple criterion for interpreting negative gravity anomalies. Geophysics, 27(3), P376-381.

BP Statistical Energy Survey, (2012). BP Statistical Review of World Energy. 45p. http://www.bp.com/content/dam/bp/pdf/Statistical-Review 2012/

Branch, T., Ritter, O. and Weckmann, U., (2007). The Whitehill Formation − A High Conductivity Marker Horizon in the Karoo Basin. South African Journal of Geology, vol. 110, p. 465-476.

Brauer, B., Ryberg, T. and Lindeque, A.S., (2007). Shallow seismic velocity structure of the Karoo basin, South Africa. South Africa Journal of Geology, vol. 110, p 439-448.

Buhmann, C., (1992). Smectite-to-illite conversion in a geothermally and lithologically complex Permian sedimentary sequence. The Clay Minerals Society, vol. 40, no 1, p 53-64.

Cadle, A.B., Cairncross, B., Christie, A.D.M. and Roberts, D.L., (1993). The Karoo Basin of South Africa: type basin for the coal-bearing deposits of southern Africa. International Journal of Coal Geology, vol. 23, p 117-157.

Catuneanu, O., (2004). Retroarc foreland systems: evolution through time. Journal of African Earth Sciences, vol. 38, p 225-242.

Catuneanu, O., and Elango, H.N., (2001). Tectonic control on fluvial styles: the Balfour Formation of the Karoo Basin, South Africa. Sedimentary Geology. vol. 140, p. 291- 313.

Catuneanu, O., Hancox, P. J. and Rubidge, B.S., (1998). Reciprocal flexural behaviour and contrasting stratigraphies: a new basin development model for the Karoo retroarc foreland system, South Africa. Basin Research, vol. 10, p 417-439.

Catuneanu, O., Hancox, P.J., Cairncross, B. and Rubidge, B.S., (2002). Foredeep submarine fans and forebulge deltas: orogenic off-loading in the underfilled Karoo Basin. Journal of African Earth Sciences, vol. 35, p 489–502.

Catuneanu, O., Wopfner, H., Eriksson, P.G., Cairncross, B., Rubidge, B.S., Smith, R.M.H. and Hancox, P.J., (2005). The Karoo basins of south-central Africa. Journal of African Earth Sciences, vol. 43, p 211-253.

Cerovsk I. and Pasteka R., (2003). Imaging and clustering of depth estimations for Werner and 2D Euler deconvolution. Contributions to Geophysics and Geodesy,33/2.

Chevallier, L., Cole, D., de Beer, C., Gibson, L., Macey, P., Nhleko, L., Oosthuizen, B., Siegfried, P., Viljoen, J., Goedhart, M., Majokweni, L. and Rohwer, M., (2004). Geological cross sections across the Table Mountain Group for Water Research Commission project no K5/1419/1. Internal Report No. 2004–0119. Council for Geoscience, Pretoria, South Africa, 17pp.

Chevallier, L. and Woodford, A.C., (1999). Morpho-tectonics and mechanism of emplacement of the dolerite rings and sills of the western Karoo, South Africa. South African Journal of Geology, 102, 43–54.

Chevallier, L., Goedhart, M. and Woodford, A.C. (2001). The influences of dolerite sill and ring complexes on the occurrence of groundwater in Karoo fractured aquifers: a morpho-tectonic approach. Water Research Commission Report, 937/1/01, 146p.

Chovitz, B. H., (1981). Modern geodetic Earth reference models. EOS-Transactions of the American Geophysical Union 62(7), p 65-67.

Clark, D.A., (1997). Magnetic petrophysics and magnetic petrology: aids to geological interpretation of magnetic surveys. AGSO Journal of Australian Geology and Geophysics, vol. 17 (2), p 83-103.

Cloetingh, S., Lankreijer, A., De Wit, M.T., and Martinez, I., (1992). Subsidence history analysis and forward modelling of the Cape and Karoo Supergroup. In: de Wit, M.J. and Ransome, I.G.D., (Ed.), Inversion Tectonics of the Cape Fold Belt, Karoo and Cretaceous Basins of Southern Africa. Balkema, Rotterdam, Netherlands, p 239-248.

Coetzee, H., (2008). Acquisition, processing and enhancement of multi-channel radiometric data collected with ultralight aircraft mounted detectors. School of Geosciences. Johannesberg, University of the Witwatersrand. PhD Thesis: 357.

Cole, D.I., (1998). Uranium in the Mineral Resources of South Africa (M.G.C. Wilson and C.R. Anhaeusser, eds.), Handbook, Councilfor Geoscience, v. 16, p. 642-658.

Cole, D.I., (1992). Evolution and Development of the Karoo Basin. In: de Wit, M.J. and Ransome, I.G.D., (Ed.), Inversion Tectonics of the Cape Fold Belt, Karoo and Cretaceous Basins of Southern Africa. Balkema, Rotterdam, Netherland, p 87-100.

Cole, D.I. and McLachlan, I.R., (1994). Oil Shale Potential and Depositional Environment of the Whitehill Formation in the Main Karoo Basin. Internal Report No. 1994–0213, Council for Geoscience, Pretoria, South Africa, 146pp.

Cole, D.I. and Smith, R.M.H., (2008). Fluvial architecture of the Late Permian Beaufort Group deposits, S.W. Karoo Basin: Point bars, crevasse splays, palaeosols, vertebrate fossils and uranium. Field Excursion Guidebook, American Association of Petroleum Geologists International Conference, Cape Town, FT02, p 1 - 110.

Cole, D.I. and Wipplinger, P.E., (2001). Sedimentology and molybdenum potential of theBeaufort in the main Karoo Basin, South Africa. *Memoir, Council for Geoscience*, vol. 80, p 1-225.

Coney, L., Reimold, W.U., Hancox, P.J., Mader, D., Koeberl, C., McDonald, I., Struck, U., Vajda, V., and Kamo, S.L., (2007). Geochemical and mineralogical investigation of the Permian- Triassic boundary in the continental realm of the southern Karoo Basin, South Africa: Palaeoworld, v. 16, p. 67–104, doi: 10.1016/j.palwor.2007.05.003.

Cook, F. A., White, D. J., Jones, A. G., Eaton, D. W., Hall, J., and Clowes, R. M., (2010). How the crust meets the mantle: Lithoprobe perspectives on the Mohorovicic´ discontinuity and crust–mantle transition. Can. J. Earth Sci., vol. 47, p. 315–351.

Cooper G. R. J. and Cowan D. R., (2003). Sunshading geophysical data using fractional order horizontal gradients. The Leading Edge, 22, p 204.

Council for Geoscience, (1995). Geological Map of South Africa 1:250000, Sheet 2922 Prieska, Geological Survey of South Africa, Pretoria.

Cowan, D.R. and Cowan, S., (1993). Separation filtering applied to aeromagnetic data, Exploration Geophysics, vol. 24, p429-436.

Cordell, L., and Grauch, V.J.S., (1985). Mapping basement magnetization zones from aeromagnetic data in the San Juan basin, New Mexico, in Hinze, W.J., (ed), The utility of regional gravity and magnetic anomaly maps. SEG, p 181-197.

Crain, E.R., (2000). Online Shareware Petrophysics Training and Reference Manual (http://www.spec2000.net)

Crundwell, G., Phan, J. and Kantardjieff, K. A. (1999). The incorporation of a single-crystal X-ray diffraction experiment into the undergraduate physical chemistry laboratory. J. Chem. vol. 76, p1242-1245.

De Beer, J.H. and Gough, D.I., (1980). Conductive structures in southernmost Africa: a magnetometer array study. Geophysical Journal of the Royal Astronomical Society, vol. 63, p 479–495.

De Beer, J.H. and Meyer, R., (1983). Geo-electrical and gravitational characteristics of the Namaqua-Natal Mobile Belt and its boundaries. special publication Geology Society of South Africa, vol. 10, p 91–100.

De Kock, M.O., and Kirschvink, J.L., (2004). Paleomagnetic constraints on the Permian-Triassic boundary in terrestrial strata of the Karoo Supergroup, South Africa: Implications for causes of the end-Permian extinction event: Gondwana Research, v. 7, p. 175–183, doi: 10.1016/S1342-937X(05)70316-6.

Decker, J. and Marot. J., (2012). Investigation of hydraulic fracturing in the Karoo of South Africa. Annexure A, Resource Assessment, Petroleum Agency of South Africa. Available at: http://www.dmr.gov.za/publications/viewdownload/182/854.html

De Wit MJ (2011). The great shale debate in the Karoo. S Afr J Sci., 107(7/8), Art. No 791, 9 pages. doi:10.4102/sajs.v107i7/8.79.

De Wit, M.J. and Horsfield, B., (2006). Inkaba ye Africa Project Surveys Sector of Earth from Core to Space. EOS, American Geophysical Union, vol. 87, p 113–117.

De Wit, M.J. and Ransome, I.G., (1992). Regional inversion tectonics along the southern margin of Gondwana. In: De Wit, M.J. and Ransome, I.G. (Ed), Inversion tectonics of the Cape Fold Belt, Karoo and Cretaceous Basins of Southern Africa. Rotterdam, 15-22.

Dobrin, M.B. and Savit, C. H. (1988). Introduction to Geophysical Prospecting, 4th Edition, McGraw-Hill, New York. 867pp.

Duncan, R.A., Hooper, P.R., Rehacek, J., Marsh, J.S. and Duncan, A.R., (1997). The timing and duration of the Karoo igneous event, southern Gondwana. Journal of Geophysical Research, 102B8, 18127-18138.

Du Toit, A.L. (1920). The Karoo dolerites of South Africa: a study in hypabyssal injection. Transactions of the Geological Society of South Africa, 23, 1–42.

Du Toit, A.L. (1954). The Geology of South Africa. Oliver and Boyd, Edinburgh.

Duncan, R.A., Hooper, P.R., Rehacek, J., Marsh, J.S. and Duncan, R.A., (1997). The timing and duration of the Karoo igneous event, Southern Gondwana. Journal of Geophysical Research, vol.102, p. 18127–18138.

Econometrix, (2012). Karoo shale gas report: special considerations surrounding potential shale gas resources in the southern Karoo of South Africa. Available at: http://www-tatic.shell.com/static/zaf/downloads/aboutshell/econometrix/econometrix_report.pdf

Energy Information Administration, (2011). World shale gas resources: an initial assessment of 14 regions outside the United States. Available at: http://www.eia.gov/analysis/studies/worldshalegas/pdf/fullreport.pdf

Energy Information Administration, (2013). South Africa has one of the world's largest synthetic fuels industries, which accounts for nearly all of its domestic liquid fuels supply. Available at: http://www.iberglobal.com/files/sudafrica_eia.pdf

Eriksson, P.G., (1983). Palaeoenvironmental Study of the Molteno, Elliot and Clarens Formations in the Natal Drakensberg and Northeastern Orange Free State. Unpublished PhD thesis, University of Natal, South Africa, 209 pp.

Eriksson, P.G., (1984). A palaeoenvironmental analysis of the Molteno Formation in the Natal Drakensberg. Transactions Geological Society of South Africa, vol. 87, p 237-244.

Featherstone, W. E., and Dentith M. C., (1997). A geodetic approach to gravity data reduction for geophysics. Computers & Geosciences. Vol. 23, No. 10, p1063-1070.

Flint, S.S., Hodgson, D.M., Sprague, A.R., Brunt, R.L., Van der Merwe, W.C., Figueiredo, J., Prélat, A., Box D., Di Celma C., and Kavanagh, J.P., (2011). Depositional architecture and sequence stratigraphy of the Karoo basin floor to shelf edge succession, Laingsburg depocentre, South Africa. Marine and Petroleum Geology 28, p 658-674.

Fildani, A., Drinkwater, N. J., Weislogel, A., McHargue, T., Hodgson, D., and Flint, S., (2007). Age controls of the Tanqua and Laingsburg deep-water systems: new insights on the evolution and sedimentary fill of the Karoo basin, South Africa. Journal of sedimentary Research, 77, 901-908.

Fildani, A., Weislogel, A., Drinkwater, N. J., McHargue, T., Tankard, A., Wooden, J., Hodgson, D. and Flint, S., (2009). U-Pb zircon ages from the southwestern Karoo Basin, South Africa-- Implications for the Permian-Triassic boundary. Geology, 37, 719-722.

Fuller, B.D., (1967). Two-dimensional frequency analysis and design of grid operators, in Hansen, D.A., Heinrichs, W.E., Holmer, R.C., MacDougall, R.E., Rogers, G.R., Sumner, J.S., and Ward, S.H., 1967, Society of Exploration Geophysicists' Mining Geophysics, Vol. 2, p. 658-708.

Galfetti, T., Bucher, H., Ovtcharova, M., Schaltegger, U., Brayard, A., Brü̈hwiler, T., Goudemand, N., Weissert, H., Hochuli, P.A., Cordey, F., and Guodun, K., (2007). Timing of the Early Triassic carbon cycle perturbations inferred from new U–Pb ages and ammonoid biochronozones: Earth and Planetary Science Letters, v. 258, p. 593–604.

Galerne, C.Y., Neumann, E.-R., and Planke, S., (2008). Emplacement mechanisms of sill complexes: information from the geochemical architecture of the Golden Valley Sill Complex, South Africa. J. Volcanol. Geoth. Res. 177 (2), 425–440.

Galerne, C.Y., Galland, O., Neumann, E.-R. and Planke, S., (2011). 3-D relationships between sills and their feeders: evidence from the Golden Valley Sill Complex (Karoo basin) and experimental modeling. Journal of Volcanology and Geothermal Research, 202, 189-199.

Gastaldo, R.A., Neveling, J., Clark, C.K., And Newbury, S.S., (2009). The terrestrial Permian–Triassic boundary event bed is a non-event: Geology, v. 37, p. 199–202.

Gates, W.C.B. and West, P.K., (2008). Estimating the unconfined compressive strength of vessicular basalts via bulk specific gravity of the rock Sample. The 42nd U.S. Rock Mechanics Symposium, San Francisco, CA. Paper No. 08-131.

Geel, C., Schulz, H., Bootha, P., de Wit, M., and Horsfield, B., (2013). Shale gas characteristics of Permian black shales in South Africa: results from recent drilling in the Ecca Group (Eastern Cape). Energy Procedia 40, p. 256 – 265.

Gough D., De Beer, J.H., and van Zijl, J., (1973). A magnetometer array study in southern Africa, Geophysical Journal of the Royal Astronomical Society, vol. 34, p 421-433.

Gradstein, F.M., Ogg, J.O., and Smith, A.G., (2004). A Geologic Time Scale: Cambridge, U.K., Cambridge University Press, 500 p.

Grant, J.A., (1998). Ten things the textbooks don't tell you about processing and archiving airborne gamma ray spectrometric data. In Current Research 1998 D. Geological Survey of Canada, Ottawa, 83-87.

Grasty, R.L., and Sander, L., (2001). Airborne gamma ray surveys over Canadian nuclear sites. Expanded Abstracts, 63rd Annual Conference, European Association of Geoscientists and Engineers.

Grasty, R.L., and Shives, R.B., (1997). Applications of gamma ray spectrometry to mineral exploration and geological mapping, Workshop presented at Exploration 97: Fourth Decennial Conference on Mineral Exploration.

Gresse, P.G., Theron, J.N., Fitch, F.J. and Miller, J.A., (1992). Tectonic inversion and radiometric resetting of the basement in the Cape Fold Belt. In: Inversion Tectonics of the Cape Fold Belt, Karoo and Cretaceous Basins of Southern Africa (Ed. by M.J. De Wit and I.G.D. Ransome), p 217 – 228.

Gunn, P.J., (1972). Application of Wiener filters to transformations of gravity and magnetic data: Geophysical Prospecting, v. 20, p. 860-871.

Gunn, P.J., Maidment, D. and Milligan, P.R., (1997). Interpreting aeromagnetic data in areas of limited outcrop. AGSO Journal of Australian Geology and Geophysics, vol.17 (2), p 175-185.

Hälbich, I.W., Fitch, F.J. and Miller, J.A., (1983). Dating the Cape orogeny, Special Publications of the Geological Society of South Africa, vol. 12, p 149–164.

Hälbich, I.W., (1993). Global Geoscience Transect 9. The Cape Fold Belt - Agulhas Bank transect across Gondwana Suture, Southern Africa. American Geophysical Union Special Publication, vol. 202, 18p.

Hammer, S., (1939). Terrain corrections for gravimeter stations. Geophysics, 4(3) p184-194.

Hammer, S., (1984). Discussion on "Airborne gravity is here!" Geophysics, 49(4) 471-472.

Hancox, P.J. and Rubidge, B.S., (2001). Breakthroughs in the biodiversity, biogeography, biostratigraphy and basin analysis of the Beaufort Group. African Earth Sciences, vol. 33, p 563–577.

Hancox, P.J. (1998). Stratigraphic, sedimentological and palaeoenvironmental synthesis of the Beaufort-Molteno contact in the Karoo Basin. Unpublished PhD Thesis, University of the Witwatersrand, South Africa, 380pp.

Hancox, J., Neveling, J. and Rubidge, B., (2010). Life in an Early Triassic lake: new developments at the Driefontein site, Burgersdorp Formation (Cynognathus Assemblage Zone), South Africa. Proceedings of the 16th Conference of the PSSA, Howick, Umgeni Valley Nature Reserve, 41-42.

Hansen, S.E., Nyblade, A.A., and Julia, J., (2009). Estimates of crustal and lithospheric thickness in Sub-sahara Africa from s-wave receiver functions. South Africa Journal of Geology, vol. 112, p 229-240.

Hartnady, C.J.H., (1985). Uplift, faulting seismicity, thermal spring and possible incipient volcanic activity in the Lesotho-Natal region, SE Africa: the Quathlamba hotspot hypothesis. Tectonics, vol.4, p 371-377.

Hartnady, C.J.H., (1990). Seismicity and plate boundary evolution in south-eastern Africa. South Africa Journal of Geology, vol. 93, p 473-474.

Harvey, J.D., De Wit, M.J., Stankiewicz, J. and Doucouré, C.M., (2001). Structural variations of the crust in the Southwest Cape, deduced from seismic receiver functions. South African Journal of Geology, vol. 104, p 231–242.

Haughton, P., Davis, C., McCaffrey W., and Barker S., (2009). Hybrid sediment gravity flow deposits – Classification, origin and significance. Marine and Petroleum Geology 26, pp. 1900 –1918.

Henke, K.R., (2011). Actualism (Modern Uniformitarianism) and its Assumptions. "Rock Solid Answers" in Oard and Reed (2009). The Biblical Truth Behind 14 Geological Questions, Master Books: Green Forest, AR, pp. 111-123.

https://sites.google.com/site/respondingtocreationism/documents/actualism-assumptions

Hobday, D.K., (1973). Middle Ecca deltaic deposits in the Muden-Tugela Ferry area of Natal. Transactional Geological Society of South Africa, vol. 76, p 309-318.

Hodgson, D.M., Flint, S.S., Hodgetts, D., Drinkwater, N.J., Johannesson, E.J., and Andluthi, S.M., (2006). Stratigraphic evolution of Permian submarine fan systems, Tanqua depocenter, South Africa: Journal of Sedimentary Research, v. 76, p. 19–39.

Hood P., (1965). Gradient measurements in aeromagnetic surveying. Geophysics 30, p 891-902

Hood, P.J., and Teskey, D.J., (1989). Aeromagnetic gradiometer program of the Geological Survey of Canada, Geophysics vol 54, p 1012-1022.

Horton, C. W., Hempkins W. B. and Hoffma, A. J., (1964). A statistical analysis of some aeromagnetic maps from the northwestern Canadian shield, Geophysics 29, pp. 582-601.

Hovgaard, J. and Grasty, R.L. (1997). Reducing statistical noise in airborne gamma ray data through spectral component analysis. Proceedings of Exploration 97: Fourth Decennial International Conference on Mineral Exploration. Toronto, pp753-764.

Hunter, D.R. and Reid, D.L. (1987). Mafic dike swarms in Southern Africa. In: H. C. Halls and W. F. Fahrig (Editors), Mafic Dike Swarms. Geological Association of Canada Special Paper, 34, 445-456.

Hynes, A., and Snyder, D. B., (1995). Deep-crustal mineral assemblages and potential for crustal rocks below the Moho in the Scottish Caledonides. Geophysical Journal International, Vol. 123, Issue 2, p. 323-339.

IAEA, (1997). Airborne Gamma Ray Spectrometer Surveying. Technical Report No. 323. International Atomic Energy Agency, Vienna, Austria.

IAEA, (2003). Guidelines for radioelement mapping using gamma ray spectrometry data. International Atomic Energy Agency, Vienna, Austria.

Ingersoll, R.V. and Busby, C.J., (1995). Tectonics of sedimentary basins. In: Tectonics of sedimentary basins (Ed. by C.J. Busby and R.V. Ingersoll), Blackwell Scientific Publications, USA, p 1-51.

Isbell, J. L., Cole, D. I. and Catuneanu, O., (2008). Carboniferous - Permian glaciation in the main Karoo Basin, South Africa: Stratigraphy, depositional controls, and glacial dynamics. In: Fielding, C.R., Frank, T.D., and Isbell, J.L. (Eds.). Resolving the Late Palaeozoic ice age in time and space. Geological Society of America Special Paper, vol. 441, p 71 - 82.

James D. E., Niub, F., and Rokosky, J., (2003). Crustal structure of the Kaapvaal craton and its significance for early crustal evolution. Lithos 71, p 413 – 429.

Jeffery, D. P., (1998). Processing and interpretation of aeromagnetic data for the Santa Cruz Basin-Patagonia mountain area, south central Arizona, Open-File Report 02- 98, USGS.

John, E. A., (2013). Palaeontological heritage study: Combined desktop and field-based assessment. In: Rehabilitation of National Route r61 (Section 3, km 24.2 to 75) between Cradock and Tarkastad, Eastern Cape. p 1-46. naturaviva@universe.co.za

Johnson, M. R., (1976). Stratigraphy and sedimentology of the Cape and Karoo sequences in the Eastern Cape Province. PhD Thesis (unpublished), Department of Geology, Rhodes University, Grahamstown.

Johnson, M.R., (1991). Sandstone petrography, provenance and plate tectonic setting in Gondwana context of the south-eastern Cape Karoo basin. South African Journal of Geology, vol. 94, p 137-154.

Johnson, M.R., van Vuuren, C.J., Hegenberger, W.F., Key, R. and Shoko, U., (1996). Stratigraphy of the Karoo Supergroup in southern Africa: an overview. Journal of African Earth Sciences, vol. 23, p 3–15.

Johnson M., van Vuuren C., Visser J., Cole D., de Wickens H., Christie A. and Roberts D., (1997). The Foreland Karoo Basin, South Africa., In: R. Selley (Editor). African Sedimentary Basins of the World, Elsevier, Amsterdam, vol. 3, 269-317.

Johnson, M.R., van Vuuren C.J., Visser, J.N.J., Cole, D.I., Wickens H. de V., Christie, A.D.M., Roberts, D.L and Brandl, G., (2006). Sedimentary Rocks of the Karoo

Supergroup. In: Johnson, M.R., Anhaeusser, C.R. and Thomas, R.L. (Eds.), The Geology of South Africa. Geological Society of South Africa, Johannesberg/Council for Geoscience, Pretoria. p 461-499.

Kakaba, M., (2010). Neotectonics and its applications for the exploration of groundwater in the fractured Karoo aquifers in the Eastern Cape, South Africa. M.Sc thesis (unpubl.), Geology department, University of Fort Hare, South Africa.

Kane, M. F., (1962). A comprehensive system of terrain corrections using a digital computer. Geophysics, 27(4), p 455-462.

Karpeta, W. P. and Johnson, M., R., (1979). The geology of Umtata area. Exploration to 1:250000 geology sheet 3128 Umtata, 16pp. Council for Geoscience, Pretoria.

Katemaunzanga, D. and Gunter, C.J., (2009). Lithostratigraphy, sedimentology and provenance of the Balfour Formation, Beaufort Group in the Fort Beaufort Alice area, Eastern Cape Province, South Africa. Acta Geologica Sinica (English Edition), vol. 83, No 5, p 902-916.

Killeen, P.G., (1979). Gamma ray spectrometric methods in uranium exploration – application and interpretation. In Geophysics and Geochemistry in the Search for Metallic Ores, edited by P.J. Hood, Geological Survey of Canada Economic Geology Report 31, 163-230.

Kingsley, C. S., (1977). Stratigraphy and sedimentology of the Ecca Group in the eastern Cape Province, South Africa. Ph.D. thesis (unpubl), Univ. Port Elizabeth, S. Afr., 290 pp.

Kock, M.O., (2003). Magnetostratigraphic studies in the main Karoo Basin (South Africa): Implications for mass extinction events and the supercontinent of Pangea. M.Sc thesis (unpubl.), Geology department, Rand Afrikaans University, South Africa.

Korte, M., Mandea, M., Kotze, P., Nahayo, E., and Pretorius, B., (2007). Improved observations at the southern Africa geomagnetic repeat station network, South Africa Journal of Geology, vol. 110, p 175-186.

Kuhlmann, G., Adams, S., Anka, Z., Campher, C., Di Primio, R., and Horsfield, B., (2011). 3D petroleum systems modelling within a passive margin setting, Orange Basin, Block 3/4, off shore South Africa: Implications for gas generation, migration and leakage. South Africa Journal of Geology, vol. 114, p 381-414.

Langel, R. A., Barraclough, D. R. Kerridge, D. J. Golovkov, V. P. Sabaka, T. J., and Estes, R. H. (1988). Definitive IGRF Models for 1945, 1950, 1955, and 1960. Journal of Geomagn. Geoelectr. Vol. 40, p 645- 683.

Li, X., (2006). Understanding 3D analytic signal amplitude.Geophysics 71(2), L13–L16. doi: 10.1190/1.2184367.

Lindeque, A., De Wit, M. J., Ryberg, T., Weber, M., and Chevallier, L., (2011). Deep crustal profile across the Southern Karoo basin and Beattie magnetic anomaly, South Africa: An integrated interpretation with tectonic implications. South Africa Journal of Geology, vol. 114, p 265-292.

Lindeque, A., Ryberg, T., Weber, M., Stankiewicz, J., and De Wit, M.J., (2007). Deep crustal seismic reflection experiment across the Southern Karoo basin, South Africa. South Africa Journal of Geology, vol. 110, p 419-438.

Liu K.W., (1999). Nature and distribution of heavy minerals in the Natal Group, South Africa. The Geological Society of London, special publications, vol. 163, p 311-325.

Lock, B.E., (1978). The Cape Fold Belt of South Africa; tectonic control of sedimentation. Geological Association of London. Proc., vol. 89, p 263-281.

Lock, B.E., (1980). Flat-plate subduction and the Cape Fold Belt of South Africa. South Africa Journal of Geology, vol. 8, p 35-39.

Louro, V.H., and Mantovani, M.S.M., (2012). 3D inversion and modelling of magnetic and gravimetric data characterising the geophysical anomaly source in Pratinha, in the south east of Brazil. Journal of Geophysics, p 110 - 120.

Lurie, J., (1981). South African geology for mining, metallurgical, hydrological and civil engineering. 3rd Edition ed. Johannesburg: McGraw-Hill Book Company.

Luyendyk, A.P.J., (1997). Processing of airborne magnetic data. AGSO Journal of Australian Geology and Geophysics, vol. 17 (2), p 31-38.

Madi, K. and Zhao, B., (2010). The role of extensional fractures and quartz veins in the formation of kaolin deposit from the Dwyka Tillite in Grahamstown, Eastern Cape Province, South Africa. 1st ICCCM and 2nd ICGGSA, p 41- 46.

Mahanyele, P.J. and Botha, W.J., (2008). Detail geophysical interpretation of high resolution airborne magnetic data, Matla mine. Exxaro internal report. 18pp.

Mahanyele, P.J., (2010). Interpretation of airborne magnetic data over selected areas of Witbank coalfield, South Africa: An aid to mine planning. M.Sc thesis (unpubl.), Geology department, university of Pretoria, South Africa.

Marquardt, D.k., (1963). An algorithm for least squares estimation of non-linear parameters. J ournal Society Industrial Applied Mathematics. Vol.11, No. 2, p 431-441.

Maslen, E. N., Fox, A. G., and Keefe, M. A. (2004). X-ray Scattering, in: E. Prince (Ed), International Tables for Crystallography, p. 554.

Maxwell, J.C., (1964). Influence of depth; temperature and geological age on porosity of quartzose sandstones. Bull. Amer. Assoc. Petrol. Geol., vol. 48, issue 5, p 697-709.

Mbendi Information Services (2014). Electrical power in South Africa.
http://www.mbendi.com/indy/powr/af/sa/p0005.htm

McCarthy, T. and Rubidge, B., (2005). The story of Earth and life: a southern African perspective on a 4.6-billion-year journey. 334pp. Struik, Cape Town.

McKenzie, D., (1978). Some remarks on the development of sedimentary basins, Earth and Planet Sci. lett., vol. 40, pp25-32.

McLachlan, I. and Davis, A., (2006). Petroleum exploration in the Karoo Basins, South Africa. Petroleum Agency of South Africa.

Meyer, W., (1965). The geology of a portion of south-western Albany. M.Sc. Thesis (unpublished.) Rhodes University, Grahamstown, 67 pp.

Milani, E. J. and De Wit, M. J., (2008). Correlations between the classic Parana and Cape-Karoo sequences of South America and Southern Africa and their basin infills flanking the Gondwanides; du Toit revisited. In: Pankhurst, R.J., Trouw, R.A.J., Brito, Neves, B.B., De Wit, M.J., (Eds.), west Gondwana: Pre-Cenozoic correlations across the south Atlantic Region. Geological Society Special Publications 294, p 319-342.

Milligan, P.R. and Gunn, P.J., (1997). Enhancement and presentation of airborne geophysical data. AGSO Journal of Australian Geology and Geophysics, vol. 17 (2), p 63-75.

Minty, B.R.S., (1997). The fundamental of airborne gamma-ray spectrometry. AGSO Journal of Australian Geology and Geophysics vol. 17 (2), p39-50.

Mitrovica, J., Mound, J., Pysklywec, R., and Milone, G., (2000). Sea-level change on a dynamic Earth. In: E.Boschi, G.Esktrom and A. Morelli, Editors, problems in Geophysics for the New Millenium, Editrice Compository, p. 499-529.

Mjelde, R., Goncharov, A., and Müller, R. D., (2013). The Moho: Boundary above upper mantle peridotites or lower crustal eclogites? A global review and new interpretations for passive margins. Tectonophysics, vol. 609, p. 636–650.

Moritz, H., (1980). Geodetic Reference System 1980. Bulletin Geodesique, Vol. 54 (3), p 395-405.

Mussett, A.E., and Khan, M.A., (2000). Looking into the Earth: an introduction to geological geophysics, published by the press Syndicate of the University of Cambridge, United Kingdom. p. 107-179.

Nabighian, M.N., (1984). Toward a three-dimensional automatic interpretation of potential field data via generalized Hilbert transforms: fundamental relations, Geophysics, vol. 49, p 780-786.

Nabighian, M.N., Grauch, V.J.S., Hansen, R.O., LaFehr, T.R., Li, Y., Pierce, J.W., Philips, J.D. and Ruder, M.E. (2005). The historical development of the magnetic method in exploration. Geophysics, 70 (6), p 33-61.

Newton, A.R., (1992). Thrusting on the northern margin of the Cape Fold Belt, nears Laingsburg. In: M. J. De Wit and I.D.G. Ransome (Editors). Inversion tectonics of the Cape Fold Belt, Karoo and Karoo and Cretaceous basins of Southern Africa, Balkema, Rotterdam, Netherlands, 193-197.

Newton, A.R., Shone, R.W. and Booth, P.W.K., (2006). The Cape Fold Belt. In: Johnson, M.R., Anhaeusser, C.R. and Thomas E.R., (Eds.). The Geology of South Africa. The Geological Society of South Africa. Johannesburg/Council for Geoscience, Pretoria, 521 - 530.

Neveling, J., (2004). Stratigraphic and sedimentological investigation of the contact between the Lystrosaurus and the Cynognathus Assemblage Zones (Beaufort Group: Karoo Supergroup): Council for Geoscience, Pretoria, Bulletin 137, 165 p.

Nicole, P., Karsten, G., and Gabriele, U., (2007). Deep crustal structure of the sheared South African continental margin: first results of the Agulhas-Karoo Geoscience Transect. South Africa Journal of Geology, vol. 110, p 393-406.

Oberbeck, V. R., Marshall J. R., and Aggarwal, H., (1993). Impacts, tillites, and the breakup of Gondwanaland. J. Geol. 101, 1–19.

Omosanga, K.O., Mosuro, G.O., Laniyan, T.A., and Ogunleye, D., (2012). Prediction of gravity anomaly from calculated densities of rocks. Advances in Applied Science Research, Pelagia Research library, www.pelagiaresearchlibrary.com

Online references (http://karoospace.co.za/dolerite-karoos-fracking-game-changer; http://en.wikipedia.org/wiki/Karoo_Supergroup).

Ovtcharova, M., Bucher, H., Schaltegger, U., Galfetti, A., Brayard, J., and Guex, J., (2006). New early to middle Triassic U-Pb ages from South China: Calibration with ammonoid biochronozones and implications for the timing of the Triassic biotic recovery: Earth and Planetary Science Letters, v. 243, p. 463–475.

Pángaro, F., and Ramos, V.A., (2012). Palaeozoic crustal blocks of onshore and offshore central Argentina: New pieces of the southwestern Gondwana collage and their role in the accretion of Patagonia and the evolution of Mesozoic south Atlantic sedimentary basins. Marine and Petroleum Geology. vol.37, p162.

Pace, D. W., Gastaldo, R. A., and Neveling, J. (2009). Early Triassic aggradational and degradational landscapes of The Karoo Basin and evidence for climate oscillation following the P–TR event. Journal of Sedimentary Research, v. 79, 316–331.

Paton, A.D., Di Primio, R., Kuhlmann, G., Van der Spuy, D. and Horsfield, B., (2006). Insight into the petroleum system evolution of the Southern Orange Basin, South Africa. South Africa Journal of Geology, vol. 110, p 261-274.

Peters, K.E. and Cassa, M.R., (1994). Applied Source Rock Geochemistry. In: Magoon, L.B., Dow, W.G. (Eds.). The Petroleum System – From Source to Trap. American Association of Petroleum Geologists Memoir, 60, 93-120.

Pettijohn F.J., (1975). Sedimentary Rocks. 3rd edition. Harper and Row, New York, 628 p.

Pettijohn F.J., Potter, P.E. and Siever R., (1987). Sand and Sandstone. 2nd edition. Springer-Verlag, New York, 553 p.

Petroleum Exploration and Production Activities in South Africa (2010). Petroleum Agency South Africa. http://www.petroleumagencysa.com/files/Hubmap_09-10.pdf.

Phillips, J.D., (1979) ADEPT: A program to estimate depth to magnetic basement from sampled magnetic profiles. U.S. Geological survey Open File Report. p 79-367.

Phillips, J. D., (2002). Processing and interpretation of aeromagnetic data for the Santa Cruz Basin. Patagonia Mountains area, South-Central Arizona. U.S. Geological Survey, Open-File, Report 02-0098. http://geopubs.wr.usgs.gov/open-file/of 02-98/

Pitts B., Mahler M., de Beer J. and Gough D., (1992). Interpretation of magnetic, gravity and magnetotelluric data across the Cape Fold Belt and Karoo Basin, In: De Wit M., and Ransome I. (Editors), Inversion tectonics of the Cape Fold Belt, Karoo and Cretaceous basins of southern Africa. Balkema, Rotterdam, Netherlands. p 27-32.

Pringle, J. K., Brunt, R. L., Hodgson, D.M., and Flint, S.S., (2010). Capturing stratigraphic and sedimentological complexity from submarine channel complex outcrops to digital 3D models, Karoo Basin, South Africa. Geological Society of London, vol. 16, p 307-330.

Pusey, W.C., (1973). The ESR method: A new technique of estimating the organic maturity of sedimentary rocks. Petroleum Times, vol. 32, p 21-24.

Rabeh, T., Abdallatif, T., Mekkawi, M., Khalil, A. and El-emam, A., (2008). Magnetic data interpretation and depth estimation constraints: a correlative study on magnetometer and gradiometer data. NRIAG Journal of Geophysics Special Issue, PP. 185 –209.

Rampino, M. R., (1994). Tillites, diamictites, and ballistic ejecta of large impacts. J. Geol. 102, 439–456.

Reeves, C.V., (2005). Aeromagnetic surveys (principles, practice and interpretation). Published by Geosoft p1–146.

Reid, A.B., Allsop, J.M., Granser, H., Millett, A.J., and Somerton, I.W., (1990). Magnetic interpretation in three dimensions using Euler deconvolution. Geophysics vol 55, pp 80-91.

Reid, D.L. and Rex, D.C., (1994). Cretaceous dikes associated with the opening of the South Atlantic: the Mehlberg dike, northern Richtersveld. South African Journal of Geology, 97, 135-145.

Reimold, W. U., von Brunn V., and Koeberl, C., (1997). Are diamictites impact ejecta? No supporting evidence from South African Dwyka Group diamictite. J. Geol. 105, 517–530.

Retallack, G.J., Metzger, C.A., Greaver, T., Jahren, A.H., Smith, R.M.H., and Sheldon, N.D., (2006). Middle-Late Permian mass extinction on land: Geological Society of America Bulletin, v. 118, p. 1398–1411, doi: 10.1130/B26011.1.

Reynold, J.M., (1997). An introduction to applied and environmental geophysics, John Wiley and Sons, NY, 806p.

Roest, W.R., J. Verhoef and M. Pilkington, (1992). Magnetic interpretation using the 3-D analytic signal. Geophysics, vol. 57 (6), p116-125.

Rubidge BS. (2005). Re-uniting lost continents – Fossil reptiles from the ancient Karoo and their wanderlust. S Afr J Geol.v.108, p135–172. http://dx.doi.org/10.2113/108.1.135

Rubidge, B. S., Hancox, P. J., and Catuneanu, O., (2000). Sequence analysis of the Ecca-Beaufort contact in the Southern Karoo of South Africa. South Africa Journal of Geology, vol. 103, p 81-96.

Rust, I.C., (1973). The evolution of the Paleozoic Cape Basin, southern margin of Africa. In: Nairn, A.E.M., Stehli, F.G. (Eds.), The Ocean Basins and Margins. The South Atlantic, Plenum Publishing Corp., New York, pp. 247-276.

Saltus, R.W. and Blakely, R.J., (1983). HYPERMAG, an interactive, two-dimensional gravity and magnetic modelling program. U S Geological Survey, Open File, Report 83-241.

Sandberg C. H., (1958). Terrain corrections for an inclined plane in gravity computations. Geophysics 23, p701–711.

SACS, South African Committee for Stratigraphy, (1980). Stratigraphy of South Africa. Part 1: Lithostratigraphy of the Republic of South Africa, South West Africa/Namibia and the Republics of Bophuthatswana, Transkei and Venda (Compiled by Kent, L.E.). Geological Survey of South Africa. Handbook, 8, 690pp.

Schlumberger Information Solutions (2013). Introduction to PetroMod (workflow/solution training and exercise guide, version 2012.2), p1-218.

Schmidt, S., (2004). The petroleum potential of the passive continental margin of South-Western Africa – A Basin Modelling Study. Unpublished PhD dissertation, Fakultät für Georessourcen und Materialtechnik der Rheinisch-Westfälischen Technischen Hochschule Aachen, Germany, 182pp.

Scott, E.D., (1997). Tectonics and sedimentation: the evolution, tectonic influences and correlation of the Tanqua and Laingsburg subbasins, southwest Karoo basin, South Africa. Ph.D. Thesis (unpubl.), Louisiana State University, 167p.

Segwabe, T., (2008). The Geological Framework and Depositional Environments of the Coal-Bearing Karoo Strata in the Central Kalahari Karoo Basin, Botswana. M.Sc thesis (unpubl.), Rhodes University, South Africa. http://eprints.ru.ac.za/1737/1/Segwabe.pdf

Sharma, S.P., and Baranwal, V.C., (2005). Delineation of groundwater-bearing fracture zones in a hard rock area integrating very low frequency electromagnetic and resistivity data. Journal of Applied Geophysics 57, p 155-166.

Sharma, S.R., Poornachandra Rao, G.V.S., and Rao, V.K., (2005). Heat flow, Curie depth and composition of lower crust beneath the India shield. Singapore, Proceedings of 2nd Asia Oceania Geosciences Society International Symposium (AOGS), 1-6.

Shea, J.H., (1982). Twelve Fallacies of Uniformitarianism. Geology, vol. 10, pp. 455-460.

Shone, R.W., Nolte, C.C., Booth, P.W.K., (1990). Pre-Cape rocks of the Gamtoos area-a complex tectonostratigraphic package preserved as a horst block. South African Journal of Geology, 93, 616-621.

Sixsmith, P., Flint, S.S., Wickens, H.Dev., and Johnson, S.D., (2004). Anatomy and stratigraphic development of a basin floor turbidite system in the Laingsburg Formation, main Karoo Basin, South Africa: Journal of Sedimentary Research, v. 74, p. 239–254.

Smart, M. C., (1998). An explanation of the 1:500000 General Hydrogeological Map Queenstown 3126. Pretoria: Department of Water Affairs.

Smith, R.A., (1984). The lithostratigraphy of the Karoo Supergroup in Botswana. Bulletin of the Geological Survey Botswana, vol. 26, 239pp.

Smith, R.M.H., (1980). The lithology, sedimentology and taphonomy of flood-plain deposits of the Lower Beaufort (Adelaide Subgroup) strata near Beaufort West. Trans. Geol. Soc. S. Aft., vol. 83, p 399- 413.

Smith, R.M.H., (1981). Sedimentology and taphonomy of the Lower Beaufort strata near Beaufort West, Cape Province. M.Sc. thesis (unpubl), Univiversity of Witwatersrand, Johannesburg, S. Afr., 119 pp.

Smith, R.M.H., (1982). The Karoo Supergroup in Botswana. The main divisions reviewed and defined. Geological Survey, Botswana. Unpublished Report.

Smith, A.G. (1982). Late Cenozoic uplift of stable continents in a reference frame fixed to South America. Nature, 296, 400-404.

Smith, R.M.H., (1987). Morphology and depositional history of exhumed Permian point bars in the southwestern Karoo, South Africa. J. Sedimen. Petrol. Vol. 57, p 19–29.

Smith, R.M.H., (1990). A review of the stratigraphy and sedimentary environments of the Karoo basin of South Africa. J. Afr. Earth Sci. vol. 10, p 117–137.

Smith, R.M.H., (1995). Changing fluvial environments across the Permian–Triassic boundary in the Karoo Basin, South Africa, and possible causes of the extinctions: Palaeogeography, Palaeoclimatology, Palaeoecology, vol. 117, p. 81–104.

Smith, R.M.H., and Botha, J., (2005). The recovery of terrestrial vertebrate diversity in the South African Karoo Basin after the end-Permian extinction: Compte Rendu Pale vol, v. 4, p. 555–568.

Smith, R.M.H., Ericksson, P.G. and Botha, W.J. (1993). A review of the stratigraphy and sedimentary environments of the Karoo-aged basins of Southern Africa. Journal ofAfrican Earth Sciences, vol. 16 (132), p 143 – 169.

Smith, R.H.M. and Ward, P.D. (2001). Pattern of vertebrate extinction across an event bed at the Permian-Triassic boundary in the Karoo Basin of South Africa. Marine and Petroleum Geology. vol. 29, p 1147-1150.

Spector, A., (1968). Spectral analysis of aeromagnetic data. Ph.D. Thesis, University of Toronto, Canada.

Spector, A., (1985). Comment on "Statistical methods for interpreting aeromagnetic data by A. Spector and F.S. Grant". Geophysics, vol. 50, 2278p.

Spector A. and Bhattacharyya B. K., (1966). Energy density spectrum and autocorrelation function of anomalies due to simple magnetic models. Geophysical Prospecting, 14, pp. 242-272.

Spector, A., and Grant, F.S., (1970). Statistical models for interpreting aeromagnetic data. Geophysics, vol 35 pp 293-302.

Spector, A., and Grant, F.S., (1975). Comments on "Two-dimensional power spectral analysis of aeromagnetic fields". Geophysics Prospecting, vol 2, 391p.

Stankiewicz, J., (2011). Shallow structure in the Karoo basin South Africa, inferred from a near vertical reflection seismic profile. South Africa Journal of Geology, vol. 114, p 293-298.

Stankiewicz, J., and De Wit, M.J. (2013). 3.5 billion years of reshaped Moho, southern Africa. Tectonophysics 609, p 675–689.

Stankiewicz, J., Ryberg, T., Schulze, A., Lindeque, A., Weber, M.H., and De Wit, M.J. (2007). Initial results from wide-angle seismic refraction lines in the Southern Cape. South Africa Journal of Geology, vol. 110, p 407-418.

Stavrakis, N., (1980). Sedimentation of the Katberg sandstone and adjacent formations in the south-eastern Karoo Basin. Transactions of the Geological Society of South Africa, vol. 83, p 361–374.

Stefan, M., and Vijay, D., (1996). Depth estimation from the scaling power spectrum of potential fields. Geophysical Journal International, vol. 124, pp 113 – 120.

Steiner, J.B., Eshet, Y., Rampino, M.R., And Schmindt, D.M., (2003). Fungal abundance spike and the Permian–Triassic boundary in the Karoo Supergroup (South Africa): Palaeogeography, Palaeoclimatology, Palaeoecology, v. 194, p. 405–414.

Stephanie, S., Jörg, E., Detlef, E., and Susan W. (2013). 3D Geophysical Modelling of the Beattie Magnetic Anomaly and Karoo Basin, South Africa. Geophysical Research Abstracts, vol. 15, EGU2013-4407, 1p.

Stevenson, D. S., Doherty, R. M., Sanderson, M. G., Collins, W. J., Johnson, C. E., and Derwent R. G., (2004). Radiative forcing from aircraft NO_x emissions: Mechanisms and seasonal dependence, J. Geophys. Res.,109, D17307, doi:10.1029/2004JD004759.

Stollhofen, H., Stanistreet, I.G., Bangert, B., Grill, H., (2000). Tuffs, tectonism and glacially related sea-level changes, Carboniferous-Permian, southern Namibia. Palaeogeography, Palaeoclimatology, Palaeoecology 161, 127-150.

Sonibare, W. A., Mikes, D., and Cole, D.I., (2011). Facies architecture of Kookfontein shelf edge delta, Tanqua-Karoo basin, South Africa: implications for facies analysis and modelling. South Africa Journal of Geology, vol. 114, p 299-324.

Svensen, H., Bebout, G., Kronz, A., Li, L., Planke, S., Chevallier, L., Jamtveit, B., (2008). Nitrogen geochemistry as a tracer of fluid flow in a hydrothermal vent complex in the Karoo Basin, South Africa. Geochim. Cosmochim. Acta 72 (20), 4929–4947.

Svensen, H., Jamtveit, B., Planke, S and Chevallier, L (2006). Structure and evolution of hydrothermal vent complexes in the Karoo Basin, South Africa. Journal of the Geological Society, London, 163, 671-682; doi: 10.1144/1144-764905-037.

Svensen, H., Planke, S., Chevallier, L., Malthe-Sorenssen, A., Corfu, F., Jamtveit, B., (2007). Hydrothermal venting of greenhouse gases triggering Early Jurassic global warming. Earth Planet. Sci. Lett. 256 (3–4), 554–566.

Svensen, H., Corfu, F., Polteau, S., Hammer, Ø., and Planke, S., (2012). Rapid magma emplacement in the Karoo large igneous province: Earth and Planetary Science Letters, v. 325–326, p. 1–9, doi:10.1016/j.epsl.2012.01.015

Talwani, M., and Heirtzler, J.R., (1964). Computation of magnetic anomalies caused by two dimensional structures of arbitrary shape. Contribution No. 621. in Computers in the Minerals Industries, part 1 vol 9 pp 464-480. Stanford University Publications, Geological Sciences.

Talwani, M., Worzel, J.L, and Landisman, M., (1959). Rapid gravity computation for two dimensional bodies with application to the Mendocino submarine fracture zone. Journal of Geophysical Research, vol 64, pp 49-59.

Tankard, A.J., Jackson, M.A., Eriksson, K.A., Hobday, D.K., Hunter, D.R. and Minter, W.E., (1982). Crustal evolution of Southern Africa. Springer-Verlag, New York, 523p.

Tankard, A., Welsink, H., Aukes, P., Newton, R. and Stettler, E., (2009). Tectonic evolution of the Cape and Karoo basins of South Africa. Marine and Petroleum Geology, vol. 26, p 1379–1412. doi:10.1016/j.marpetgeo.2009.01.022.

Tankard, A., Welsink, H., Aukes, P., Newton, R. and Stettler, E., (2012). Geodynamic interpretation of the Cape and the Karoo basins, South Africa. Phanerozoic Passive Margins, Cratonic Basins and Global Tectonics Maps. p869.

Tedla, G. E., van der Meijde, M. Nyblade A. A., and van der Meer, F. D., (2011). A crustal thickness map of Africa derived from a global gravity field model using Euler deconvolution. Geophysical Journal International, vol. 187, p1–9.

Telford, W.M., Geldart, L.P., Sheriff, R.E. and Keys, D.A., (1976). Applied Geophysics. 1st Edition. Cambridge University Press, 860pp.

Telford, W.M., Geldart, L.P., and Sheriff, R.E., (1982). Applied Geophysics. Cambridge University Press. New York 11122, U. S. A. Cap. 2, 7–103.

Telford, W.M., Geldart, L.P., and Sheriff, R.E., (1990). Applied Geophysics. 2nd Edition Cambridge University Press, 770pp.

Tenzer, R., Sirguey, P., Rattenbury, M., and Nicolson, J., (2011). A digital rock density map of Zealand. Computers and Geosciences, vol. 37, issue 8, p 1181-1191.

Thybo, H., and Artemieva, I.M., (2014). Moho and magmatic underplating in continental lithosphere. Tectonophysics, vol. 609, p. 605-619.

Thompson, D.T., (1982). EULDPH: a new technique for making computer-assisted depth estimates from magnetic data. Geophysics vol. 47, pp 31-37.

Thomas, B., Oliver, R., Ute, W., Reinhard, F.S., and Frank, S., (2007). The Whitehill Formation: a high conductivity marker horizon in the Karoo Basin. South Africa Journal of Geology, vol. 110, p 465-476.

Thomas, R.J., von Veh, M.W. and McCourt, S., (1993). The tectonic evolution of southern Africa: an overview. Journal of African Earth Sciences, 16, 1/2, 5–24.

Tinker, J, de Wit, M.J. and Brown, R. (2007). Mesozoic uplift of southern Africa: using fission track thermochronology and offshore sediment volumes to test the balance between onshore denudation and offshore accumulation since Gondwana break-up. Tectonophysics, 455, 77–93.

Tissot, B., and Welte, D.H., (1984). Petroleum formation and occurrence. Springer Verlag, Berlin. 699 pp.

Tissot, B.P., Pelet, R., and Ungerer, P., (1987). Thermal history of sedimentary basins, maturation indexes, and kinetics of oil and gas generation. AAPG Bull. 71 (12), 1445–1466.

Tordiffe, E. A. W., (1978). Aspects of the hydro-geochemistry of the Karoo Sequence in the Great Fish River Basin Eastern Cape Province: With special reference to the groundwater quality. Ph.D. thesis (unpubl.). Univ. O.F.S., Bloemfontein, 307pp.

Treitel, S., Clement, W.G. and Kaul, R.K., (1971). The spectral determination of depths of buried magnetic basement rocks. Geophysical Journal of the Royal Astronomical Society, vol.24, p 415–428.

Tudor, P., (2006). An independent competent person's report on mining assets of Exxaro Resources limited. www.exxaro.com/pdf/icpr/a/geology/coal.htm

Tucker, M. E., (1992). Sedimentary Petrology. Blackwell Scientific Publications.

Turner, B.R., (1975). The stratigraphy and sedimentary history of the Molteno Formation in the Main Karoo Basin of South Africa and Lesotho. Ph.D. thesis (unpubl.), Univ. Witwatersrand, 314p.

Turner, B.R., (1980). Braid plain deposition of the Upper Triassic Molteno Formation in the main Karoo (Gondwana) Basin, South Africa, Sedimentology 30, 77 – 89.

Turner, B.R., (1983). Braid-plain deposition of the Upper Triassic Molteno Formation in the main Karoo (Gondwana) Basin, South Africa. Sedimentology, 30, 77 – 89.

Turner, B.R. (1999). Tectono-stratigraphical development of the Upper Karoo foreland basin: Orogenic unloading versus thermally-induced Gondwana rifting. Journal of Africa Earth Science, vol. 28, p 215-238.

Turner, B.R., Thomson, K., (2005). Discussion on basin development during deposition of the Elliot Formation (Late Triassic-Early Jurassic), Karoo Supergroup, South Africa. South Africa Journal of Geology, vol. 107, p 397-412.

Ullah, K., Arif, M. and Shah M.T., (2006). Petrography of Sandstones from the Kamlial and Chinji Formations, Southwestern Kohat Plateau, NW Pakistan: Implications for Source Lithology and Paleoclimate. Journal of Himalayan Earth Sciences, vol. 39, p 1-13.

Van der Spuy, D. (2003). Aptian source rock in some South African Cretaceous basins. In: T. J. Arthur, D. S. MacGregor and N. R. Cameron (Editors), Petroleum Geology of Africa: New Themes and Developing Technologies. Geological Society, London, Special Publication 207, p 185-202.

Van der Voort, I., (2001). Risk based decision tool for managing and protecting groundwater resources. PhD Thesis University of the Free State, Bloemfontein (unpublished).

Van Straten, O.J., (1959). The Morapule coalfield, Palapye area. Mineral Resources Report No. 1, Geological Survey, Bechuanaland Protectorate, 50pp.

Van Zijl, J.SV. (2006). A review of the resistivity structure of the Karoo Supergroup, South Africa, with emphasis on the dolerites: A study in anisotropy. South Africa Journal of Geology, vol. 109, p 315-328.

Van Zijl, J.SV. (2006). Physical characteristers of the Karoo sediments and mode of emplacement of the dolerites. South Africa Journal of Geology, vol. 109, p 329-334.

Veevers, J.J., Cole, D.I. and Cowan, E.J., (1994). Southern Africa: Karoo Basin and Cape Fold Belt. In: J.J. Veevers and C. McA. Powell (Editors). Permian-Triassic Pangean Basins and Foldbelts along the Pathalassan Margin of Gondwanaland. Boulder Colorado, Geological Society of America Memoir, vol. 184, p 223–279.

Viljoen, J.H.A., (1994). Sedimentology of the Collingham Formation, Karoo Supergroup. S. Aft J Geol., vol. 97, p 167–1 83.

Visser, J.N.J., (1983). A review of the Stormberg Group and Drakensberg volcanics in southern Africa, Palaeont.Afr. vol.25, p 5-27.

Visser, J.N.J., (1987). The palaeogeography of part of south-western Gondwana during the Permo-Carboniferous glaciation: Palaeogeography, Palaeoclimatology, Palaeoecology, vol. 61, p. 205–219.

Visser, J.N.J., (1992a). Basin tectonics in south-western Gondwana during the Carboniferous and Permian. In: Inversion Tectonics of the Cape Fold Belt, Karoo and Cretaceous Basins of Southern Africa, (Ed. by M.J. De Wit and I.G.D. Ransome), 109 – 115.

Visser, J.N.J., (1992b). Deposition of the Early to Late Permian Whitehill Formation during a sea-level highstand in a juvenile foreland basin: South African Journal of Geology, 95, p 89-105.

Visser, J.N.J., (1993). Sea-level changes in a back-arc foreland transition-the Late Carboniferous – Permian Karoo Basin of South Africa. Sediment. Geol., vol. 83, p 115 – 131.

Visser, J.N.J., (1995). Post-glacial Permian stratigraphy and geography of southern and central Africa: boundary conditions for climatic modelling. Palaeogeog., Palaeoclimatol., Palaeocol. 118, 213-243.

Visser, J.N.J., (1997). Deglaciation sequences in the Permo-Carboniferous Karoo and Kalahari basins of southern Africa: a tool in the analysis of cyclic glacio-marine basin fills. Sedimentology, 44 (3), 507 – 521.

Visser, J.N. J. and Botha, B.J.V., (1980). Meander belt, point bar, crevasse splay and aeolian deposits from the Elliot Formation in Barkly Pass, northeastern Cape. Transactions of the Geological Society of South Africa, vol. 83, p 55-62.

Visser, J.N.J. and Dukas, B.A., (1979). Upward fining fluviatile megacycles in the Beaufort Group, north of Graaff-Reinet, Cape Province. Trans. Geol. Soc. S. Afr., vol. 82, p 149-154.

Visser, J.N.J. and Loock, J.C., (1974). The nature of the Ecca-Beaufort transition in the western and central Orange Free State. Trans. Geol. Soc. S. Aft., vol. 77, p 371-372.

Visser, J.N.J. and Loock, J.C., (1978). Water depth in the main Karoo Basin, South Africa, during Ecca (Permian) sedimentation. Trans. Geol. Soc. S. Aft., vol. 81, p 185-191.

Visser, D.J.L., Gordon, J.F., and Venter, C.P., (1984). Geological map of the Republic of South Africa, Transkei, Bophuthatswana, Venda and Ciskei, and the Kingdoms of Lesotho and Swaziland: Gravity edition, Geol. Surv. Rep. South Africa, Pretoria.

Visser, J.N.J. and Praekelt, H.E., (1996). Subduction, mega-shear systems and Late Palaeozoic basin development in the African segment of Gondwana. Geologische Rundschau, 85, 632–646.

Von Brunn, V., (1994). Glaciogenic deposits of the Permo-Carboniferous Dwyka Group in the eastern region of the Karoo basin, South Africa, 60-69. In: Deynoux, M., Miller, J.M.G., Domack, E.W., Eyles, N., Fairchild, I. and Young, G.M., eds., (1994). Earth's Glacial Record: Cambridge, UK, Cambridge University Press, 266pp.

Von Veh, M.W., (1992). Compressional and extensional tectonics in the southermost exposures of the Cape Fold Belt. In: De Wit, M.J. and Ransome, I.G.D. (Ed.), inversion tectonics of the Cape Fold Belt, Karoo and Cretaceous Basins of Southern Africa. Balkema, Rotterdam, Netherland, p 185-192.

Ward, P.D., Botha, J., Buick, R., De Kock, M.O., Erwin, D.H., Garrison, G., Kirschvink, J., And Smith, R.H.M., (2005). Abrupt and gradual extinction among Late Permian land vertebrates in the Karoo Basin, South Africa: Science, v. 307, p. 79–714.

Weckmann U., Ritter O., Jung A., Branch T. and De Wit M., (2007a). Magnetotelluric measurements across the Beattie magnetic anomaly and the Southern Cape Conductive Belt, South Africa, Journal of Geophysical Research, vol. 112, BB05416, doi:10.1029/2005JB003975.

Weckmann, U., Jung, A., Branch, T. and Ritter, O., (2007b). Comparison of electrical conductivity structures and 2D magnetic modelling along two profiles crossing the Beattie Magnetic Anomaly, South Africa. South African Journal of Geology, vol. 110, p 449–464.

Weckmann, U., Ritter, O., Chen, X., Tietze, K. and de Wit, M.J., (2012). Magnetotelluric image across the Cape Fold Belt, South Africa. Terra Nova. Vol. 24, p 207 – 212.

West, A. R., (1999). Basic Solid State Chemistry, second edition, John Wiley and Sons.

Wickens, H. DeV., (1994). Basin Floor Fan Building Turbidites of the South-western Karoo Basin, Permian Ecca Group, South Africa. Unpublished Ph.D. thesis, University of Port Elizabeth, South Africa, 233pp.

Wickens, H. DeV., and Bouma, A.H., (2000). The Tanqua Fan Complex, Karoo Basin, South Africa – Outcrop analogue for fine-grained, deepwater deposits. In: Fine-grained turbidite systems (Ed. by A.H. Bouma and C.G. Stone), AAPG Memoir 72/SEPM Special Publication, 68, p 153 – 164.

Williams, H., Turner, F.J. and Gilbert, C., (1954). Petrology. An introduction to the study of rocks in thin sections. Freeman & Co., San Francisco, 406pp.

Williams, H., Turner, F. and Gilbert, C., (1982). Petrology. An introduction to the study of rocks in thin sections. Freeman & Co., San Francisco, 626pp.

Williamson, I.T., (1996). The geology of the area around Mmamabula and Dibete: including an account of the Greater Mmamabula Coalfield. District Memoir 6. Geological Survey, Botswana, 239pp.

Winter, H. de LA R., (1984). Tectonostratigraphy, as applied to the analysis of South African Phanerozoic basins. Geological Society of South Africa, vol. 87, p 169-179.

Winter, H. de La R. and Venter, J.J. (1970). Lithostratigraphic correlation of recent deep boreholes in the Karroo-Cape Sequence. In Proceedings and papers, Second Gondwana Symposium. Council for Scientific and Industrial Research, 395-408.

Won, I.J. and Bevis, M.G., (1987). Computing the gravitational and magnetic anomalies due to a polygon: algorithms and Fortran subroutines. Geophysics, vol. 52, p 232-238.

Woodford, A.C. and Chevallier, L. (2002). Regional characterization and mapping of Karoo fractured aquifer systems - an integrated approach using a geographical information system and digital processing. Water Research Commission Report, 653/1/02, 192p.

Wygrala, B.P., (1989). Integrated study of an oil field in the southern Po basin, northern Italy Berichtekern for Schungsanlagejulich 2313: p217.

Xiong Li and Götze, H., (2001). Ellipsoid, geoid, gravity, geodesy, and geophysics. Geophysics, vol. 67(3). p1660-1667.

Zhou, S. and Thybo, H. (1998). Power spectra analysis of aeromagnetic data and KTB susceptibility logs, and their implication for fractal behaviour of crustal magnetization. Pure and Applied Geophysics, v. 151, pp. 147–159.

APPENDIX A

1. Petrography and mineralogy

Sedimentary rocks are formed by the consolidation of sediments derived from pre-existing rocks. Their mineralogical compositions and textural characteristics of the detrital sediments are determined by their parent rocks and diagenetic processes that exist at the time of sediment deposition and post-depositional processes since the sediments have been transported from their source area to the point of deposition. Thus, physical and chemical processes have acted and influenced/altered the rocks.

The detrital sediments could exist as minerals or lithics which are broken fragments of the parent rocks. However, some of the minerals eventually become distinctive minerals which give clues about the source area. Williams *et al.* (1954) elucidated that some of the detrital types of sediments have components that indicate a distinct source however the composition of few of the detrital type sediment reflects the characteristics of the source area in a general perspective.

The variation in the mineralogical composition between the parent rock and the sediments is due to alteration and recrystallization of the minerals although some of the minerals are completely destroyed as a result of being less resistant to physical and chemical changes. Minerals that are more resistant to alteration or changes (both physical and chemical) become the primary minerals in the rock. The less resistant minerals (weaker minerals) are altered or recrystallized to another mineral therefore becoming the ground matrix whilst the least resistant minerals are completely destroyed. The sediments size, shape, sorting and degree of sphericity usually reflect the level of transportation or distance travelled by the sediments from the source area.

1.1 X-ray powder diffraction

X-ray powder diffraction is one of the analytical methods used to characterise X-ray scattering from crystalline materials. Crystals or crystalline solids are solid materials whose component atoms are orderly or regularly arranged in three-dimensions. Individual crystalline solid has its own distinctive X-ray powder pattern that serves as a "fingerprint" for its

identification (West, 1999). X-rays are electromagnetic radiation of wavelength of approximately 1 Å (10^{-10} m) which is roughly equal to the size of an atom (West, 1999).

X-rays are produced when high-energy charged particles accelerated by a potential difference of several tens kV (possesses sufficient energy to ionize some of the electron shells i.e., K-shell) strike a metal target (anode) like copper in such a way that an electron is being ejected (knocked out) from the inner electronic shell (e.g. 1s level) thus creating a hole in the electronic shell. An electron in the outmost shell instantly drops to fill the hole in the 1s level, therefore emitting X-ray photons of a characteristic energy or wavelength. The interaction of the X-ray with matter is either by Compton scattering, Rayleigh scattering, pair production and photoelectric effect (Crundwell *et al*., 1999).

The movement of an electron from a higher energy level (2p level) to fill the lower energy level (1s level) in the K-shell is known as Kα whilst the movement from 3p level to fill the 1s level is called K_β. The energies for each movement or transition have fixed values; though depend on the type of the material with each element having its own characteristic X-ray results. Thus X-ray diffraction analysis assists in identifying and quantifying the number of elements present in each sample (West, 1999).

X-ray powder diffraction works on the principle of Bragg's law which states that when X-rays hit the surface of a crystal, the angle of incidence, will be the same with the angle of scattering in which the X-rays will be reflected back. The diffracted beams will create interference that could either be constructive interference or destructive interference. Crundwell *et al*. (1999) stated that constructive interference occurs when the beams are in phase whilst destructive interference occurs when the beams are not in or out of phase. For Bragg's law to be satisfied, constructive interference must occur, thus the angle of incidence must be equal to the angle of scattering and the pathlength difference must be equal to an integer number (n) of wavelengths (Birkholz *et al*., 2004).

The Bragg's law elucidate the relationship between incident X-rays and how it is reflected off the crystal surface. The interference pattern of the scattered X-rays gives clues in solving diffraction in 3D crystals provided that each crystal plane is made of semi-transparent mirror. When monochromatic X-rays strike a crystal at an angle (θ) with interplanar distance (d) between the planes, the incident X-rays are in phase and parallel until the beam strikes the atom Z and changes direction (see Figure A1). The second incident X-ray continues to the

next layer, hits atom B, becomes scattered and changes direction to that which is adjacent and parallel to the beam that hits the atom Z (Figure A1). For the two incident X-rays to be in phase, the extra distance travelled by the second incident X-ray in the second layer must be an integral multiple of the wavelength (AB = λ, 2λ, 3λ……nλ).

The Bragg's law uses the crystals in the reflection geometry to analyse the intensity and wavelengths of X-rays (spectra) produced by different samples. A diffraction pattern is obtained when the intensity of the scattered waves is measured as a function of scattering angle. When scattered X-rays satisfy Bragg's conditions, very strong intensities are seen in the diffraction pattern which is known as the Bragg's peaks (Birkholz *et al*., 2004).
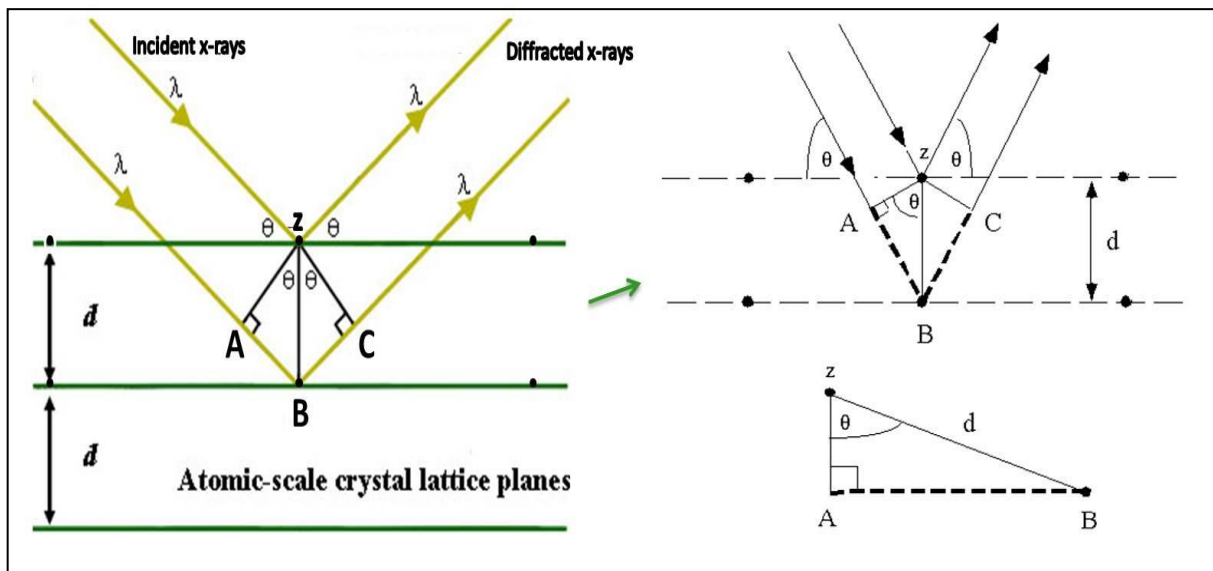
Figure A1 Illustration of Bragg's Law using the reflection geometry.

By solving the trigonometry (AB = BC),

$$AB = d \sin\theta \qquad\qquad 1.1$$

$$n\lambda = AB + BC = 2AB \qquad\qquad 1.2$$

$$n\lambda = 2 d \sin\theta \qquad\qquad 1.3$$

where λ = X-ray wavelength; d = interplanar distance; θ = angle of incident; n = an integer.

The prepared samples were well positioned in the sample holder in order to have a smooth flat surface. The sample holder was placed in a free position in the 9-sample sample-changer and the values of the fixed slits were recorded. A monochromatic beam of X-rays was directed into the powdered sample whose crystals are randomly arranged in every possible orientation. Some of the sample crystals were arranged at the Bragg angle to the incident beam, hence resulting in diffraction at every possible orientation of 2θ. The samples were rotated in order to homogenize anisotropy within the plane of the sample holder, thus improving the data quality. The LED green ready light was displayed and the XRD Commander program was run.

The Eva program was used to analyse the data (saved file). The program XRD Commander was used to set up and monitor data collection. A job was created in a new folder in the program XRD Commander and sample details such as sample position, sample name, location of the parameter (dql) file to be used, and the name and location of the output file (raw file) were provided and saved. Constraints (e.g. scan type, scan mode, no of steps, and sample rotation) were assigned such that changing any of the constraints will automatically alter the total scan time. The parameters were set and the auto check box was deactivated before running the search.

Minerals were searched manually by their names (one by one) using the normal search/match (scan) in the data command panel. Once the search is completed, the patterns of the mineral that is being searched for was added to the database. In the database, the first pattern for a mineral was selected and the corresponding ghost stick patterns (sticks and dotted lines) were displayed in the graphical view. The stick patterns were compared with the current scan and the stick pattern that matches with the current scan was selected (marked). Colours were assigned to the selected pattern such that the image of its stick pattern remains even after deselecting the pattern in the database. Then the peaks of the stick pattern (ghost peaks) were also compared to the scanned peaks. If the peaks of the stick pattern match with the scan, the stick pattern is selected and saved whilst the non-matching stick patterns were left unselected or unchecked. This procedure was repeated for all other minerals that were thought to be present (searched minerals) in the rock sample. The program displays the diffraction patterns as shown in Figure A2 - A12.
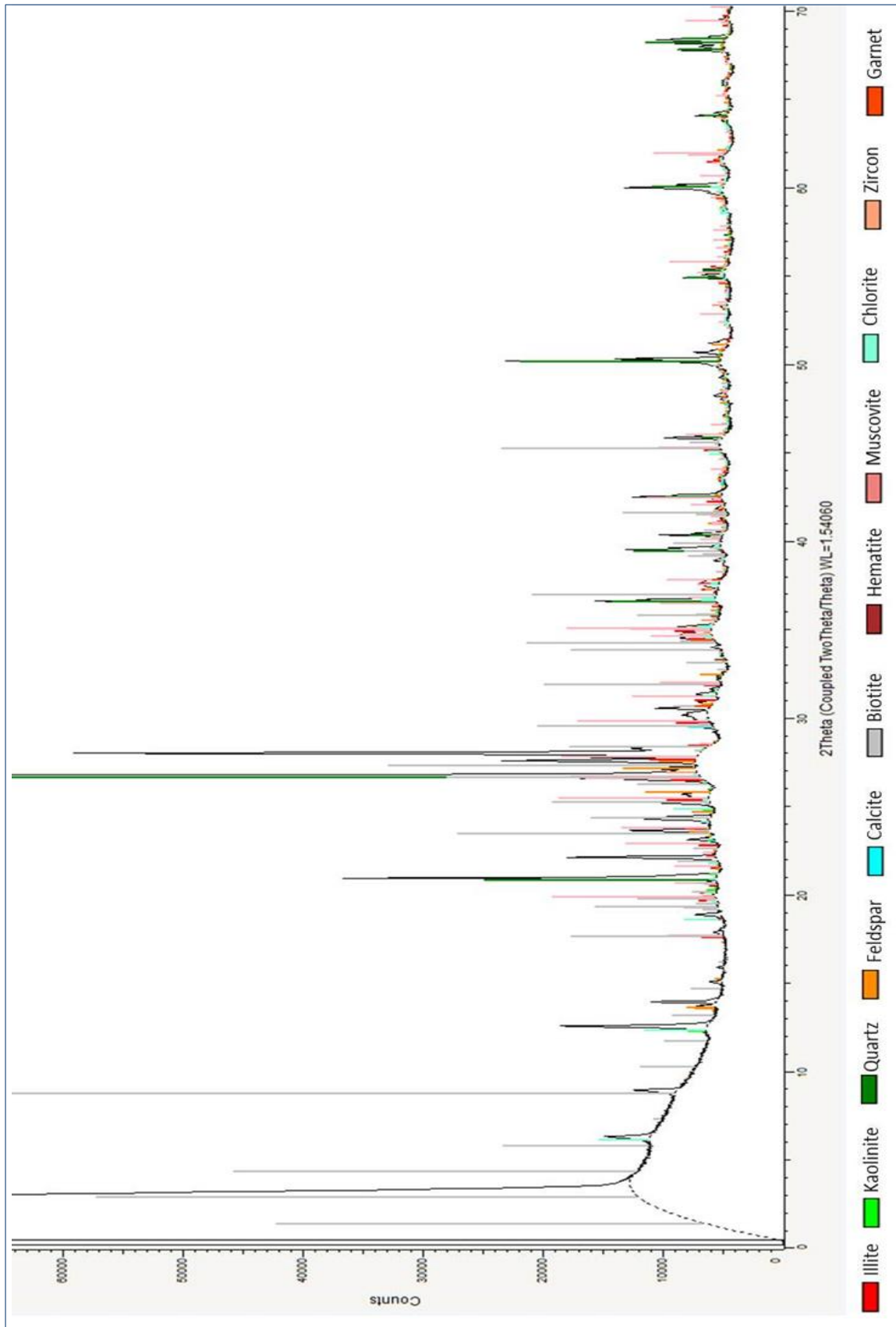
Figure A2 X-ray diffraction pattern for the Dwyka diamictite.
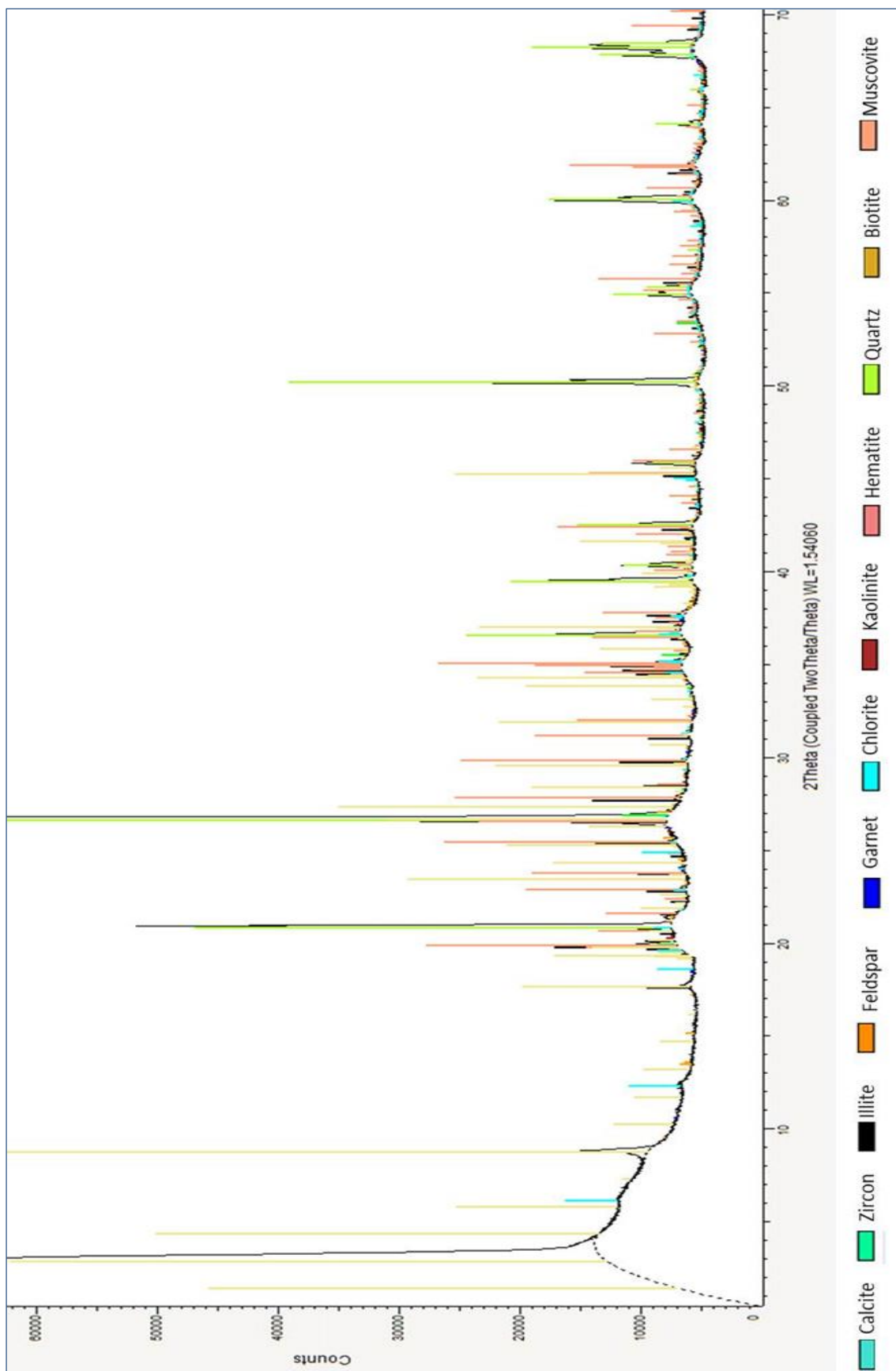
Figure A3 X-ray diffraction pattern for the shale from Prince Albert Formation.
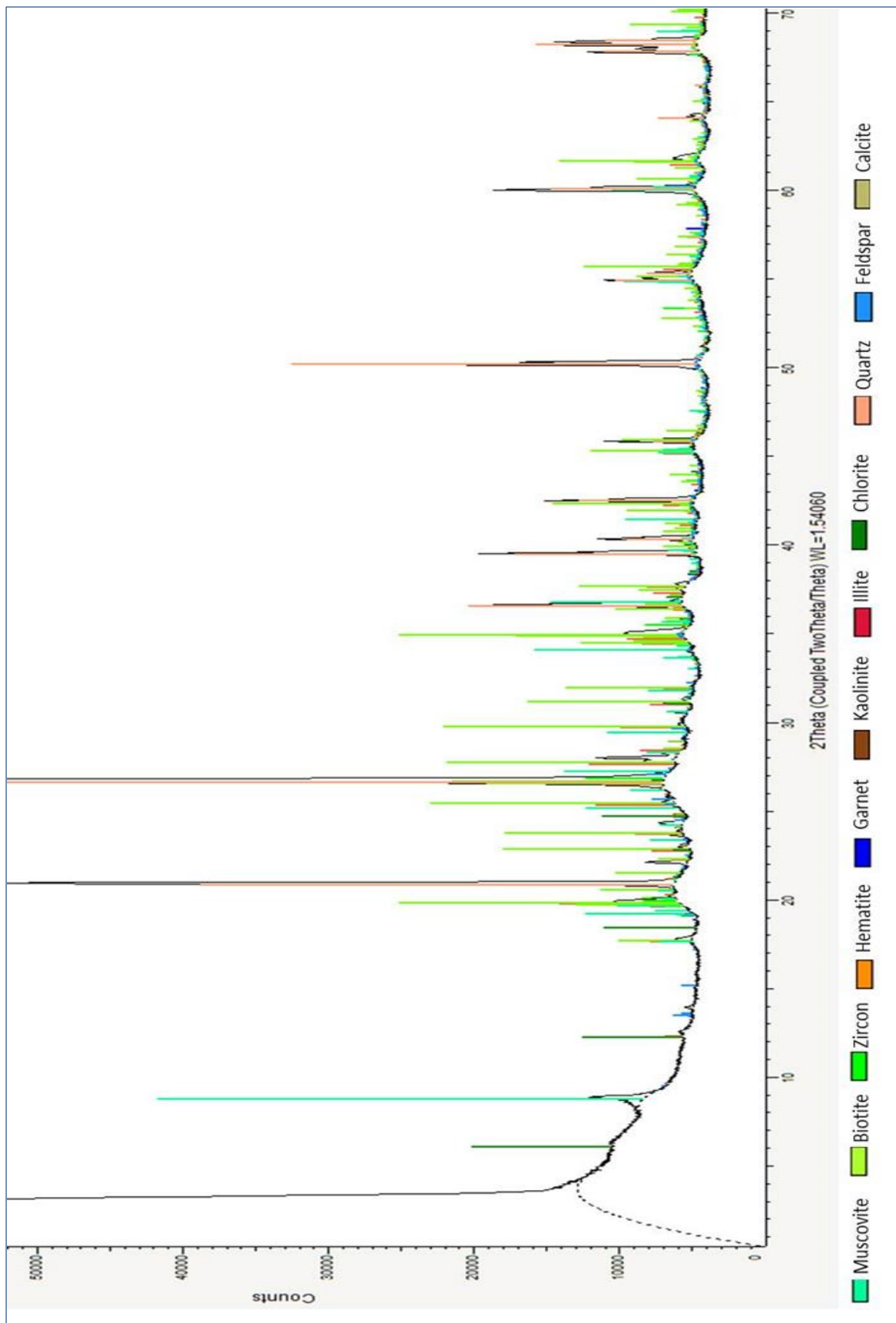
Figure A4 X-ray diffraction pattern for the carbonaceous shale of the Whitehill Formation.
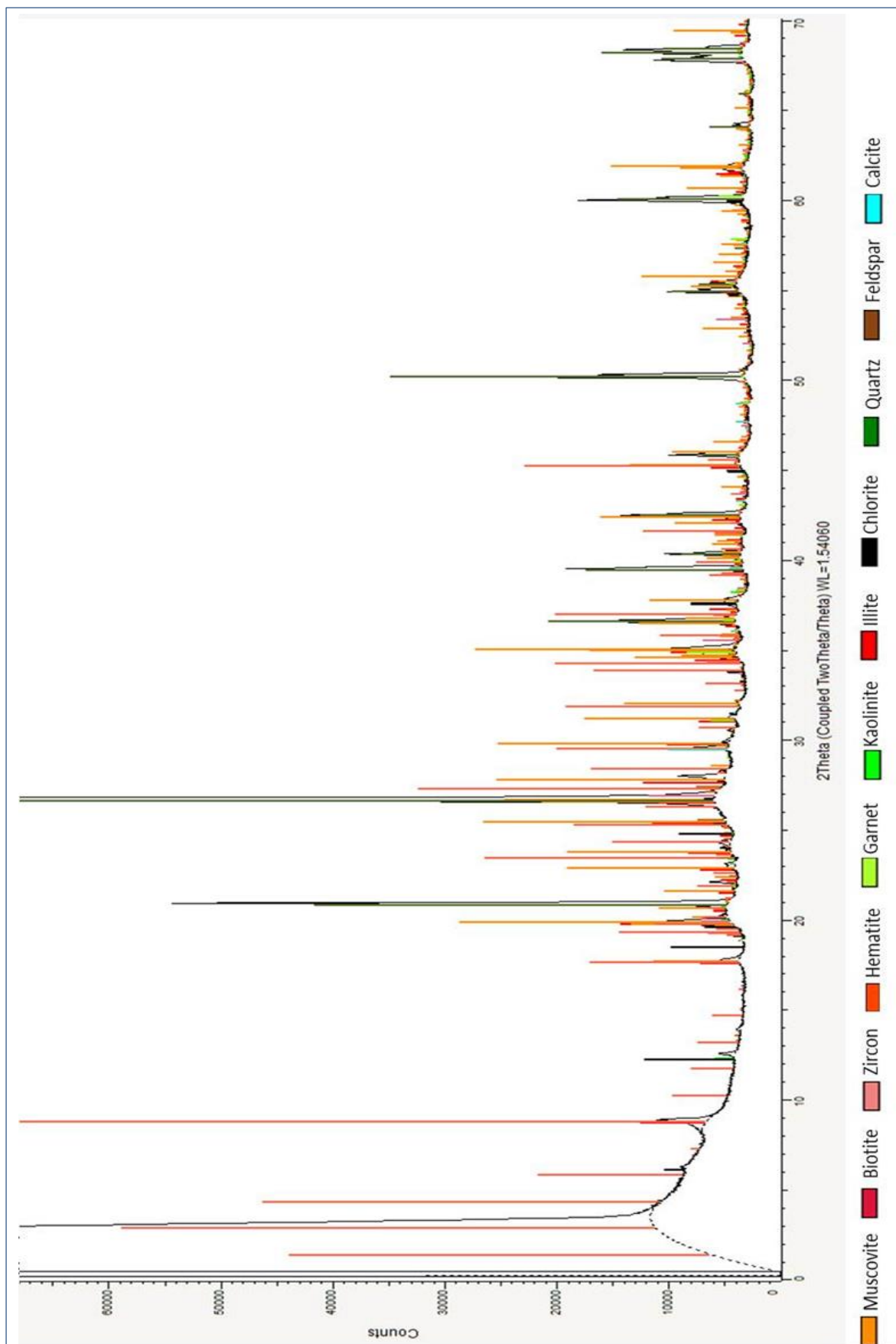
Figure A5 X-ray diffraction pattern for the sandstones from Collingham Formation.
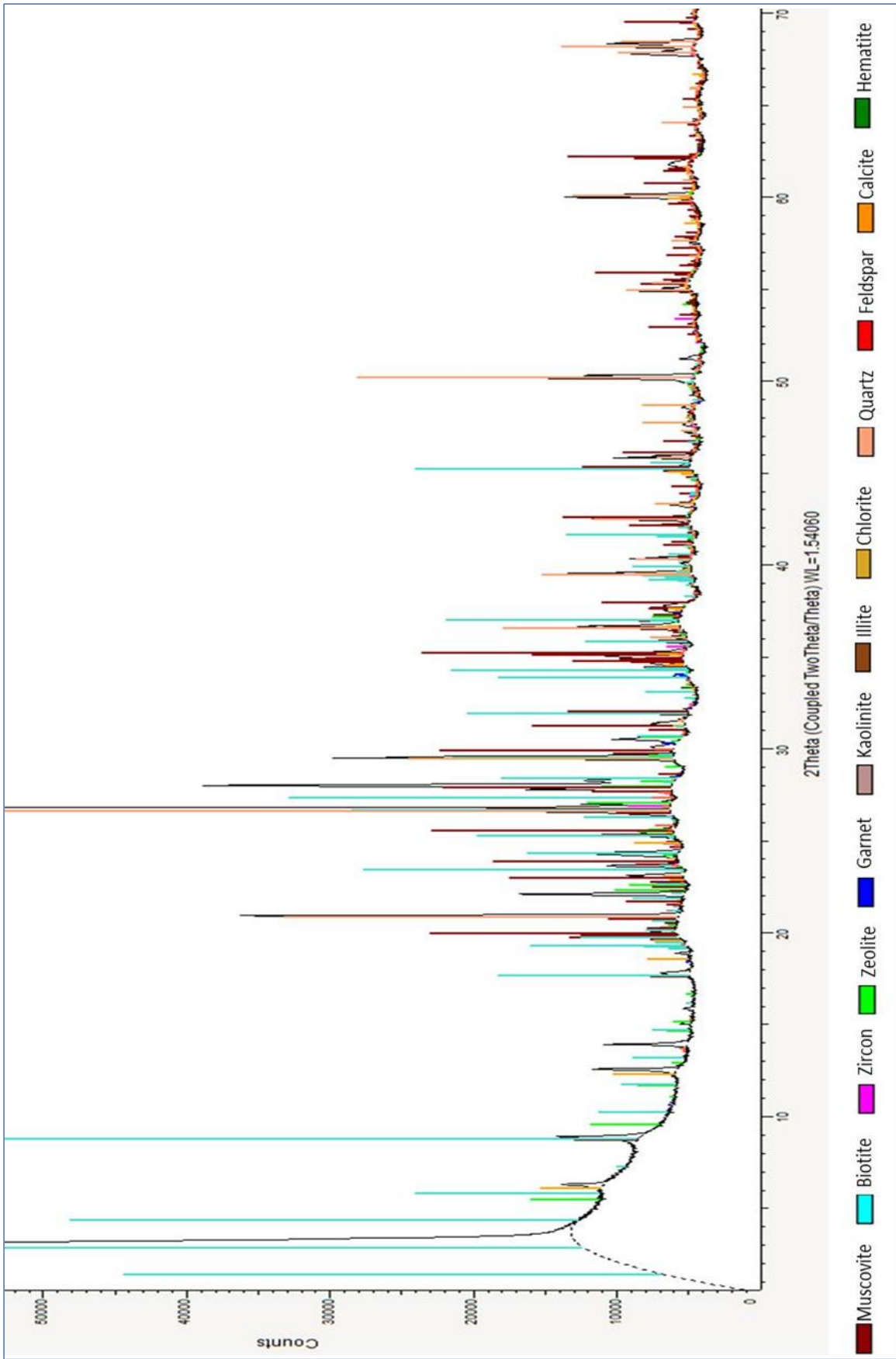
Figure A6 X-ray diffraction pattern for the sandstones from Ripon Formation.
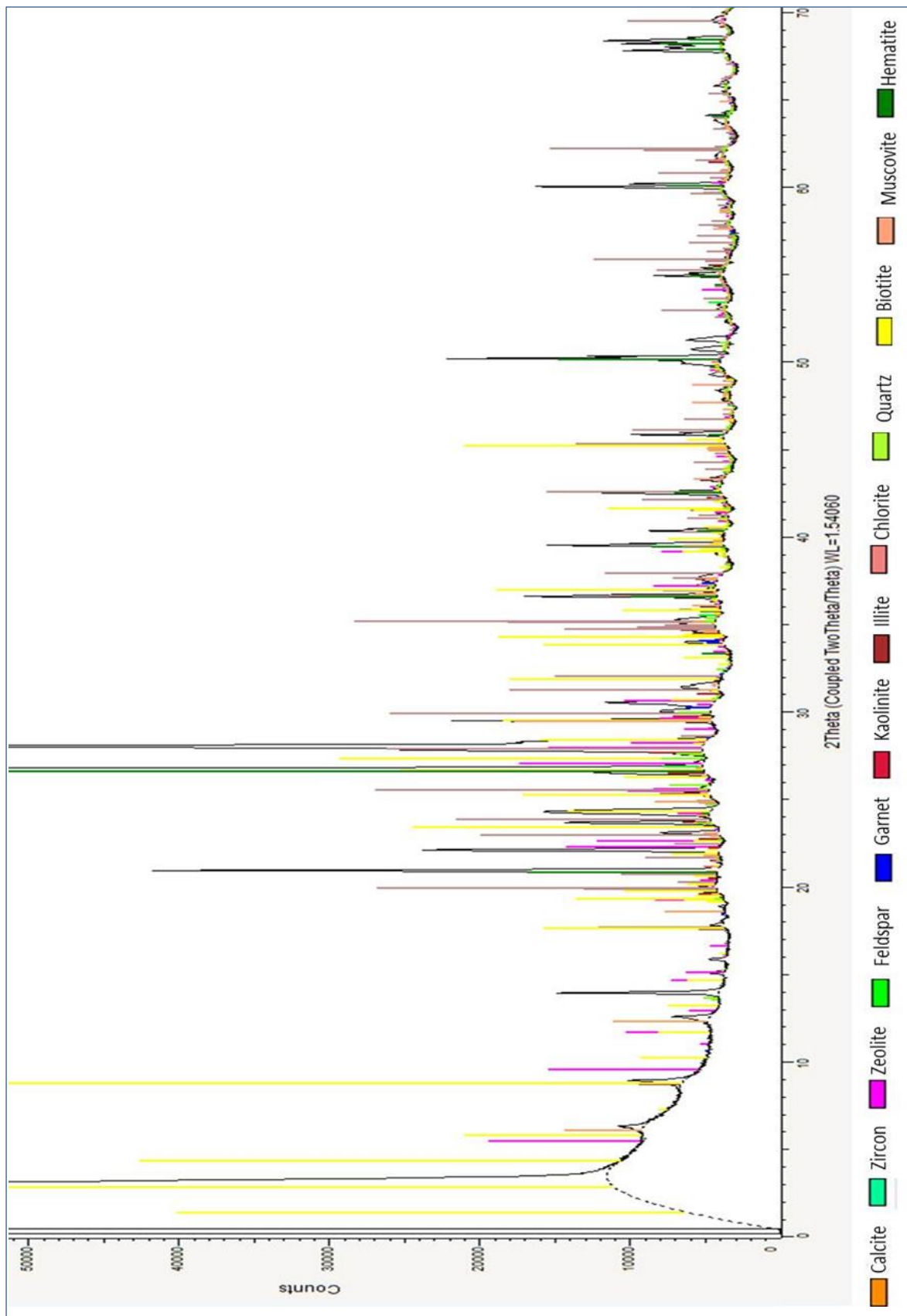
Figure A7 X-ray diffraction pattern for the sandstones from Fort Brown Formation.
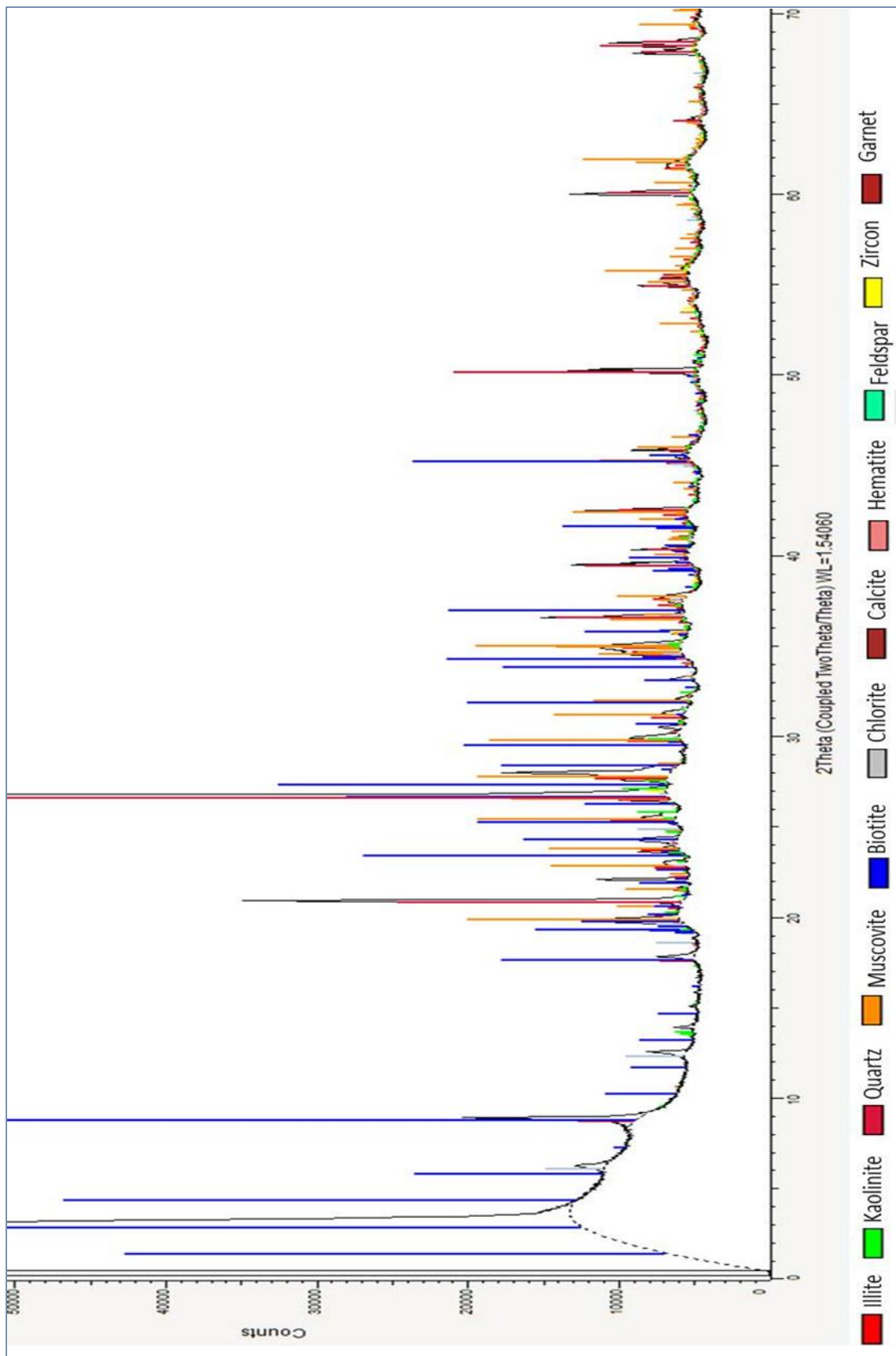
Figure A8 X-ray diffraction pattern for the mudstones from Middleton Formation.
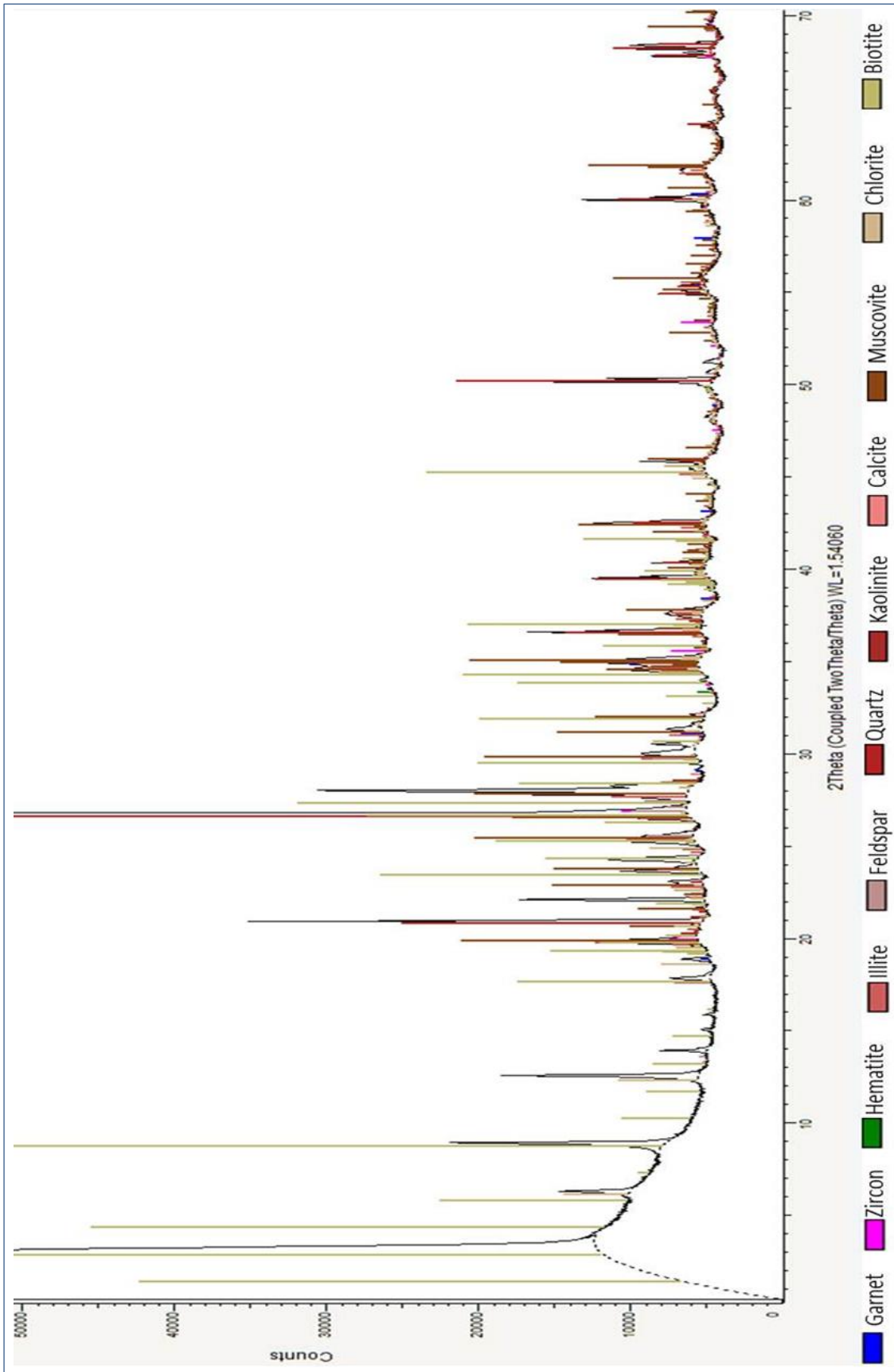
Figure A9 X-ray diffraction pattern for the sandstones from Koonap Formation.
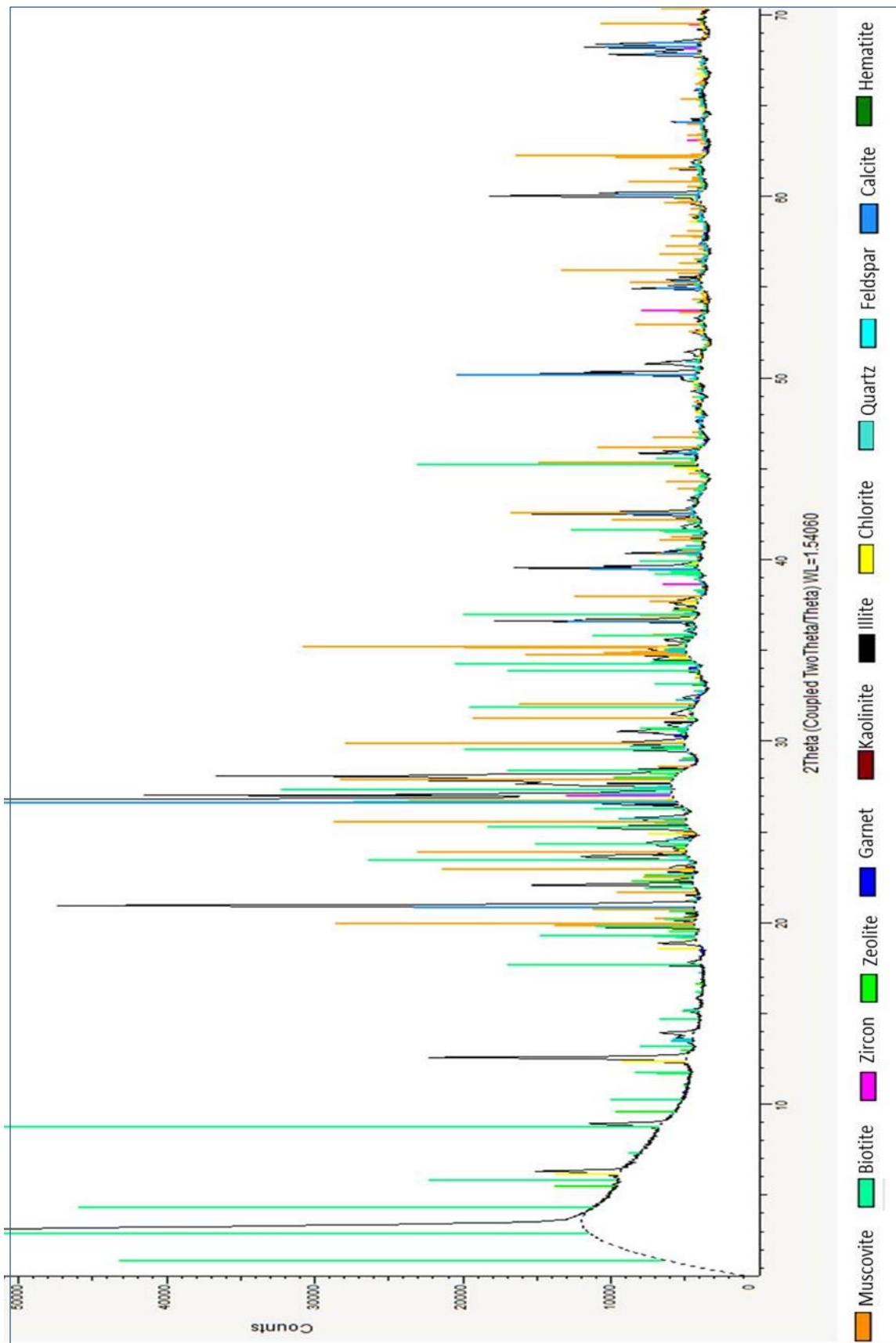
Figure A10 X-ray diffraction pattern for the sandstones from Balfour Formation.
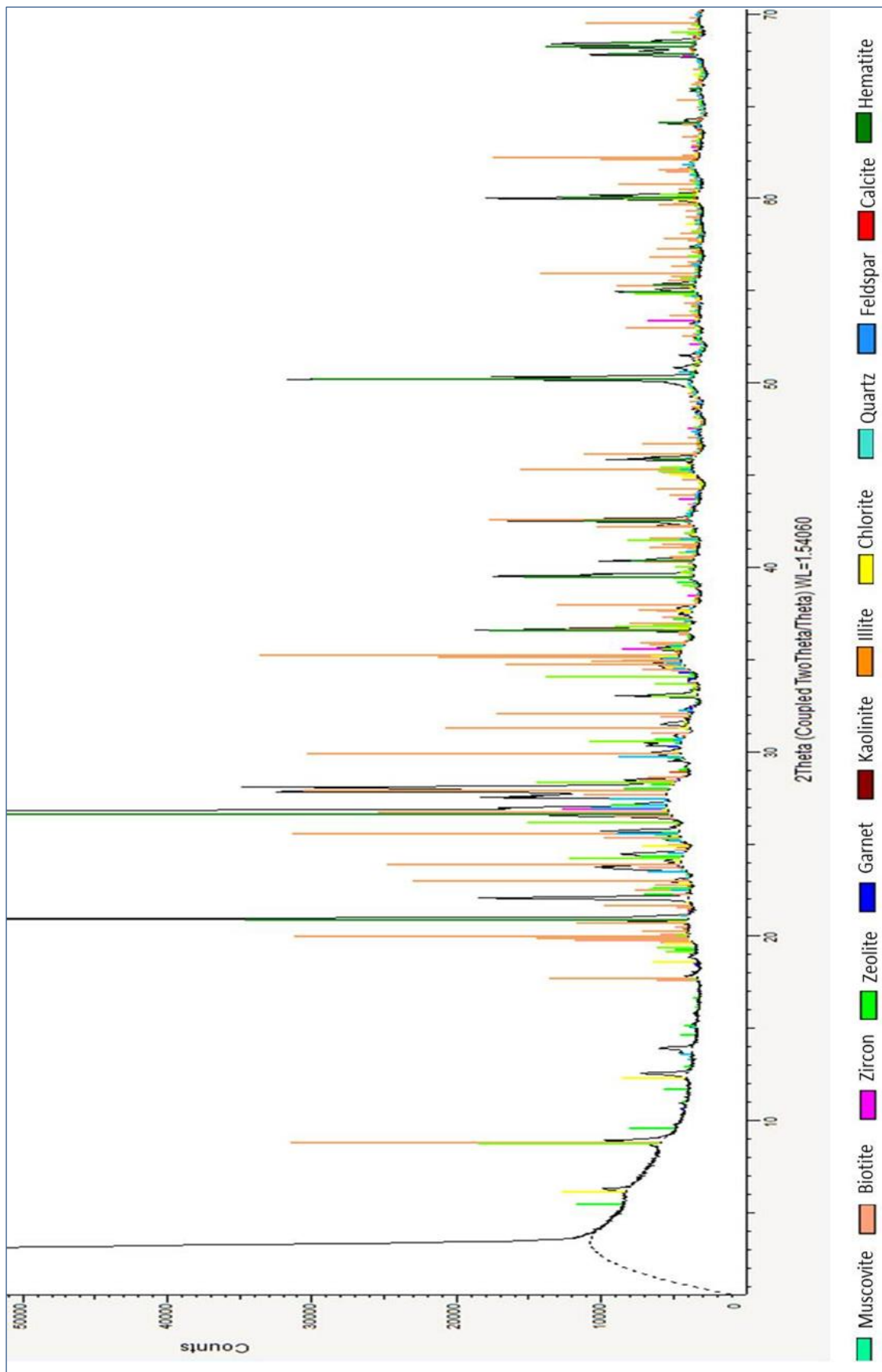
Figure A11 X-ray diffraction pattern for the sandstones from Katberg Formation.
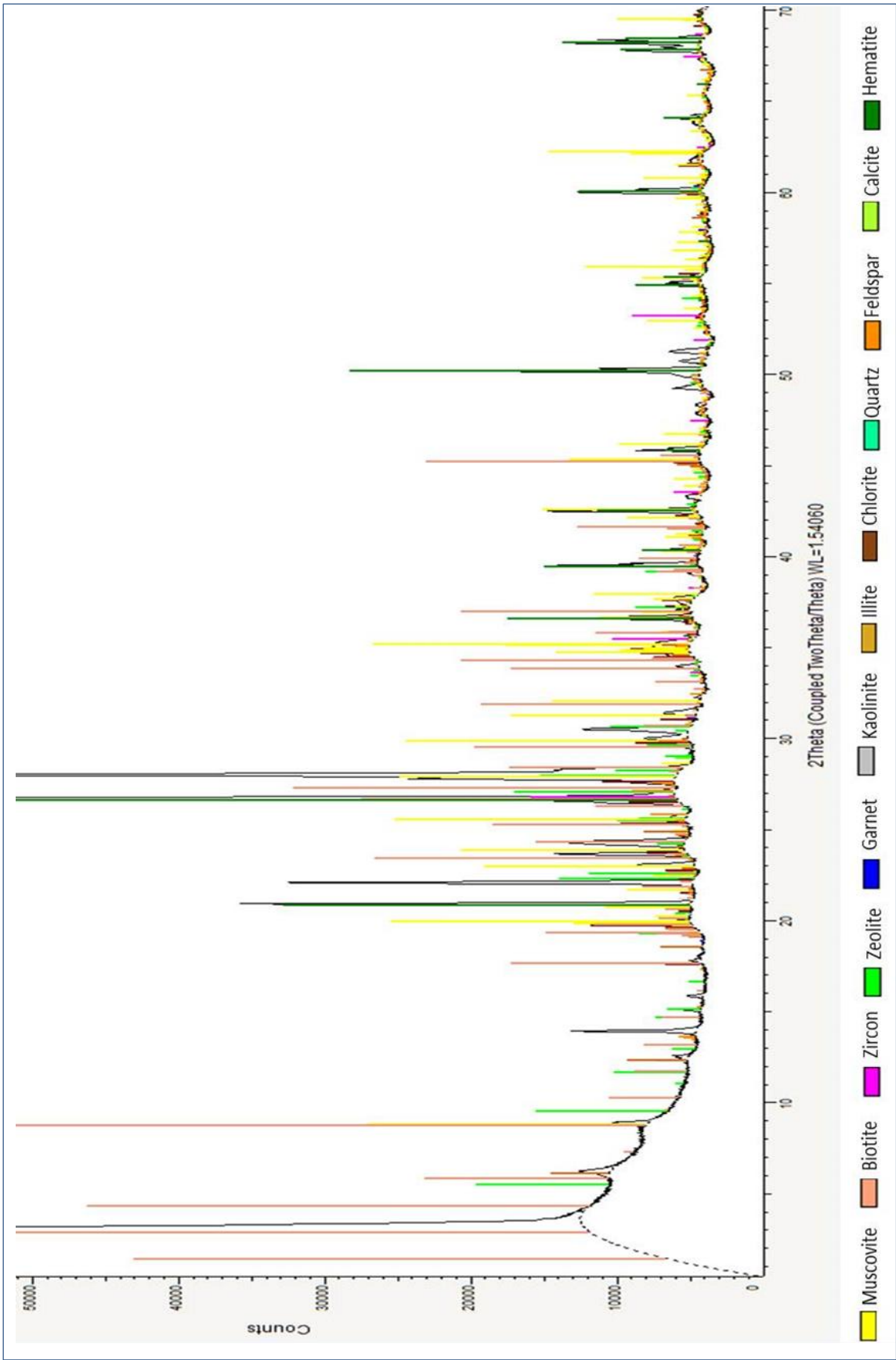
Figure A12 X-ray diffraction pattern for the sandstones from Burgersdorp Formation.

APPENDIX B

Magnetic method

1. Elements of the Earth's magnetic field

The geomagnetic field at any point on the Earth's surface is a vector field and can be defined by three magnetic elements, namely; three orthogonal strength components, the total field strength and two angles or two strength components and an angle (Figure B1).
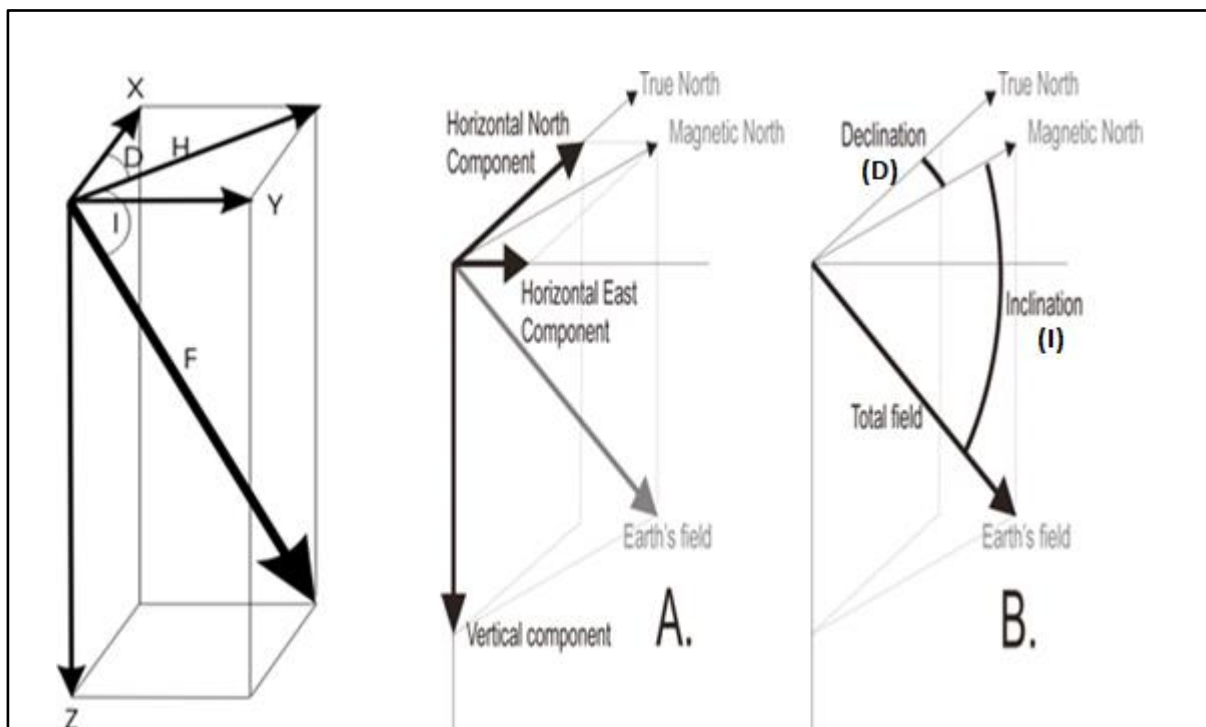
Figure B1 The vector total magnetic field (modified by the author after Reeves, 2005).

The three (3) orthogonal strength components (see Figure B1) include;

- The north component of the magnetic field (X)
- The east component of the magnetic field (Y)
- The vertical component of the magnetic field (Z)

The total field strength and two angles (see Figure B1) include;

- The total intensity of the magnetic field vector (F)

- Magnetic declination (D)
- Magnetic inclination (I)

The two strength components and an angle include;
- The horizontal component of the magnetic field vector (H)
- The vertical component of the magnetic field vector (Z)
- Magnetic declination (D)

The magnetic inclination (I) is the angle the total field vector (F) makes above and below the horizontal plane or the angle measured from the horizontal plane to the magnetic field vector (Reeves, 2005). Conventionally, inclination is positive to the north of the magnetic equator and negative to the south of the magnetic equator $(-90^o \leq I \leq +90^o)$. Reeves (2005) alludes that the simple dipole theory predicts the relationship between the magnetic inclination (I) and the geographic latitude (Φ) to be:

$$\tan I \ = 2 \tan \Phi \qquad\qquad 2.1$$

Measurements of inclination (I) compared to calculated values from equation 2.1 show deviations which suggests that the inclination (I) also changes with latitude.

According to Reeves (2005), the magnetic declination (D) is the angle between the vertical plane containing total field (F) and the geographic true north or the angle between true north and the horizontal component of the field measured east of the true north. Magnetic declination (D) is usually less than 15°, positive to the east and negative to the west. The relationships between the seven elements are given in equation 2.2 – 2.7.

$$\text{Declination (D)} = \tan^{-1}\left({Y}/{X}\right) \qquad\qquad 2.2$$

$$\text{Inclination (I)} = \tan^{-1}\left({Z}/{H}\right) \qquad\qquad 2.3$$

$$\text{Horizontal (H)} = \sqrt{X^2 + Y^2} \qquad\qquad 2.4$$

North $(X) = H \cos (D)$ 2.5

East $(Y) = H \sin (D)$ 2.6

Intensity $(F) = \sqrt{X^2 + Y^2 + Z^2}$ 2.7

2. Main field

The main geomagnetic field is produced by a flow of electric current in the conductive liquid outer core due to slow convective movements within it. The field has dipolar and non-dipolar components. Reynolds (1997) explained that the dipolar field behaves like a dipolar electromagnet located at the Earth's centre and inclined at 11.5° to the axis of rotation. The main field is constant when considered on a daily basis although it varies over years (it currently decreases by 1/2000 annually) (Reynolds, 1997). This variation is termed secular variation and is non-dipolar in character. Secular variations are variations in the main magnetic field that occur over long time span due to the movement of fluids in the Earth's outer core (Reynolds, 1997). The main global effects of secular variation are associated with changes in size and position of the departures from a simple dipolar field over a long period of time. These variations occur slowly relative to the time taken by the magnetic survey. Thus, they have little or no effect on data reduction over a small/local survey. However, it is vital to remove/correct for secular variations when carrying out a regional survey.

3. Crustal magnetic field

This is the induced and remanent magnetisation in crustal rocks. Induced magnetisation is the capability to hold/retain magnetisation in the presence of an inducing magnetic field. It is acquired by rocks containing ferrous minerals when they are placed in an external field (e.g. the main field). Remanent magnetisation is the capability to hold/retain magnetisation when the inducing magnetic field is absent/removed or in the presence of a different magnetic field. This occurs when the magnetic material has relatively high magnetic susceptibilities (e.g. ferromagnetic and ferromagnetic materials) or in the presence of a strong inducing magnetic field. Variations in the magnetic field of the Earth that are caused by changes in the subsurface geologic structure or differences in the magnetic properties of near-surface rocks are of interest in exploration (Reynolds, 1997).

247

4. External field

The external field is produced from magnetic sources outside/external to the earth, usually a small portion of the observed magnetic field and results in the temporal variations (i.e. diurnal variation, magnetic storm and micropulsation) in the magnetic field. Reynolds (1997) stated that the external field results from the interactions of the Earth's ionosphere with the solar wind. These temporal variations are correlated to solar activity.

5. Temporal external variations of the Earth's magnetic field

The magnetic field varies with time ranging from seconds to million years and can be classified into three main types depending on their rate of occurrence and source. These include the diurnal variation, magnetic storms and micropulsations.

5.1 Diurnal variations

These are daily variations in the magnetic field due to changes in strength and direction of currents circulating in the ionosphere (Figure B2). They are related to variations in the Earth's external magnetic field. The variations range from 20 to 30 nT per day and they are not predictable, but should be monitored and accounted for by using a base station magnetometer or a tie line method when conducting magnetic surveys (Reynolds, 1997).
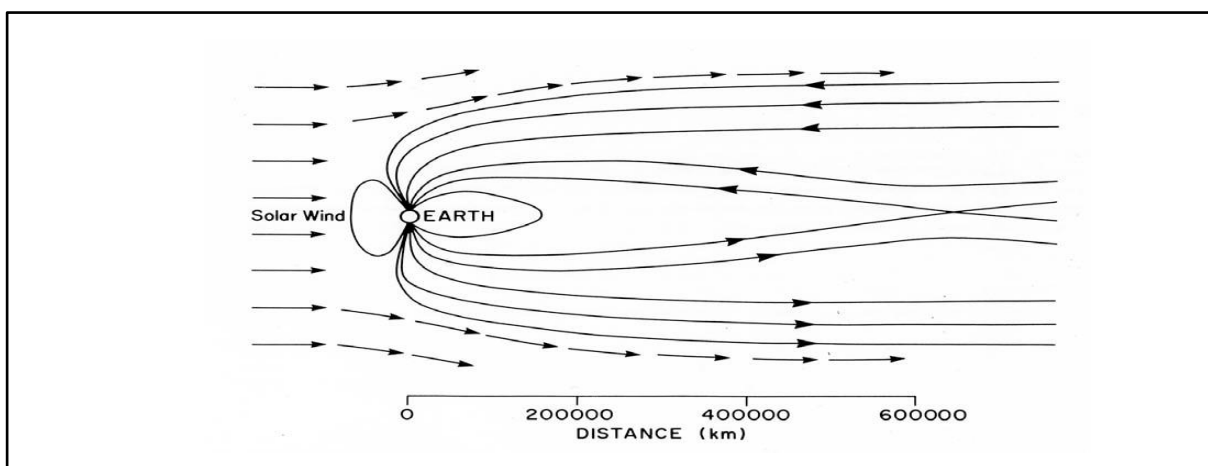
Figure B2 The solar wind distorts the outer reaches of the Earth's magnetic field (Reeves, 2005).

5.2 Micropulsations

These are rapid or very short period variations of the Earth's magnetic field due to hydromagnetic disruption in the outermost exosphere, usually ranging from a fraction of a second to tens of minutes (Figure B3). Reeves (2005) stated that micropulsations are transitory variations of small amplitude of a few nanotesla (nT) and micropulsations sequence with shape varying from place to place over a few tens of kilometres. They leave no permanent effects on the field, but the effect measured in an aircraft or at a base station on the ground needs to be removed.
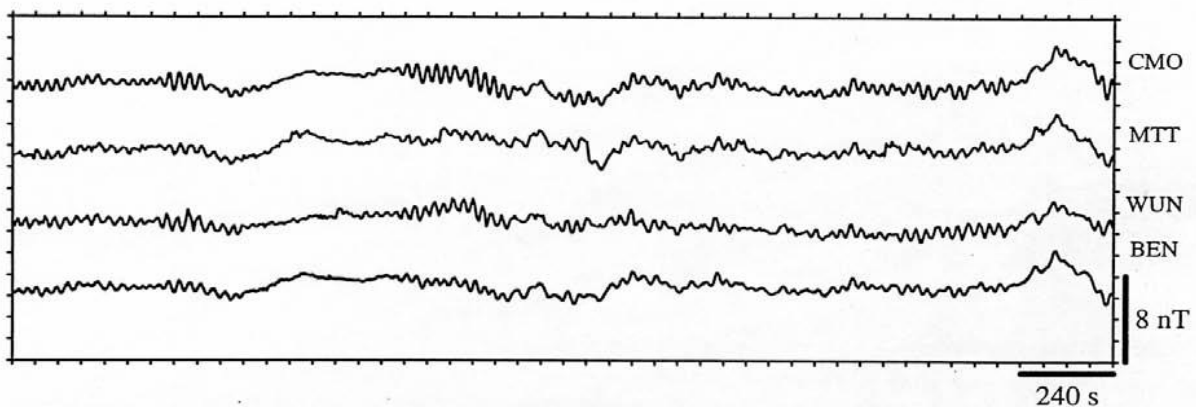
Figure B3 Micropulsations recorded at stations a few tens of kilometres apart (Reeves, 2005).

5.3 Magnetic storms

These are isolated periods of high magnetic variation that correlate with sunspot activity (Figure B4). The magnetic field observed during such times is highly irregular and unpredictable; sometimes start suddenly to a certain extent, having amplitudes as large as 1000 nT within an hour (Reeves, 2005). Since the effect of magnetic storms cannot be corrected, magnetic surveys should not be conducted or should be stopped until the storm ceases.
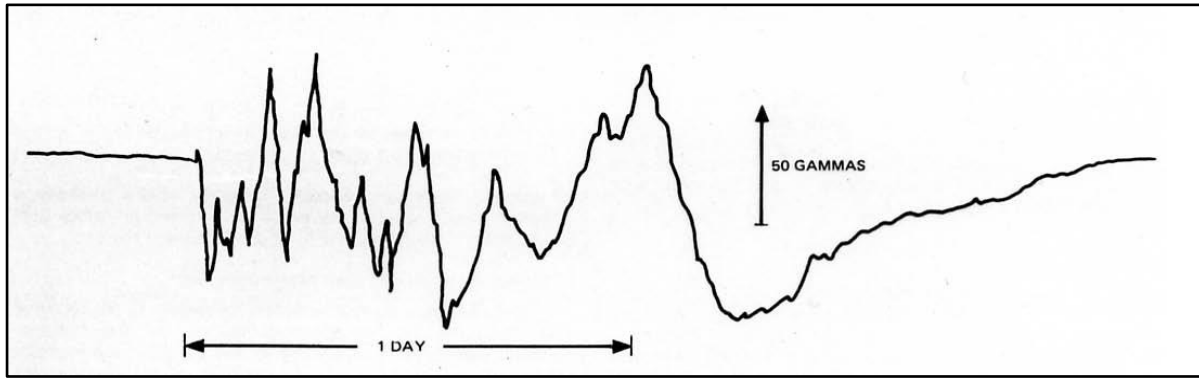
Figure B4 Magnetic storm associated with high solar activity (Reeves, 2005).

6. Magnetic properties of rocks

6.1 Magnetic susceptibility (k)

Magnetic susceptibility is a property that indicates how easily and strongly a material can be magnetised. Magnetic susceptibility (k) of a material can be expressed as the ratio of intensity of magnetisation induced in the material (J_i) to the magnetising field (H) in which the material is placed (see equation 2.8).

$$k = J_i/H \qquad\qquad 2.8$$

The magnetic susceptibility is dimensionless and depends on the mineral content, alignment and shape of the magnetic grains scattered in the rock. Magnetic susceptibility of rocks can be measured in the laboratory and at outcrops (using susceptibility meter), in a drill hole (using susceptibility logging and magnetometer profiling).

6.2 Magnetic permeability (µ)

Magnetic permeability is the ratio of magnetic induction (B) inside a medium to the magnetising field (H) inside the same medium (equation 2.9) or the proportionality constant that exists between magnetic induction (B) and magnetic field intensity which is equal to 1.257×10^{-6} H/m in free space (vacuum).

$$\mu = B/H \qquad\qquad 2.9$$

The constant varies or changes in other medium because of different rate or ability of passage of magnetic lines of force through different medium. It is measured in Henry per meter (H/m). Magnetic permeability of a material could change with time and temperature or with the intensity of the applied magnetic field (Reynolds, 1997).

6.3 Induced magnetisation (J_i)

The induced magnetisation results from the re-arrangement of atoms and molecules such that their magnetic moments are arranged and produce a magnetisation that is added to the magnetising field within the body. The induced magnetisation (J_i) is directly proportional to the magnetic field strength or intensity H (see equation 2.10).

$$J_i = kH \qquad\qquad 2.10$$

Magnetic field strength (H) is a measure of the magnetising field produced by electric current flow in a coil of wire (equation 2.11).

$$H = B/\mu \qquad\qquad 2.11$$

where μ = absolute permeability of the medium and B = magnetic flux density.

The magnetic flux density (B) is a measure of the actual magnetic field within a material considered as a concentration of magnetic field lines. The induced magnetisation due to the Earth's field F is expressed in equation 2.12, where μ_o is the absolute permeability of vacuum ($4\pi \times 10^{-7}$).

$$J_i = kF/\mu_o \qquad\qquad 2.12$$

For a medium other than vacuum, the absolute permeability of the medium is:

$$\mu = \mu_r \mu_o \qquad\qquad 2.13$$

where μ_r is the relative permeability ($\mu_r = 1 + k$).

6.4 Remanent magnetisation (J_r)

Remanent magnetisation (defined in Section 3) can be classified into different types. These include the natural, thermal, chemical and detrital remanent magnetisations. Reynolds (1997) noted that the natural remanent magnetisation (NRM) is acquired by rocks under natural conditions before laboratory treatments whilst the thermal remanent magnetisation (TRM) is mostly seen in volcanic rocks as they cool below the Curie temperature. At this temperature, rocks that possess magnetic properties begin to acquire a magnetic field which is in the same direction as the ambient Earth's field.

The chemical remanent magnetisation (CRM) is acquired by rocks as at the time of growth and crystallization of magnetic minerals below the Curie temperature in an ambient field. The detrital or depositional remanent magnetisation (DRM) is acquired by sediments with magnetic particles which align with magnetic field during settling to form consolidated sediments before any chemical changes owing to diagenetic processes. Physical processes like bioturbation and compaction may also act on the sediments after deposition to produce sediments with post-depositional remanent magnetisation (PDRM). Reynolds (1997) stated that remanent magnetisation is the component of the material's magnetisation that is used to map the movement of continents and ocean basins that resulted from plate tectonics.

6.5 Total magnetisation (J)

The sum of the induced magnetisation and the remanent magnetisation is known as total magnetization (**J**).

$$\mathbf{J} = \mathbf{J_i} + \mathbf{J_r} \qquad\qquad 2.14$$

Igneous rocks generally have a higher remanent magnetisation than sedimentary rocks (sedimentary rocks are usually less or non-magnetic except when they have a substantial amount of magnetite) whilst magnetism in metamorphic rocks varies. In most places $\mathbf{J_i}$ is much larger than $\mathbf{J_r}$ (e.g. four times).

6.6 Königsberger ratio (Q)

The ratio of the remanent magnetisation (J_r) to the induced magnetization (J_i) is called as Königsberger ratio (Q).

$$Q = J_r/J_i \qquad\qquad 2.15$$

$$Q = \mu_o J_r/(kF) \qquad\qquad 2.16$$

$$J_i = k(F/\mu_o) \qquad\qquad 2.17$$

7. International Geomagnetic Reference Field (IGRF)

The standard mathematical expression which describes the Earth's main magnetic field and its rate of change annually (secular variation) is known as the International Geomagnetic Reference Field (IGRF). It is a series of a mathematical model generated by geomagnetists all over the world and usually revised every five years. IGRF models are standardized for a specific year, showing the most precise measurements accessible at that particular time. It is approved by the International Association of Geomagnetism and Aeronomy (IAGA). According to Langel *et al.* (1988), the IGRF model uses the spherical harmonics expansion of the scalar potential. In the absence of an external source on and above the Earth's surface, but presence of sources internal to the Earth, the main field is the negative gradient of a scalar potential V which can be expressed as:

$$V(r, \emptyset, \theta) = a \sum_{l=1}^{L} \left(\frac{a}{r}\right)^{l+1} \sum_{m=-l}^{l} (g_l^m \cos m\emptyset + h_l^m \sin m\,\emptyset)\, P_l^m(\cos\theta) \qquad 2.18$$

where r = radial distance from the Earth's center, L = maximum degree of the expansion, $\emptyset$ = East longitude, θ = colatitude (the polar angle), a = Earth's radius, g_l^m and h_l^m = Gauss coefficients, and $P_l^m(\cos\theta)$ = Schmidt normalized associated Legendre functions of degree l and order m.

The sets of coefficients used in the IGRF model for the description of the Earth's magnetic field for the years (e.g. 1970, 1975 and 1980) depend on all the data sources that are available globally, including measurement of geomagnetic field from ships, satellites, aircrafts and observatories. More information on the IGRF model can be found in Langel *et al.* (1988).

8. Instrumentation

The instrument used to measure magnetic fields is known as a magnetometer. There are different types of magnetometers which include; fluxgate, optical absorption, proton-precession and alkali vapour magnetometers. The fluxgate magnetometer records either the total field or one of its three vector components and works on the principle of magnetic saturation of a circuit whilst the alkali vapour magnetometers are based on the excitation of electrons to different energy levels by irradiating an alkali gas with light of an exact energy (Reynolds, 1997). The optical absorption magnetometer works on the principle of Larmor precession. Detailed information on the types and working principle of magnetometers can be found in Reeves (2005) and Telford *et al.* (1976; 1982; 1990).

9. Data enhancement

9.1 Continuation

This enhancing method transforms the potential field data from one level vertically upward or downward to that which would be seen on different levels or surfaces either below or above the real observation level. Reynolds (1997) stated that continuation is a type of stripping because magnetic effects or anomalies which are due to shallow sources can be enhanced or suppressed. The process of continuation can be subdivided into upward continuation and downward continuation.

9.1.1 Upward continuation

The upward continuation enhances deeper sources by suppressing out the short wavelength anomalies, attenuating their amplitudes and decrease noise. It is usually used to compare anomalies obtained from ground-based survey to that from airborne data. Ground survey data

are better continued upward rather than downward in order to avoid amplifying noise. According to Reeves (2005), the upward continuation filter in the wavenumber domain can be expressed as shown in equation 2.19 below, where h is the continuation distance (m) and ω is the wave number.

$$F(\omega) = e^{-h\omega} \hspace{6cm} 2.19$$

9.1.2 Downward continuation

The downward continuation enhances high frequency signals (shallow sources) by reducing the wavelength of the anomalies and increasing the amplitude as well as high frequency noise. Thus it encourages flying the survey close to the ground, causing anomalies to have fewer spatial overlap, so that it can be easily differentiated from one another by increasing the amplitude. According to Reeves (2005), downward continuation can be expressed as shown in equation 2.20 below, where h is the distance (m) to be continued downward and ω is the wave number.

$$F(\omega) = e^{h\omega} \hspace{6cm} 2.20$$

9.2 Derivatives

9.2.1 Vertical derivative

The vertical derivatives tend to sharpen the boundaries and enhance shallow magnetic sources as well as noise since they are kind of high-pass filter. It accounts more for local effect than broad/regional effects, thus give a clear view than the total field map. The first calculated vertical derivative is the first-order derivative. The second-order vertical derivative can be calculated if the first order result is unacceptable (too noisy), but when the calculated second-order vertical derivative is often too noisy for interpretation then the calculated first-order vertical derivative result would be used. The vertical derivative was calculated in order to clearly show/delineate or outline high frequency features in areas where they are covered or shadowed by low frequency and high amplitude features. Reeves (2005) give a mathematical expression for vertical derivative as shown in equation 2.21.

$$F(\omega) = \omega^n \qquad\qquad 2.21$$

where n is the order of the vertical derivative.

9.2.2 Total horizontal derivative

The total horizontal derivative (THDR) enhances high frequencies and outlines the edges or boundaries of the sources. Thus its peaks lie directly over the edges or boundaries of broad bodies. The filter calculates the nth horizontal directives in x and y directions. The THDR varies with inclination, gives a clearer or sharper image and produces a better anomaly peak centred over the edges of the body. Cordell and Grauch (1985) stated that THDR is suitable for edge detection and can be expressed as:

$$THDR = \sqrt{\left[\frac{dF}{dx}\right]^2 + \left[\frac{dF}{dy}\right]^2} \qquad\qquad 2.22$$

where F is the magnetic field, dF/dx and dF/dy are the two orthogonal horizontal derivatives of the magnetic field (F).

9.3 Analytical signal

The analytical signal is also known as total gradient. It uses a combination of derivatives (e.g. vertical and horizontal gradients) to produce features that are independent of the inclination of the main field and magnetisation direction (either induced or remanent magnetisation direction). In addition, the analytical signal peaks directly over the edges (boundaries) of the wide or broad bodies and directly over the centres of narrow bodies (Nabighian, 1984; Milligan and Gunn, 1997). This implies that if the geometry of the magnetic sources or bodies is the same then they will have the same analytical signals. Li (2006) stated that the features produced in 3D case is dependent on the magnetisation direction but when the magnetic source is more than one, the features that are produced on the analytical signal map are effects of shallow sources. Nabighian *et al*. (2005) expressed the amplitude for analytical signal (A) as:

$$|A(x, y)| = \sqrt{\left[\frac{dF}{dx}\right]^2 + \left[\frac{dF}{dy}\right]^2 + \left[\frac{dF}{dz}\right]^2} \qquad\qquad 2.23$$

where A is the amplitude of the analytical signal and F is the observed magnetic field.

9.4 Reduction to the pole (RTP)

The magnetic anomalies are asymmetric anywhere except at the magnetic poles as a result of the dipolar nature of the Earth's magnetic field. Thus interpretation of magnetic data becomes more complex. RTP is performed on magnetic data in order to remove the asymmetry caused by the inclined main field or convert it to a symmetrical shape. It changes the data to that which would have been observed at the magnetic poles (north and south poles) where the main field is vertical, hence allowing the anomalies to be centred over the causative body instead of being offset/skewed at one end. Due to the asymmetrical nature of anomalies at lower latitude (e.g. South Africa) causing the anomaly peaks not to match with the centre of the causative body, it is very vital to reduce the field to the pole using the formula below (equation 2.24) in order to remove the effects of inclination and declination.

$$L\ (\Theta) = \frac{1}{[\sin(I) + i\cos(I)\cos(D-\theta)]^2} \qquad\qquad 2.24$$

where Θ = wavenumber direction, I = inclination, and D = declination

9.5 Power spectrum

Rabeh *et al*. (2008) reported that depth estimation from spectral method worked on the principle that the measured magnetic field at the surface is an integral part of the magnetic signature from different depths. The process of calculating and interpreting the spectrum of potential field data is known as spectral analysis. Spectral analysis of magnetic data is used to estimate the depth to definite geological features such as the magnetic basement given that the shape of the radially averaged power spectrum is invariably dominated by the depth factor (Spector and Grant, 1970). Horton *et al*. (1964) were the first to use power spectrum method to analyse aeromagnetic data and then Spector and Bhattacharyya (1966) produced it by using Fourier method.

Spector and Grant (1970) proposed the use of statistical models in the interpretation of aeromagnetic data which was later improved on by Treitel *et al*. (1971). Spector and Grant (1970) explained that the radial power spectrum is averagely calculated such that the effect of noise is minimised ensuring a more accurate result than other commonly used methods. The power spectrum is displayed with a logarithmic stretch in order to show the strength of the sine and cosine components at each frequency since lower frequency Fourier components usually dominate aeromagnetic datasets due to the enormous changes in the amplitudes of the different spectral components. The radially averaged power spectrum of the field increases with decrease in depth (h) by a factor that is proportional to exponential ($-4\pi hk$), where k is the wavenumber. Stefan and Vijay (1996) stated that if the depth factor dominates the shape of the power spectrum, then the logarithm of the power spectrum must be proportional to $-4\pi h$. Thus the slope of the log of the radially averaged spectrum can be used directly to estimate the depth to source (Figure B5). The power spectrum F^2 (k) with wavenumber (k) for an ensemble of rectangular prism is:

$$F^2(k) = \left[e^{-4\pi hk}\right]\left[\left(1 - e^{-2\pi tk}\right)^2\right]\left[S^2(ka)\right] \qquad 2.25$$

where the square brackets denote azimuthal and ensemble averaging, k is the wave number and equal to $1/\lambda$ with λ being wavelength, h is depth to the top of prism, t is thickness of prism, and $S^2(ka)$ is a function of the horizontal dimensions of the prism.

The first term usually dominates and therefore log $F^2(k)$ versus k gives a straight line of slope which is equal to $-4\pi h$. The averaged radial power spectrum is calculated and displayed in a semi-log paper of amplitude against spatial wave number such that straight line or lines can be visually drawn through the points in order to determine the slope of the spectrum which is used to estimate the depth to the top of the buried magnetic body (Spector, 1985). Spector and Grant (1975) and Spector (1985) recommended the use of averaged radial power spectrum to estimate depth of magnetic sources and this is not totally reliable when applied in quantitative depth estimates. Average radial power spectrum sometimes give a meaningful result due to the width effect which needs to be refined since it is very difficult to predict how an average body width in the field can be estimated where magnetic sources are elongated.
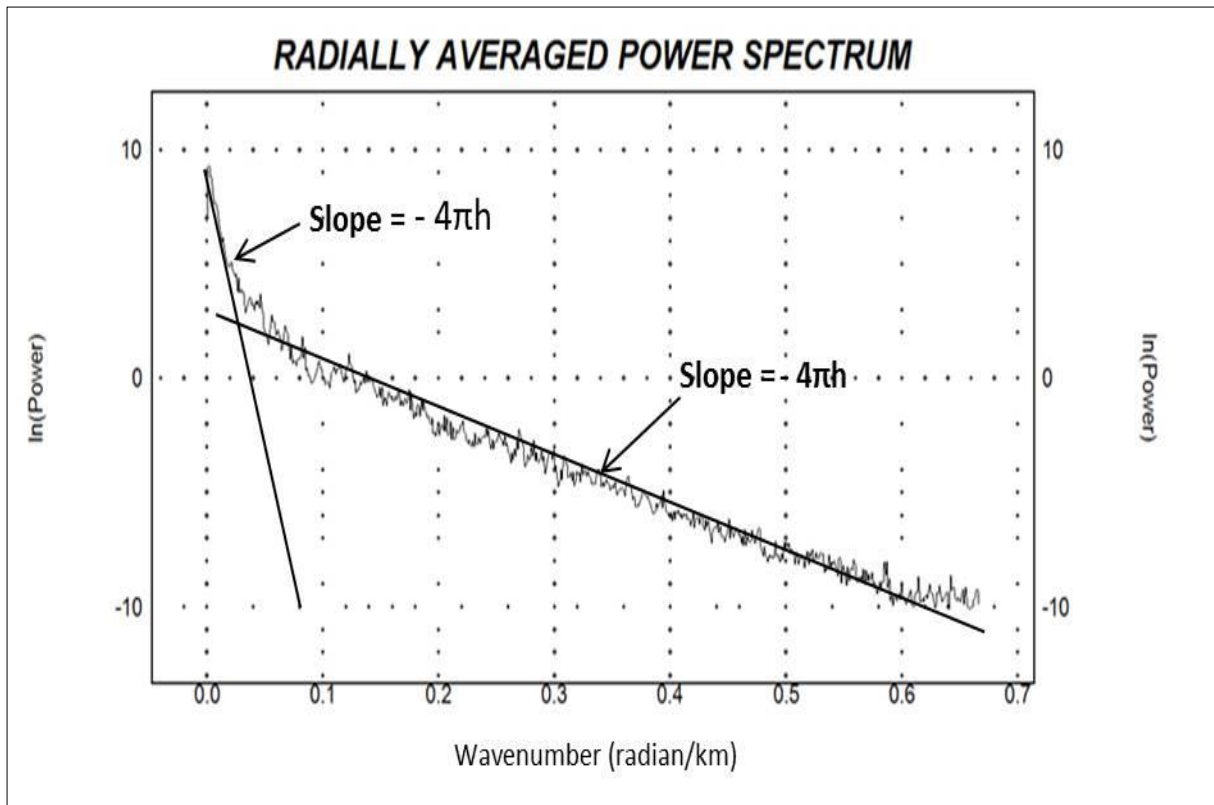
Figure B5 Radially averaged power spectrum. The slope of the log of the radially averaged spectrum which is equal to $-4\pi h$ can be used directly to estimate the depth to source.

9.6 Depth slicing

Depth to sources is connected to wavelength or frequency of the potential field data. The depth slices highlight specific interval of spatial frequencies (wavelength) that matches with the calculated or estimated depth in the subsurface by generating separate magnetic maps for a sequence of horizons with increasing depth. It aids comparison of amplitude response, thus the appearance and disappearance of a magnetic unit at different depth is recognised. Depth slicing works on the principle of Wiener filtering, which assumes that potential field signals (e.g. magnetic and gravity) results from two or more uncorrelated arbitrary processes (Fuller, 1967). Fuller (1967) stated that the various components of the data can be separated by highlighting the effects of shallow sources from deeper sources. Most magnetic anomalies at the surface, usually originate at shallow depth while obscure magnetic anomalies usually originate from a deeper depth (Gunn, 1972).

Radiometric method section

9.7 Instrumentation

The instrument used to detect gamma rays is known as the gamma ray spectrometer. The spectrometer detects gamma rays by counting the number of times each gamma ray of specific energy intersect it. It measures an energy spectrum of at least 256 contiguous channels of data in the range 0 - 3 MeV and consists of two main parts, namely; the detector which senses the gamma rays, and the analyser which analyses the signal and displays the result. The integral and differential spectrometers are the two main types of spectrometers. The same detectors are used in the different types of spectrometers, but the electronic analysers used are different (Minty, 1997). Detailed information on the types and working principle of spectrometers can be found in Coetzee (2008), and Stevenson *et al*. (2004).

9.8 Acquisition of data

Airborne gamma ray data were collected by Council for Geoscience (CGS) using the real time data acquisition unit that was mounted at the back of the aircraft. The aircraft was flown in a north-south direction at 80 m above the ground level with 200 m line spacing. The sodium iodide scintillation crystals installed in the rear end of the aircraft measure gamma rays emanating from the surface whilst the photomultiplier tubes that were attached to the scintillation crystals record and magnify the gamma ray induced signal.

The survey was flown in blocks and data (total count) were acquired over a sample interval of 1 s while the fixed-wing aircraft traverses about 55 m along the line during the sample interval. The tie line was flown in an east-west direction in order to aid levelling of the data. The dead time (the dead time is the time after each count/event during which the system is not able to record another count/event) required to measure and record each detected gamma ray is negligible for normal detection rates (less than 5 microseconds for 256 channels summed spectra). All gamma ray energy above 0.05 MeV are measured by the total count (TC). ^{40}K indicator has energy of 1.38 MeV, ^{238}U indicator has energy of 1.66 MeV and ^{232}Th indicator has energy of 2.38 MeV. The total count measurement is always greater than the sum of the three radioactive elements (K, U and Th) because other radionuclides add to the gamma-rays.

9.9 Processing and presentation of data

The different data processing approaches such as pre-processing, spectral smoothing techniques, live/dead time correction, energy calibration, aircraft background corrections, cosmic background corrections, radon background correction stripping corrections, height correction, reduction to elemental concentrations and levelling the data were carried out by Council for Geoscience in order to correct the observed data for non-geologic influences like noise and background estimation errors.

APPENDIX C
Gravity method

1. Gravity data reduction

1.1 Instrument drift

These are changes that occur in gravimeter readings at the same location with time due to changes in environmental conditions (temperature and pressure) causing elastic creep in the gravimeter springs. These changes can be accounted for by repeating measurements every 1 - 2 hours at a selected station called a base station. The gravity measurements at the base station are plotted against time to determine the instrument drift with respect to the first measurement (Figure C1).
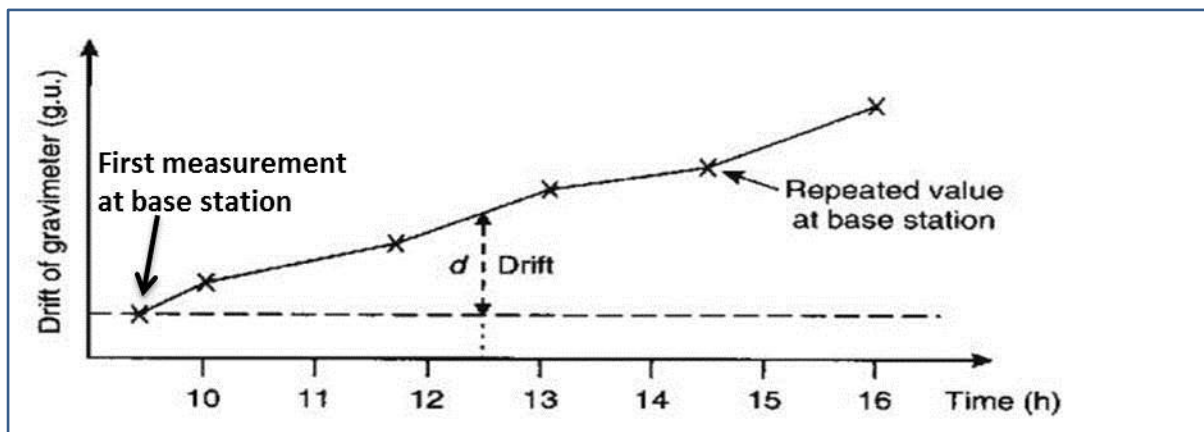
Figure C1 Graph of drift of gravimeter against time (Modified from Reeves, 2005).

To correct the effect of instrumental drift, the drift value is subtracted from the observed gravity as shown in equation 1 below

$$\Delta g = g_{obs} - ID \qquad\qquad 1$$

where $g_{obs} = g_{relative} \times$ scale factor of gravity, and $g_{relative}$= measured relative gravity.

1.2 Tidal correction

The gravitational pull of the moon and the sun gives rise to variations in gravity at any location on the Earth with the effect of the moon being greatest. This pull called the tidal effect changes with time and location. It accounts for up to 3 g.u. with a minimum period of 12 hours (Figure C2). It can be corrected by using a computer program or published tidal gravity correction tables.
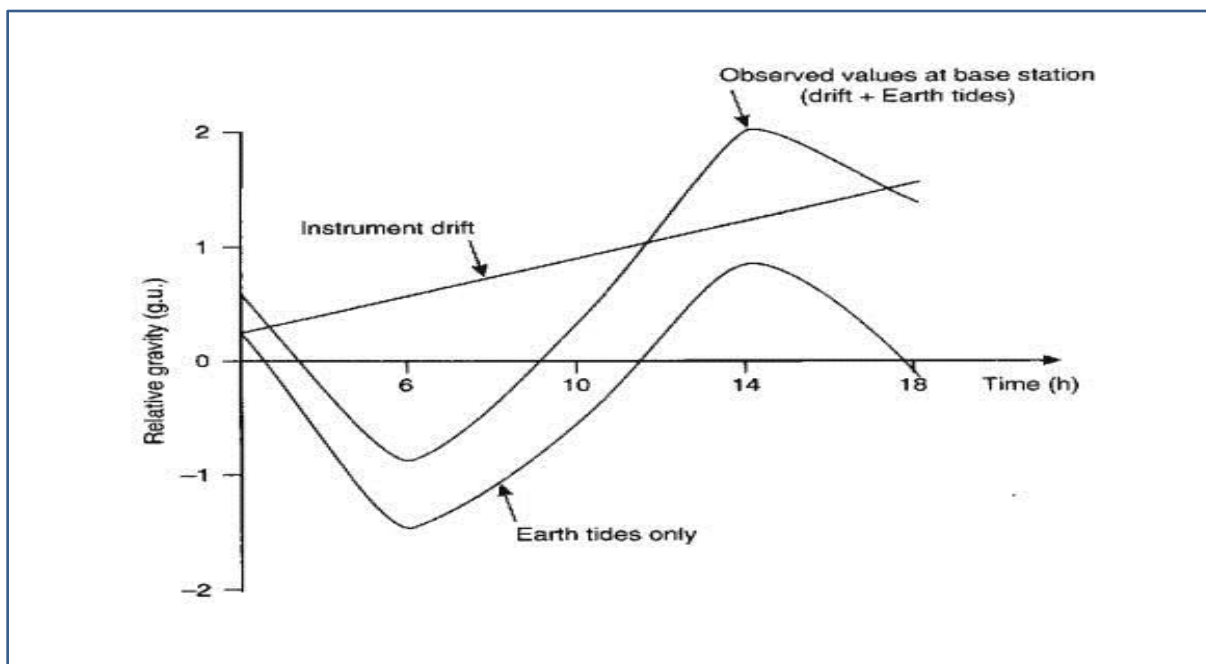
Figure C2 Graph of the effects of Earth tides and instrumental (Reeves, 2005).

To correct for tidal effect, the tidal value is subtracted from the observed gravity value as shown in equation 2 below;

$$\Delta g = g_{obs} - ID - TD \qquad\qquad 2$$

1.3 Latitude correction

The mathematical figure of the rotating Earth is an oblate spheroid bulging along the equator and flattened at the poles. The equatorial radius minus the polar radius is equal to about

21.385 km (Reynolds, 1997). Thus gravity increases from the equator towards the poles. It is therefore necessary to remove the latitude effect. The mathematical expression which approximates the shape of the Earth is known as the Earth ellipsoid also called the Geodetic Reference System (GRS). Chovitz (1981) stated that Hayford developed the international ellipsoid in 1910. It was accepted and recommended for international use by the International Union of Geodesy and Geophysics (IUGG) in 1930.This reference ellipsoid is now known as the GRS-30. The Geodetic Reference System (GRS-67) was later introduced in 1967 and recommended for use in areas that require high accuracy. It was approved by IUGG in 1971 to replace the GRS-30. The GRS-67 was modified to the GRS-80 in 1980 because the GRS-67 does not exactly represent the size, shape and the Earth's gravitation field. There are very slight differences between the GRS-67 and GRS-80 (see Table 1). The GRS-67 is the widely used Geodetic Reference System up to now.

Table 1 Geometric parameters for different reference ellipsoids (Xiong and Götze, 2001).

Reference ellipsoid name	Equatorial radius (m)	Polar radius (m)	Inverse flattening	Square of first eccentricity
GRS-30	6,378,388	6,356,911.946	297	0.006722670022
GRS-67	6,378,160	6,356,774.516	298.247167427	0.006 694 605 328
GRS-80	6,378,137	6,356,752.3141	298.257222101	0.006 694 380 022

The theoretical sea level gravity at specific geographic latitude $\emptyset$ is defined by the 1967 Geodetic Reference System (GRS 67) as:

$$g_\emptyset = \frac{g_e\left[1+K\,\mathrm{Sin}^2\,\emptyset\right]}{\sqrt{\left[1-e^2\,\mathrm{Sin}^2\,\emptyset\right]}} \quad \text{g.u.}$$

where g_e = 9780318.4558 g.u. (sea level gravity at the equator), K = 0.00193166338321 (gravity constant), e^2 = 0.00669460532856 (square of eccentricity) and Ø is the geodetic latitude.

This formula can be approximated with a truncated series to an accuracy of 0.04 g.u. to give the widely used GRS-67 expression as;

$$g_\emptyset = g_e[1 + B_2 Sin^2 \emptyset + B_4 Sin^2 \emptyset]$$

where g_e = 9780318.4558 g.u., B_2 = 0.005278895, and B_4 = 0.000023462 (Xiong and Götze, 2001).

Hence to remove the latitude effect the correction is subtracted from the observed gravity value as shown in equation 7.44 below;

$$\Delta g = g_{obs} - TD - ID - g_\emptyset \qquad\qquad 3$$

1.4 Free-air correction

The free-air correction accounts for the decrease in magnitude of gravity due to increase in elevation (height) above the datum (e.g. sea level) without considering the mass of the rock underneath. Reynolds (1997) expressed the free-air correction as 3.086h g.u. which is the difference between the measured gravity at sea level and at an elevation (h) above the datum, assuming there is no rock in between (Figure C3).
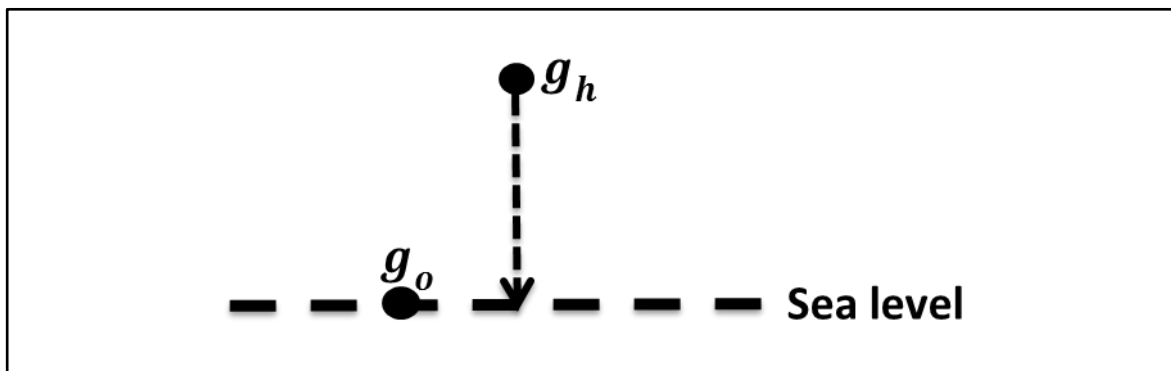
Figure C3 Schematic representation of free-air correction (Reeves, 2005).

The free-air correction is added to the observed absolute gravity in order to remove the effect of the height or elevation above the datum. Given that $\partial g_F = 3.086h$ g.u., the free air anomaly $[\Delta g_{FAA}]$ can be expressed as:

$$\Delta g_{FAA} \;=\; g_{obs} - TD - ID - g_{\emptyset} + 3.086h \text{ g. u.} \qquad\qquad 4$$

1.5 Bouguer correction

The Bouguer correction accounts for the effect of the mass of rock that lies between the datum or sea level and station (Figure C4). This is a function of rock density. The correction assumes that the gravity station is on an infinite horizontal slab whose thickness is equal to the difference in elevation between the station and the datum.
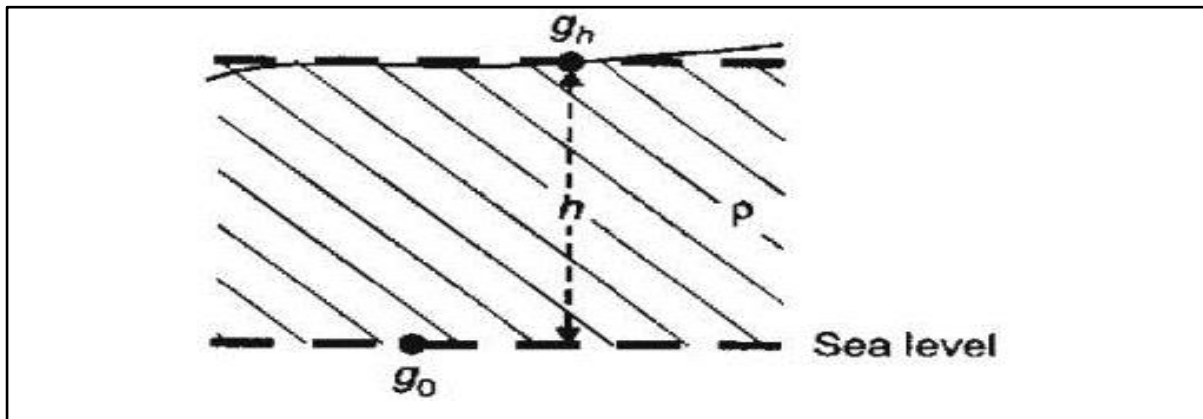
Figure C4 Schematic representation of Bouguer correction (Reeves, 2005).

The Bouguer correction is the gravitational attraction due to a Bouguer slab of thickness h and is given in the expression below:

$$g_{Slab} \;=\; 2\pi G \rho_B h$$

where ρ_B is the density of the slab, and h is the height (m) above the datum and
$G = 6.672 \times 10^{-11}$ N m^2 Kg^{-2}.

The simple Bouguer anomaly is given as:

$$g_{SBA} \;=\; g_{obs} - TD - ID - g_{\emptyset} + [3.086h - 2\pi G \rho_B h] \text{ g. u.}$$

It is common to use a Bouguer reduction density $\rho_B = 2670$ kg m^{-3} and the above expression becomes:

$$g_{SBA} = g_{obs} - TD - ID - g_\emptyset + (3.086h - 0.4191 \text{ x } 10^{-3}\rho h) \text{ g. u.} \qquad 5$$

The term in brackets is known as the combined elevation factor which reduces to 1.967 h g.u. for $\rho_B = 2670$ kg m^{-3}. The expression above (equation 5) is used in geologic interpretation.

1.6 Terrain correction

The terrain correction accounts for the assumption in Bouguer correction that the station rests on an infinite slab with a thickness equal to the difference in elevation between the station and the datum (Telford *et al*., 1982). Terrain above the station plane (e.g. hill) produces an upward gravitational attraction and reduces the gravity at the station. Terrain below the station plane (e.g. valley) results in mass deficiency that gives a reducing effect as a result of failure in exerting a downward force on the station (Telford *et al*., 1990). Thus, all gravity terrain corrections whether excess or deficiencies of mass are positive. The terrain correction (TC) values for a station are added to the observed gravity value as shown in equation 6 below to get the complete Bouguer anomaly (g_{CBA}).

$$g_{CBA} = g_{obs} - TD - ID - g_\emptyset + (3.086h - 0.4191 \text{ x } 10^{-3}\rho h) + TC \text{ g. u.} \qquad 6$$

A digital terrain model of the survey area can be used to calculate terrain corrections by computer. Alternatively, it can be done manually following any of the methods suggested by several authors, e.g. Hammer (1939; 1984), Sandberg (1958), Bott (1959; 1960 and 1962), Kane (1962) and Telford *et al*. (1976; 1982; 1990).

2. Density

Density is expressed as the mass of a substance per unit volume or as the ratio of mass in air of a unit volume of a sample at a given temperature. The bulk density of rock samples is a function of individual grains, porosity and pore-fluid (fluid that fills the pore spaces). Density can be subdivided into three main types namely; dry density (when the pore space is empty), wet density (when the pores are filled with fluids such as water) and grain or particle density (Reynolds, 1997). According to Tenzer *et al*. (2011), the dry density is equal to the dry mass of the sample divided by the total volume of the sample provided that the sample have been dried long enough to remove any moisture from the voids. The wet density is equal to the wet mass of the sample divided by the total volume of the sample given that the sample has been saturated under reduced pressure long enough that all the voids are filled with fluid (water).

The particle or grain density is equal to the mass of the mineral grain divided by the total grain volume of the sample, where the grain volume is the total volume less the volume of the voids. The different types of volume that can be measured include: bulk volume, particle volume, specific volume and true volume. The bulk volume is the mass of the particles in the sample divided by the total volume occupied by the particles. Particle volume is the total volume of the particle plus the closed pores, but without the open pores. Specific volume is the ratio of the sample's volume to its mass whilst the true volume is the volume without open and closed pores (Tenzer *et al*., 2011).

Archimedes' principle states that "any object completely or partially immersed in a fluid (i.e., water), experiences an upward force that is equal to the weight of the fluid displaced by it". The displaced fluid weight is directly proportional to the displaced fluid volume, provided that the surrounding fluid is of constant density. This principle is applicable to all fluids and objects in both floating and submerged state. The upward force experienced by the body is termed the buoyancy force (Tenzer *et al*., 2011).

The buoyant force is equal to the weight of the fluid that was displaced by the body. It depends on the weight of the displaced fluid but does not depend on the weight or the shape of the submerged object. The weight of the fluid displaced by the body is directly proportional to the volume of the displaced fluid, provided that the density of the fluid is constant. Thus, a rock sample density is the ratio of its mass in air to the difference in mass when the sample is weighed in air and weighed when immersed in water.

2.1 Dry density

Dry density (ρ_{dry}) is equal to the dry sample mass (M_a) in air divided by the difference in mass when the dry sample is weighed in air (M_a) and when the sample was submerged in water (M_b). The sample must be dried long enough (e.g. in the sun or oven) to remove any moisture from the voids.

Buoyancy = weight of displaced fluid

weight of displaced fluid = weight in air – apparent immersed weight

apparent immersed weight = weight in air – weight of the displaced fluid

$$F_{air} = W_{air} = M_{air} \times g \qquad\qquad 7$$

where m_{air} is the mass in air and g is the gravitational acceleration.

A rock sample completely submerged in water experiences an upthrust on it which is equal to the weight of the fluid displaced (Archimedes' principle) such that its new weight:

$$W_{immersed} = W_{air} - M_{water\ displaced} \times g \qquad\qquad 8$$

Re-write eqn 8:

$$M_{immersed} \times g = M_{air} \times g - M_{water\ displaced} \times g$$

$$M_{immersed} = M_{air} - M_{water\ displaced} \qquad\qquad 9$$

$$M_{water\ displaced} = M_{air} - M_{immersed} \qquad\qquad 10$$

$$\text{Mass} = \text{Density} \times \text{Volume} \qquad\qquad 11$$

$$M_{water\ displaced} = \rho_{water} \times V_{sample} \qquad\qquad 12$$

$$V_{sample} = \frac{M_{water\ displaced}}{\rho_{water}} \qquad\qquad 13$$

$$V_{sample} = \frac{M_{air} - M_{immersed}}{\rho_{water}} \qquad\qquad 14$$

Re-write eqn 14 and substitute in eqn 11:

$$\text{Density } (\rho) = \frac{\text{Mass}}{\text{Volume}}$$

$$\text{Density } (\rho) = \frac{M_{air}}{M_{air} - M_{immersed}} \times \rho_{water} \qquad 15$$

$$\text{Dry density } (\rho_{dry}) = \left[\frac{M_a}{M_a - M_b} \right] \times \rho_w \qquad 16$$

where M_a = mass of dry sample in air; M_b = mass of sample in water and ρ_w = density of water.

2.2 Particle or grain density

Particle or grain density ($\rho_{particle}$) is equal to the dry sample mass (M_a) in air divided by the difference in mass when the dry sample was weighed in air (M_a) and when the wet sample was immersed in water (M_c). Given that, the wet sample has been saturated under reduced pressure long enough that all the voids are filled with fluid (water), then:

$$W_{immersed(wet)} = W_{air} - M_{water\ displaced} \times g \qquad 17$$

Re-write eqn (17):

$$M_{immersed(wet)} \times g = M_{air} * g - M_{water\ displaced} \times g$$

$$M_{immersed(wet)} = M_{air} - M_{water\ displaced} \qquad 18$$

$$M_{water\ displaced} = M_{air} - M_{immersed\ (wet)} \qquad 19$$

$$\text{Mass} = \text{Density} \times \text{Volume} \qquad 20$$

$$M_{water\ displaced} = \rho_{water} \times V_{sample} \qquad 21$$

$$V_{sample} = \frac{M_{water\ displaced}}{\rho_{water}} \qquad 22$$

$$V_{sample} = \frac{M_{air} - M_{immersed\ (wet)}}{\rho_{water}} \qquad 23$$

270

$$M_{\text{water displaced}} = \frac{M_{\text{air}} - M_{\text{immersed (wet)}}}{\rho_{\text{water}}} \qquad\qquad 24$$

Re-write eqn 7.21:

$$\text{Density } (\rho_p) = \frac{M_{\text{air}}}{M_{\text{air}} - M_{\text{immersed (wet)}}} \times \rho_{\text{water}} \qquad\qquad 25$$

$$\text{Particle density } (\rho_p) = \left[\frac{M_a}{M_a - M_c}\right] \times \rho_w \qquad\qquad 26$$

where ρ_p = particle density; M_a = mass of sample in air; M_c = mass of wet sample in water and ρ_w = density of water.

Also, the particle density(ρ_p) is equal to the density of the dry sample (ρ_d) divided by one minus porosity (Φ) (equation 34). Given that the total mass (M) of the submerged sample is equal to the sum of the solid grain mass (M_s) and the mass of the pore fluid (M_f). The total volume (V) is the sum of the volume of solid grains (V_s) and the volume of void space which is the volume of the pore fluid (V_f). This can be expressed as:

$$M = M_s + M_f \qquad\qquad 27$$

$$V = V_s + V_f \qquad\qquad 28$$

Particle density (ρ_p) is equal to the mass of the mineral grain (M_s) divided by the total grain volume of the sample (V_s), where the grain volume is the total volume less the volume of the voids.

$$\rho_p = \frac{M_s}{V_s} = \frac{M_s}{V - V_f} \qquad\qquad 29$$

$$M_s = \rho_p[V - V_f] \qquad\qquad 30$$

Dry density (ρ_d) is the ratio of the mass of the solid grains (M_s) to the total volume (V).

$$\rho_d = \frac{M_s}{V} = \frac{\rho_p[V-V_f]}{V}$$
31

$$\rho_d = \frac{\rho_p[V-V_f]}{V} = \rho_p\left[\frac{V}{V} - \frac{V_f}{V}\right]$$
32

Given that:

$$\text{Porosity } (\Phi) = \frac{\text{volume of pore fluid}}{\text{total volume}} = \frac{V_f}{V}$$

$$\rho_d = \rho_p[1 - \Phi]$$
33

$$\rho_p = \left[\frac{\rho_d}{1-\Phi}\right]$$
34

2.3 Porosity

Porosity (Φ) is the ratio of the volume of the voids or pore spaces (V_f) to the total volume (V) of the rock sample (equation 35).

$$\text{Porosity } (\Phi) = \frac{V_f}{V}$$
35

Recall:

$$\rho_d = \rho_p[1 - \Phi]$$

$$\Phi = \left[1 - \frac{\rho_d}{\rho_p}\right]$$
36

Alternatively, the porosity is defined by and is often expressed as a percentage (equation 37).

$$\Phi = \left[1 - \frac{\rho_d}{\rho_p}\right] \times 100\%$$
37

2.4 Wet density

Wet density (ρ_{wet}) can be simply expressed as the sum of dry density (ρ_{dry}) with the product of porosity (Φ) and density of water (ρ_w). The sample was soaked under reduced pressure long enough that all the voids are filled with fluid (water).

$$\rho_{wet} = \frac{M_{solid} + M_{pore\,fluid}}{V_{total}} = \frac{M_s + M_f}{V} \qquad 38$$

where M_s = mass of solid, M_f = mass of pore fluid and V = total volume.

Recall:

$$\rho_d = \frac{M_s}{V}$$

$$M_s = \rho_d * V \qquad 39$$

$$\rho_{wet} = \frac{M_s + M_f}{V} = \frac{[[\rho_d * V] + M_f]}{V} \qquad 40$$

$$\rho_{wet} = \frac{V[\rho_d]}{V} + \frac{M_f}{V}$$

$$\rho_{wet} = \rho_d + \frac{M_f}{V} \qquad 41$$

$$V = \frac{V_f}{\Phi} \; ; \rho_w = \frac{M_f}{V_f}$$

$$\rho_{wet} = \rho_d + \left[M_f * \frac{\Phi}{V_f}\right] \qquad 42$$

$$\rho_{wet} = \rho_d + \left[\Phi * \frac{M_f}{V_f}\right] \qquad 43$$

$$\rho_{wet} = \rho_d + [\Phi * \rho_w] \qquad 44$$

where ρ_{wet} = wet density; ρ_d = dry density; Φ = porosity; ρ_w = density of water; V_f = volume of voids.

3. Density bar chart and density-porosity relationship plots
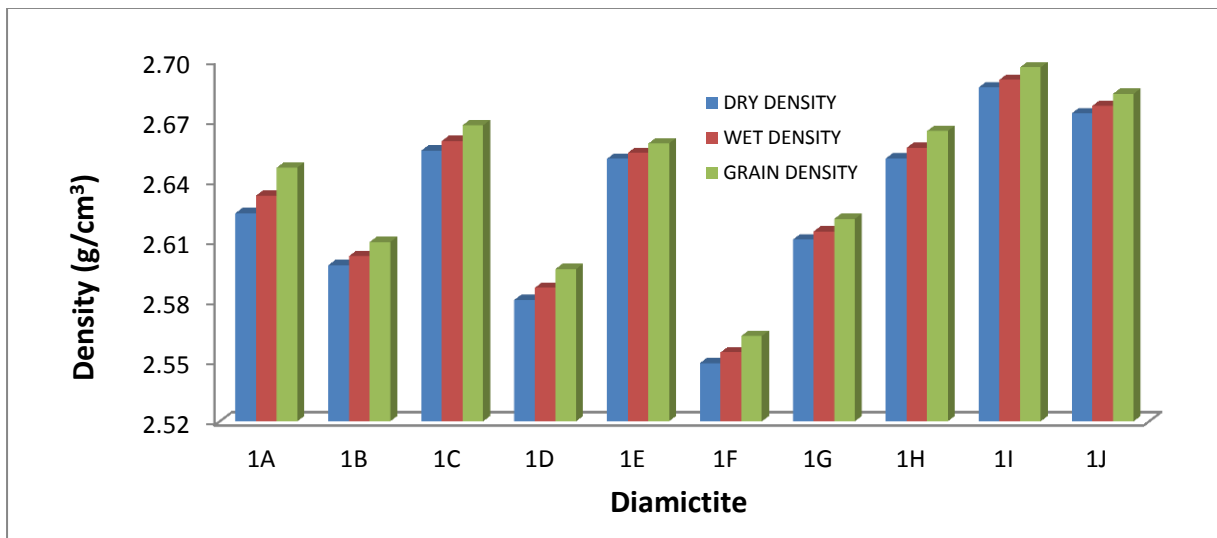
Figure C5 Bar chart of dry, wet and grain densities for the Dwyka diamictite.
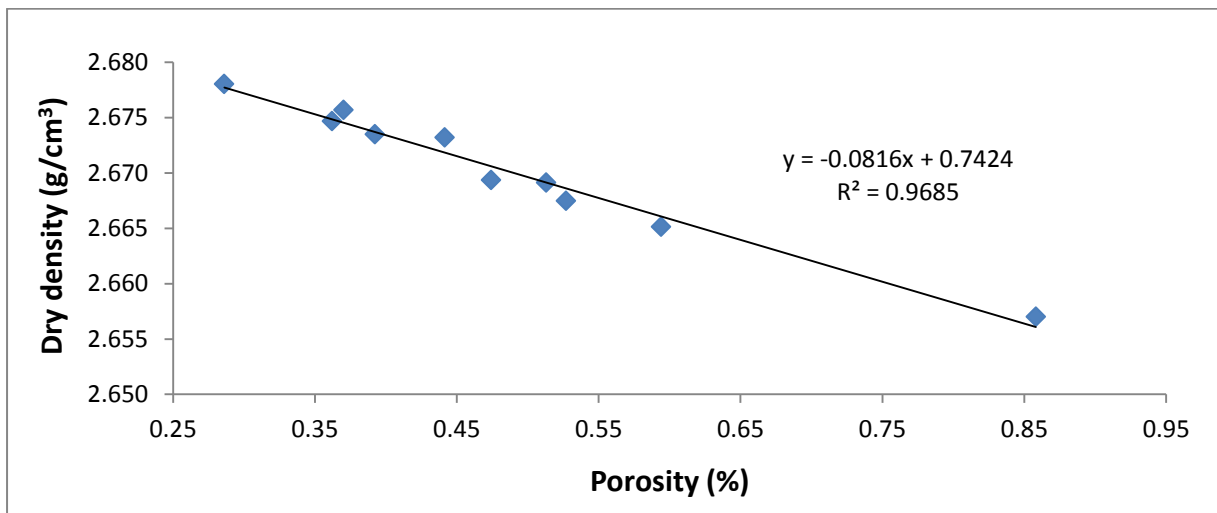
Figure C6 Dry density - porosity relationship for the Dwyka diamictite.

Figure C6 shows the plot of dry density versus porosity with regression lines correlating the dry density with the porosity. The study of the relationship between the parameters indicate that the coefficient of determination (R^2) value is 0.9685; thus the correlation coefficient (R) is 0.9841 which is close to +1, which implies that the variables are closely related. The negative correlation implies that, the higher the porosity, the lower the density and vice versa.
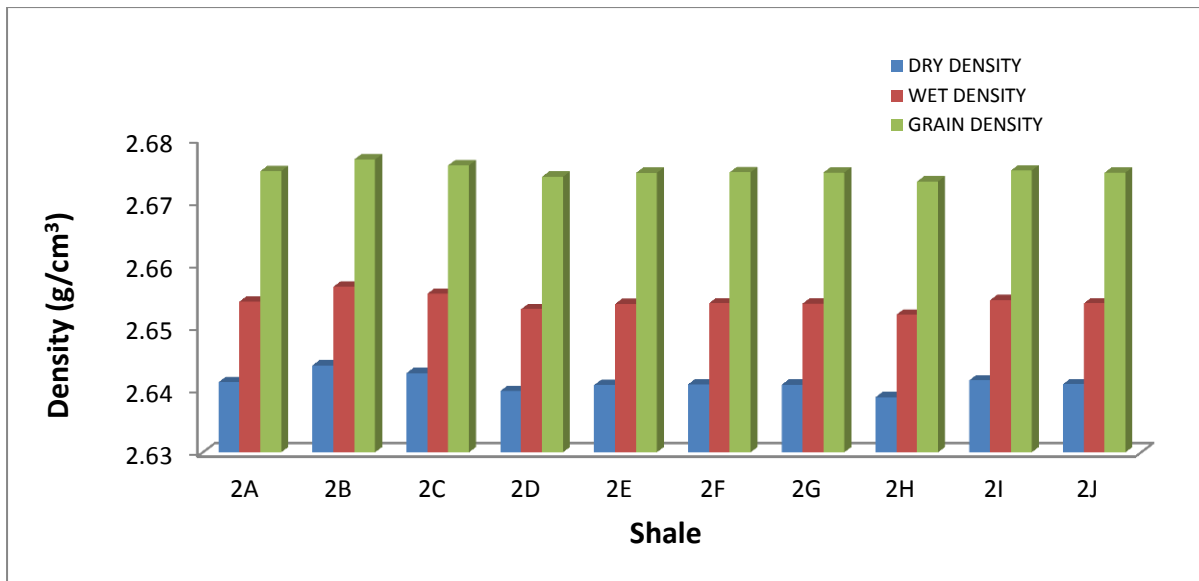
Figure C7 Bar chart of dry, wet and grain densities for shale of the Prince Albert Formation.
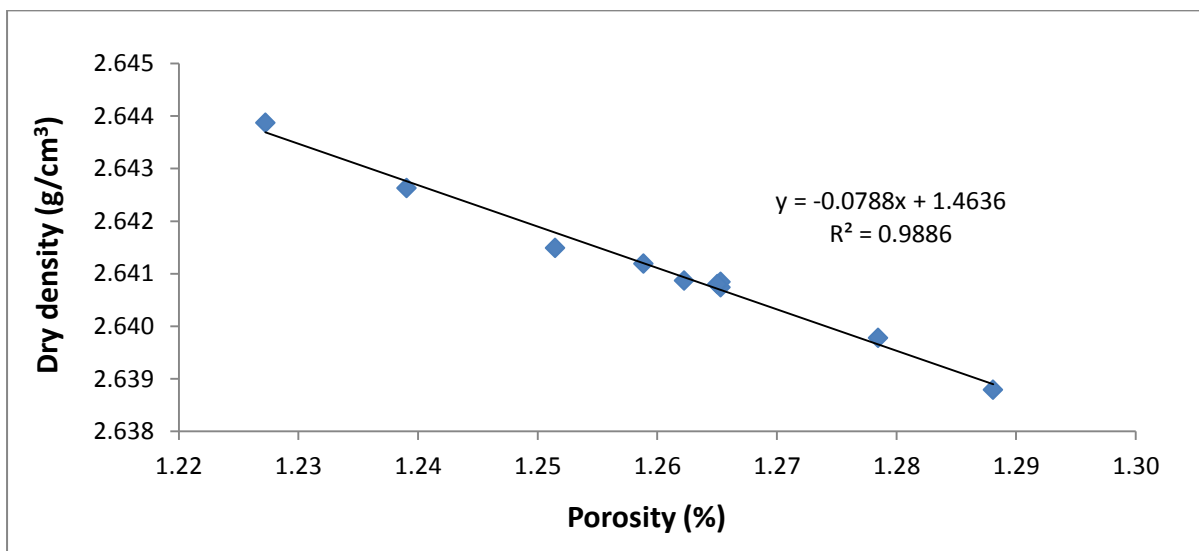
Figure C8 Dry density - porosity relationship for shale from the Prince Albert Formation.

The study of the relationship between dry density and porosity (Figure C8) also indicates a negative correlation between the two parameters with a high correlation coefficient value (R = 0.9943) which implies that the variables (dry density and porosity) are closely related.

275
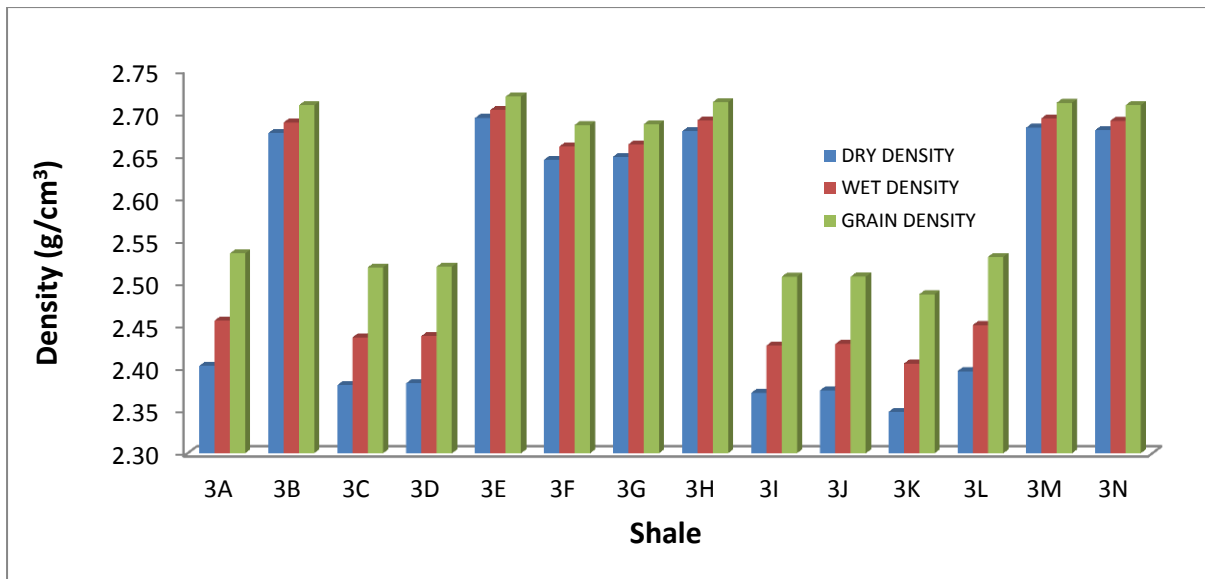
Figure C9 Bar chart of dry, wet and grain densities for shale from Whitehill Formation.
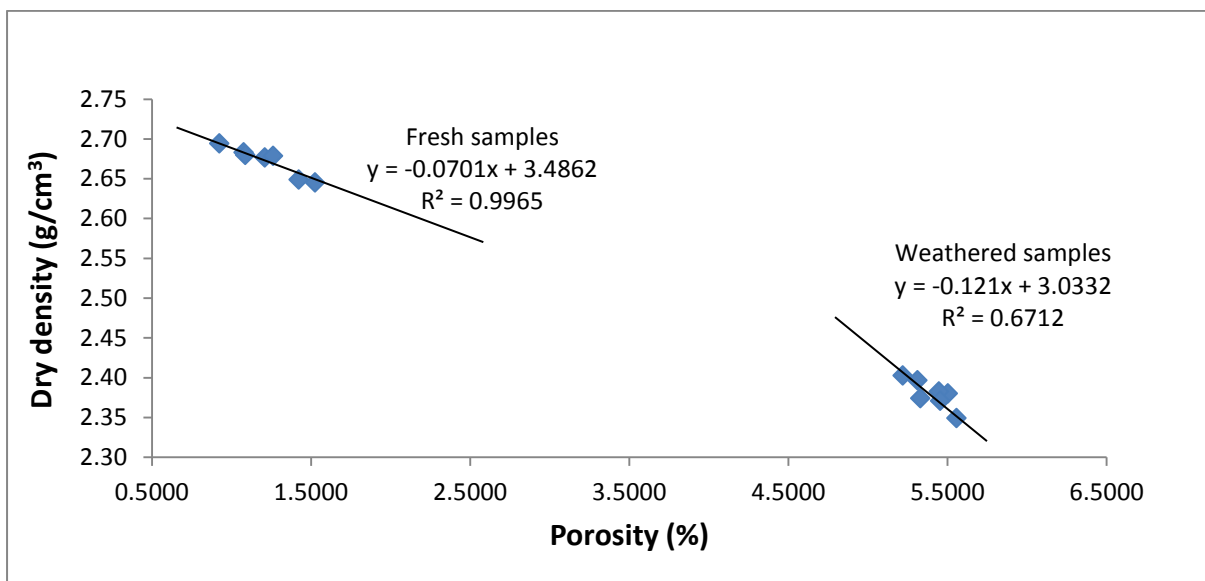
Figure C10 Dry density - porosity relationship for shale of the Whitehill Formation.

The plot of dry density versus porosity for shale of the Whitehill Formation (fresh samples; Figure C10) shows negative correlation between the two parameters. The study of the relationship between the parameters indicates a correlation coefficient (R) value of 0.9982. The high correlation value of 0.9982 implies that the variables are closely related.
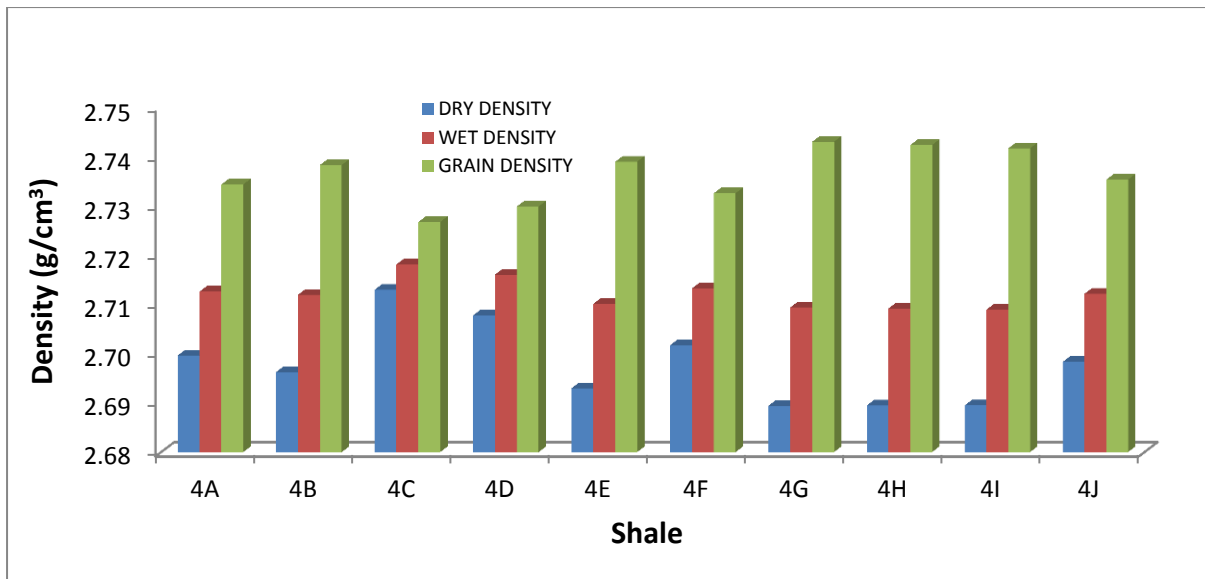
Figure C11 Bar chart of dry, wet and grain densities for shale from Collingham Formation.
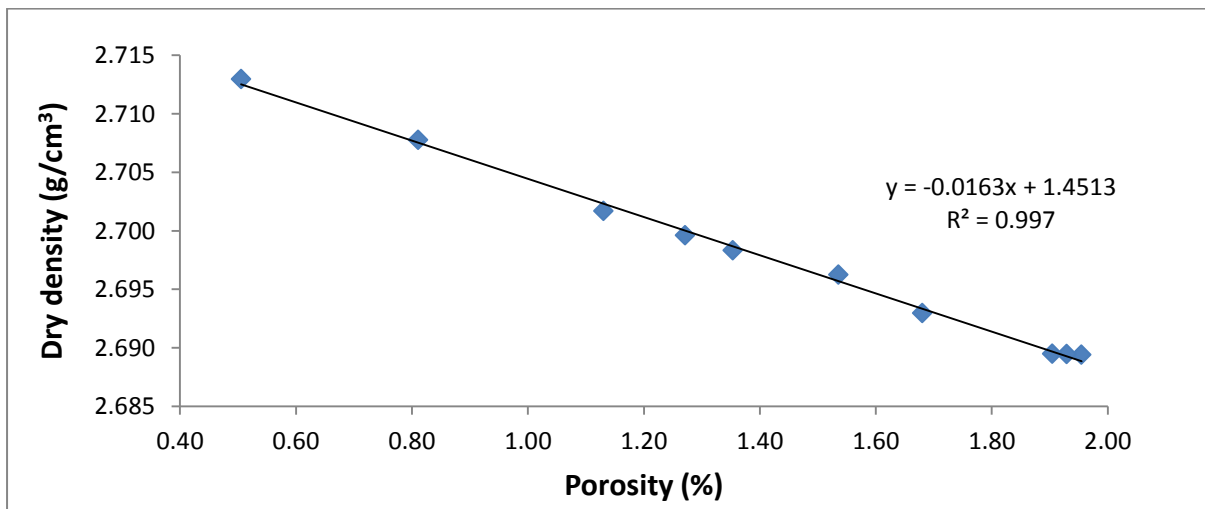
Figure C12 Dry density - porosity relationship for shale of the Collingham Formation.

The plot of dry density versus porosity for shale of the Collingham Formation is shown in Figure C12. The correlation coefficient value (R = 0.9885) which is close to +1 indicate that the variables (dry density and porosity) are closely related.
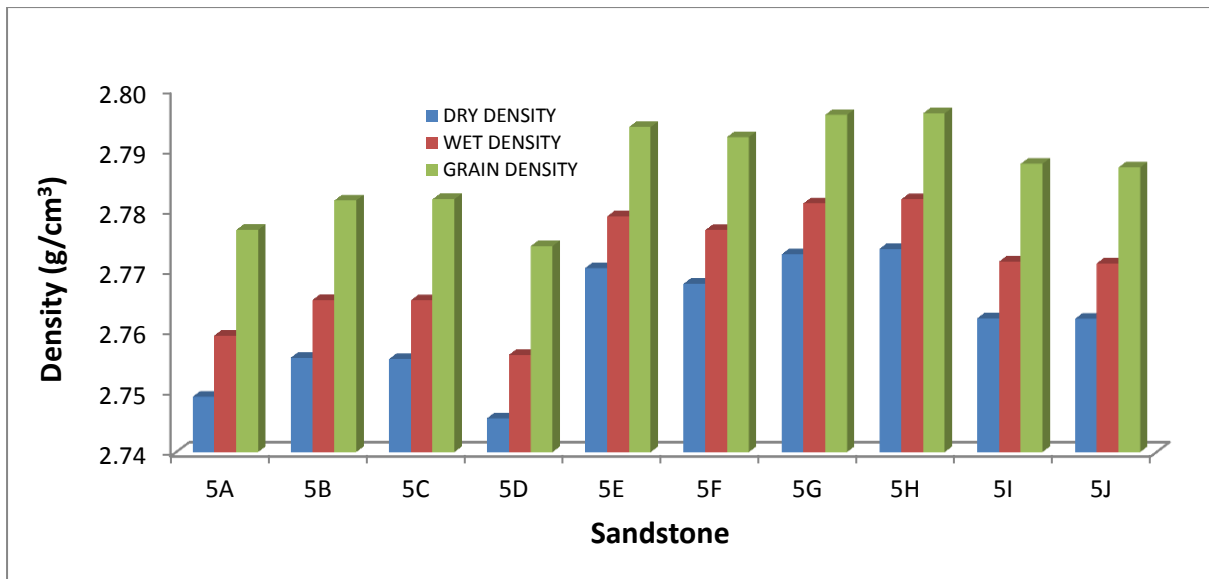
Figure C13 Bar chart of dry, wet and grain densities for sandstones from the Ripon Formation.
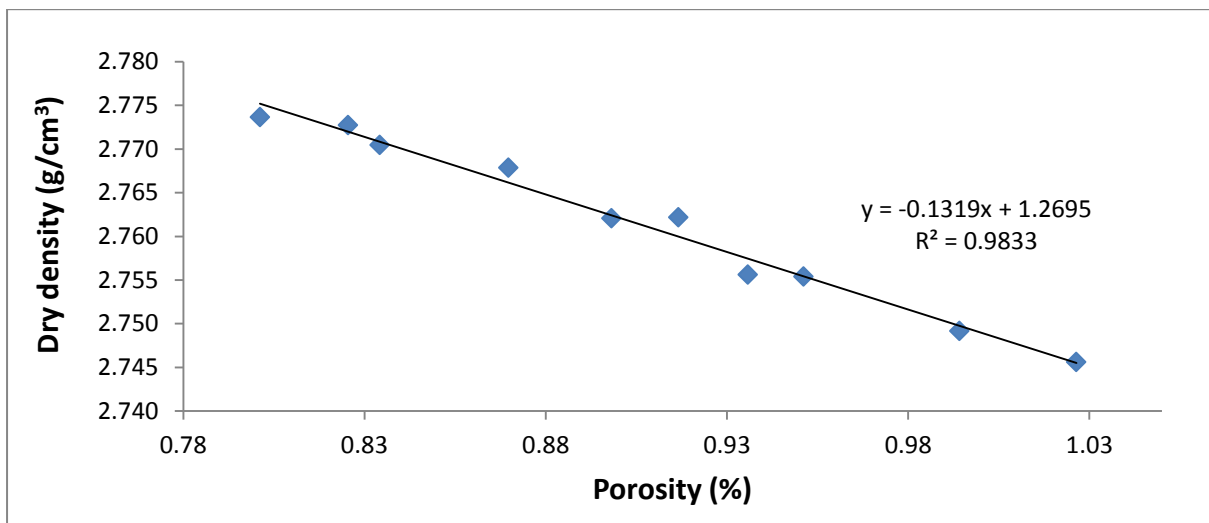
Figure C14 Dry density - porosity relationship for sandstones from the Ripon Formation.

Figure C14 shows the plot of dry density versus porosity for sandstones from the Ripon Formation. The coefficient of determination (R^2) value is 0.9833; hence the correlation coefficient R is 0.9916 which is close to +1, indicating that the variables (dry density and porosity) are closely related.
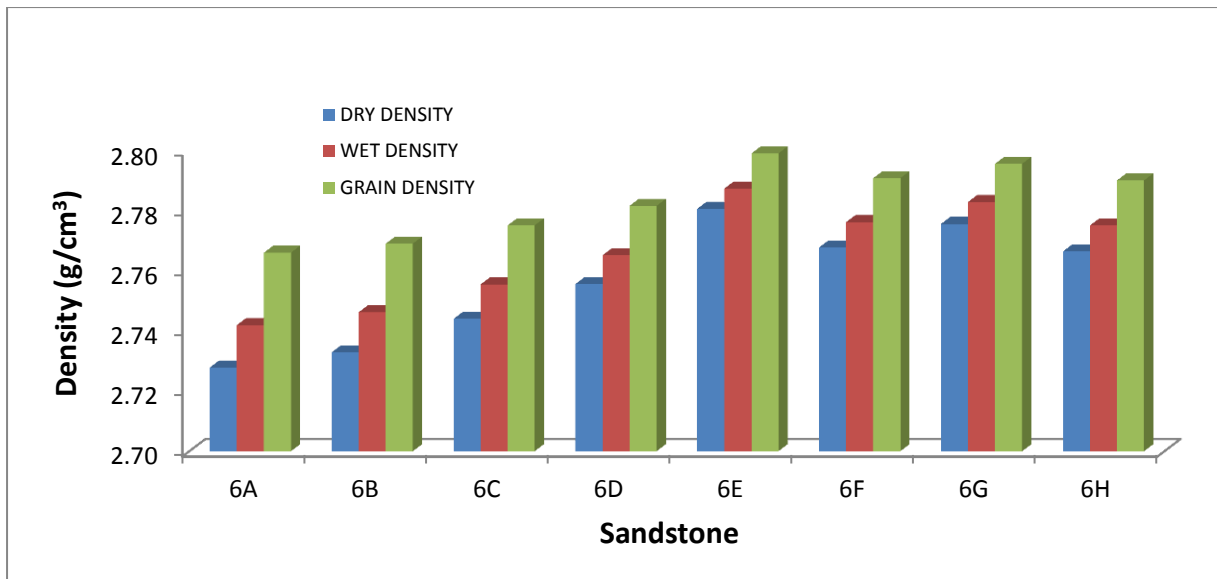
Figure C15 Bar chart of dry, wet, and grain densities for shale from the Fort Brown Formation.
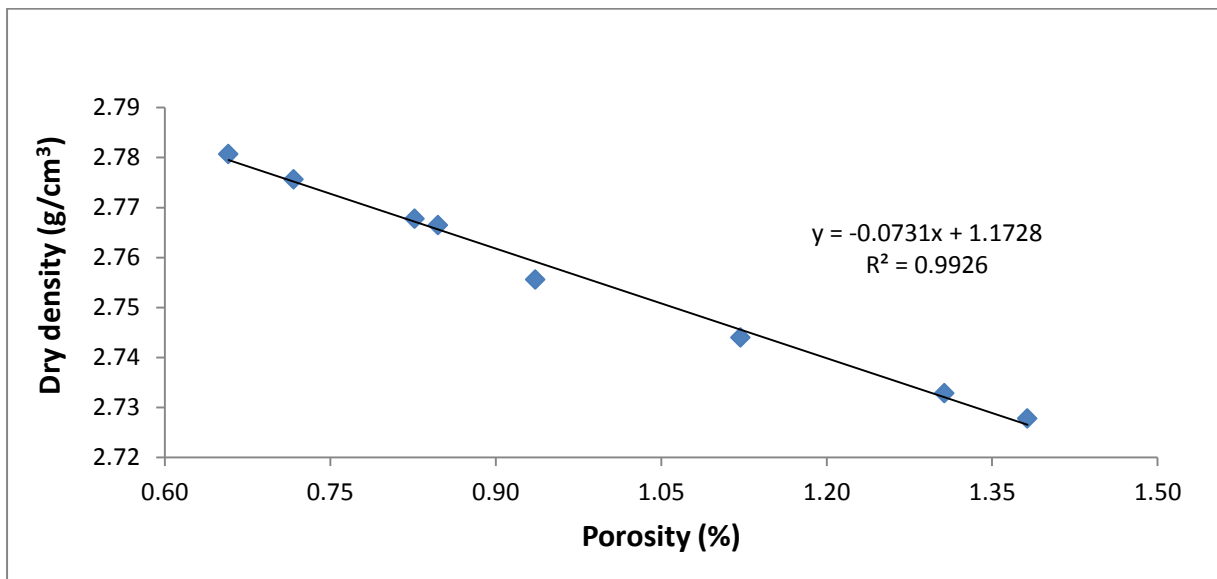
Figure C16 Dry density - porosity relationship for the Fort Brown Formation.

Figure C16 shows the plot of dry density against porosity. The coefficient of determination (R^2) value is 0.9926, thus the correlation coefficient R is 0.9963 which is close to +1, signifying that the variables are closely related. The negative correlation also indicates that, the lower the density, the higher the porosity and vice versa.
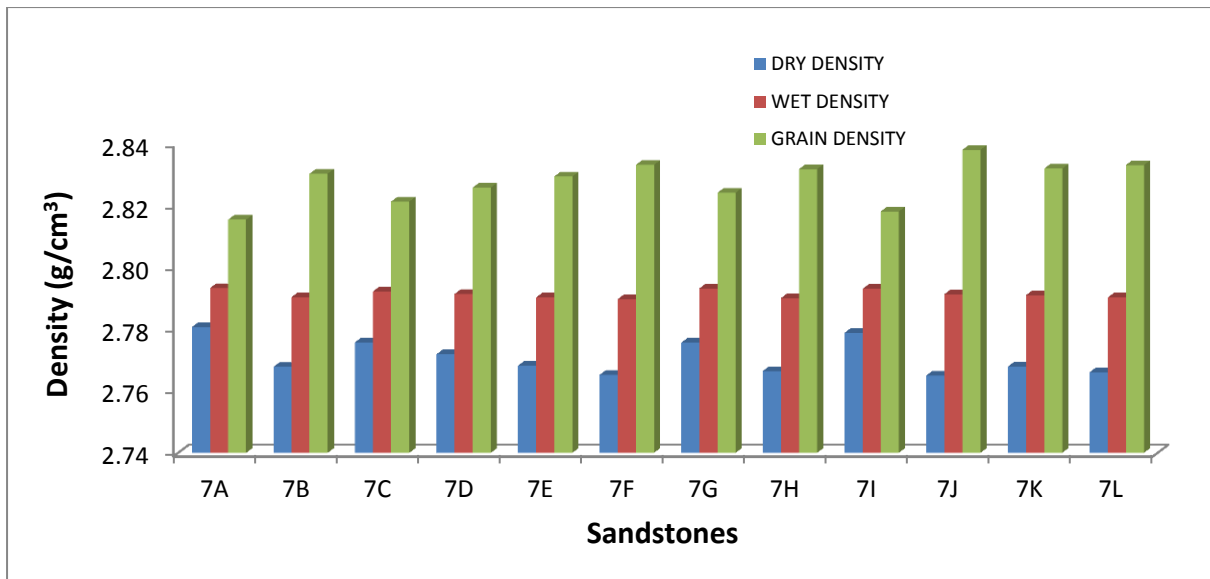
Figure C17 Bar chart of dry, wet and grain densities for the Koonap Formation.
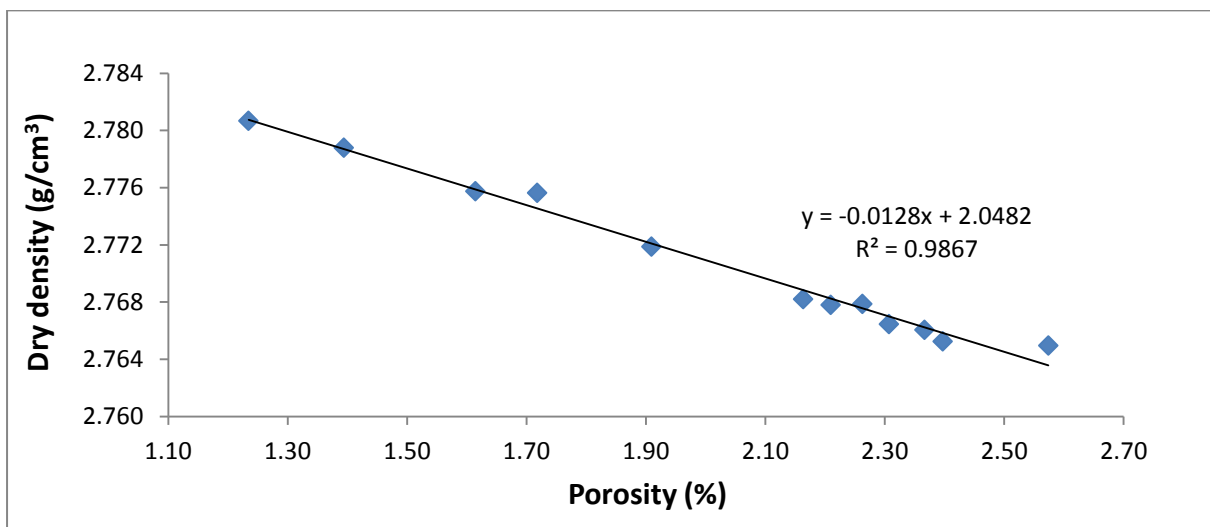
Figure C18 Dry density - porosity relationship for the Koonap Formation.

Figure C18 shows the plot of dry density against porosity of sandstones from the Koonap Formation. The regression line indicates a linear relationship. The coefficient of determination (R^2) is 0.9867, hence the correlation coefficient value is high (R = 0.9933). This high value of correlation coefficient is close to +1 therefore implying that the variables are closely related.
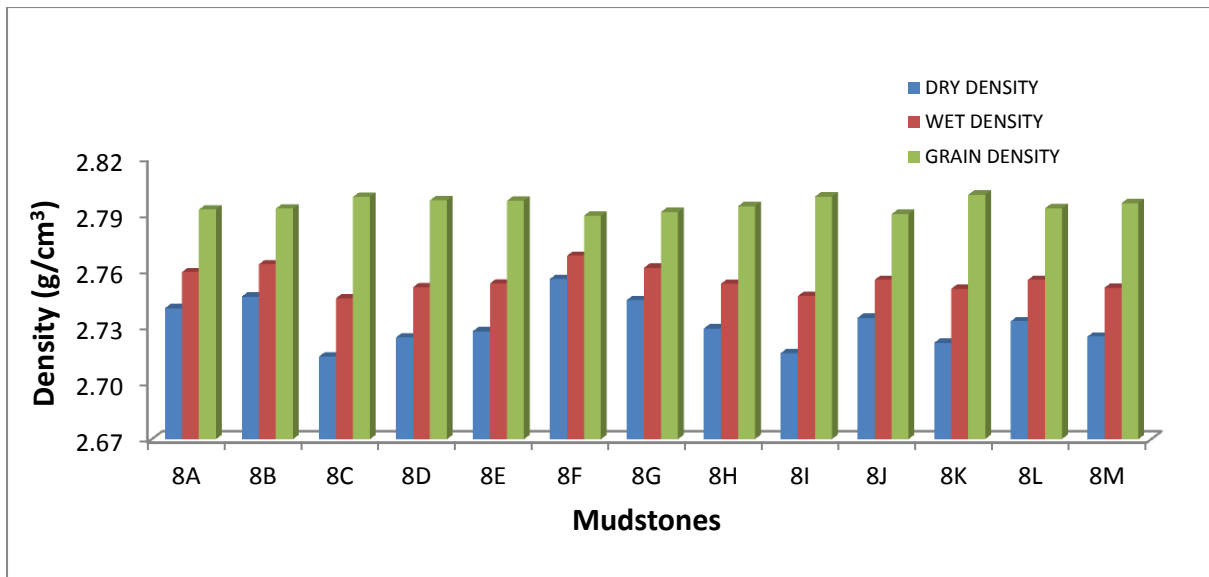
Figure C19 Bar chart of dry, wet and grain densities for the Middleton Formation.
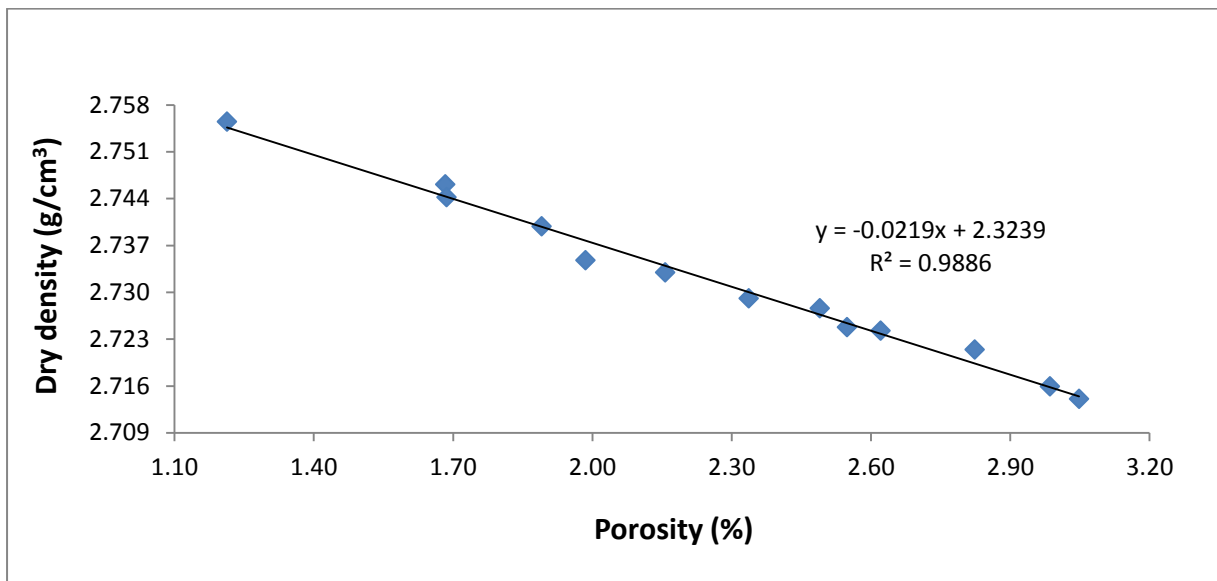
Figure C20 Dry density - porosity relationship for the Middleton Formation.

Figure C20 shows the plot of dry density versus porosity of mudstones from the Middleton Formation. The coefficient of determination (R^2) value is 0.9886; hence the correlation coefficient (R) is 0.9943 which is close to +1, signifying that the variables are closely related. The negative correlation also indicates that, the lower the density, the higher the porosity and vice versa.
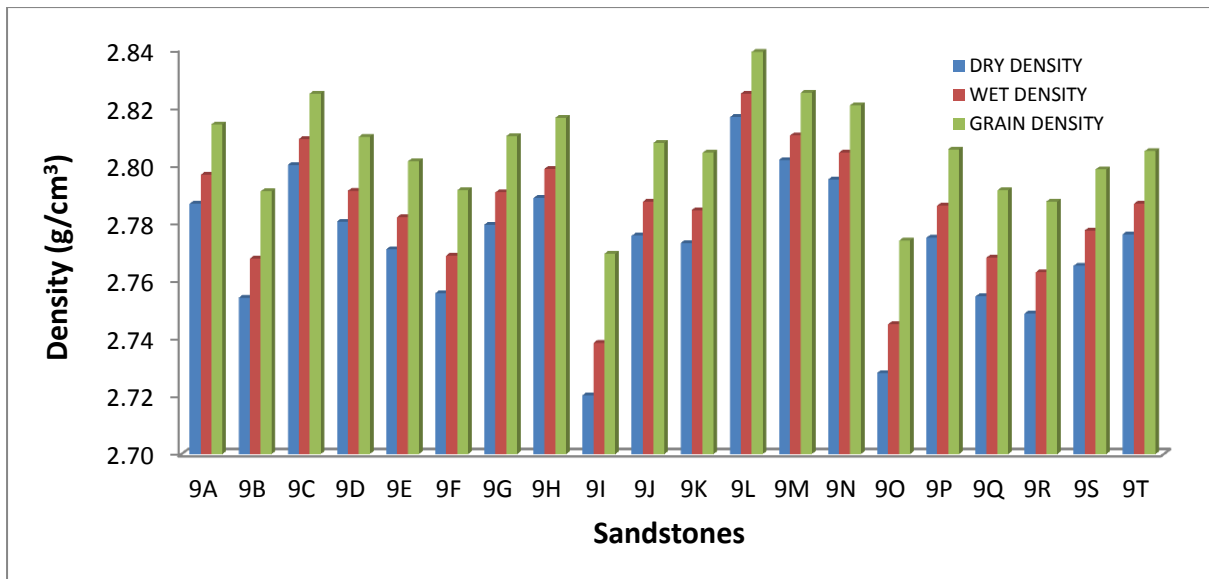
Figure C21 Bar chart of dry, wet and grain densities for the Oudeberg Member.
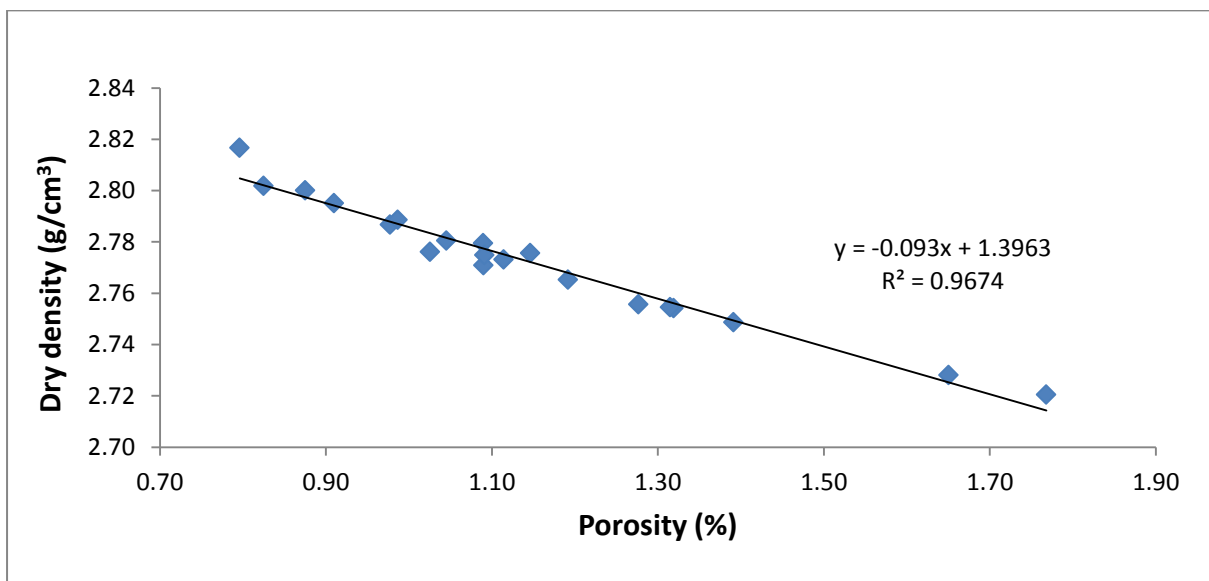
Figure C22 Dry density - porosity relationship for sandstones from the Oudeberg Member.

Figure C22 shows the plot of dry density against porosity. The coefficient of determination (R^2) value is 0.9674; hence the correlation coefficient (R) is 0.9836 which is close to +1, signifying that the variables are closely related. The negative correlation also indicates that, the lower the density, the higher the porosity and vice versa.
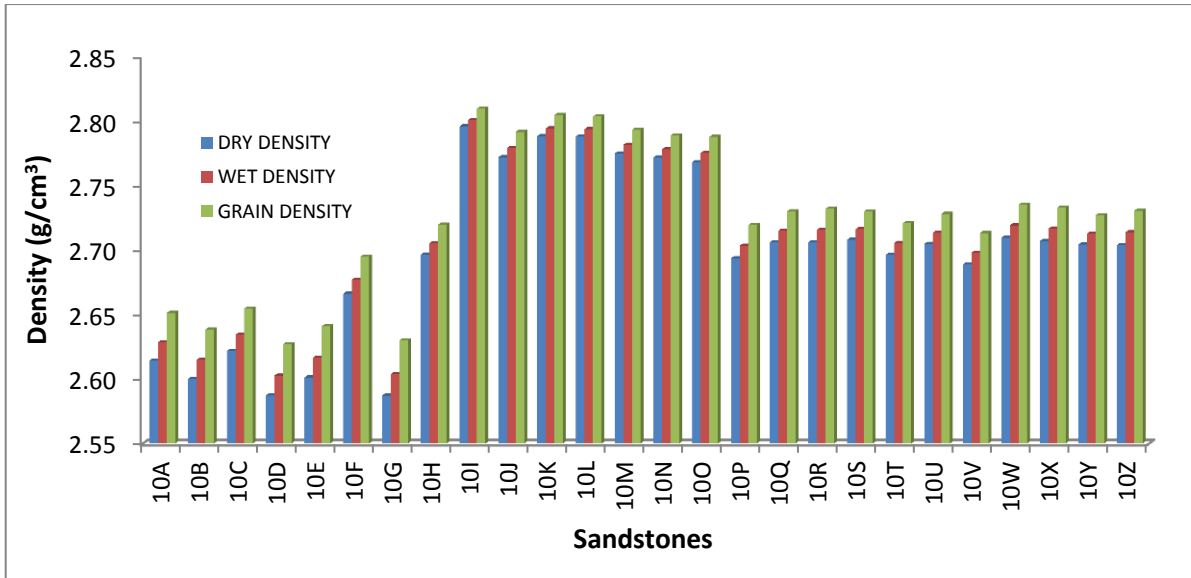
Figure C23 Bar chart of dry, wet and grain densities for the Daggaboersnek Member.
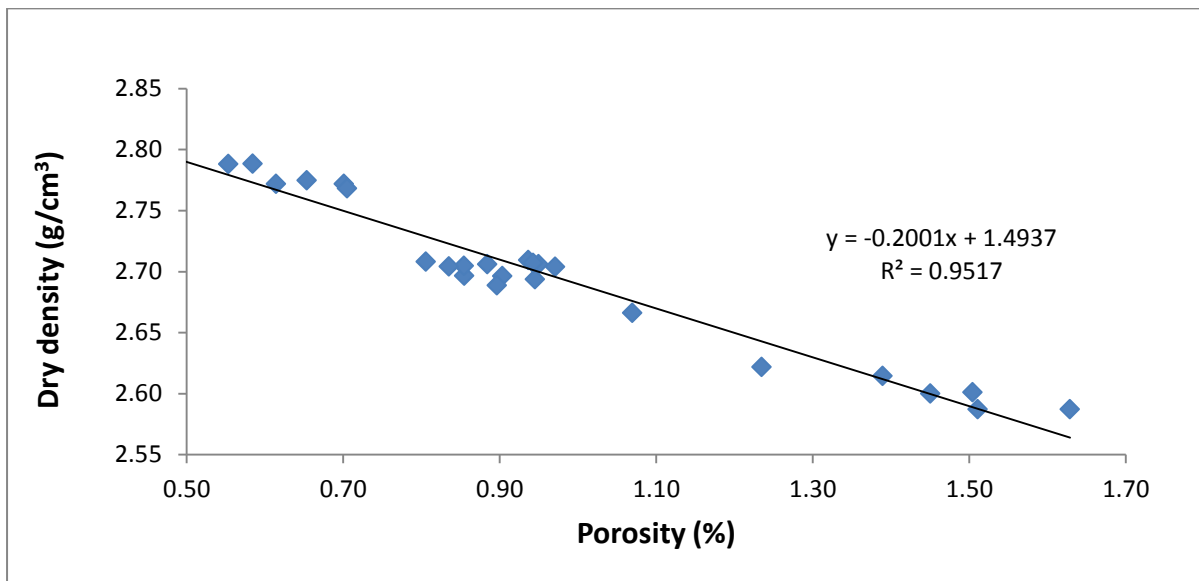
Figure C24 Dry density - porosity relationship for the Daggaboersnek Member.

The plot of dry density versus porosity for sandstone from the Daggaboersnek Member (Figure C24) shows a linear relationship. The regression line which correlates the dry density with porosity indicate that the coefficient of determination (R^2) value is 0.9517; thus the correlation coefficient (R) is 0.9756 which is close to +1, which implies that the variables are closely related.
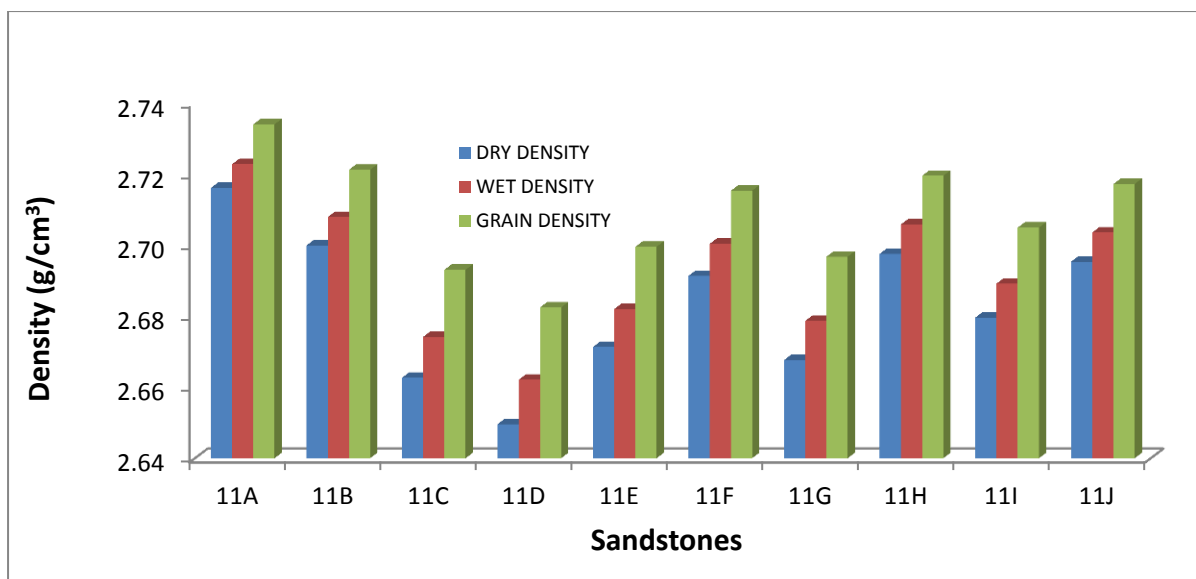
Figure C25 Bar chart of dry, wet and grain densities for the Barberskrans Member.
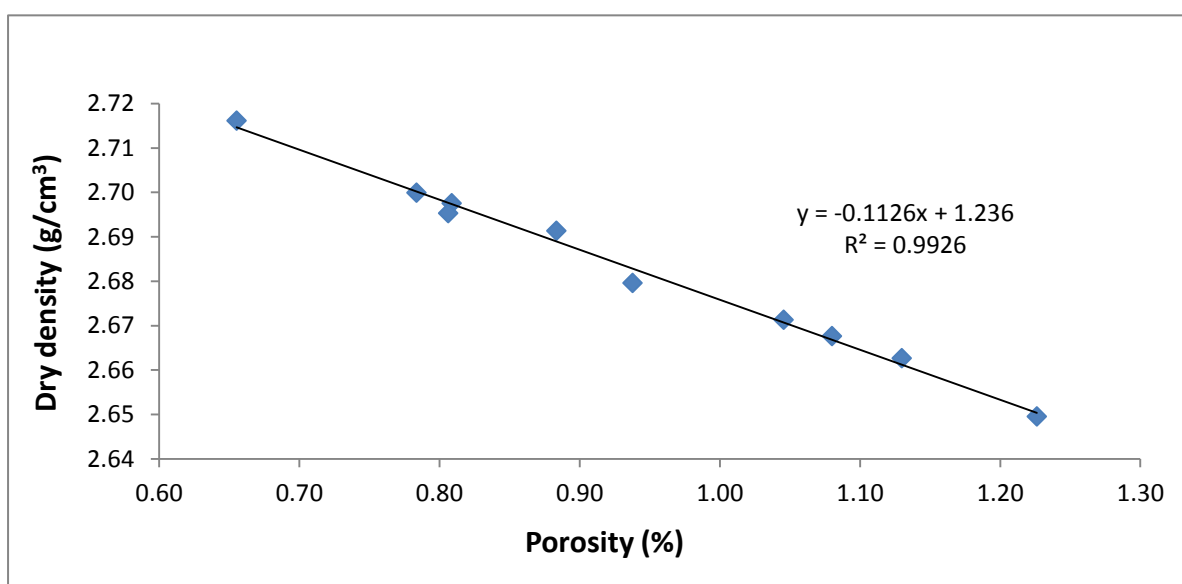
Figure C26 Dry density - porosity relationship for sandstone from the Barberskrans Member.

The plot of dry density versus porosity for sandstone from the Barberskrans Member shows a linear relationship (Figure C26). The regression line which correlate the dry density with porosity indicate a correlation coefficient value (R = 0.9963) which is close to +1, thus signifying that the variables are closely related.
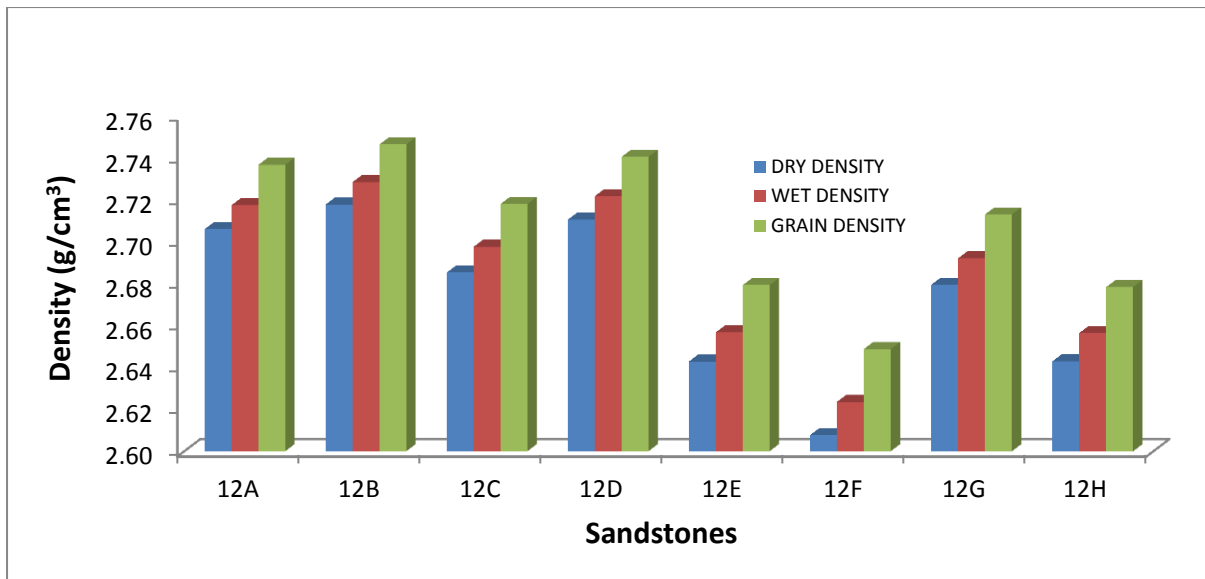
Figure C27 Bar chart of dry, wet and grain densities for the Elandsberg Member.
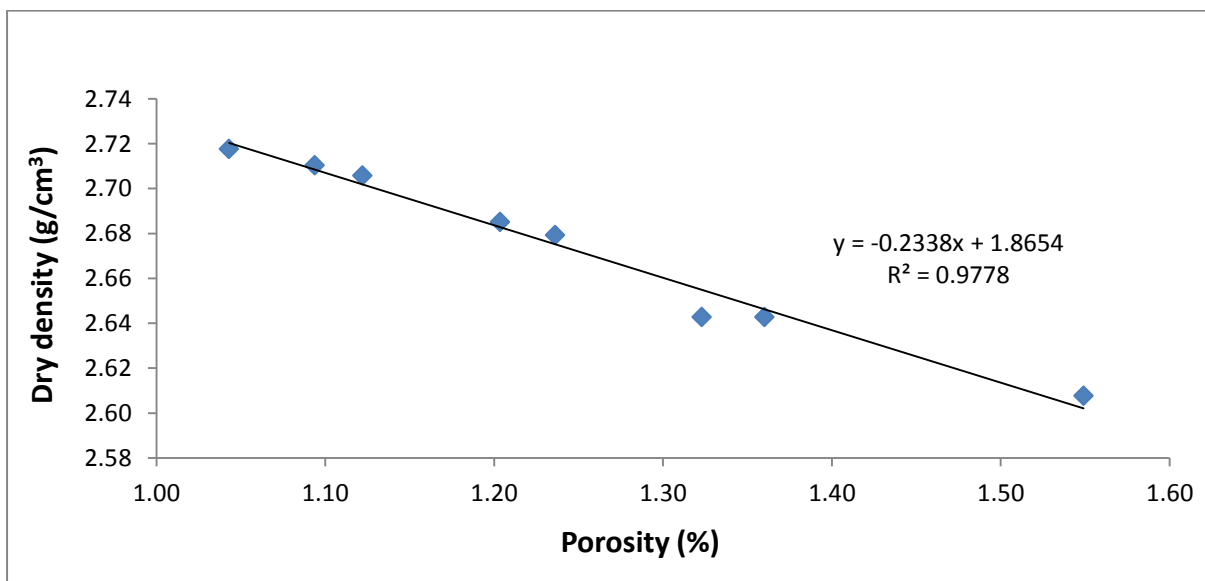
Figure C28 Plot of dry density - porosity of sandstones from the Elandsberg Member.

Figure C28 shows dry density – porosity relationship of sandstones from the Elandsberg Member. The coefficient of determination (R^2) value is 0.9778, thus the correlation coefficient (R) is 0.9888 which is close to +1, signifying that the variables (dry density and porosity) are closely related.
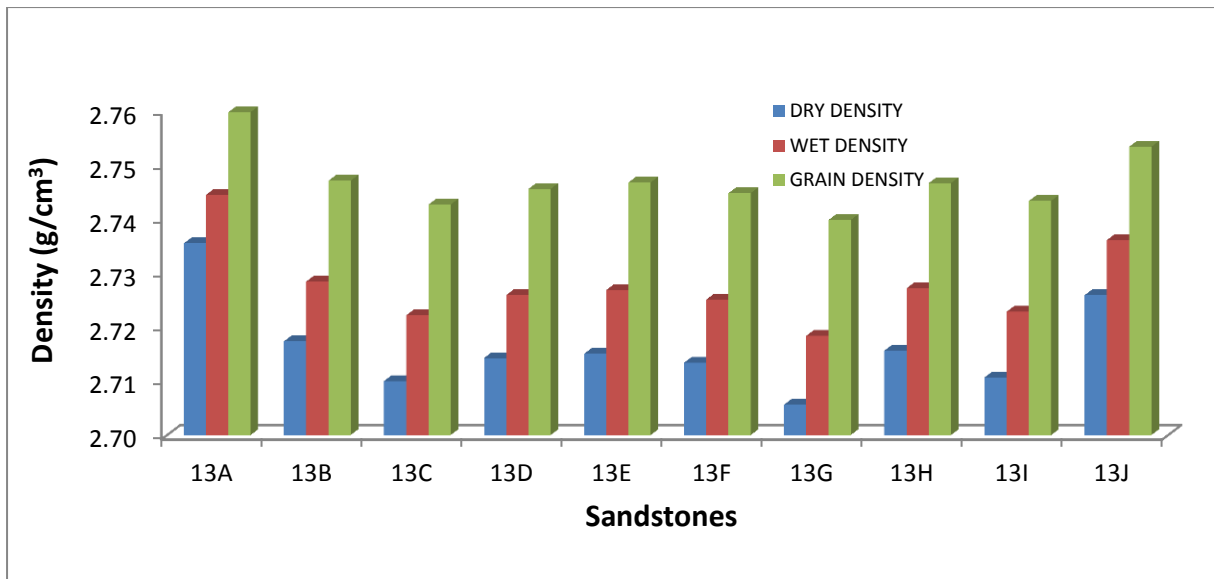
Figure C29 Bar chart of dry, wet and grain densities for the Palingkloof Member.
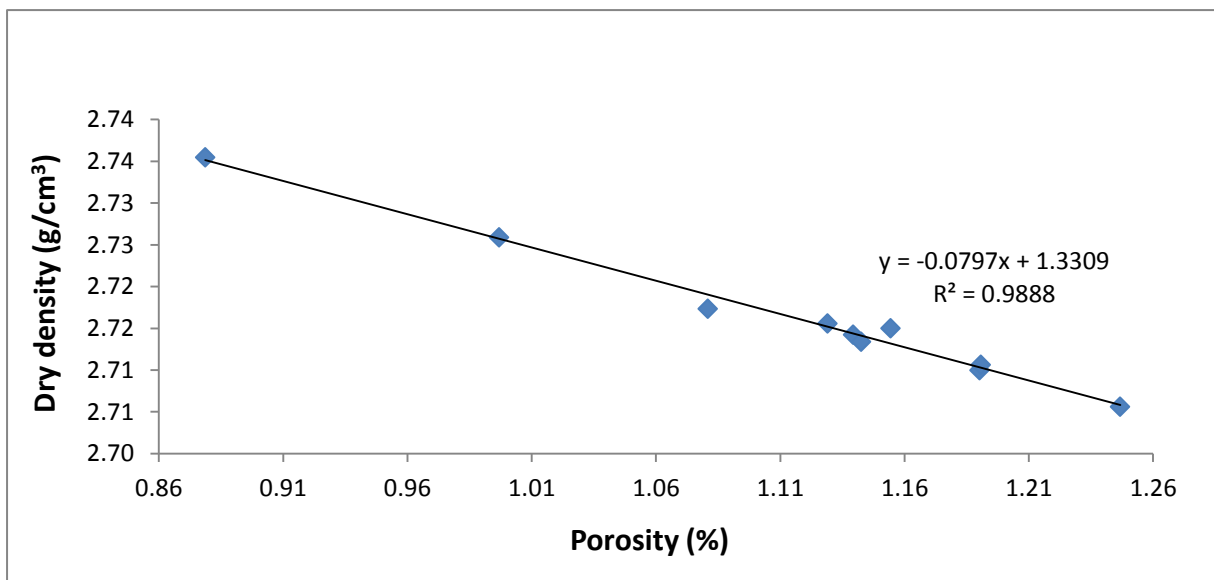
Figure C30 The plot of dry density versus porosity for sandstones from the Palingkloof Member showing linear relationship. The regression line which correlate the dry density with porosity indicate a high negative correlation with a coefficient value (R = 0.9944) which is close to +1, thus implying that the variables (dry density and porosity) are closely related.
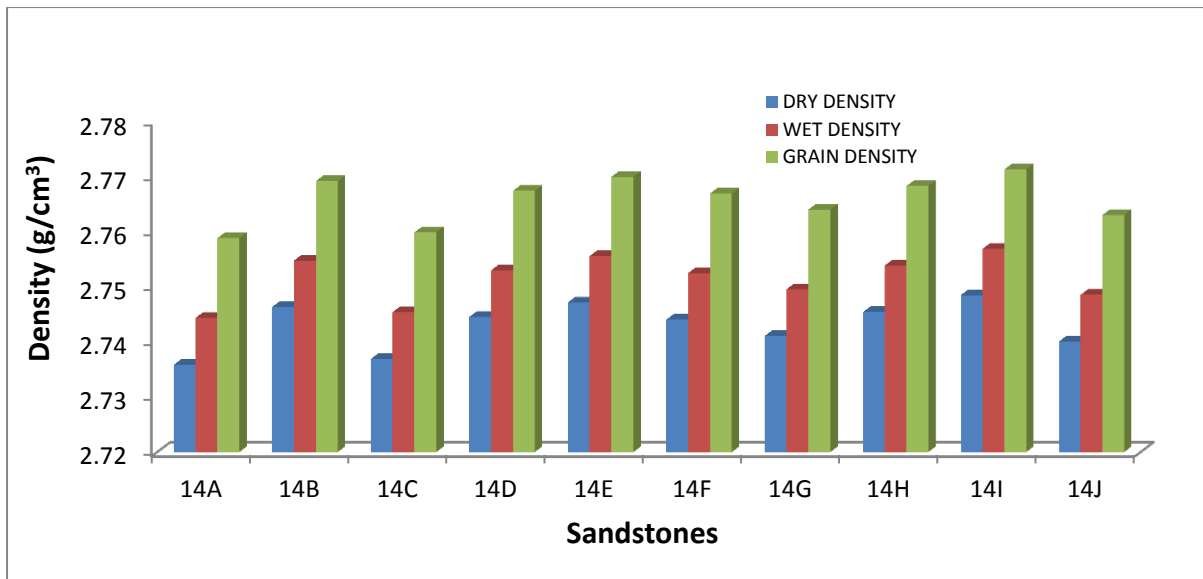
Figure C31 Bar chart of dry, wet and grain densities for the Katberg Formation.
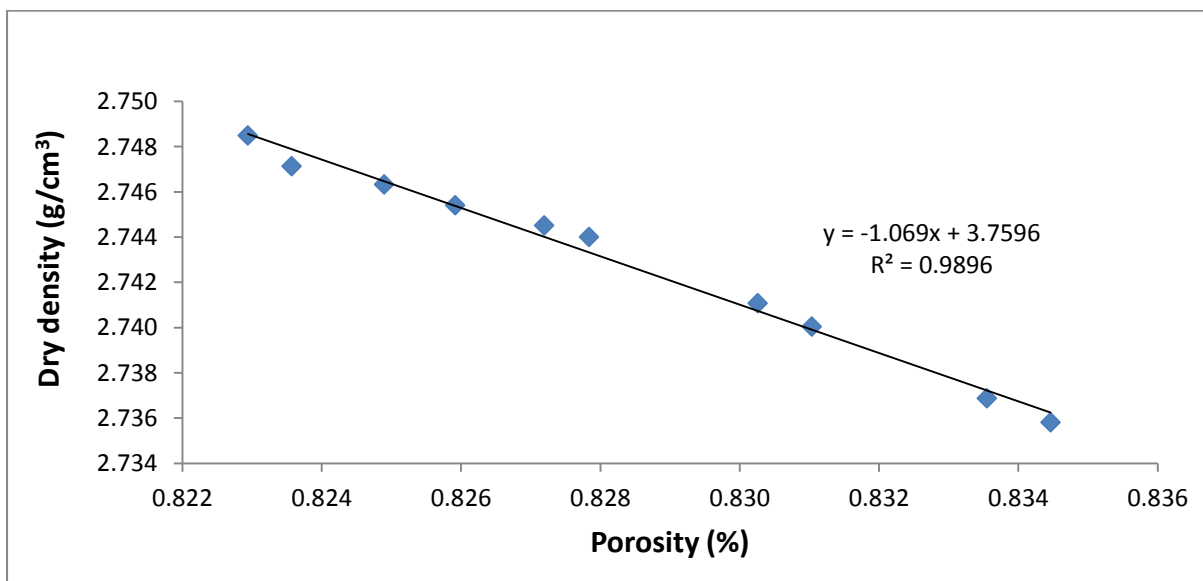
Figure C32 Plot of dry density against porosity for sandstones from the Katberg Formation.

The study of the relationship between dry density and porosity (Figure C32) indicate a negative correlation with a coefficient value (R = 0.9948) which is close to +1, hence suggesting that the variables (dry density and porosity) are closely related. This negative correlation implies that the lower the density, the higher the porosity and vice versa.
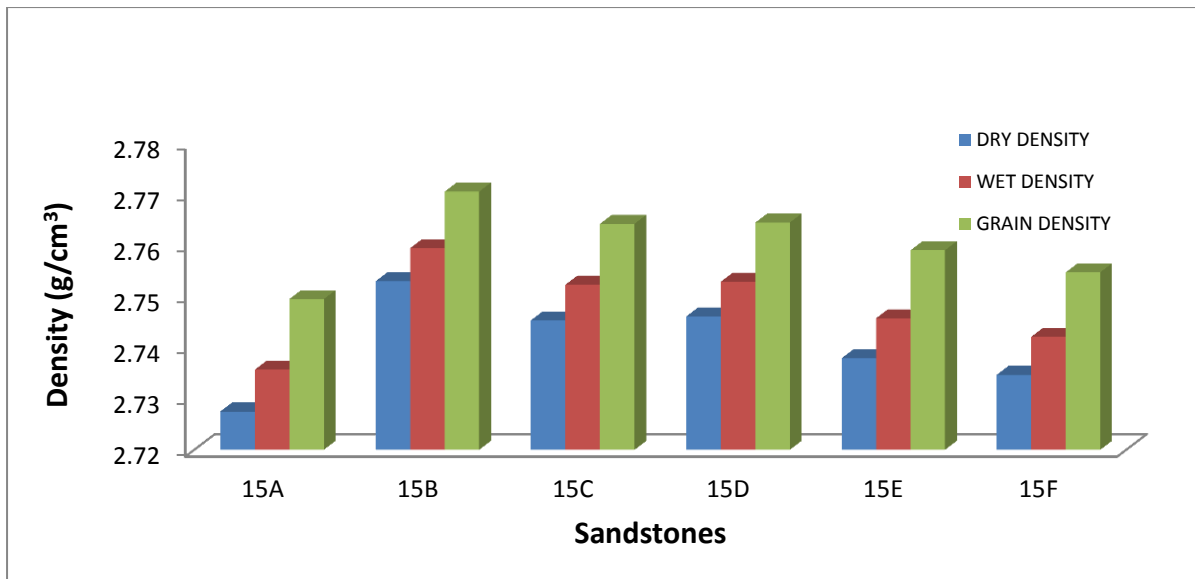
Figure C33 Bar chart of dry, wet and grain densities for the Burgersdorp Formation.
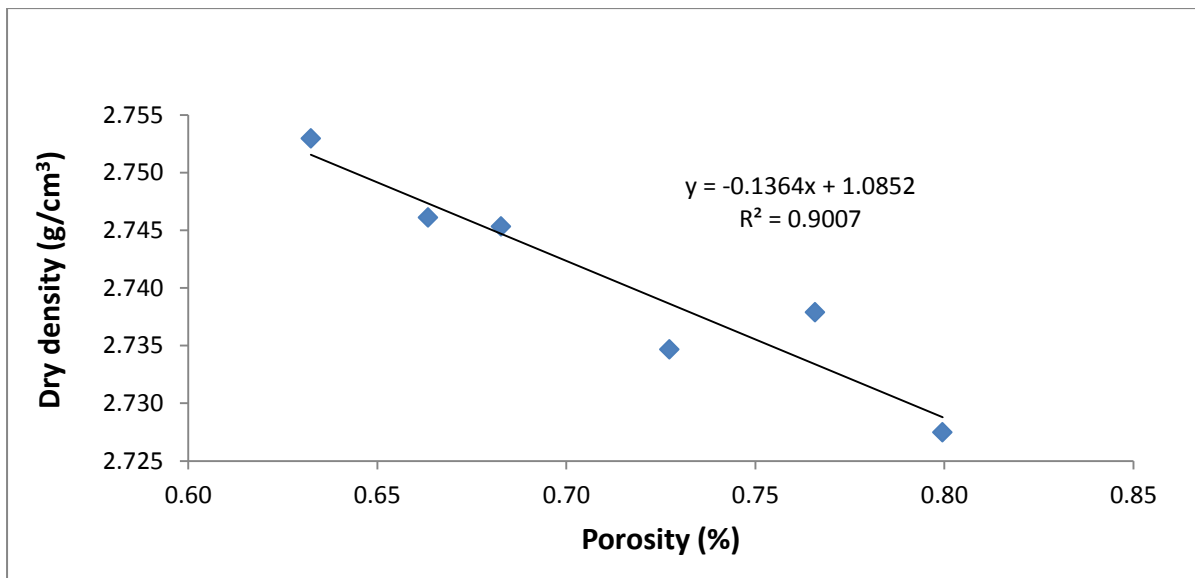
Figure C34 shows the plot of dry density versus porosity for mudstones from the Burgersdorp Formation. The coefficient of determination (R^2) value is 0.9007, thus the correlation coefficient (R) is 0.9491 which is close to +1, signifying that the variables (dry density and porosity) are closely related. This negative correlation implies that the lower the density, the higher the porosity and vice versa.

Calculated dry density, wet density, grain density and porosity of rocks samples from the Karoo and Cape Supergroups using Archimedes principles

SAMPLE NO	FORMATION	LITHOLOGY	DRY DENSITY (g/cm3)	WET DENSITY (g/cm3)	GRAIN DENSITY (g/cm3)	POROSITY (%)
1A	Dwyka	Diamictite	2.6570	2.6660	2.6805	0.8760
1B	Dwyka	Diamictite	2.6732	2.6779	2.6856	0.4627
1C	Dwyka	Diamictite	2.6693	2.6742	2.6822	0.4784
1D	Dwyka	Diamictite	2.6651	2.6715	2.6819	0.6263
1E	Dwyka	Diamictite	2.6780	2.6810	2.6858	0.2909
1F	Dwyka	Diamictite	2.5854	2.5909	2.5994	0.5396
1G	Dwyka	Diamictite	2.6735	2.6776	2.6844	0.4078
1H	Dwyka	Diamictite	2.6691	2.6744	2.6830	0.5188
1I	Dwyka	Diamictite	2.6757	2.6794	2.6856	0.3678
1J	Dwyka	Diamictite	2.6747	2.6784	2.6844	0.3624
2A	Prince Albert	Shale	2.6412	2.6541	2.6749	1.2588
2B	Prince Albert	Shale	2.6439	2.6564	2.6767	1.2272
2C	Prince Albert	Shale	2.6426	2.6553	2.6758	1.2390
2D	Prince Albert	Shale	2.6398	2.6528	2.6740	1.2785
2E	Prince Albert	Shale	2.6407	2.6537	2.6746	1.2653
2F	Prince Albert	Shale	2.6408	2.6538	2.6747	1.2653
2G	Prince Albert	Shale	2.6408	2.6537	2.6746	1.2650
2H	Prince Albert	Shale	2.6388	2.6520	2.6732	1.2881
2I	Prince Albert	Shale	2.6415	2.6543	2.6750	1.2515
2J	Prince Albert	Shale	2.6409	2.6538	2.6746	1.2623
3A	Whitehill	Shale	2.4026	2.4560	2.5349	5.2187
3B	Whitehill	Shale	2.6764	2.6888	2.7092	1.2099
3C	Whitehill	Shale	2.3800	2.4362	2.5186	5.5038
3D	Whitehill	Shale	2.3822	2.4379	2.5195	5.4463
3E	Whitehill	Shale	2.6943	2.7038	2.7195	0.9254
3F	Whitehill	Shale	2.6452	2.6608	2.6861	1.5253
3G	Whitehill	Shale	2.6487	2.6632	2.6869	1.4225
3H	Whitehill	Shale	2.6786	2.6915	2.7129	1.2632
3I	Whitehill	Shale	2.3708	2.4266	2.5076	5.4545
3J	Whitehill	Shale	2.3740	2.4285	2.5077	5.3297
3K	Whitehill	Shale	2.3489	2.4056	2.4871	5.5566
3L	Whitehill	Shale	2.3966	2.4509	2.5310	5.3110
3M	Whitehill	Shale	2.6829	2.6940	2.7122	1.0781
3N	Whitehill	Shale	2.6798	2.6909	2.7092	1.0879
4A	Collingham	Shale	2.6996	2.7126	2.7344	1.2710
4B	Collingham	Shale	2.6963	2.7120	2.7383	1.5354
4C	Collingham	Shale	2.7130	2.7181	2.7267	0.5052
4D	Collingham	Shale	2.7078	2.7160	2.7299	0.8106
4E	Collingham	Shale	2.6930	2.7101	2.7390	1.6801

4F	Collingham	Shale	2.7017	2.7132	2.7326	1.1305
4G	Collingham	Shale	2.6894	2.7094	2.7430	1.9548
4H	Collingham	Shale	2.6895	2.7092	2.7424	1.9294
4I	Collingham	Shale	2.6895	2.7090	2.7417	1.9044
4J	Collingham	Shale	2.6983	2.7122	2.7353	1.3532
5A	Ripon	Sandstone	2.7491	2.7593	2.7767	0.9942
5B	Ripon	Sandstone	2.7556	2.7652	2.7816	0.9358
5C	Ripon	Sandstone	2.7554	2.7651	2.7818	0.9511
5D	Ripon	Sandstone	2.7456	2.7561	2.7741	1.0264
5E	Ripon	Sandstone	2.7705	2.7790	2.7938	0.8342
5F	Ripon	Sandstone	2.7678	2.7767	2.7921	0.8697
5G	Ripon	Sandstone	2.7727	2.7812	2.7958	0.8254
5H	Ripon	Sandstone	2.7736	2.7818	2.7960	0.8012
5I	Ripon	Sandstone	2.7621	2.7715	2.7877	0.9166
5J	Ripon	Sandstone	2.7621	2.7712	2.7871	0.8982
6A	Fort Brown	Sandstone	2.7278	2.7420	2.7661	1.3820
6B	Fort Brown	Sandstone	2.7329	2.7462	2.7691	1.3069
6C	Fort Brown	Sandstone	2.7440	2.7555	2.7751	1.1218
6D	Fort Brown	Sandstone	2.7556	2.7652	2.7816	0.9358
6E	Fort Brown	Sandstone	2.7807	2.7874	2.7991	0.6578
6F	Fort Brown	Sandstone	2.7678	2.7762	2.7909	0.8264
6G	Fort Brown	Sandstone	2.7756	2.7829	2.7957	0.7168
6H	Fort Brown	Sandstone	2.7665	2.7751	2.7901	0.8478
7A	Koonap	Sandstone	2.7807	2.7933	2.8154	1.2347
7B	Koonap	Sandstone	2.7678	2.7904	2.8303	2.2095
7C	Koonap	Sandstone	2.7757	2.7923	2.8213	1.6146
7D	Koonap	Sandstone	2.7719	2.7914	2.8258	1.9095
7E	Koonap	Sandstone	2.7682	2.7903	2.8294	2.1635
7F	Koonap	Sandstone	2.7652	2.7897	2.8332	2.3974
7G	Koonap	Sandstone	2.7756	2.7932	2.8241	1.7179
7H	Koonap	Sandstone	2.7665	2.7900	2.8318	2.3074
7I	Koonap	Sandstone	2.7788	2.7930	2.8181	1.3942
7J	Koonap	Sandstone	2.7650	2.7913	2.8380	2.5740
7K	Koonap	Sandstone	2.7679	2.7910	2.8319	2.2627
7L	Koonap	Sandstone	2.7660	2.7902	2.8331	2.3669
8A	Middleton	Mudstone	2.7398	2.7591	2.7926	1.8910
8B	Middleton	Mudstone	2.7461	2.7633	2.7931	1.6835
8C	Middleton	Mudstone	2.7140	2.7452	2.7994	3.0482
8D	Middleton	Mudstone	2.7243	2.7510	2.7976	2.6208
8E	Middleton	Mudstone	2.7276	2.7531	2.7973	2.4904
8F	Middleton	Mudstone	2.7555	2.7679	2.7893	1.2130
8G	Middleton	Mudstone	2.7442	2.7614	2.7913	1.6860
8H	Middleton	Mudstone	2.7290	2.7529	2.7943	2.3369
8I	Middleton	Mudstone	2.7159	2.7464	2.7995	2.9860
8J	Middleton	Mudstone	2.7348	2.7551	2.7902	1.9853

8K	Middleton	Mudstone	2.7214	2.7503	2.8005	2.8237
8L	Middleton	Mudstone	2.7330	2.7550	2.7932	2.1572
8M	Middleton	Mudstone	2.7248	2.7508	2.7960	2.5486
9A	Balfour(Oud)	Sandstone	2.7867	2.7967	2.8142	0.9772
9B	Balfour(Oud)	Sandstone	2.7542	2.7676	2.7910	1.3189
9C	Balfour(Oud)	Sandstone	2.8001	2.8091	2.8248	0.8749
9D	Balfour(Oud)	Sandstone	2.7805	2.7912	2.8099	1.0452
9E	Balfour(Oud)	Sandstone	2.7709	2.7820	2.8014	1.0897
9F	Balfour(Oud)	Sandstone	2.7557	2.7687	2.7913	1.2767
9G	Balfour(Oud)	Sandstone	2.7795	2.7906	2.8101	1.0896
9H	Balfour(Oud)	Sandstone	2.7887	2.7987	2.8164	0.9865
9I	Balfour(Oud)	Sandstone	2.7204	2.7385	2.7694	1.7681
9J	Balfour(Oud)	Sandstone	2.7756	2.7873	2.8078	1.1463
9K	Balfour(Oud)	Sandstone	2.7731	2.7845	2.8043	1.1142
9L	Balfour(Oud)	Sandstone	2.8167	2.8248	2.8393	0.7961
9M	Balfour(Oud)	Sandstone	2.8018	2.8103	2.8252	0.8250
9N	Balfour(Oud)	Sandstone	2.7951	2.8044	2.8207	0.9099
9O	Balfour(Oud)	Sandstone	2.7281	2.7450	2.7739	1.6504
9P	Balfour(Oud)	Sandstone	2.7749	2.7860	2.8055	1.0911
9Q	Balfour(Oud)	Sandstone	2.7546	2.7680	2.7913	1.3147
9R	Balfour(Oud)	Sandstone	2.7487	2.7629	2.7875	1.3913
9S	Balfour(Oud)	Sandstone	2.7652	2.7774	2.7986	1.1918
9T	Balfour(Oud)	Sandstone	2.7761	2.7866	2.8049	1.0257
10A	Balfour (Daga)	Sandstone	2.6144	2.6286	2.6512	1.3892
10B	Balfour (Daga)	Sandstone	2.6001	2.6150	2.6384	1.4501
10C	Balfour (Daga)	Sandstone	2.6218	2.6344	2.6546	1.2346
10D	Balfour (Daga)	Sandstone	2.5872	2.6027	2.6269	1.5107
10E	Balfour (Daga)	Sandstone	2.6012	2.6166	2.6409	1.5042
10F	Balfour (Daga)	Sandstone	2.6661	2.6771	2.6950	1.0693
10G	Balfour (Daga)	Sandstone	2.2742	2.2875	2.3042	1.3031
10H	Balfour (Daga)	Sandstone	2.6965	2.7052	2.7197	0.8548
10I	Balfour (Daga)	Sandstone	2.7959	2.8009	2.8096	0.4870
10J	Balfour (Daga)	Sandstone	2.7720	2.7791	2.7915	0.7008
10K	Balfour (Daga)	Sandstone	2.7884	2.7943	2.8048	0.5843
10L	Balfour (Daga)	Sandstone	2.7881	2.7937	2.8036	0.5530
10M	Balfour (Daga)	Sandstone	2.7749	2.7815	2.7931	0.6535
10N	Balfour (Daga)	Sandstone	2.7719	2.7781	2.7890	0.6141
10O	Balfour (Daga)	Sandstone	2.7681	2.7753	2.7878	0.7049
10P	Balfour (Daga)	Sandstone	2.6936	2.7033	2.7193	0.9451
10Q	Balfour (Daga)	Sandstone	2.7060	2.7150	2.7301	0.8839
10R	Balfour (Daga)	Sandstone	2.7061	2.7158	2.7320	0.9497
10S	Balfour (Daga)	Sandstone	2.7080	2.7163	2.7300	0.8056
10T	Balfour (Daga)	Sandstone	2.6963	2.7055	2.7208	0.9033
10U	Balfour (Daga)	Sandstone	2.7048	2.7135	2.7281	0.8541
10V	Balfour (Daga)	Sandstone	2.6888	2.6980	2.7131	0.8964

10W	Balfour (Daga)	Sandstone	2.7095	2.7191	2.7351	0.9364
10X	Balfour (Daga)	Sandstone	2.7070	2.7167	2.7328	0.9425
10Y	Balfour (Daga)	Sandstone	2.7043	2.7128	2.7271	0.8352
10Z	Balfour (Daga)	Sandstone	2.7039	2.7138	2.7304	0.9709
11A	Balfour (Barb)	Sandstone	2.7161	2.7228	2.7341	0.6552
11B	Balfour (Barb)	Sandstone	2.6999	2.7079	2.7212	0.7836
11C	Balfour (Barb)	Sandstone	2.6626	2.6742	2.6931	1.1298
11D	Balfour (Barb)	Sandstone	2.6496	2.6621	2.6825	1.2263
11E	Balfour (Barb)	Sandstone	2.6713	2.6820	2.6996	1.0456
11F	Balfour (Barb)	Sandstone	2.6914	2.7004	2.7154	0.8836
11G	Balfour (Barb)	Sandstone	2.6676	2.6787	2.6968	1.0800
11H	Balfour (Barb)	Sandstone	2.6976	2.7058	2.7196	0.8088
11I	Balfour (Barb)	Sandstone	2.6796	2.6892	2.7050	0.9378
11J	Balfour (Barb)	Sandstone	2.6953	2.7036	2.7172	0.8063
12A	Balfour (Elan)	Sandstone	2.7059	2.7173	2.7366	1.1221
12B	Balfour (Elan)	Sandstone	2.7177	2.7283	2.7463	1.0431
12C	Balfour (Elan)	Sandstone	2.6852	2.6975	2.7179	1.2035
12D	Balfour (Elan)	Sandstone	2.7104	2.7216	2.7404	1.0937
12E	Balfour (Elan)	Sandstone	2.6428	2.6567	2.6792	1.3601
12F	Balfour (Elan)	Sandstone	2.6077	2.6235	2.6487	1.5491
12G	Balfour (Elan)	Sandstone	2.6794	2.6920	2.7129	1.2361
12H	Balfour (Elan)	Sandstone	2.6429	2.6564	2.6783	1.3230
13A	Balfour (Park)	Sandstone	2.7355	2.7444	2.7597	0.8786
13B	Balfour (Park)	Sandstone	2.7173	2.7284	2.7470	1.0809
13C	Balfour (Park)	Sandstone	2.7100	2.7221	2.7426	1.1902
13D	Balfour (Park)	Sandstone	2.7142	2.7259	2.7455	1.1393
13E	Balfour (Park)	Sandstone	2.7150	2.7268	2.7467	1.1544
13F	Balfour (Park)	Sandstone	2.7134	2.7251	2.7447	1.1426
13G	Balfour (Park)	Sandstone	2.7056	2.7184	2.7398	1.2468
13H	Balfour (Park)	Sandstone	2.7156	2.7271	2.7466	1.1290
13I	Balfour (Park)	Sandstone	2.7106	2.7228	2.7433	1.1907
13J	Balfour (Park)	Sandstone	2.7259	2.7361	2.7533	0.9970
14A	Katberg	Sandstone	2.7358	2.7443	2.7588	0.8345
14B	Katberg	Sandstone	2.7463	2.7548	2.7692	0.8249
14C	Katberg	Sandstone	2.7369	2.7454	2.7599	0.8336
14D	Katberg	Sandstone	2.7445	2.7530	2.7674	0.8272
14E	Katberg	Sandstone	2.7471	2.7556	2.7699	0.8236
14F	Katberg	Sandstone	2.7440	2.7525	2.7669	0.8278
14G	Katberg	Sandstone	2.7411	2.7496	2.7640	0.8303
14H	Katberg	Sandstone	2.7454	2.7539	2.7683	0.8259
14I	Katberg	Sandstone	2.7485	2.7569	2.7713	0.8229
14J	Katberg	Sandstone	2.7400	2.7485	2.7630	0.8310
15A	Burgersdorp	Mudstone	2.7275	2.7357	2.7495	0.7995
15B	Burgersdorp	Mudstone	2.7530	2.7594	2.7705	0.6324
15C	Burgersdorp	Mudstone	2.7453	2.7523	2.7642	0.6827

15D	Burgersdorp	Mudstone	2.7461	2.7529	2.7644	0.6634
15E	Burgersdorp	Mudstone	2.7379	2.7457	2.7590	0.7658
15F	Burgersdorp	Mudstone	2.7347	2.7421	2.7547	0.7273
16A	Wittberg	Quartzitic sandstone	2.7043	2.7183	2.7418	1.3667
16B	Wittberg	Quartzitic sandstone	2.7109	2.7251	2.7490	1.3887
16C	Wittberg	Quartzitic sandstone	2.7083	2.7219	2.7447	1.3263
16D	Wittberg	Quartzitic sandstone	2.7019	2.7159	2.7394	1.3666
16E	Wittberg	Quartzitic sandstone	2.7137	2.7276	2.7513	1.3660
16F	Wittberg	Quartzitic sandstone	2.7129	2.7268	2.7502	1.3555
16G	Wittberg	Quartzitic sandstone	2.7023	2.7165	2.7402	1.3820
16H	Wittberg	Quartzitic sandstone	2.7077	2.7214	2.7445	1.3409
16I	Wittberg	Quartzitic sandstone	2.7071	2.7208	2.7438	1.3352
16J	Wittberg	Quartzitic sandstone	2.7093	2.7230	2.7461	1.3415
17A	Bokkeveld	Quartzite	2.6360	2.6500	2.6725	1.3630
17B	Bokkeveld	Quartzite	2.6335	2.6481	2.6717	1.4301
17C	Bokkeveld	Quartzite	2.6325	2.6459	2.6677	1.3199
17D	Bokkeveld	Quartzite	2.6301	2.6505	2.6837	1.9950
17E	Bokkeveld	Quartzite	2.6331	2.6487	2.6740	1.5282
17F	Bokkeveld	Quartzite	2.6334	2.6483	2.6725	1.4626
17G	Bokkeveld	Quartzite	2.6364	2.6517	2.6766	1.5022
17H	Bokkeveld	Quartzite	2.6332	2.6461	2.6668	1.2599
17I	Bokkeveld	Quartzite	2.6314	2.6437	2.6634	1.1996
17J	Bokkeveld	Quartzite	2.6333	2.6456	2.6652	1.1968
18A	Table Mountain	Conglomerate	2.6907	2.7062	2.7321	1.5142
18B	Table Mountain	Conglomerate	2.7188	2.7339	2.7597	1.4815
18C	Table Mountain	Conglomerate	2.7032	2.7180	2.7430	1.4502
18D	Table Mountain	Conglomerate	2.7165	2.7304	2.7539	1.3554
18E	Table Mountain	Conglomerate	2.6980	2.7115	2.7343	1.3292
18F	Table Mountain	Conglomerate	2.7051	2.7189	2.7422	1.3539
18G	Table Mountain	Conglomerate	2.6949	2.7085	2.7313	1.3318
18H	Table Mountain	Conglomerate	2.7004	2.7157	2.7414	1.4957
18I	Table Mountain	Conglomerate	2.7123	2.7276	2.7537	1.5029
18J	Table Mountain	Conglomerate	2.7036	2.7186	2.7438	1.4636
19A	Pre Cape	Limestone	2.7341	2.7471	2.7693	1.2710
19B	Pre Cape	Limestone	2.7341	2.7467	2.7683	1.2329
19C	Pre Cape	Chert	2.7386	2.7564	2.7872	1.7460
19D	Pre Cape	Chert	2.7274	2.7398	2.7610	1.2190
19E	Pre Cape	Schist	2.8199	2.8325	2.8550	1.2288
19F	Pre Cape	Schist	2.8035	2.8153	2.8363	1.1566
19G	Pre Cape	Quartz schist	2.7368	2.7457	2.7609	0.8735
19H	Pre Cape	Fine schist	2.7230	2.7351	2.7556	1.1833
19I	Pre Cape	Fine schist	2.7396	2.7515	2.7720	1.1686
20	Intrusion	dolerite	2.7090	2.7105	2.7129	0.1454
21	Intrusion	dolerite	2.7797	2.7813	2.7841	0.1576
22	Intrusion	dolerite	2.7782	2.7794	2.7817	0.1257

23	Intrusion	dolerite	2.8287	2.8315	2.8365	0.2764
24	Intrusion	dolerite	2.7109	2.7148	2.7214	0.3868
25	Intrusion	dolerite	2.7174	2.7185	2.7203	0.1084
26	Intrusion	dolerite	2.7625	2.7649	2.7690	0.2346
27	Intrusion	dolerite	2.7840	2.7852	2.7871	0.1118
28	Intrusion	dolerite	2.7256	2.7286	2.7337	0.2983
29	Intrusion	dolerite	2.8210	2.8233	2.8274	0.2269
30	Intrusion	dolerite	2.7200	2.7224	2.7264	0.2341
31	Intrusion	dolerite	2.7876	2.7888	2.7909	0.1163
32	Intrusion	dolerite	2.7258	2.7290	2.7342	0.3081
33	Intrusion	dolerite	2.7841	2.7858	2.7888	0.1668
34	Intrusion	dolerite	2.7001	2.7016	2.7042	0.1529